Expansion Microscopy (ExM) as a tool to study organelles and intracellular pathogens

Expansionsmikroskopie (ExM) als Tool zur Untersuchung von Organellen und intrazellulären Pathogenen

Doctoral thesis

for a doctoral degree at the Graduate School of Life Sciences,

Julius-Maximilians-Universität Würzburg,

Section Infection and Immunity

submitted by

Tobias C. Kunz

from

Hanau

Würzburg, 2020

Submitted on:

Members of the Thesis Committee

Chairperson: Prof. Dr. Thomas Dandekar

Primary Supervisor: PD Dr. Vera Kozjak-Pavlovic

Supervisor (Second): Prof. Dr. Georg Nagel

Supervisor (Third): Prof. Dr. Thomas Rudel

Supervisor (Fourth): Prof. Dr. Markus Sauer

Date of public Defense:

Date of Receipt of Certificates:

Summary

The resolution of fluorescence light microscopy was long believed to be limited by the diffraction limit of light of around 200-250 nm described in 1873 by Ernst Abbe. Within the last decade, several approaches, such as structured illumination microscopy (SIM), stimulated emission depletion STED and (direct) stochastic optical reconstruction microscopy (d)STORM have been established to bypass the diffraction limit. However, such super-resolution techniques enabling a resolution <100 nm require specialized and expensive setups as well as expert knowledge in order to avoid artifacts. They are therefore limited to specialized laboratories. Recently, Boyden and colleagues introduced an alternate approach, termed expansion microscopy (ExM). The latter offers the possibility to perform superresolution microscopy on conventional confocal microscopes by embedding the sample into a swellable hydrogel that is isotropically expanded. Since its introduction in 2015, expansion microscopy has developed rapidly offering protocols for 4x, 10x and 20x expansion of proteins and RNA in cells, tissues and human clinical specimens.

Mitochondria are double membrane-bound organelles and crucial to the cell by performing numerous tasks, from ATP production through oxidative phosphorylation, production of many important metabolites, cell signaling to the regulation of apoptosis. The inner mitochondrial membrane is strongly folded forming so-called cristae. Besides being the location of the oxidative phosphorylation and therefore energy conversion and ATP production, cristae have been of great interest because changes in morphology have been linked to a plethora of diseases from cancer, diabetes, neurodegenerative diseases, to aging and infection. However, cristae imaging remains challenging as the distance between two individual cristae is often below 100 nm. Within this work, we demonstrate that the mitochondrial creatine kinase MtCK linked to fluorescent protein GFP (MtCK-GFP) can be used as a cristae marker. Upon fourfold expansion, we illustrate that our novel marker enables visualization of cristae morphology and localization of mitochondrial proteins relative to cristae without the need for specialized setups. Furthermore, we show the applicability of expansion microscopy for several bacterial pathogens, such as *Chlamydia trachomatis*, *Simkania negevensis*, *Neisseria gonorrhoeae* and *Staphylococcus aureus*. Due to differences in bacterial cell walls, we reveal important aspects for the digestion of pathogens for isotropic expansion. We further show that expansion of the intracellular pathogens *C. trachomatis* and *S. negevensis*, enables the differentiation between

the two distinct developmental forms, catabolic active reticulate bodies (RB) and infectious elementary bodies (EB), on a conventional confocal microscope. We demonstrate the possibility to precisely locate chlamydial effector proteins, such as CPAF or Cdu1, within and outside the chlamydial inclusion. Moreover, we show that expansion microscopy enables the investigation of bacteria, herein *S. aureus*, within LAMP1 and LC3-II vesicles. With the introduction of the unnatural α-NH$_2$-ω-N$_3$-C$_6$-ceramide, we further present the first approach for the expansion of lipids that may also be suitable for far inaccessible molecule classes like carbohydrates. The efficient accumulation and high labeling density of our functionalized α-NH$_2$-ω-N$_3$-C$_6$-ceramide in both cells and bacteria enables in combination with tenfold expansion nanoscale resolution (10-20 nm) of the interaction of proteins with the plasma membrane, membrane of organelles and bacteria. Ceramide is the central molecule of the sphingolipid metabolism, an important constituent of cellular membranes and regulates many important cellular processes such as differentiation, proliferation and apoptosis. Many studies report about the importance of sphingolipids during infection of various pathogens. While the transport of ceramide to *Chlamydia* has been reported earlier, one of the unanswered questions remaining was if ceramide forms parts of the outer or inner bacterial membrane. Expansion of α-NH$_2$-ω-N$_3$-C$_6$-ceramide enabled the visualization of ceramide in the inner and outer membrane of *C. trachomatis* and their distance was determined to be 27.6 ± 7.7 nm.

Zusammenfassung

Aufgrund der Beugungseigenschaften des Lichtes wurde bereits 1873 durch Ernst Abbe für die Lichtmikroskopie eine theoretische Auflösungsgrenze von 200-250 nm definiert. Durch die Einführung verschiedener hochauflösender Mikroskopiemethoden, wie beispielsweise SIM-Mikroskopie (structured illumination microscopy), STED-Mikroskopie (stimulated emission depletion) und (d)STORM-Mikroskopie ((direct) stochastic optical reconstruction microscopy), konnte im letzten Jahrzehnt jedoch die Auflösung auf unter 100 nm verbessert werden. Allerdings benötigen solche Hochauflösungstechniken sowohl spezialisierte und kostenintensive Geräte als auch Expertenwissen zur Vermeidung von Artefakten, sodass diese nur in wenigen Laboren angewendet werden können. Ein alternativer Ansatz, die sogenannte Expansionsmikroskopie, wurde kürzlich von der Arbeitsgruppe um Ed Boyden etabliert. Hierbei wird eine Probe mit einem quellfähigen Gel vernetzt, welches daraufhin isotrop expandiert wird, sodass auch an konventionellen konfokalen Mikroskopen Hochauflösung ermöglicht wird. Seit ihrer Einführung im Jahre 2015 hat sich die Expansionsmikroskopie schnell entwickelt und bietet Protokolle für 4-fache, 10-fache oder sogar 20-fache Expansion von Proteinen als auch RNA in Zellen oder sogar komplexen Geweben.

Mitochondrien besitzen zwei Membranen und sind für die Zelle von großer Bedeutung, da sie eine Vielzahl wichtiger Aufgaben übernehmen - von der ATP-Produktion durch die oxidative Phosphorylierung über die Produktion vieler wichtiger Metabolite bis hin zur Regulation zellulärer Signalwege. Die innere Mitochondrienmembran ist stark gefaltet und bildet Einstülpungen, die sogenannten Cristae, in welchen die oxidative Phosphorylierung und somit die Energieumwandlung und ATP-Synthese stattfindet. Morphologische Veränderungen der Cristae können sowohl beim Altern von Zellen, als auch bei verschiedenen Infektionen beobachtet werden und können darüber hinaus auch im Rahmen diverser Erkrankungen, wie beispielsweise Krebs, Diabetes oder neurodegenerativen Erkrankungen auftreten. Die Visualisierung der Cristae durch Fluoreszenzmikroskopie ist herausfordernd, da der Abstand zwischen einzelnen Cristae oftmals unter 100 nm beträgt. In der vorliegenden Arbeit wird gezeigt, dass die Expression der mitochondrialen Kreatinkinase gekoppelt an das Fluoreszenzprotein GFP (MtCK-GFP) als Cristaemarker genutzt werden kann. In Kombination mit vierfacher Expansion ermöglicht unser Marker die Untersuchung morphologischer Veränderungen von Cristae, sowie die Lokalisierung mitochondrialer Proteine relativ zu den

Cristae. Darüber hinaus wird im Rahmen dieser Arbeit die Anwendbarkeit der Expansionsmikroskopie für mehrere bakterielle Pathogene, und zwar *Chlamydia trachomatis*, *Simkania negevensis*, *Neisseria gonorrhoeae* und *Staphylococcus aureus,* gezeigt. Hierbei verdeutlichen wir wichtige Aspekte für den vollständigen Verdau unterschiedlicher bakterieller Zellwände und somit isotropen Expansion. Die Expansion der intrazellulären Pathogene *C. trachomatis* und *S. negevensis* ermöglichte es uns an konventionellen konfokalen Mikroskopen zwischen den zwei verschiedenen Entwicklungsstadien, der katabolisch aktiven Retikulärkörperchen (RBs) und der infektiösen Elementarkörperchen (EBs), zu unterscheiden. Außerdem konnte die Möglichkeit der präzisen Lokalisierung chlamydialer Proteine wie CPAF und Cdu1 innerhalb und außerhalb der chlamydialen Inklusion gezeigt werden und Bakterien, in diesem Fall *S. aureus*, in LAMP1 und LC3-II Vesikeln visualisiert werden. Mit der Einführung des unnatürlichen α-NH$_2$-ω-N$_3$-C$_6$-Ceramides, präsentieren wir zudem ein erstes Konzept für die Expansion von Lipiden, welches möglicherweise auch für deutlich unzugänglichere Molekülklassen wie beispielsweise Kohlehydrate geeignet ist. Die effiziente Akkumulierung unseres funktionalisierten α-NH$_2$-ω-N$_3$-C$_6$-Ceramides in Zellen sowie Bakterien ermöglicht in Kombination mit zehnfacher Expansion die Untersuchung der Interaktion von Proteinen mit der Zellmembran, Membranen von Organellen und Bakterien mit einer räumlichen Auflösung von 10-20 nm. Ceramid ist das zentrale Molekül des Sphingolipidstoffwechsels, ein wichtiger Baustein zellulärer Membrane und reguliert viele essentielle Prozesse wie die Zelldifferenzierung, die Proliferation als auch die Apoptose. Viele Studien berichten von der Bedeutung der Sphingolipide während der Infektion verschiedener Pathogene. So wurde beispielsweise zuvor berichtet, dass Ceramide aktiv zu *Chlamydien* transportiert und in deren Membranen eingebaut werden. Hierbei verblieb allerdings die Frage, ob Ceramide in der äußeren oder inneren bakteriellen Membran lokalisiert sind. Die Expansion unseres α-NH$_2$-ω-N$_3$-C$_6$-Ceramides ermöglichte es uns Ceramide in der inneren und äußeren Membran von *C. trachomatis* zu visualisieren und den Abstand zwischen beiden Membranen auf 27.6 ± 7.7 nm zu bestimmen.

Table of contents

Table of contents

Introduction

Mitochondria

Mitochondria are well defined double membrane-bound organelles in eukaryotic cells and are thought to be the result of an endosymbiotic event between an α-proteobacterium and a host cell that took place around 1.5-2 billion years ago (Sicheritz-Ponten et al., 1998). Their numerous tasks include the citric acid cycle, fatty acid metabolism, ATP-synthesis through oxidative phosphorylation, apoptosis induction and calcium homeostasis (Westermann, 2010). Mitochondria possess their own genome encoding for only 13 mitochondrial proteins in mammals (Anderson et al., 1981). As in bacteria, the mitochondrial DNA (mtDNA) is a circular double-stranded molecule, organized in nucleoids and tethered to the inner mitochondrial membrane (Chen and Butow, 2005). While mtDNA encodes only for a few
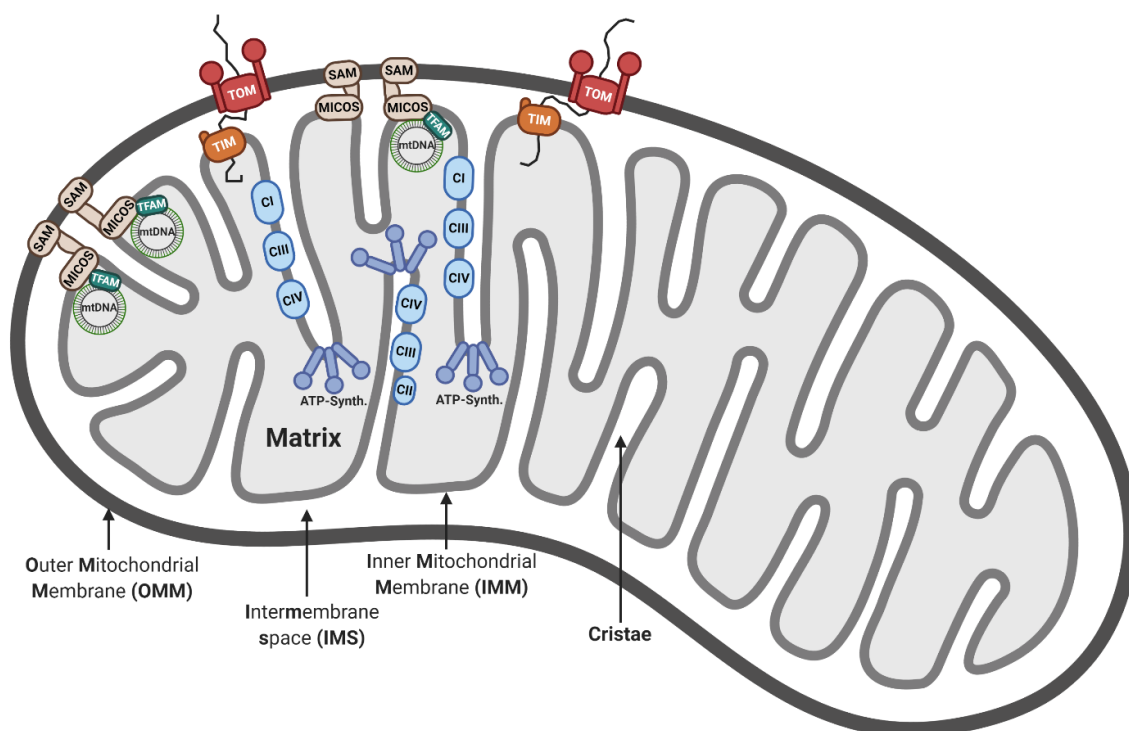
Figure 1: Schematic overview of mitochondria

The powerhouse of the cell can be subdivided into four different compartments: Outer mitochondrial membrane (OMM), intermembrane space (IMS), inner mitochondrial membrane (IMM) and matrix. The IMM is strongly folded increasing the membrane surface and forming mitochondrial cristae. It is subdivided by the cristae-junctions (CJs) into the cristae membrane and the inner boundary membrane that is located close to the OMM. The cristae membrane harbors the OXPHOS complexes (CI-CIV) and the ATP-Synthase. CJs are formed by the so-called mitochondrial cristae organizing system (MICOS) complex. Nuclear-encoded proteins are imported through the translocase of the outer membrane (TOM) to the mitochondrial intermembrane space and through the translocase of the inner membrane (TIM) to the mitochondrial matrix.

proteins, mitochondria possess about 1000 (yeast) to 1500 (mammalian) proteins (Meisinger et al., 2008; Reinders et al., 2006). It is thought that through evolution the information for most mitochondrial proteins shifted to the DNA in the nucleus (Gabaldon and Huynen, 2003). The two mitochondrial membranes divide the organelle into four compartments: The outer mitochondrial membrane (OMM), the intermembrane space (IMS), the inner mitochondrial membrane (IMM) and the mitochondrial matrix. The IMM is strongly folded to increase the membrane surface forming invaginations, the so-called cristae. Cristae harbor the respiratory chain complexes as well as the ATP-synthetase, producing most of the cells ATP and are thus crucial for the well-being of the cell (**Figure 1**) (Friedman and Nunnari, 2014).

Mitochondrial dynamics

While mitochondria are often depicted as single-rod shaped structures, they form a highly dynamic network throughout the cytosol, constantly fusing and dividing. These processes are described as mitochondrial dynamics, fusion and fission, and are crucial for the regulation of mitochondrial processes and adaption to environmental changes and are therefore important for optimal cellular health. Thus, mitochondrial dynamics is regulated by a well-conserved set of cytoplasmic and mitochondrial proteins (Hoppins et al., 2007). Several studies demonstrated that stimulation of OXPHOS activity stimulates mitochondrial fusion and elongation, indicating that elongated mitochondria are more efficient in energy conversion. Fragmented mitochondria, on the other hand, were shown to be more capable to produce reactive oxygen species (Jezek et al., 2018). Moreover, mitochondrial dynamics were found to control calcium homeostasis (Szabadkai et al., 2004).

Under starvation, the cell reacts by fusing and hence elongating mitochondria. Since mitochondria have a double membrane structure, fusion is performed in two steps. First, fusion of the outer membrane by the mitofusins Mfn1 and Mfn2 and second, fusion of the inner membrane mediated by Opa proteins. Mfn1 and Mfn2 form homotypic and heterotypic dimers via hydrophobic HR2 regions, allowing the close contact between two individual mitochondrial fragments. Upon GTP-dependent conformational change in the Mfn1 structure, the gap between two fragments is closed (Galloway and Yoon, 2013). After the fusion of the outer membrane, different isoforms of the OPA1 protein mediate the fusion of the inner mitochondrial membrane, leading to the exchange of matrix proteins. There are eight long

isoforms of the OPA1 protein undergoing further modification by proteolytic cleavages through mitochondrial proteases, generating shorter isoforms of OPA1, the so-called S-OPA1 (Delettre et al., 2001). It has been shown that both, long and short, isoforms of OPA1 are important for successful mitochondrial fusion (Song et al., 2007). Under various stress conditions, OMA1 degrades the longer OPA1 isoforms and consequently inhibits mitochondrial fusion (Baricault et al., 2007; Duvezin-Caubet et al., 2006; Guillery et al., 2008; Ishihara et al., 2006; Song et al., 2007). In addition, the loss of the ATP dependent AAA protease Yme1L leads to an impairment of OPA1 cleavage and thus S-OPA1 production. This leads to a fragmentation of the mitochondrial network, perturbs cristae morphogenesis and promotes apoptosis (Griparic et al., 2007; Stiburek et al., 2012). Mitochondrial fission is modulated by Drp1 (Dynamin-related protein 1) possessing a conserved GTPase. Contrarily to mitochondrial fusion, mitochondrial fission does not necessitate independent processes for the fission of outer and inner membrane (Yoon et al., 2011). Several proteins have been shown to be important key players of mitochondrial fission by recruiting Drp1 to facilitate mitochondrial fission (Loson et al., 2013). Human Drp1 self-assembles into ring-like oligomers around the mitochondria in the presence of GTP. Upon GTP hydrolysis, the Drp1 ring undergoes conformational changes leading to the constriction of the ring and consequently to mitochondrial fission (Ingerman et al., 2005; Mears et al., 2011).

Mitochondrial import

Interestingly, 20-25% of the mitochondrial proteome is necessary to maintain, regulate and express the mitochondrial genome, which only codes for around 1% of mitochondrial proteins. As most mitochondrial proteins are encoded in nuclear genes and are expressed on the cytosolic ribosomes, eukaryotic cells had to develop a highly regulated mitochondrial import system, transporting mitochondrial proteins to the designated mitochondrial compartment (**Figure 2**). The mitochondrial protein organization and insertion has been recently reviewed in detail by Pfanner et al (Pfanner et al., 2019).

Around 60% of all mitochondrial precursor proteins are transported through the classical import pathway, synthesized with a targeting sequence directing mitochondrial proteins to mitochondrial surface proteins and subsequently the correct mitochondrial compartment (Vogtle et al., 2009). These presequences form to a large extent positively charged
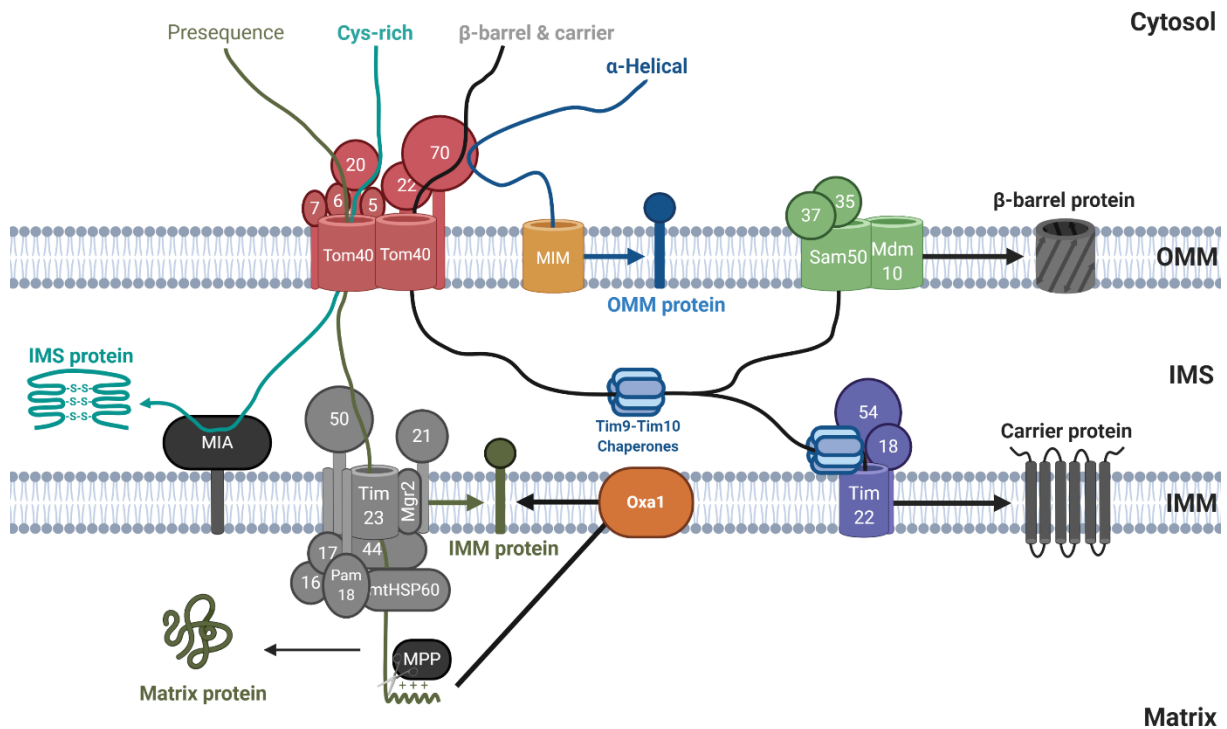
Figure 2: Mitochondrial protein import pathways

Nuclear encoded proteins can be imported to mitochondria by five different major pathways. The most common pathway is importing presequence-carrying cleavable precursor proteins. First, these precursor proteins are bound by Tom20 and Tom22 and translocated by the Tom40 channel into the intermembrane space. Afterwards, they are translocated by Tim23 to the mitochondrial matrix, where the presequence gets cut off by MPP. If these proteins are destined to the inner membrane, they are either transported to the matrix and are then inserted to the IMM by the oxidase assembly (Oxa1) insertase or carry additional hydrophobic sorting signals stopping the translocation by Tim23 and permitting the release to the inner membrane by the lateral gatekeeper Mgr2. Multi-spanning inner membrane proteins are transported by an alternative pathway, the so-called carrier pathway. Here, the precursors are bound by Tom70 and translocated to the intermembrane space by Tom40. The precursors are then transferred to small Tim-chaperones and inserted into the inner membrane by the Tim22 carrier translocase. β-barrel proteins, typically inserted into the outer membrane, follow the same pathway as carrier proteins but are inserted by the sorting and assembly machinery (SAM). Lastly, many intermembrane space proteins contain characteristic cysteine motifs. These proteins are translocated by Tom40 and then recognized by the MIA system, maturating the precursors by forming internal disulfide bonds.

amphipathic α-helices that are typically bound by the TOM receptors Tom20 and Tom22 and are then directed from the cytosol through the main protein translocation channel Tom40 into the IMS (Abe et al., 2000; Kuszak et al., 2015; Melin et al., 2014; van Wilpe et al., 1999). Afterwards, the protein is transferred through the translocase of the inner membrane Tim23 through the IMM (Lohret et al., 1997). The ATP-driven mitochondrial heat shock protein 70 (mtHsp70) of the presequence translocase associated motor (PAM) then promotes, together with five co-chaperons, the translocation of the entire polypeptide to the mitochondrial matrix. In the matrix, the presequence is cleaved by the mitochondrial processing peptidase (MPP) and mtHsp70 and other chaperones, such as Hsp60-Hsp10, promote proper folding of

the imported protein in its active form (Cheng et al., 1989; Fukasawa et al., 2015; Ostermann et al., 1989). Proteins destined for the IMM can either be inserted from the matrix by the oxidase assembly (Oxa1) insertase, which is also responsible for the insertion of proteins expressed at mitochondrial ribosomes, or by possessing an additional hydrophobic sorting signal behind the presequence (Stiller et al., 2016). In that case, the translocation stops at the Tim23 complex and the lateral gatekeeper Mgr2 permits a release of the protein to the IMM. This process is called stop transfer pathway (Ieva et al., 2014).

Hydrophobic multi-spanning IMM proteins are imported by the carrier pathway. The precursors of these proteins have no amino-terminal targeting presequences but rather internal hydrophobic targeting signals. In contrast to the classical import pathway, the precursors of the carrier pathway are delivered to the receptor Tom70, rather than Tom20 and Tom22, by cytosolic chaperons, namely Hsp90 and Hsp70 (Young et al., 2003). After binding of Tom70, the precursor proteins dissociate from the chaperons and are transported through the Tom40 channel in a loop formation. They are then engaged by small TIM chaperons of the IMS to prevent aggregation of the hydrophobic precursors and to guide the precursors to the carrier translocase Tim22 for membrane insertion into the IMM (Koehler et al., 1998; Okamoto et al., 2014; Sirrenberg et al., 1998; Vial et al., 2002; Wiedemann et al., 2001). Interestingly, while it has been shown that the import of multi-spanning alpha-helical proteins happen through the receptor Tom70, the exact mechanism for single-spanning proteins is unknown. Another class of proteins within mitochondrial membranes are β-barrel proteins. Precursors of this protein family initially follow the same pathway as carrier proteins through the TOM complex to the IMS (Jores et al., 2016) where they also interact with TIM chaperones (Weinhaupl et al., 2018). However, these precursors carry the carboxy-terminal β-strand directing the interaction with the sorting and assembly machinery (SAM) in a process involving translocation through the SAM channel and lateral release into the hydrophobic phase of the OMM (Hohr et al., 2018; Klein et al., 2012; Kozjak et al., 2003; Kutik et al., 2008; Paschen et al., 2003; Wiedemann et al., 2003). In contrast, α-helical transmembrane segments are usually not imported through the Tom40 channel. The sorting signal here consists of positively charged amino acids flanking the transmembrane segments and are recognized by the mitochondrial import (MIM) channel for membrane insertion (Becker et al., 2011; Dimmer et al., 2012; Hulett et al., 2008; Kruger et al., 2017; Papic et al., 2011; Popov-Celeketic et al.,

2008). IMS proteins usually contain characteristic cysteine motifs that, in order to form mature proteins, are oxidized in the IMS to form dimers by the formation of covalent disulfide bonds between subunits. First, upon translocation through Tom40, the precursors are recognized by the subunit Mia40, an oxireductase with disulfide isomerase activity, of the mitochondrial intermembrane space import and assembly (MIA) system. Mia40 forms a transient disulfide bond which it then transfers to the precursor protein to form the mature protein (Chacinska et al., 2004; Koch and Schmid, 2014). After each transfer, Mia40 becomes reduced and re-oxidized by Erv1, another subunit of the MIA complex. Hence, Erv1 restores the disulfide bonds of Mia40 that are transferred to the precursors for the protein maturation during the import of IMS proteins (Hell, 2008).

Cristae morphology

For a long time, the morphology of the folds of the IMM, cristae, were believed to be static. In the 1960s, however, Charles Hackenbrock observed that the addition of ADP reversibly changed the IMM connectivity in rat liver mitochondria (Hackenbrock, 1966; Hackenbrock, 1968). Moreover, another study revealed in the early 2000s that cristae reorganization occurs during fusion and fission events (Mannella et al., 2001) and during induction of apoptosis (Scorrano et al., 2002). With the rise of super-resolution in the last decade, it could be shown in living samples that cristae membranes are highly dynamic (Stephan et al., 2019). Cristae generally adopt a tubular shape directing to the inner matrix and are adapting to different cellular conditions and stimuli like nutrient depletion or changes in lipid and protein composition. Changes in cristae morphology are often linked to diseases, e.g. Barth syndrome, Alzheimer's disease, various types of cancer, Wolf-Hirschhorn syndrome, autosomal dominant optic atrophy (ADOA), Down syndrome, neuropathy, ataxia and retinitis pigmentosa (NARP), maternally inherited Leigh syndrome (MILS) or Parkinson's disease (Zick et al., 2009). The mitochondrial cristae biogenesis has been recently reviewed in detail by Kondadi et al (Kondadi et al., 2019).

Cristae are separated from the inner boundary membrane by cristae junctions (CJs) with a diameter of 12-40 nm (Nicastro et al., 2000; Perkins et al., 2003). It was proposed that these cristae junctions restrict the normal passage of proteins, metabolites and even protons towards and away from cristae, creating another distinct subcompartment of mitochondria

(Mannella et al., 1997; Vogel et al., 2006). Mitofilin, also referred to as Mic60, was shown to be crucial for cristae formation. It was also shown that mitofilin is the central part of the so-called MICOS-complex (**Figure 3**). This very large complex is located at the CJ and required for CJ formation and the formation of contact sites between the inner boundary membrane and OMM (Harner et al., 2011; Hoppins et al., 2011; Huynen et al., 2016; von der Malsburg et al., 2011). The complex consists of 7 main subunits, namely Mic60/Mitofilin, Mic10, Mic19, Mic25, Mic13, Mic26 and Mic27 (Wollweber et al., 2017). Loss of any of the individual subunits results in the loss or reduction of CJs and cristae detaching from the inner boundary membrane forming concentric rings (Harner et al., 2011; Hoppins et al., 2011; von der Malsburg et al., 2011). Mic60 is considered the central unit of the MICOS complex and is necessary for the CJ formation and the contact between inner boundary membrane and OMM due to the interaction with several OMM proteins, such as the TOM-complex, Sam50 or metaxin (Abrams et al., 2015; Genin et al., 2016; Glytsou et al., 2016; Korner et al., 2012; Ott et al., 2012; Pinero-Martos et al., 2016; Xie et al., 2007). The depletion of Mic10, a relatively small self-oligomerizing protein, also results in the loss of CJ and the appearance of cristae stacks (Barbot et al., 2015; Bohnert et al., 2015; Milenkovic and Larsson, 2015). Together, Mic60 and Mic10 have the capability to bend membranes and thus to control the cristae biogenesis (Barbot et al., 2015; Hessenberger et al., 2017; Tarasenko et al., 2017). The loss of Mic13 has also been demonstrated to be important for the formation of CJs as its loss leads to the drastic destabilization of other Mic-proteins, being Mic10, Mic26 and Mic27. Interestingly, the loss of Mic13 does not affect the assembly of Mic60, Mic19 and Mic25, suggesting two distinct subcomplexes, which are Mic60-19-25 and Mic10-13-26-27 (Anand et al., 2016; Guarani et al., 2015; Kondadi et al., 2019). Mic26 and Mic27 have been shown to be essential for the maintenance of cristae morphology and respiration but not for the formation of CJs (Koob et al., 2015; Weber et al., 2013). While the exact role of the MICOS complex is unknown, the depletion of these subunits affects cristae formation, respiration, protein import, lipid transport, mtDNA organization, apoptosis and autophagy. Changes in the levels of MICOS components were associated with a high subset of pathologies, such as diabetes, epilepsy, Down syndrome and Parkinson's disease. Mutations in Mic13 cause severe mitochondrial encephalopathy (Guarani et al., 2016; Zeharia et al., 2016). Taken together, the very large complex is crucial for cristae formation, CJ formation and mitochondrial function. The most prominent protein complexes located in cristae membranes are the respiratory chain

complexes and the F_1F_O ATP synthase for energy conversion. Besides ATP-production, the F_1F_O-ATP synthase has been demonstrated to be important in the maintenance of cristae shape. The F_1 subunit of the synthase is the catalytic subunit, is facing the mitochondrial matrix and is sufficient for ATP-production. The F_O subunit is embedded in the cristae membrane and enables the dimerization and oligomerization improving the stability of the complex and furthermore was shown to bend the IMM by association at a defined angle contributing in cristae formation (Blum et al., 2019; Davies et al., 2011; Hahn et al., 2016; Strauss et al., 2008; Wittig et al., 2007). Conformingly, the depletion of dimer-specific subunits of the F_O subunit results in perturbed cristae structure (Paumard et al., 2002). It has been shown that Mic10 binds to oligomeric F_1F_O-ATP synthase and further promotes its oligomerization together with Mic26 (Eydt et al., 2017; Rampelt et al., 2017). Moreover, Mic60 plays an antagonist role to the e and g subunit of the F_1 unit of the ATP synthase (Rabl et al., 2009). These interactions possibly modulate the curvature of the IMM near CJs. Besides the importance of the
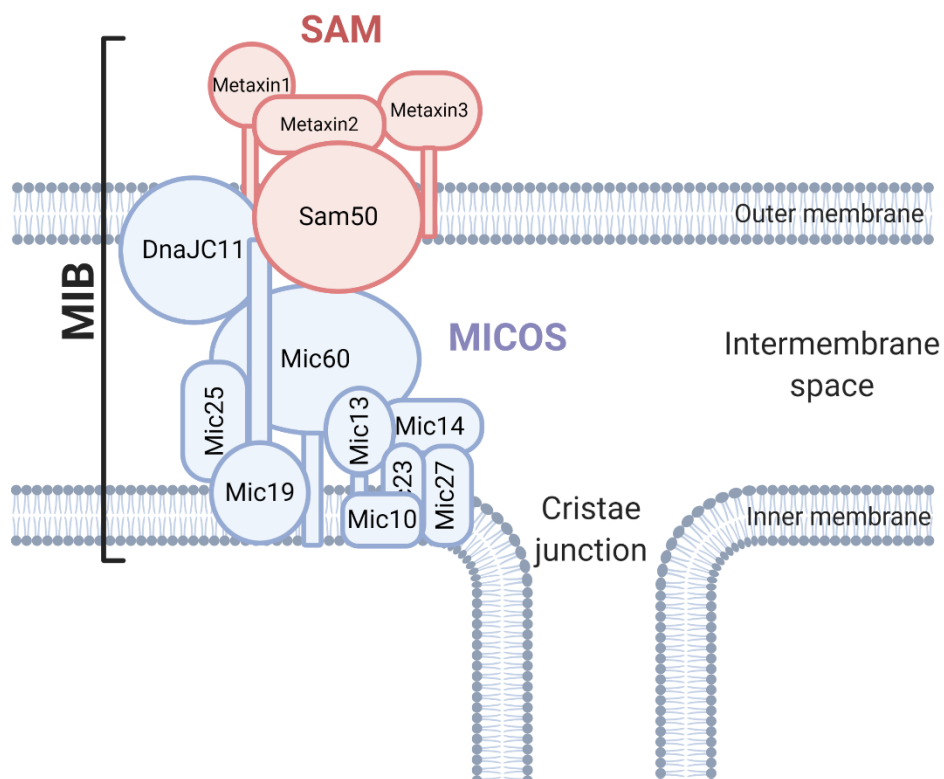
Figure 3: Schematic overview of the MIB-complex

The mitochondrial intermembrane space bridging (MIB) complex consists of the mitochondrial contact site and mitochondrial cristae organising system (MICOS) and the sorting and assembly machinery (SAM) and hence bridges the outer and inner mitochondrial membrane. Among many critical functions, the MICOS and MIB complexes are crucial for the formation of cristae junctions and thus in determining cristae morphology. The central component of the complex is mitofilin (Mic60). Modified after Kozjak-Pavlovic (Kozjak-Pavlovic, 2017).

interaction of ATP-synthase and the MICOS complex and besides being crucial for the fusion of the IMM, short- and long-form Opa1 has been shown to be necessary to keep CJs closed and hence to limit release of metabolites including cytochrome C (Frezza et al., 2006; Olichon et al., 2003). Opa1 was discovered to be important for the maintenance of mtDNA (Elachouri et al., 2011). The loss of the inner membrane protein Optic atrophy 1 (OPA1) leads to cristae membrane widening and results in the induction of apoptosis. Recently, it was proposed that after OMM fusion, the IMM in proximity is tethered by Mgm1, the yeast ortholog of OPA1, to initiate the fusion of the IMM along the IMM/OMM contact sides. This would result in the generation of cristae-shaped sacs protruding into the matrix (Harner et al., 2016). On the contrary, tubular cristae are supposedly formed by invaginations of the IMM (Zick et al., 2009). Opa1 was also reported to induce oligomerization of the F_1F_O-ATP synthase for protection against oxidative stress (Quintana-Cabrera et al., 2018), to function epistatic to the MICOS complex in order to regulate the width of CJs (Glytsou et al., 2016) and to interact with Mic60 (Barrera et al., 2016). However, Opa1 is influencing but not crucial for CJ formation (Barrera et al., 2016).

Chlamydia

Discovery of *Chlamydia* and the Taxonomy of Chlamydiales

In 1907 *Chlamydia* have first been described by the German dermatologist and radiologist Halberstädter and Austrian bacteriologist Prowazek. In their studies, Halberstädter and Prowazek demonstrated that scraping particles of patients suffering from trachoma gave rise to conjunctival infection in the eyes of orangutans. In addition, they found similar inclusion bodies in the urethral scrapings of men suffering from non-gonococcal urethritis (Halberstaedter, 1907). At that time, *Chlamydia* were described as a class of protozoans cloaking around the nucleus and were thus called *Chlamydia* after the ancient Greek term "chlamys" for mantle (Byrne, 2003). For a long time, *Chlamydia* were mistaken as a virus because they were passing bacterial filters and exhibit an obligate intracellular lifestyle. In the late 1960s, however, James W. Moulder revealed via electron microscopy that *Chlamydia* show cellular structure reminiscent of bacteria including a gram-negative cell wall. Furthermore, he showed that *Chlamydia* possess ribosomal particles and DNA-RNA metabolism pathways exclusive to bacteria (Moulder, 1966).

The order of Chlamydiales encompasses gram-negative, obligate intracellular parasites of eukaryotic cells, exhibiting a unique biphasic life cycle. Initially, the genus *Chlamydia* was subdivided into only two species, *Chlamydia trachomatis* for human pathogens and *Chlamydia psittaci* for strains isolated from a broad variety of animal sources (Page, 1968). In the late 1980s, the rise of 16S and 23S rRNA sequencing led to an improvement in phylogeny analysis (Woese and Fox, 1977). However, the first proposal to rearrange the chlamydial taxonomy based on rRNA sequencing was made in 1999, sub-dividing the order of Chlamydiales in four families: Simkaniaceae, Waddliaceae, Parachlamydiaceae and Chlamydiaceae (Everett et al., 1999). The latter was further subdivided into two genera *Chlamydophila* and *Chlamydia*, compromising *Chlamydophila abortus*, *Chlamydophila caviae*, *Chlamydophila felis*, *Chlamydophila psittaci*, *Chlamydophila pecorum*, *Chlamydia muridarum*, *Chlamydia suis* and the two important human pathogens *Chlamydophila pneumoniae* and *Chlamydia trachomatis* (**Figure 4**) (Bush and Everett, 2001; Everett et al., 1999). Even though this is still valid today, the two-genera classification has been challenged recently to reunite to a single genus *Chlamydia* (Greub, 2010; Sachse et al., 2015).
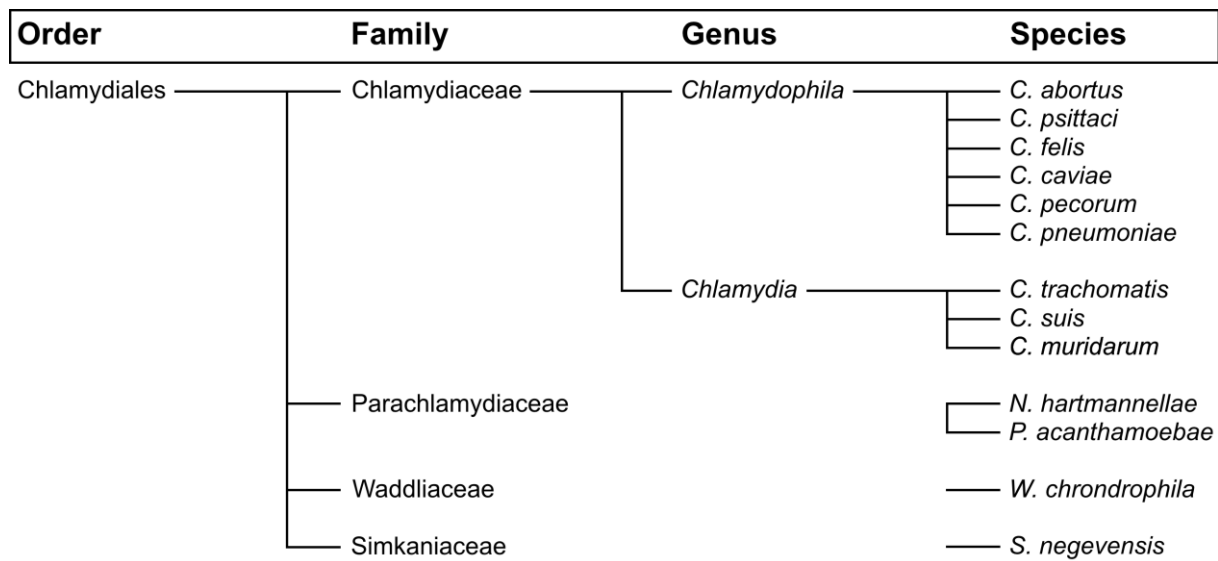
Order	Family	Genus	Species
Chlamydiales	Chlamydiaceae	*Chlamydophila*	*C. abortus* *C. psittaci* *C. felis* *C. caviae* *C. pecorum* *C. pneumoniae*
		Chlamydia	*C. trachomatis* *C. suis* *C. muridarum*
	Parachlamydiaceae		*N. hartmannellae* *P. acanthamoebae*
	Waddliaceae		*W. chrondrophila*
	Simkaniaceae		*S. negevensis*

Figure 4: Taxonomy of the order Chlamydiales

Classification of the order of Chlamydiales based on 16S and 23S rRNA sequencing. The order comprises four families: Chlamydiaceae, Parachlamydiaceae, Waddliaceae and Simkaniaceae. The Chlamydiaceae family is subdivided in two genera, *Chlamydophila* and *Chlamydia*. They consist of 9 different species, which also comprises the important human pathogens *Chlamydophila pneumoniae* and *Chlamydia trachomatis*. The distance of the drawn lines does not correlate to the phylogenetic distance.

Pathogenesis of Chlamydiales

Members of the order Chlamydiales infect a broad range of different hosts and different tissues and therefore have very diverse pathologies. Pathogenic *Chlamydia* infecting humans most likely are *C. trachomatis* and *C. pneumoniae* (Collingro et al., 2011). Furthermore, *C. psitacci* and *C. abortus* were shown to be capable of infecting humans through zoonotic transmission. While *C. psittaci* usually infects birds, it can cause psittacosis in humans, resulting in flu-like symptoms to serious pneumonia (Chau et al., 2015; Knittler and Sachse, 2015). *C. abortus* causes abortion in horses, rabbits, guinea pigs, mice and pigs, but can also cause abortion in humans (Thomson et al., 2005; Wheelhouse and Longbottom, 2012).

C. trachomatis exclusively infects human tissue and is the most sexually transmitted disease (STD). It is subdivided by serological classifications to the serovars A to C, causing chronic inflammatory ocular trachoma, the serovars D to K, causing sexually transmitted bacterial diseases affecting the ano-urogenital regions, and L1 to L3, causing Lymphogranuloma Venerum (LGV) (Harrop et al., 1940; Wang and Grayston, 1970).

C. trachomatis can lead to urethritis in men and cervical infections in women. A cervicitis can eventually lead to pelvic inflammatory disease, which is a major risk for infertility and ectopic pregnancy. Moreover, infection with *C. trachomatis* in the genital tract of women is linked to cancer development (Meijer et al., 1989; Ness et al., 2003; Zhu et al., 2016). The urethritis in men can progress to the upper genital tracts, potentially leading to epidymitis and infertility (Schachter et al., 1976). Furthermore, *C. trachomatis* is the causative agent of ocular trachoma, which can possibly lead to blindness, especially in countries with poor health care and insufficient access to antibiotics. According to the world health organization (WHO), trachoma is a public health problem in 44 countries, responsible for 1.9 million people suffering from blindness or visual impairment with another 137 million people threatened to develop trachoma induced blindness or visual impairment (Cogan, 2020).

C. pneumoniae can infect humans, but can also infect marsupials, horses and frogs (Grayston et al., 1990). It causes a plethora of diseases, from pulmonary disorder, reactive arthritis to asthma and in more specific cases coronary heart disease, multiple sclerosis and lung cancer (Belland et al., 2004; Chaturvedi et al., 2010; Fainardi et al., 2008; Hahn et al., 1991; Joshi et al., 2013).

The unique biphasic life cycle of *Chlamydia*

Chlamydia developed a unique biphasic life cycle, changing between two morphologically and physiologically distinct forms, to overcome the obstacles of infection, from entry, living and replicating within the host cell as survival to transitioning to new host cells (**Figure 5**) (Gaylord, 1954; Omsland et al., 2012). The first phase of the cycle is the electron dense, infectious elementary body (EB) with a diameter of only 0.3 μm (Constable, 1959). The metabolism of EBs is strongly reduced to survive harsh extracellular conditions (Omsland et al., 2012). Upon attachment and entry to the host cell, *Chlamydia* form a membrane-bound compartment, the so-called inclusion, in which EBs differentiate to the non-infectious, metabolically active and replicative reticulate bodies (RBs), with a much larger diameter of up to 1 μm. Within the inclusion, RBs replicate via a unique polarized budding process (Abdelrahman et al., 2016). *Chlamydia* may also persist over long time inside the host cell, differentiating into aberrant bodies (ABs) as a response to stress e.g. starvation. In this form, the chlamydial particles exhibit a strongly reduced metabolic activity and inhibit cell division but remain viable for a

long period of time and can redifferentiate asynchronously into RBs once conditions improve (Allan and Pearce, 1983; Raulston, 1997; Wyrick, 2010).
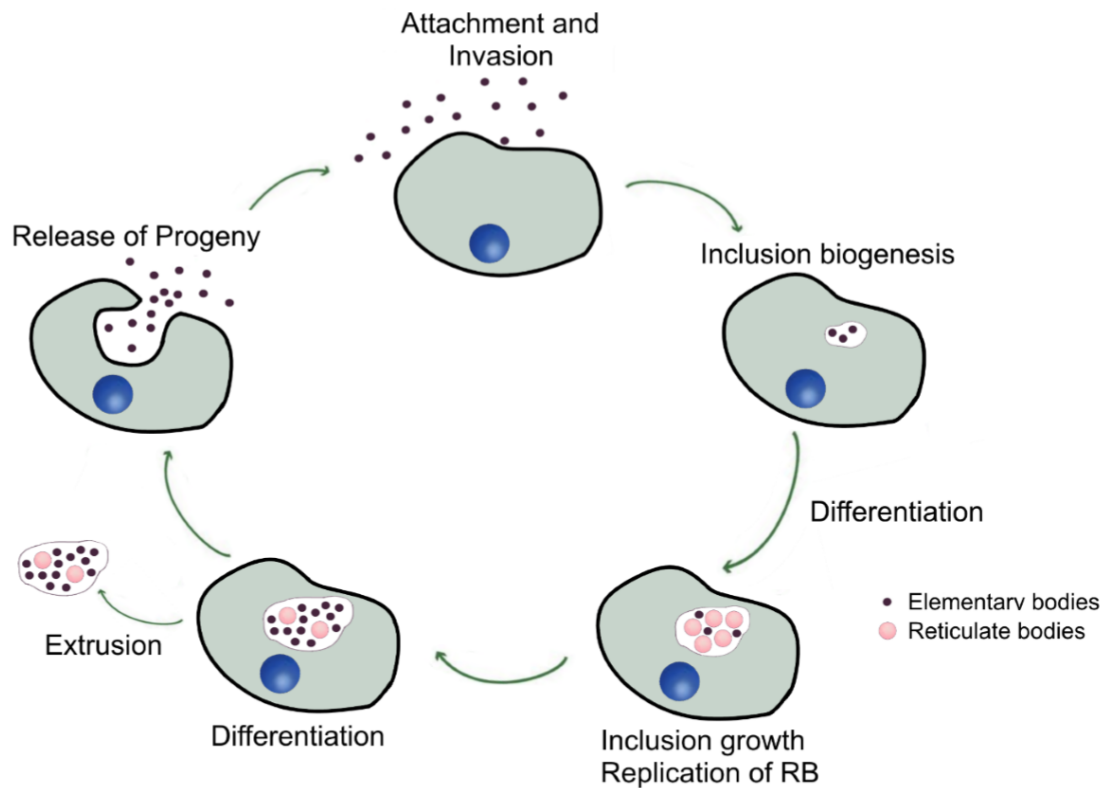

Figure 5: *Chlamydia* **and their unique biphasic life cycle**

The chlamydial life cycle starts with the infectious elementary body (EB) attaching to the host cell membrane and its uptake via endocytosis. The EB then differentiate to the non-infectious, metabolically active and replicative reticulate body (RB). After propagation, the reticulate bodies redifferentiate into infectious EBs, which then get released via host cell lysis or inclusion extrusion to infect new host cells (Kunz, 2017).

The attachment of EBs is mediated through several chlamydial ligands and host surface proteins like a reversible electrostatic interaction with heparan sulfate moieties (Abdelrahman and Belland, 2005). Attachment then leads to the injection of chlamydial effector proteins to the host cell cytoplasm through a type III secretion system (T3SS), which are among other things responsible for actin remodeling and consequent uptake of *Chlamydia* by receptor mediated endocytosis (Clifton et al., 2004). Upon internalization, the infectious EBs differentiate to RBs and form the membrane bound vacuole called inclusion, which gets heavily modified with type III secreted inclusion proteins (Inc) to ensure a microtubule-based transport to the Golgi apparatus and to avoid lysosomal fusion (Grieshaber et al., 2003; Scidmore et al., 2003). While *C. pneumonia* infected cells contain several inclusions, *C. trachomatis* mediate homotypic fusion of several inclusions via IncA (Weber et al., 2016). For

the replication via binary fission, the inclusion interacts with host organelles, such as ER, Golgi and mitochondria, for nutrient acquisition and inhibition of apoptosis (Elwell et al., 2016). After several rounds of replication, the RBs redifferentiate asynchronously to EBs. Although the exact stimulus for redifferentiation is unknown, a recent study suggests that the conversion is controlled by the size of RBs and may be triggered by RBs "falling off" the inclusion membrane in the lumen of the inclusion (Wilson et al., 2006). Redifferentiation can be strongly inhibited by antibiotics or the lack of nutrients. It has been shown that among others, sphingolipids, especially ceramides, are crucial for conversion. Under normal conditions and after redifferentiation, the infectious EBs get released either by host cell lysis or inclusion extrusion and can then infect new cells (Hybiske and Stephens, 2007).

Simkania negevensis

In the last decades, a big subset of *Chlamydia*-related bacteria has been discovered and described, among those *Simkania negevensis* (Everett et al., 1999; Kahane et al., 1993). All these bacteria are classified in the Chlamydiales order and exhibit the biphasic life cycle with infectious elementary bodies (EBs) and replicative reticulate bodies (RBs) (Kahane et al., 1999; Kahane et al., 1993). Due to the lack of diagnostics of those bacteria, very little is known regarding their pathogenicity.

The first *Chlamydia*-like organism, *S. negevensis*, was discovered as a cell culture contaminant in 1993 (Kahane et al., 1993). Even though *S. negevensis* exhibits a similar life cycle as *Chlamydia*, it could not be recognized by *Chamydia*-specific PCR primers or antibodies. The comparison of the 16S/23S rRNA encoding genes of *S. negevensis* with *Chlamydia* led to the description of the *Simkaniaceae* family within the order of Chlamydiales (Everett and Andersen, 1997). *S. negevensis* was shown to infect a broad range of hosts, from amoeba (Kahane et al., 2001), arthropods (Croxatto et al., 2014; Sixt et al., 2012), human and simian epithelial cells to macrophages and monocytes (Kahane et al., 2008; Kahane et al., 2007; Kahane et al., 1993). Interestingly, the genome of *S. negevensis* is characterized by a 2-3-fold larger size compared to *Chlamydia*, most-likely contributing to the adaptability of the bacterium (Collingro et al., 2011). Furthermore, *S. negevensis* can remain within host cells for up to 10 days without host cell lysis, building enormous inclusions. However, simkanial propagation is characterized by an exponential growth within the first three days of infection,

followed by a plateau phase and the start of infectious progeny release (Vouga et al., 2017). *S. negevensis* has been associated with community-acquired pneumonia in adults (Lieberman et al., 1997) and bronchiolitis in infants (Kahane et al., 1998). The *S. negevensis* containing vacuole (SnCV) was shown to be surrounded almost entirely by endoplasmic reticulum (ER). While very little is known about the association of *Simkania* and the ER, Mehlitz et al. revealed that *S. negevensis* is capable of inhibiting ER-stress response despite strong initial activation, promoting host survival and subsequently simkanial survival and replication (Mehlitz et al., 2014). Moreover, as previously established for *Chlamydia*, some reports demonstrate the close interaction of *Simkania* with mitochondria. As shown for *Chlamydia*, mitochondria might represent additional sources of nutrients and ATP (Croxatto and Greub, 2010). However, so far very little is known about the interaction of *Simkania* and host organelles.

Staphylococcus aureus

Staphylococcus aureus is a round-shaped and gram-positive human pathogen and part of the microbiota. It is frequently found in the upper respiratory tract and on the skin. While usually commensal of the human microbiota, *S. aureus* can become an opportunistic pathogen causing bacteremia, endocarditis (Salvador et al., 2017), skin infections such as abscesses (Becker and Bubeck Wardenburg, 2015), bone and joint infections (Josse et al., 2015), respiratory infections as sinusitis, food poisoning and hospital-acquired infections. The emergence of antibiotic-resistant strains of *S. aureus* like methicillin-resistent *S. aureus* (MRSA) cause worldwide problems in clinical medicine (Chambers and Deleo, 2009). In addition, *S. aureus* forms biofilms on medical devices such as implants or pacemakers that further increase antibiotic resistance (Hogan et al., 2015; Suresh et al., 2019). Due to the niche within the human nares as a commensal, *S. aureus* is confronted with the bacteriolytic lysozyme, a 1,4-β-N-acetylmuramidase cleaving the glycosidic bond between N-acetyl muramic acid (MurNAc) and N-acetyl glucosamine in peptidoglycan of bacteria (Laux et al., 2019). Thus, *S. aureus* secretes enzymes to O-acylate peptidoglycan to lower the affinity of lysozyme (Bera et al., 2005). Furthermore, the cell wall of *S. aureus* possesses a particularly high cross-link ratio between peptidoglycan chains, which consists mostly of pentaglycine motifs (Bastos et al., 2010). Taken together, the cell wall of *S. aureus* is extremely durable, which further increases the resistance of the bacterium.

Neisseria gonorrhoeae

N. gonorrhoeae are obligate human and gram-negative diplococci, infecting a broad variety of tissues, from endocervix to pharynx, urethra, rectum and conjunctiva (Britigan et al., 1985). In rare cases, *N. gonorrhoeae* can even enter the bloodstream, causing systemic disseminated gonococcal infections with serious consequences like endocarditis and arthritis (Lee et al., 2015). After *C. trachomatis*, *N. gonorrhoeae* are the second most frequent STD with over 100 million cases per year according to the WHO. Recently, *N. gonorrhoeae* was classified as a 'superbug' due to the emergence of multi-drug-resistant variants (Unemo and Shafer, 2014).

Sphingolipids

Sphingolipids are a class of lipids defined by their amino-alcohol backbone. Initially, they were considered to be ubiquitous constituents of the eukaryotic cell membrane, where they are crucial for the formation of membrane microdomains called lipid rafts that are important for cell signaling (Simons and Ikonen, 1997). However, sphingolipids have also been established as bioactive lipids and signaling molecules, regulating many important cellular processes, such as autophagy and apoptosis (Cuvillier et al., 1996; Harvald et al., 2015). More recently, it has been demonstrated that sphingolipids and sphingolipid signaling is also of crucial importance for infection. Sphingolipids have been shown to both stimulate and inhibit bacterial growth, depending on the sphingolipid and the correlative pathogen (Kunz and Kozjak-Pavlovic, 2019).

Sphingolipid metabolism

Sphingolipids differ strongly in structure and function. However, their synthesis and degradation are mediated by common synthetic and catabolic pathways with ceramide being the central sphingolipid. All three pathways for the synthesis of sphingolipids, the *de novo* synthesis, the hydrolysis of sphingomyelin and the salvage pathway, recovering sphingosine from complex sphingolipids, result in the creation of ceramide (**Figure 6**) (Gault et al., 2010). Ceramide is the starting point of complex sphingolipids and therefore involved in many regulating processes. Ceramide itself is also a signaling molecule, regulating growth and development and promoting cell survival and division (Mencarelli and Martinez-Martinez, 2013). The endoplasmic reticulum (ER) is the starting point of the *de novo* biosynthesis of ceramide. In the first step, an enzyme called serine palmitoyltransferase, catalyzes the condensation of serine and fatty acid-CoA to 3-ketosphinganine, which then gets reduced by the enzyme 3-ketosphinganine reductase. Afterwards, the reduced 3-ketosphinganine gets further processed by dihydroceramide synthase to dihydroceramide. Lastly, a dihydroceramide desaturase introduces a double bond to create ceramide (Menaldino et al., 2003; Perry, 2002). Sphingolipids and Glycosphingolipids are constitutively degraded in late endosomes and lysosomes at acidic pH forming sphingosine (Kolter and Sandhoff, 2005; Riboni et al., 1997). Here, the oligosaccharides of glycosphingolipids are removed step by step through exohydrolases. Within the salvage pathway, the long chain sphingoid bases are degraded to sphingosine. An enzyme called ceramide synthase then transforms sphingosine
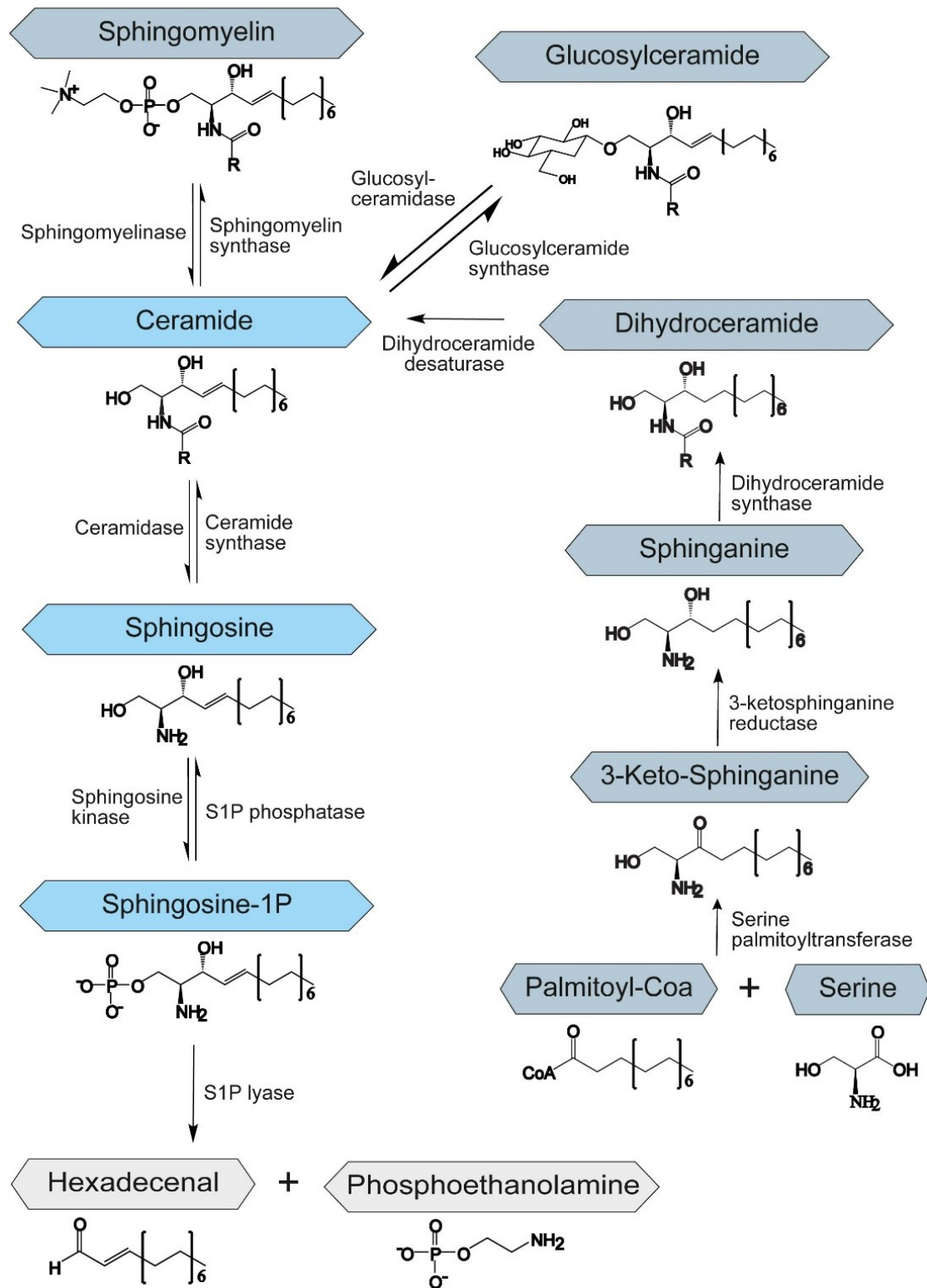
Figure 6: Schematic overview of the sphingolipid metabolism

Ceramide plays the central role of the sphingolipid metabolism. It can be synthesized either *de novo* from serine and palmitoyl-CoA, by hydrolysis of sphingomyelin or through the salvage pathway by recovery of sphingosine from complex sphingolipids. Sphingolipids are degraded by an enzyme called S1P-lyase catalyzing the degradation of Sphingosine-1P (S1P) to hexadecenal and phosphoethanolamine (Kunz and Kozjak-Pavlovic, 2019).

to ceramide by reacylation of different fatty acyl chains at the C_2-amino group. Differences in chain length lead to a great diversity of sphingolipids and may lead to altered membrane bilayer dynamics or differential signaling properties by recruitment of different binding partners. It is thought that ceramide synthase family members trap free sphingosine from lysosomes at the surface of the ER or in ER-associated membranes. The salvage pathway is estimated to contribute with 50-90% to the sphingolipid biosynthesis (Gillard et al., 1998; Tettamanti et al., 2003).

Sphingolipids and infection

Glycosphingolipids, manipulation of the sphingolipid signaling as well as ceramide-enriched lipid rafts have been shown to be important for the adhesion and consequent uptake of various pathogens, from *Escherichia coli*, *Pseudomonas aeruginosa*, *Bordetella pertussis*, *Mycoplasma pneumoniae* and *Helicobacter pylori* (Hanada, 2005). Moreover, once inside the cell, many bacteria, such as *Legionella pneumophila* or *Salmonella enterica*, manipulate the sphingolipid metabolism to avoid bacterial killing by autophagy or to control cell death induction (Huang, 2017; Rolando et al., 2016). In addition, sphingolipids were demonstrated to exhibit antimicrobial effects on a plethora of bacteria (Kunz and Kozjak-Pavlovic, 2019). Due to the significance within this work, the interaction of *Chlamydia* and *Simkania* with sphingolipids is introduced more extensively in the chapter "Chlamydiales and Sphingolipids" and the interaction of *Neisseria* and sphingolipids in the chapter "*Neisseria* and Sphingolipids". **Figure 7** summarizes the current knowledge of sphingolipid involvement in bacterial infection.

Roles of sphingolipids for bacterial adhesion and uptake

While *Neisseria* activate the acid sphingomyelinase (ASM) purposely for host cell entry, the uptake of bacteria through the activation of sphingomyelinases can also be triggered as a host defense mechanism. In tissues infected with *P. aeruginosa*, a bacterium causing serious hospital-acquired and opportunistic infections, the ASM is activated to mediate pathogen internalization by the creation of plasma membrane ceramide-enriched platforms. This is followed by the induction of apoptosis and cytokine response (Grassme et al., 2003). Furthermore, cell death for the clearance of infection of *P. aeruginosa* was observed in macrophages and neutrophils (Zhang et al., 2008). To evade this defense mechanism, *P.*

aeruginosa secretes hemolytic phospholipase C, synthesizing sphingomyelin from ceramide, and alkaline ceramidase to break down ceramide. Hence, by processing or degrading ceramide, both secreted enzymes aid *P. aeruginosa* by lowering ceramide levels to avoid the generation of ceramide-enriched platforms and subsequently internalization and bacterial clearance (Okino and Ito, 2007; Okino et al., 1998).

The pathogenicity of bacteria is often mediated by the secretion and binding of bacterial toxins to gangliosides and glycosphingolipids as demonstrated for the Shiga toxin from *Shigella dysenteriae* (Kavaliauskiene et al., 2017) and *S. aureus* and its α-toxin, which was reported to activate ASM leading to changes in permeability and lung edema (Becker et al., 2018). Moreover, sphingolipids may also play an important role for the uptake of *Mycobacteria*, among which are the causative agents for leprosy and tuberculosis, as the depletion of sphingolipids in macrophages led to a decreased uptake of *Mycobacterium smegmatis* (Viswanathan et al., 2018). Intracellularly, *Mycobacterium tuberculosis* was shown during infection in macrophages and dendritic cells to express a protein called Rv0888, a protein exhibiting a sphingomyelinase activity to cleave sphingomyelin to ceramide and
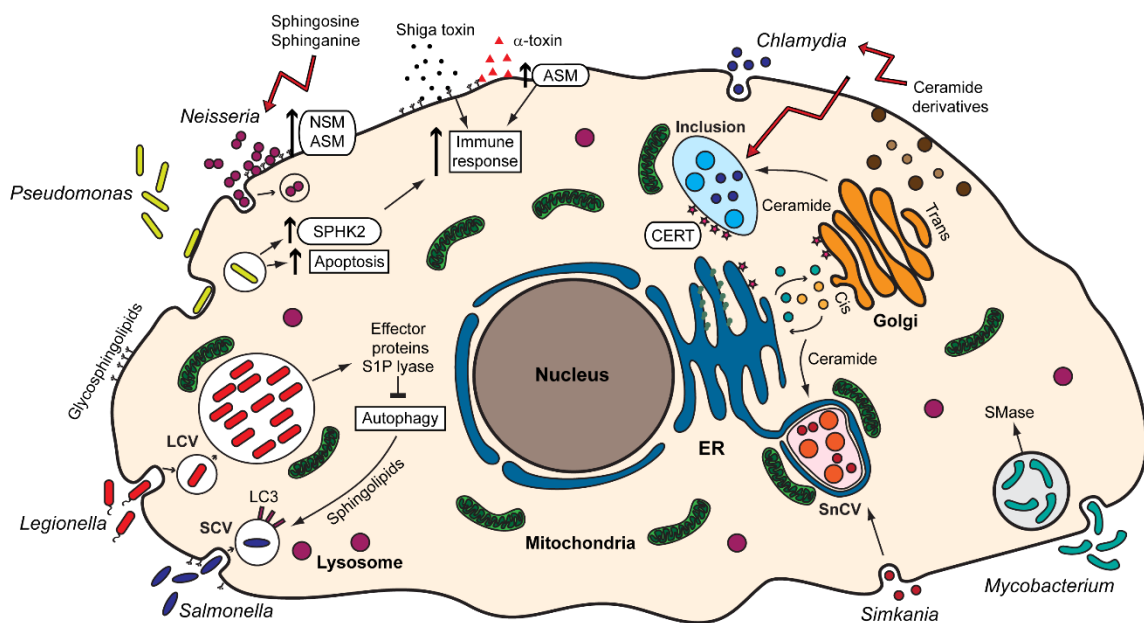

Figure 7: Bacterial pathogens and their interaction with sphingolipids and the sphingolipid signaling pathways

ASM, acid sphingomyelinase; CERT, ceramide transfer protein; ER, endoplasmic reticulum; NSM, neutral sphingomyelinase; LCV, *Legionella*-containing vacuole; LC3, Microtubule-associated protein 1A/1B-light chain 3; S1P, sphingosine-1-phosphate; SCV, *Salmonella*-containing vacuole; SnCV, *Simkania negevensis*-containing vacuole; SMase, sphingomyelinase; SPHK2, sphingosine kinase 2. Modified after (Kunz and Kozjak-Pavlovic, 2019).

phosphorylcholine. These compounds are then used as a source of carbon, nitrogen and phosphorus (Speer et al., 2015). However, the sphingomyelinase activity of *M. tuberculosis* might also be important to modulate sphingolipid signaling and subsequently to control the host immune response (Castro-Garza et al., 2016).

Manipulation of sphingolipids to control autophagy

Autophagy and apoptosis play crucial roles in controlling infection of various pathogens and therefore an important role in innate immunity. Pathogens manipulate both pathways to evade degradation or even to benefit by creating a niche (Rudel et al., 2010; Siqueira et al., 2018). While ceramide is associated with induction of apoptosis, S1P is promoting cell survival (Young et al., 2013). The regulation of the cells fate by interconversion between ceramide and S1P has been termed "sphingolipid rheostat" (Newton et al., 2015). S1P has additionally been demonstrated to upregulate autophagy and therefore promote cell survival but also as an inhibitor of autophagy through the activation of mammalian target of rapamycin (mTOR) (Harvald et al., 2015). Ceramide on the other hand was shown to induce autophagy and mitophagy. Furthermore, it is believed that ceramide is important for the fusion of autophagosomes and lysosomes and to induce autophagic cell death. In addition, the function of ceramide is linked to the chain length further increasing the complexity of sphingolipid signaling (Harvald et al., 2015; Young et al., 2013). *L. pneumophila*, the causative agent of Legionaires' disease, is a gram-negative bacterium that has been described to interfere with host signaling by secreting eukaryotic-like proteins into the host that are rarely found in prokaryotic genomes (Cazalet et al., 2004). These proteins were possibly acquired through horizontal gene transfer (Gomez-Valero and Buchrieser, 2013). Interestingly, Rolando et al (Rolando et al., 2016) described three of such eukaryotic-like effectors to be similar to eukaryotic proteins of the sphingolipid metabolism: LpSPL (S1P lyase), Lpp2295 (putative sphingosine kinase) and Lpp2641 (putative sphingomyelinase). LpSPL degrades S1P, which has previously been shown to be a critical mediator controlling the balance of sphingolipid-induced autophagy and cell death. Accordingly, this effector has been shown to restrain autophagy by acting on autophagosome biogenesis. Moreover, in macrophages infected with *L. pneumophila*, Rolando et al could further demonstrate an overall reduction of bioactive sphingolipids. In LpSPL mutants, however, the amounts of sphingosine compared to wildtype

L. pneumophila were significantly higher. Thus, this bacterium actively modulates the sphingolipid metabolism by mimicking eukaryotic proteins for infection.

Bactericidal activity of sphingolipids

Sphingolipids can be applied as antimicrobials to control growth and propagation of bacteria. In the 1990's, Bibel and colleagues showed for the first time that diverse sphingolipids exhibit microbial effects. They reported that sphinganine influenced growth of *Neisseria meningitidis* and *Acinetobacter lwoffii* and damaged the cell wall of *S. aureus* (Bibel et al., 1993). Additionally, Bibel and colleagues tested sphinganine on human volunteers as a preventative antiseptic drug against *S. aureus*. They reported a 3-log reduction in the population of bacteria compared to untreated controls (Bibel et al., 1995). Besides the effects on *S. aureus*, they reported that sphingosine efficiently kills *Streptococcus pyogenes*, *Micrococcus luteus*, *Propionibacterium acnes*, *Staphylococcus epidermidis,* lowers the levels of *P. aeruginosa* but has no effect on *Escherichia coli* and *Serratia marcescens* (Bibel et al., 1992). Due to the increasing antibiotic resistances for many pathogens, sphingolipids regained broader interest as antimicrobials within the last decade. In 2014, Banhart et al (Banhart et al., 2014) demonstrated that applying the sphingomyelin synthase inhibitor D609 reduces the growth of *C. trachomatis*. Furthermore, they synthesized several ceramide derivates to investigate the effect of sphingomyelin, e.g. the nitrobenzooxadiazole (NBD)-labeled 1-O-methyl-C_{16}-ceramide. Treatment with this novel analogue inhibited chlamydial growth similar to the antibiotic chloramphenicol and 17 times more efficient than D609. Interestingly, this functionalized ceramide is the long-chain version of 1-O-methyl-C_6-ceramide, that was shown to not be converted to sphingomyelin (Banhart et al., 2014).

Further studies investigated bactericidal effects of sphingosine, C_6-ceramide, C_{16}-ceramide and azido functionalized analogues. C_6-ceramide and ω-N_3-C_6-Ceramide were demonstrated to exhibit bactericidal effects on *N. meningitidis* and *N. gonorrhoeae*. The uptake of these analogues was described to happen rapidly within the first 5 minutes but killing occurred only after 2 hours. While bacterial killing by C_6-ceramide and ω-N_3-C_6-Ceramide could not be observed for *E. coli* and *S. aureus* (Becam et al., 2017), it could be shown in another study for dihydrosphingosine and sphingosine (Fischer et al., 2013). Recently, it was reported that sphingosine can also target intracellular *N. gonorrhoeae* and possibly exerts a direct

bactericidal effect inside host cells (Solger et al., 2020). Moreover, during infection of *P. aeruginosa*, levels of sphingosine are reduced and upon normalization of these levels the susceptibility to *P. aeruginosa* could be decreased (Pewzner-Jung et al., 2014). Lastly, sphingosine, sphinganine and phytosphingosine were demonstrated to have strong effects on biofilm formation and adherence of *Streptococcus mutans* (Cukkemane et al., 2015).

Chlamydiales and Sphingolipids

Obligate intracellular bacteria like *C. trachomatis* are highly dependent on host metabolism to ensure nutrient supply. Among others, sphingolipids are important for inclusion membrane formation. *Chlamydia* were shown to fuse with trans-Golgi network-derived secretory vesicles in an Akt and Rab14-mediated way to directly obtain ceramide from the host cell Golgi to incorporate it into the inclusion membrane (Capmany and Damiani, 2010; Capmany et al., 2019; Hackstadt et al., 1995; van Ooij et al., 2000). Moreover, *C. trachomatis* causes Golgi fragmentation and induces the formation of ministacks in the vicinity of the inclusion membrane supporting lipid acquisition (Heuer et al., 2009). Furthermore, *C. trachomatis* co-opts Golgi-specific Brefeldin A resistance guanine nucleotide factor 1 (GBF1). This factor is important for the assembly and maintenance of the Golgi stack and for sphingomyelin acquisition and was further established to be important for the growth and stability of the chlamydial inclusion (Elwell et al., 2011). During replication, *Chlamydia* recruit ceramide transfer protein (CERT), which in uninfected cells regulates the non-vesicular transport of ceramide to the Golgi from the ER, through the chlamydial infector protein IncD present at the inclusion membrane (**Figure 8**) (Agaisse and Derre, 2014; Elwell et al., 2011). This process was found to be essential for the pathogen survival as the inhibition of CERT by HPA-12 inhibited chlamydial propagation. Additionally, it was observed that the chlamydial effector protein IncV interacts with VAPs on the surface of the ER to tether the inclusion in proximity to the ER (Stanhope et al., 2017), possibly facilitating the lipid uptake by CERT. During replication, *Chlamydia* was also shown to recruit vesicle associated membrane-associated protein A (VAP-A) and sphingomyelin synthases, SMS1 and SMS2 to the inclusion membrane. Hence, they obtain ceramide and convert it into sphingomyelin in proximity of the inclusion (Elwell et al., 2011). Mital and Hackstadt (Mital and Hackstadt, 2011) report that the Src family tyrosine kinase and Moore et al (Moore et al., 2011) that the trans-Golgi SNARE protein syntaxin 6 are involved in sphingolipid trafficking to the inclusion. Similar mechanisms were shown for both, *C. pneumoniae* and *C. psitacci*, involving exocytic vesicles or CERT (Koch-

Edelmann et al., 2017; Wolf and Hackstadt, 2001). Lastly, *S. negevensis* has also been reported to obtain ceramide from the host in a process that is thought to be dependent on the retrograde transport (Herweg et al., 2016).
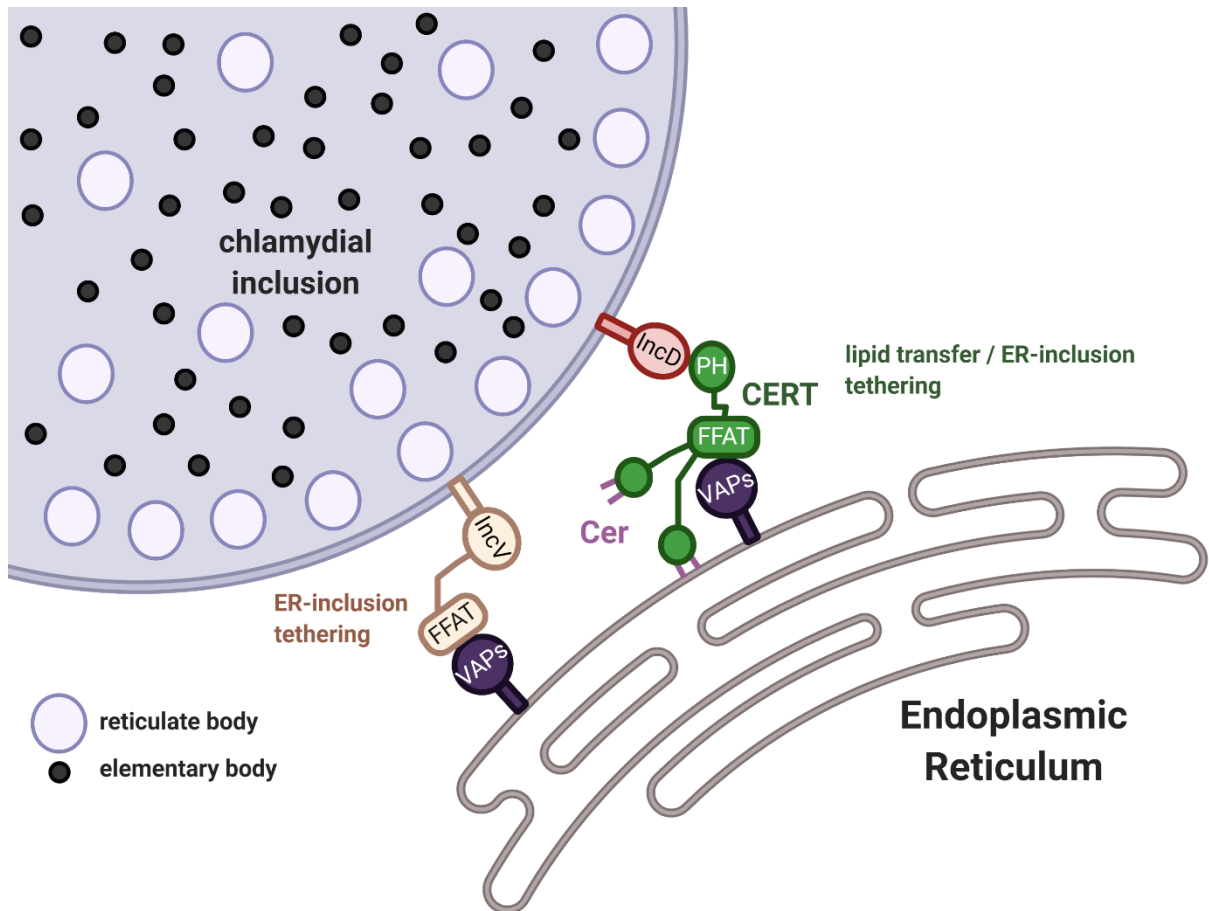

Figure 8: *Chlamydia trachomatis* hijacks CERT vesicles for lipid uptake

The chlamydial effector protein IncD interacts with CERT vesicles, which interact with VAP via a FFAT motif. In uninfected cells, CERT is regulating the non-vesicular transport from the Golgi to the ER in host cells. The interaction of *Chlamydia* with CERT is required for host lipid uptake, such as ceramides. Moreover, the chlamydial effector protein IncV interacts with VAP through a mimicry of FFAT motifs to tether the inclusion to the ER, possibly to facilitate CERT interaction.

Neisseria and Sphingolipids

The expression of highly variable lipooligosaccharides (LOS) on the neisserial surface mimics glycosphingolipids found on human cells. LOS undergo phase variation important for immune evasion, adherence and invasion. In all cases, invasion contributes to the evasion of the immune system and tissue spreading (Harvey et al., 2001). Neisserial invasion is highly dependent on intact membrane rafts, dynamic microdomains enriched with sphingolipids.

Upon attachment of gonococci and in contrast to *P. aeruginosa*, *N. gonorrhoeae* purposely activates ASM for the entry into non-phagocytic cells by the OPA-mediated interaction of bacteria and carcinoembryonic antigen-related cell adhesion molecule (CEACAM) receptors (Grassme et al., 1997; Hauck et al., 2000). The neutral sphingomyelinase (NSM) enables the independent mechanism of the so-called PorBIA-mediated low phosphate-dependent invasion (Faulstich et al., 2015; Kuhlewein et al., 2006). The causative agent for meningitis and meningococcal sepsis, *N. meningitidis*, specifically binds glycosphingolipids found on the host cell surface of human granulocytes and oropharyngeal epithelium. Like *N. gonorrhoeae*, *N. meningitidis* activates the ASM in brain endothelial cells, which was linked to the expression of outer membrane protein OpcA and binding to cell surface heparan sulfate proteoglycans (HSPGs) (Simonis et al., 2014). Only recently, Peters et al (Peters et al., 2019) described the role of the meningococcal pilus in the translocation of ASM to the surface of infected cells. As mentioned before, we recently showed that sphingosine can target intracellular *N. gonorrhoeae* and possibly exerts a direct bactericidal effect inside host cells (Solger et al., 2020).

Fluorescence Microscopy

In the late 17th century, Antonie van Leeuwenhoek contributed to the invention of the light microscope. Using his home-built setups, consisting of one small, yet strong lens, Antonie van Leeuwenhoek observed bacteria and protozoa, which he called animalcules (Van Leeuwenhoek, 1677). Ever since, light microscopy further evolved and has been one of the most applied tools in life sciences. Unfortunately, the light microscope suffers from poor contrast. The discovery of fluorescence in 1852 (Stokes, 1852), the explanation of the physical background (**Figure 9**) (Jablonski, 1935) and the discovery of the green fluorescent protein GFP (Shimomura, 1979), gave rise to fluorescence microscopy. Fluorescence enables labeling of specific targets with an excellent signal to noise ratio. Fluorescent molecules possess a delocalized π-electron-system in which electrons remain in an unexcited ground state, referred to as singlet state S_0. These electrons can be excited by light of a specific wavelength to reach energetic higher states (S_1 and S_2). Within these states, they lose part of their energy via vibrational relaxation (VR) within the energy state or via internal conversion (IC).
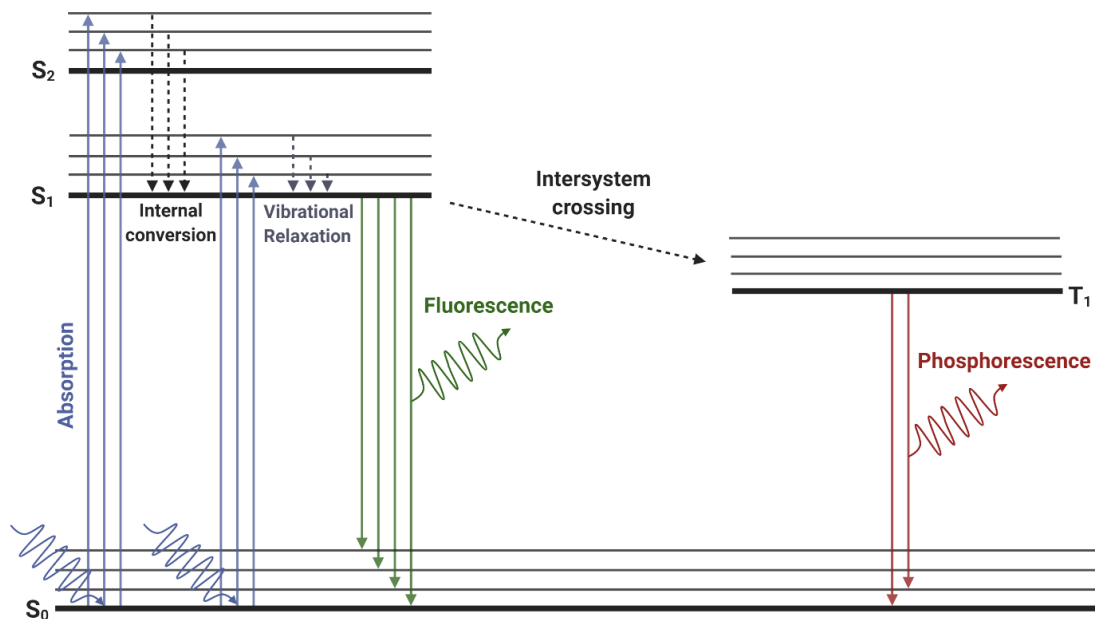

Figure 9: Jablonski diagram

After excitation at the ground state (S_0), electrons are lifted to the energetically higher S_1- and S_2-states. Within these states, the electrons lose energy via relaxation or internal conversion. The electrons then return to the ground state S_0 emitting red-shifted light, the so-called fluorescence. Alternatively, electrons can enter the triplet state (T_1) through intersystem crossing from where they return to the ground state emitting even stronger red-shifted light, the so-called phosphorescence.

Eventually, the electrons fall back to the ground state, emitting energy in form of light. Due to the energy loss within the excited states by vibrational relaxation and internal conversion, the energy of the emitted light, also referred to as fluorescence, is lower than the energy of the absorbed light. This red-shift, or Stoke-shift, in wavelength from excitation to emission enables the separation of the two light paths by optical filters. Moreover, it is possible that excited molecules transit to the so-called triplet state T_1 by radiationless intersystem crossing. From here, the electrons return to the ground state S_0 much slower emitting the so-called phosphorescence, which is typically having even higher Stoke shifts (**Figure 9**) (Sauer et al., 2018). In 1873 Ernst Abbe described that light microscopy is limited by the diffraction limit of around 200-250 nm. Abbe described that the resolution (d) of a microscope depends on the numerical aperture (NA) of the objective and the emission wavelength (λ) (Abbe, 1873):

$$d = \frac{\lambda}{2NA}$$

It was also described that a single fluorescence emitting object or point results in a circular diffracted spot with an intensity maximum in the center surrounded by concentric rings with decreasing intensity, the so-called airy disc (Airy, 1835). Additionally, Rayleigh defined the minimum distance two single spots or airy discs need to still be distinguishable. He described that the maxima of two diffraction limited spots cannot be closer than the radius of the single spots and defined the Rayleigh formula (Rayleigh, 1903):

$$d = \frac{1.22\lambda}{2NA}$$

Nowadays, there is a plethora of different fluorescent proteins, quantum dots and organic dyes ranging through the entire spectrum of visible light (Grimm et al., 2016; Michie et al., 2017). Those dyes were also conjugated to a variety of different labels, from antibodies, biotins to self-labeling tags and oligonucleotides (Cole, 2013; Los et al., 2008). Thus, there are many possibilities and one can choose the labeling method according to the application. Due to the high specificity, dense labeling and large number of different labels, fluorescence is further important for flow cytometry, genetic analysis and molecular diagnostics.

Widefield and confocal microscopy

Fluorescence microscopy is mostly performed using two different setups: widefield and confocal microscopes (**Figure 10**). In widefield microscopy, the excitation light is filtered by an excitation filter for a specific wavelength, reflected by a dichroic mirror and then focused by the objective on the entire specimen. The red-shifted emission of the fluorophores then gets focused by the same objective on the detector. Due to the red shift, the wavelength can pass the dichroic mirror. In contrast, in a confocal microscope, the light is emitted by a laser of a specific wavelength, which then passes through a pinhole, gets reflected by a dichroic mirror
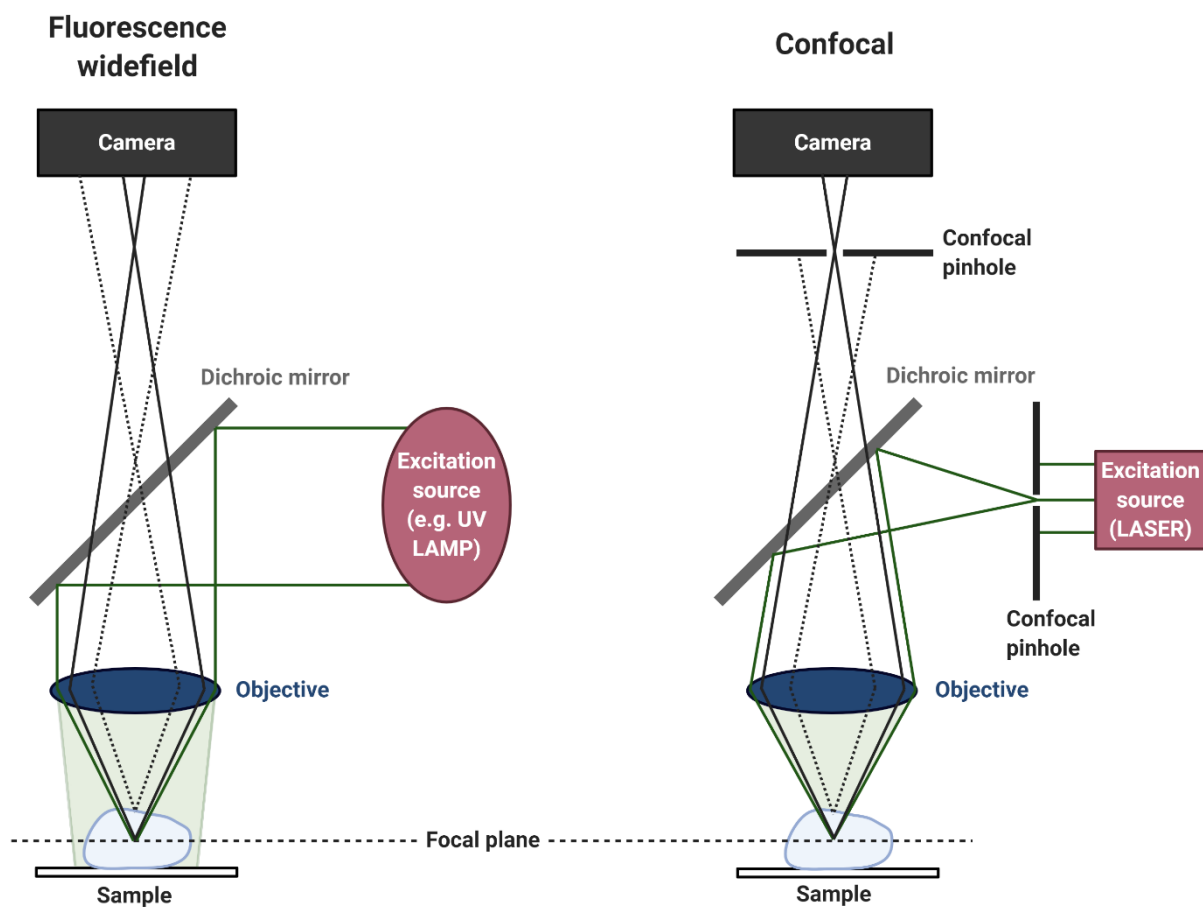

Figure 10: Principle of widefield and confocal fluorescence microscopy

In contrast to widefield microscopy, the excitation light in confocal microscopes passes through a confocal pinhole, focusing the light through the objective after reflection of the dichroic mirror on one specific spot of the sample. While widefield microscopy illuminates the whole sample at the same time, samples in confocal microscopes are imaged point-by-point. The emitted light is then captured in the same objective and focused on the camera. In confocal systems, the emission light is again passing through a confocal pinhole before detection by the camera, allowing only light from the focus plane to pass. By guiding the light through confocal pinholes, the background is therefore strongly reduced. However, due to the point-by-point imaging, confocal imaging is way slower than conventional widefield microscopy.

and focused by the objective on the sample. The pinhole is situated in a conjugate plane (confocal) with a scanning point on the specimen. The sample is imaged point-by-point, resulting in longer acquisition time. Afterwards, the red-shifted fluorescence emitted by the fluorophores also gets focused by the objective on the camera. However, the emitted light, after passing the dichroic mirror, is filtered again by a confocal pinhole, allowing mainly light from the focus plane to reach the detector. Thus, background emitted by fluorophores out-of-focus is strongly reduced. Therefore, especially in thick samples like spheroids and tissues, confocal microscopy enhances the image quality compared to widefield microscopy enormously. On the other hand, widefield microscopy is much faster and can be observed directly on the ocular. Both microscopy techniques, however, are limited in resolution by the diffraction limit (Wilson, 2017).

Superresolution microscopy - expansion microscopy (ExM)

Within the last two decades, several approaches enabled to bypass the diffraction limit of light microscopy approaching virtually molecular resolution (Schermelleh et al., 2019). These novel superresolution methods, e.g. structured illumination microscopy (SIM) (Gustafsson, 2000), stimulated depletion (STED) (Hell, 2007), photoactivated localization microscopy (PALM) (Betzig et al., 2006) and (direct) stochastic optical reconstruction microscopy ((d)STORM) (Heilemann et al., 2008) can be applied to biological samples and provided novel insights on structural organization of the cells and biomolecular assemblies. However, multicolor experiments remain challenging, 3D experiments are often axially limited, and laboratories require high-cost specialized setups and intensive trainings (Burgert et al., 2015).

SIM uses the principle of interference-generated light patterns, usually stripes, to create a Moiré effect. For this, several images have to be collected with a different orientation and position of the stripes. As a result of interference between the striped excitation pattern and the sub-diffraction details in the sample emission, it produces moiré patterns, containing high-frequency spatial information. By processing with a specialized computational algorithm, this information is extracted from the raw images resulting in the reconstructed final image with an approximately doubled spatial resolution. In comparison to other superresolution setups, SIM microscopy is relatively simple to use. First, samples can be prepared in the same way as for conventional fluorescence microscopy without the need of sophisticated labeling

protocols. Second, as SIM microscopy is an extension to widefield fluorescence microscopy, it enables multicolor imaging and optical sectioning. However, fluorophores have to be reasonably resistant to photobleaching, errors in grating position can introduce artifacts and the improvement in resolution compared to other superresolution methods is only moderate (Heintzmann and Huser, 2017).

To overcome the limitations of other superresolution methods, expansion microscopy (ExM) was introduced by Boyden and coworkers in 2015 (Chen et al., 2015). This method physically expands the sample and thus bypasses the resolution limit by enlarging the sample rather than improving the resolution of the microscope. Hence, expansion microscopy enables superresolution microscopy on a conventional confocal setup. For this, the sample is labeled
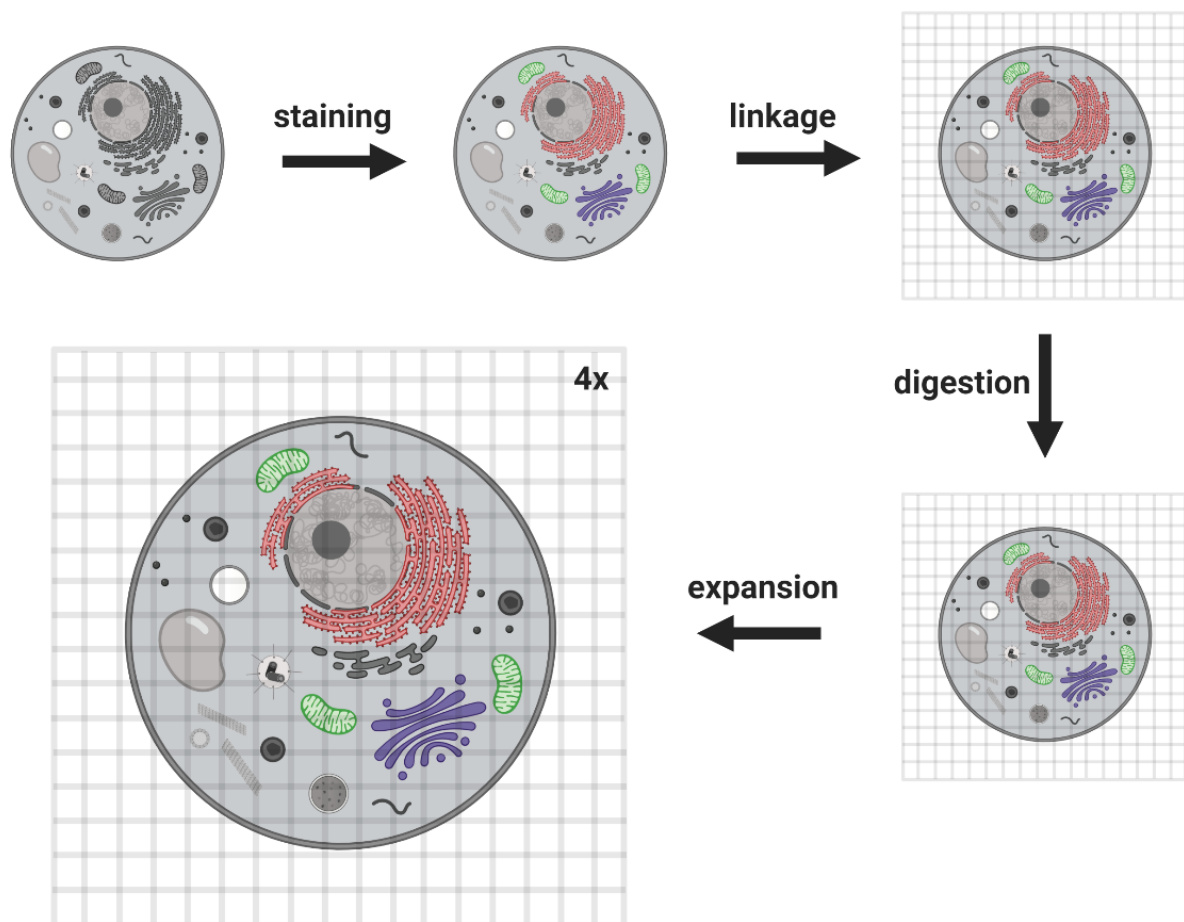

Figure 11: Schematic illustration of Expansion Microscopy (ExM)

In the protocol of Chozinski et al (Chozinski et al., 2016) glutaraldehyde (GA) is used to label primary amines as a polymer-linking group after conventional immunostaining with fluorophore-labeled antibodies. After treatment with GA, the sample follows gelation, digestion with a protease and expansion through dialysis into deionized water. The decoration of the sample with GA allows linkage to the hydrogel.

with an amine or acrydite containing label (Chen et al., 2015), linked into a swellable acrylamide gel with AcX (Tillberg et al., 2016), MA-NHS, glutaraldehyde (Chozinski et al., 2016) or for RNA Label-X (Chen et al., 2016) and digested by application of proteinase K to enable isotropic expansion in ddH$_2$O (**Figure 11**). Due to the simple application and the possibility to perform superresolution microscopy on a conventional setup, the method develops at an enormous speed with multiple protocols for not only 4x, but also 10x (Truckenbrodt et al., 2018; Truckenbrodt et al., 2019) and even 20x expansion by iterative expansion microscopy (Chang et al., 2017), for both cell culture and tissues (Ku et al., 2016). Moreover, expansion microscopy has already been used in combination with other superresolution microscopy methods further improving resolution (Gao et al., 2018). While easy to implement, the expansion of novel structures must be taken with caution as protocols might need to be adjusted to enable isotropic expansion as shown for the digestion of complex cell walls of different fungi (Gotz et al., 2020b) or bacteria (Lim et al., 2019).

Materials and Methods

Cell culture

In this work HeLa229 (ATCC CCL-2.1^{tm}), human epithelial conjunctival Chang cells and Sam50 knockdown cells *sam50kd-2* (Kozjak-Pavlovic et al., 2007) were cultured in 10% (v/v) heat inactivated FBS (Sigma-Aldrich, St. Louis, USA) RPMI1640 + GlutaMAX^{tm} medium (Gibco, Thermo Fisher Scientific, Massachusetts, USA). The cells were grown in a humidified atmosphere containing 5% (v/v) CO_2 at 37 °C. For the induction of the shRNA-mediated knockdown of Sam50, *sam50kd-2* cells were treated with 1 µg/ml doxycycline for 72 hours prior seeding.

Bacteria

HeLa229 cells were used for infection with *C. trachomatis* and *S. negevensis*, Chang cells for infection with *N. gonorrhoeae*. In this study, *C. trachomatis* serovar L2/434/Bu (ATCC VR-902B^{tm}), *C. trachomatis* mutant strains (cdu1:: Tn *bla*, CPAF mutant (RSTE4)), the EB-RB reporter strain *Ct* mCh(GroL2) GFP(OmcAL2) (Cortina et al., 2019), *S. negevensis*, *N. gonorrhoeae* (strain MS11, derivative N927) and *S. aureus* JE2 (Community-acquired *S. aureus*, methicillin-resistant, USA300 background considered as wildtype, (Fey et al., 2013)) were used.

C. trachomatis and *S. negevensis* were cultivated as previously described. For this, the bacteria were propagated in HeLa229 cells at a multiplicity of infection (MOI) of 1 for 48 hours (*C. trachomatis*) or 72 hours (*S. negevensis*). The cells were then lysed and detached by scraping with a rubber policeman, transferred into 50 ml centrifuge tubes containing glass beads (3mm, Roth) to lyse the cells while vortexing for 3-4 minutes. After low centrifugation (10 minutes at 2000 g at 4°C for *C. trachomatis* and 10 minutes at 600 g at 4°C for *S. negevensis*) the supernatant was transferred to high speed centrifugation (30 minutes at 30.000 g at 4°C for *C. trachomatis* and 30 minutes at 20.000 g at 4°C for *Simkania negevensis*) to pellet bacteria. The pellet was then washed and resuspended in 1x SPG buffer (7.5% sucrose, 0.052% KH_2PO_4, 0.122% $NaHPO_4$, 0.072% L-glutamate). After resuspension, the bacteria were stored at -80°C and titrated for a MOI of 1 for infections. After infection, the cells were incubated in a humidified atmosphere with 5% (v/v) CO_2 at 35°C. For secondary infections, HeLa229 cells

were infected with *C. trachomatis* for 48 hours and then lysed using glass beads (3 mm, Roth). Afterwards, the supernatant containing chlamydial progeny was diluted 1:100 to infect other cells. Both, cell lines and bacteria, were tested to be free of Mycoplasma via PCR.

N. gonorrhoeae was cultivated on gonococci (GC) agar plates (ThermoScientific, Waltham, USA) supplemented with 1% vitamin mix at 37°C and 5% CO_2 for 16 hours. For infection, bacteria were transferred to a liquid culture in protease-peptone medium (PPM), supplemented with 1% vitamin mix and 0.5% sodium bicarbonate 8.4% solution (PPM+) at 37°C and 120 rpm. The gonococci were grown to an OD_{550} 0.4 to 0.6. Prior to infection, the liquid culture medium was changed to 4-(2-Hydroxyethyl)piperazine-1-ethanesulfonic acid (HEPES buffer) medium by centrifugation with 2778 g for 5 minutes. Infection was stopped after 4 hours by washing the cells three times with Hepes medium.

S. aureus JE2 expressing GFP, encoded by a pJL74 plasmid, was grown in brain heart infusion medium (BHI, Sigma Aldrich) complemented with 10 µg/ml erythromycin. The culture was diluted to OD_{600} 0.4 in BHI medium and regrown to exponential phase (OD_{600} 0.6-1.0). Bacteria were then washed in Dulbeccos´s Phosphate-Buffered Saline (DPBS, ThermoFisher), diluted in infection medium (RPMI Medium with GlutaMAX (ThermoFisher)/ 10% fetal bovine serum (Sigma Aldrich)/ 1 mM sodium pyruvate (ThermoFisher)) and counted in a Thoma counting chamber. HeLa229 cells were infected at MOI of 5 or 10 by centrifugation at 800 g for 8 minutes. After 1 hour, the infection was stopped by addition of 20 µg/ml lysostaphin (AMBICINL, AMBI PRODUCTS LLC, New York, USA) for 1 hour.

Transfection

HeLa229 cells were transfected in 12 well plates using Viromer® RED (230155; Biozym, Oldendorf, Germany) according to manufacturer's instructions. For this, in one tube DNA was diluted in 90 µL Buffer Red in a total concentration of 1 µg/ml while in a second tube 0.4 µl Viromer® RED was mixed properly with 9.6 µl Buffer Red and then vortexed for ~10 seconds. After vortexing, the DNA/Buffer Red mix was pipetted onto the Viromer® RED/Buffer Red mix and incubated for 15-20 minutes. In the meantime, the medium of the cells was exchanged for 1 ml fresh RPMI1640 + GlutaMAX^{tm} medium. After incubation, the DNA-mix was added to the cells and then incubated for 24 hours. MtcK gene was amplified from HeLa cDNA and cloned by Shiqiang Gao into the pCDNA3 vector (Thermo Fisher Scientific, Massachusetts,

USA) where previously the GFP sequence was introduced, enabling C-terminal fusion and tagging.

Inhibitors

For the inhibition of CPAF, HeLa229 cells were treated with 150 µM clasto-lactacystin beta-lactone for 1 hour prior to fixation as previously demonstrated by Johnson et al. (Johnson et al., 2015).

For CERT-Inhibition, HeLa229 cells infected with *C. trachomatis* were treated for 8 hours with 10 or 30 µM at 24 hours post infection.

LDH-assay

LDH-assays were performed using Cytotoxicity Detection KitPLUS (LDH) (Sigma) according to the manufacturer's protocol.

Chemical Synthesis of α-NH$_2$-ω-N$_3$-C$_6$-Ceramide
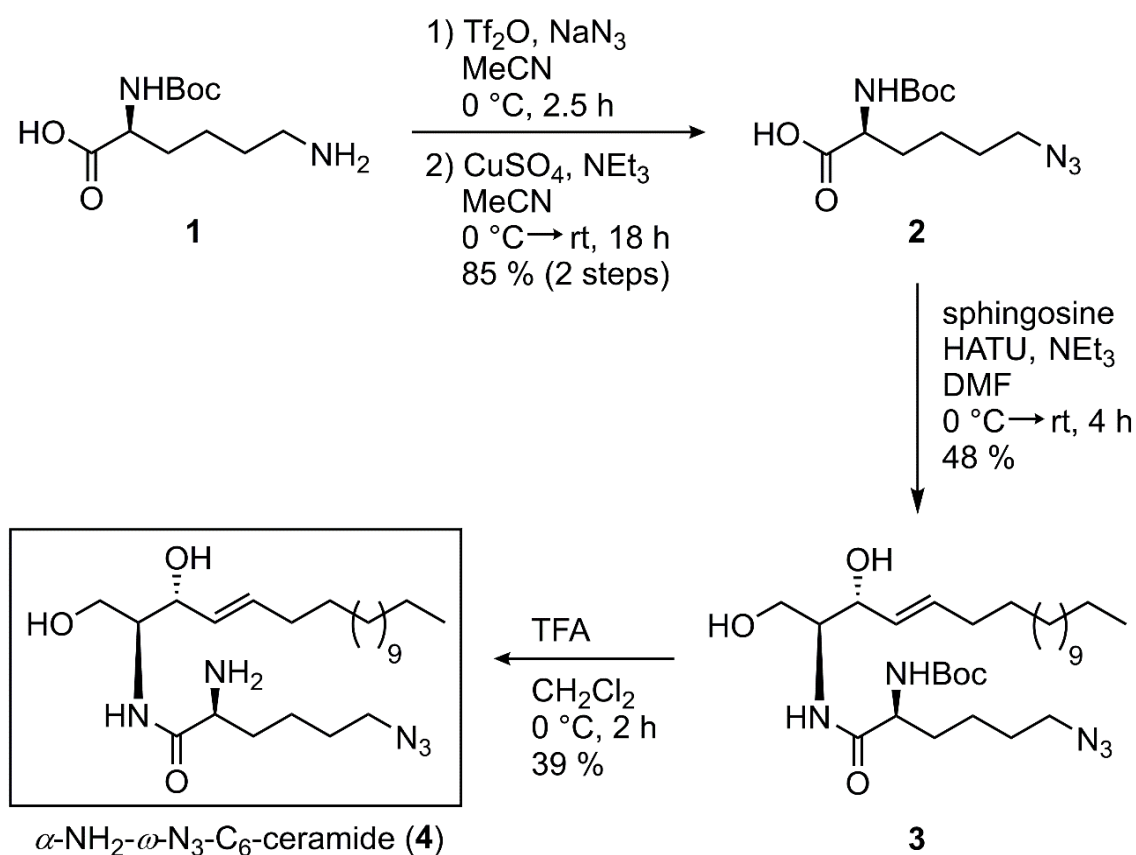
Figure 12: Synthesis of clickable amino-ceramide probe 4.

Synthesis of α-NH$_2$-ω-N$_3$-C$_6$-Ceramide as well as quality control was performed by Julian Fink. Starting from N-Boc-protected L-lysine the introduction of the azide-functionality was accomplished via catalytic diazotransfer reaction to obtain azido-acid **2** in 85 % yield. First, Triflyl azide was prepared with a reduced amount of highly toxic sodium azide and triflyl anhydride. Subsequent amide coupling of **2** with sphingosine was performed in DMF under basic conditions using HATU as coupling reagent. The resulting Boc-protected azidoceramide analogue **3** was isolated in 48% yield. In the last step, the amine group was deprotected by the treatment with TFA in dichloromethane. After basic workup, followed by column chromatography, the target ceramide analogue **4** was successfully isolated in 39% yield. All isolated compounds were characterized by a combination of HRMS, NMR and IR spectroscopy (**Supplementary Figures S1-S13**).

Sphingolipid treatment and Click Chemistry

Seeded cells were fed with 10 µM final concentration of α-NH$_2$-ω-N$_3$-C$_6$-ceramide, ω-N$_3$-C$_6$-ceramide, C$_6$-ceramide or ω-N$_3$-sphingosine for 1 hour at 37 °C. Samples infected with *C. trachomatis* were fed with ceramide-analogues 23 hours and samples infected with *S. negevensis* at 71 hours post infection. For the infection with *N. gonorrhoeae*, the cells were fed for 30 minutes with 10 µM ω-N$_3$-sphingosine before infection. Afterwards, the cells were fixed with 4% PFA and 0.1% GA for 15 minutes, followed by 3x washing with 1x PBS. The samples were then permeabilized for 15 minutes in 0.2% Triton X-100, washed again 3x in 1x PBS, and incubated with 5 µM DBCO-488 (Jena Bioscience, CLK1278-1) or 5 µM Click-IT Alexa Fluo® 488 DIBO alkyne dye (ThermoScientific, Waltham, USA) at 37 °C for 30 minutes. When additionally stained with antibodies, the samples were then blocked and stained as described in the following chapter.

Immunostaining

Before immunostaining, the cells were washed with 1xPBS and fixed with 4% PFA (or 4% PFA with 0.1% GA for samples fed with ceramide) for 10-30 minutes at RT. Afterwards, the cells were washed 3x with 1xPBS and permeabilized for 15 minutes in 0.2% Triton-X100. When expanding *S. aureus*, the samples were then predigested with 20 µg/ml lysostaphin for 15 minutes. After permeabilization, the cells were washed 3x in 1x PBS and blocked for 1 hour in 2% FCS or 5% BSA. Upon blocking, the cells were incubated for 1 hour at RT in a humidified

chamber with the corresponding primary antibody. **Table 1** shows the primary antibodies, their hosts, dilutions, article number and company, used in this study.

Target	Host	Dilution	Article number	Company
Chlamydial HSP60	mouse	1:100 (IF)	sc-57840	Santa Cruz
	rabbit	1:200 (IF)	-	Provided by A. Fischer, University of Würzburg
		1:1000 (WB)		
B-actin	Mouse	1:4000 (WB)	A5441	Sigma Aldrich
CPAF	mouse	1:100 (IF)	-	Provided by G. Zhong, Texas Health Science Center
Cdu1	mouse	1:50 (IF)	-	Provided by A. Fischer, University of Würzburg
Tom20	mouse	1:25 (IF)	sc-17764	Santa Cruz
Tim44	mouse	1:50 (IF)	612582	BD Biosciences
Mic60	rabbit	1:100 (IF)	ab48139	Abcam
		1:500 (WB)		
Sam50	rabbit	1:500 (WB)	-	Gramsch laboratories
LAMP1	mouse	1:100 (IF)	H5G11	Santa Cruz
LC3B	rabbit	1:100 (IF)	2775	Cell Signaling
Chlamydial LPS	mouse	1:300 (IF)	MCA2718	Bio-Rad
LTA	rabbit	1:100 (IF)	BP984	Origene
TFAM	rabbit	1:100 (IF)	TA332462	Origene
TFAM-Alexa 546 (self-conjugated)	rabbit	1:50 (IF)	TA332462	Origene
TFAM-Alexa 546	rabbit	1:100 (IF)	sc-166965	Santa Cruz
PRX3	rabbit	1:100 (IF)	TA322472	Origene
CERT	rabbit	1:100 (IF)	ab72536	Abcam
Neisseria	rabbit	1:200 (IF)	N0600-02	US biological
GFP	mouse	1:100 (IF)	ab1218	Abcam
	rabbit	1:100 (IF)	SP3005P	Origene
mCherry	rabbit	1:100 (IF)	ab167453	Abcam

Table 1: Primary antibodies

After incubation with the primary antibody, the cells were incubated for 1 hour at RT in the corresponding secondary antibody listed in **table 2**.

Materials and Methods

Dye	Host	Dilution	Article Number	Company
Alexa-488	mouse	1:200 (IF)	A11017	Thermo Fisher Scientific
Alexa-488	rabbit	1:200 (IF)	A11070	Thermo Fisher Scientific
NHS-ATTO643 (self-conjugated)	mouse	1:50 (IF)	AD 643-31	ATTO-TEC
ATTO647N	rabbit	1:200 (IF)	610-156-121S	Rockland Immunochemicals
CF568	rabbit	1:100 (IF)	SAB4600310	Sigma Aldrich
Cy3	mouse	1:300 (IF)	111-165-146	Dianova

Table 2: Secondary antibodies

For 3 color images of mitochondrial cristae, the cells were then incubated with anti TFAM-Alexa 546 antibody (TA332462 self-conjugated for SIM images and sc-166965; Santa Cruz Biotechnology, Dallas, USA, for confocal images).

Antibody conjugation

For Antibody conjugation, the buffer of the anti-TFAM (TA332462, rabbit; Origene, Rockville, USA) antibody was exchanged to 100 mM $NaHCO_3$ with 0.5 ml 7 kDA Spin Desalting Columns (89882; Thermo Fisher Scientific, Massachusetts, USA). The antibody was then incubated for conjugation in 5 molar excess of NHS-Alexa Fluor 546 (A20002; Thermo Fisher Scientific, Massachusetts, USA) or NHS-ATTO 643 (AD 643-31; ATTO-TEC; Siegen, Germany) for 3 hours at RT. Afterwards, the unreacted dye was filtered from the antibody using 0.5 ml 7 kDA Spin Desalting Columns. Moreover, the buffer was exchanged to 0.02% NaN_3 dissolved in PBS. The degree of labeling (DOL) was determined by the absorption of the antibody-dye with a UV-vis spectrophotometer (Jasco V-650). The labeled antibodies were stored at 4°C. Antibody conjugation was performed by Ralph Götz.

mCling

mCling (Biosyntan) was labeled as previously shown by Revelo et al. (Revelo et al., 2014): 150 nmol mCling was incubated in 3 molar excess of ATTO 643-Maleimide (ATTO-TEC, AD 643-45) in 100 mM TCEP shaking and overnight. The label product was purified by HPLC (JASCO) and the concentration determined using a UV-vis spectrophotometer (Jasco V-650). Staining with

mCling was performed by the incubation of living cells in 0.5 μM mCling in cell culture media for 10 minutes at 37°C.

Gelation and Expansion

Expansion microscopy was performed entirely collaboratively with Ralph Götz, except of neisserial and staphylococcal expansion, and performed as described previously (Chozinski et al., 2016; Kunz et al., 2019). For this, fixed and stained cells were incubated for 10 minutes in 0.25% glutaraldehyde, washed three times with 1x PBS and then gelated with, in case of 4x expansion, a monomer solution containing 8.625% sodium acrylate (408220, Sigma-Aldrich, St. Louis, USA), 2.5% acrylamide (A9926, Sigma-Aldrich, St. Louis, USA), 0.15% N,N'-methylenbisacrylamide (A9926, Sigma-Aldrich, St. Louis, USA), 2 M NaCl (S5886, Sigma-Aldrich, St. Louis, USA), 1x PBS, 0.2% ammonium persulfate (APS, A3678; Sigma-Aldrich, St. Louis, USA) and tetramethylethylenediamine (TEMED, T7024; Sigma-Aldrich, St. Louis, USA,). Adding TEMED and APS starts the gelation process and were thus added only prior gelation. The gelation was performed for 1 hour at RT in humidified gelation chambers. In case of 10x expansion, 1 ml of the monomer solution containing 0.267 g DMAA (Sigma, 274135) and 0.064 g sodium acrylate (Sigma, 408220) dissolved in 0.57 g ddH$_2$O was degassed for 45 min with nitrogen on ice followed by the addition of 100 μl KPS (0.036 g/ml, Sigma, 379824). After another 15 minutes of degassing and the addition of 4 μl TEMED, gelation was performed for 30 minutes at RT followed by an incubation of 1.5 hours at 37 °C. The gelated samples were then digested for 3 hours or overnight in digestion buffer (50 mM Tris pH 8.0, 1 mM EDTA (Sigma, ED2P), 0.5 % Triton X-100 (Thermo Fisher, 28314) and 0.8 M guanidine HCl (Sigma, 50933)), supplied with 8 U/ml protease K (Thermo Fisher, AM2548) and for expansion of *Neisseria* additional 1 mg/ml lysozyme (Lim et al., 2019). Due to the robust cell wall, digestion of *S. aureus* required 20 μg/ml lysostaphin prior gelation as well as 2 mg/ml lysozyme and 50 μg/ml lysostaphin for 30 minutes post gelation, followed by 30 minutes treatment with 8 U/ml protease K. After digestion, the gels were washed and consequently expanded in hourly changed ddH$_2$O until the expansion saturated. The expansion factor was determined either by the gel size prior and after expansion or by imaging of the very same cell prior and post expansion. Expanded gels were stored at 4 °C in ddH$_2$O until imaging (maximum of one week) and immobilized on PDL coated imaging chambers (734-2055, Thermo Fischer Scientific,

Massachusetts, USA) for imaging. To avoid shrinking, drops of water were placed on top of the gel during image acquisition.

Microscopy

Imaging was performed on a confocal system, either Zeiss LSM700 (63x water-objective, C-Apochromat, 1.2 NA) or TCS SP5 confocal microscope (63x oil-immersion UV objective, 1.4 NA), and for superresolution on a structured illumination microscope Zeiss Elyra S.1 SIM (63x oil-immersion objective, Plan-Apochromat, 1.4 NA or for expanded samples 63x water-objective, C-Apochromat, 1.2 NA). Images were processed with Imaris 8.4.1 and FIJI 1.51n (Schindelin et al., 2012).

dSTORM imaging was performed by Ralph Götz on a home-built setup using an inverted widefield microscope (Olympus IX-71) with an Olympus Apon 60xO TIRF oil objective with a numerical aperture of 1.49. The setup is equipped with a 639 nm excitation laser (Genesis MX639-1000, Coherent). To separate the excitation beam from the emitted fluorescence, a dichroic mirror (ZT405/514/635rpc, Chroma) was used. The emission was additionally filtered by an emission filter (Brightline HC 679/41 (Semrock)) in front of an EMCCD-camera (iXon Ultra 897, Andor). Before imaging, switching buffer containing 100 mM ß-mercaptoethylamin pH 7.4 was added. 15.000 frames were recorded at 50 Hz using laser densities of ~ 7 kW/μm. The super-resolved images were reconstructed using the software rapidSTORM 3.3.

For FRAP imaging performed by Jan Schlegel, HeLa229 cells were seeded in an 8-well chambered high precision coverglass (Sarstedt) and incubated for 24 hours at 37°C and 5% CO_2. The cells were fed for 30 minutes with α-NH_2-ω-N_3-C_6-ceramide or as a control ω-N_3-C_6-ceramide and then washed with HBSS containing magnesium and calcium and fixed with 4% PFA and 0.1% GA. The ceramides were then labeled by click-chemistry with DBCO-Alexa Fluor 488. After labelling, the cells were washed and FRAP-imaging was performed at the LSM700 (63x oil-immersion objective, Plan-Apochromat, 1.4 NA). Images were acquired every 1.5 seconds for 30 frames. After three frames a circular region of interest with a diameter of 1.8 μm was bleached and fluorescence recovery followed over time.

Western Blot

Protein lysates were collected by lysing the samples in prewarmed (95°C) 2x laemmli-buffer and then cooked for 5 minutes at 95°C. The proteins were separated according to mass by a 10% polyacrylamide gel across a constant voltage for 2 hours. For precise estimation of protein sizes, the samples were run next to 8µl PageRuler Prestained Protein Ladder (Thermo). After separation, the proteins were transferred from the gel to a PVDF membrane via semi-dry electroblotting. After transfer, the membrane was blocked in Tris-buffer containing 0.05% Tween 20 and 5% dry milk powder for 1 hour and then incubated in the according primary antibody over night at 4°C. The antibodies used for western blotting within this work are: cHSP60 (Santa Cruz, sc-57840, dilution 1:1000), β-actin (Sigma, A5441, dilution 1:10000), Mic60 (Abcam, ab48139, dilution 1:500) and Sam50 (homemade, dilution 1:500). Proteins were detected with secondary antibodies coupled to horseradish peroxidase (Santa Cruz Bioscience) using the ECL system (Pierce) on an Intas Chem HR 16-3200 reader.

BioRender

Figure 1-3, 8-11 and 46 were created with BioRender.com.

Results

Expansion microscopy of mitochondrial cristae

Mitochondrial cristae are important for several crucial cellular processes, including apoptosis and ATP-production. These processes are determined by the integrity and morphology of cristae (Cogliati et al., 2016). Thus, we aimed to find an approach for the visualization of mitochondrial cristae without impacting their morphology. To do so, our goal was to find a marker protein localizing at mitochondrial cristae that can be overexpressed and correctly targeted when fused to a fluorescent marker protein while neither affecting mitochondrial function nor morphology. After testing several candidates, we chose the most promising one,
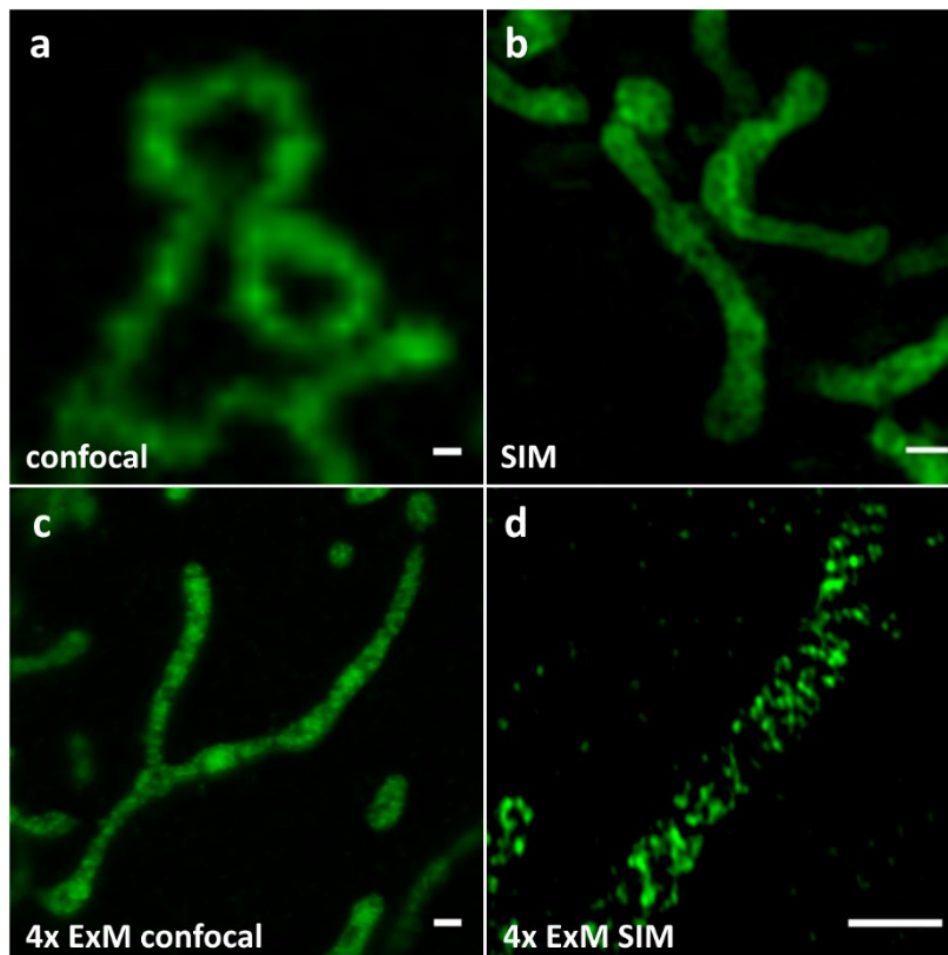

Figure 13: Expansion Microscopy enables visualization of mitochondrial cristae.

HeLa229 cells were transfected for 24 hours with MtCK-GFP (green) and immunolabeled for GFP to visualize mitochondrial cristae with (a) confocal, (b) SIM, (c) 4x ExM confocal (d) 4x ExM SIM. Scale bars, (a,b) 0.5 µm and (c, d) 2 µm (Kunz et al., 2020).

the mitochondrial creatine kinase MtCK, an enzyme catalyzing the reversible transfer of phosphate from mitochondrial ATP to cytosolic creatine, generating phosphocreatine, of which the phosphate can be transferred to ADP by cytosolic isoenzymes, regenerating ATP. This offers a possibility to transfer energy from mitochondria to the cytosol. In addition, the transfer of phosphate from phosphocreatine to ADP generates ATP very quickly. Therefore, phosphocreatine, MtCK and its cytosolic counterparts act as a temporal and spatial energy buffer to maintain cellular energy homeostasis. MtCK was previously shown to localize in the mitochondrial IMS (Schlattner et al., 2006). When overexpressing MtCK coupled to GFP at its carboxy-terminus in HeLa229 cells, we did not observe any changes in mitochondrial length or distribution. With the newly established marker protein, we performed expansion microscopy using the Chozinski protocol to improve the resolution in order to distinguish individual cristae (Chozinski et al., 2016). **Figure 13** compares the difference in resolution of (a) unexpanded samples imaged on a confocal system with an estimated lateral resolution of ~240 nm, (b) unexpanded samples imaged on SIM with a lateral resolution of ~120 nm, (c) 4x expanded samples on a confocal system with a lateral resolution of ~60 nm and (d) 4x expanded samples on SIM with a lateral resolution of ~30nm. Expansion microscopy enabled to differentiate between individual cristae, especially when additionally combined with SIM.

After establishing expansion microscopy with a cristae marker, we aimed to compare the localization of mitochondrial proteins relative to cristae on a confocal system (**Figure 14**) and SIM (**Figure 15**). First, we chose peroxiredoxin (PRX3), a mitochondrial thioredoxin-dependent hydroperoxidase present exclusively in the mitochondrial matrix (Cunniff et al., 2014), to assess the efficiency of MtCK-GFP to visualize cristae with its even distribution through the IMS (**Figure 14a** and **Figure 15a**). The signals for MtCK-GFP and PRX3 showed alternating signals and no overlap, enabling the clear differentiation between mitochondrial cristae and matrix (**Figure 14d** and **Figure 15b,c**). We then aimed to localize Mic60 relative to mitochondrial cristae. Mic60 is a central component of the MICOS complex, which together with SAM in the OMM forms the MIB complex. MIB is a large complex that is crucial for the maintenance of mitochondrial cristae morphology, CJs, inner membrane architecture and formation of contact sites between the two mitochondrial membranes (John et al., 2005; Kozjak-Pavlovic, 2017; Ott et al., 2015). In accordance with the literature, we could demonstrate that Mic60 is localizing at CJs closer to the mitochondrial surface (**Figure 14b,e**
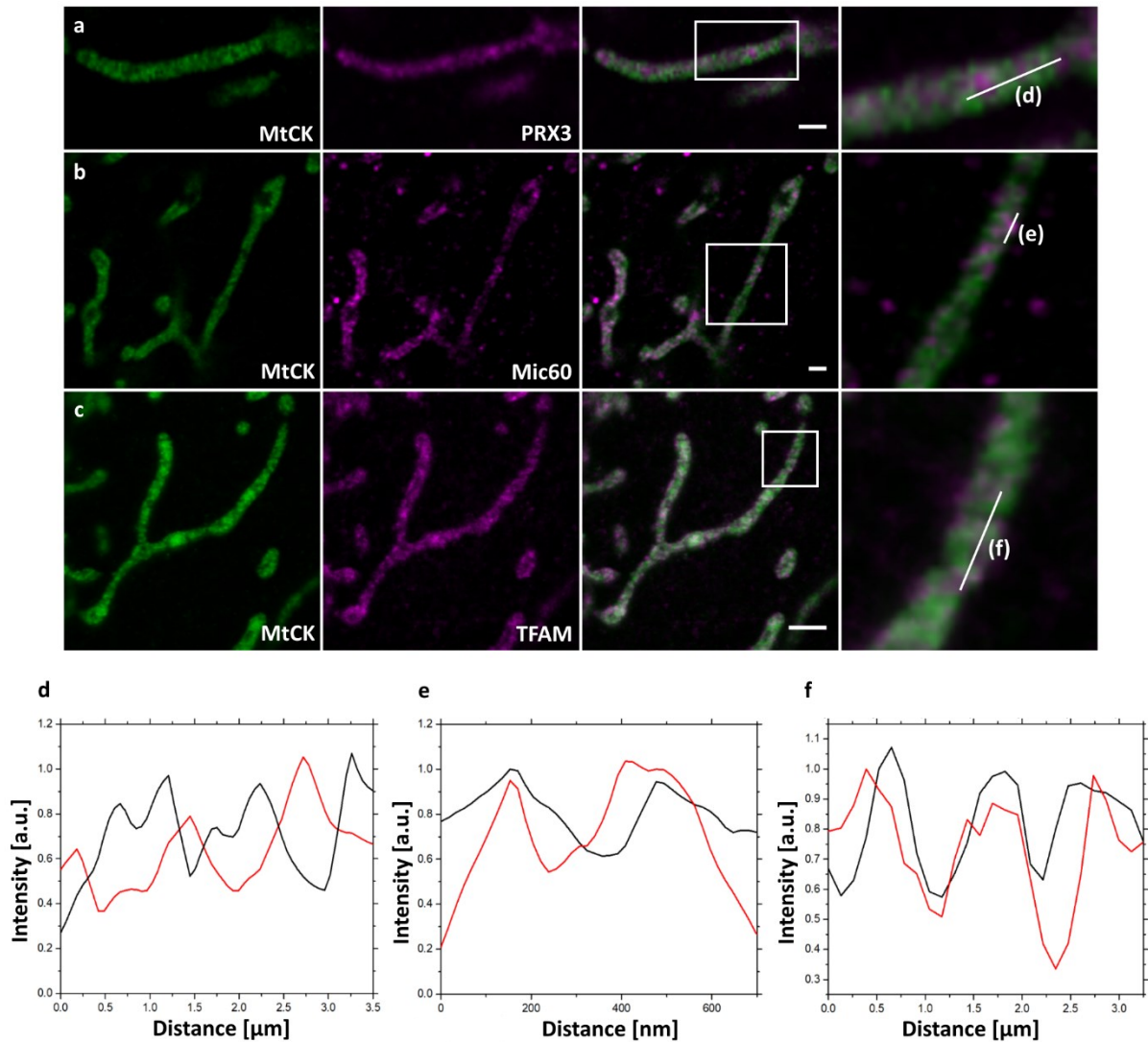
Figure 14: 4x confocal ExM can resolve localization of proteins at mitochondrial cristae.

4x ExM confocal fluorescence images of HeLa229 cells transfected for 24 hours with MtCK-GFP (green) and immunolabeled for GFP and (a) PRX3, (b) Mic60 and (c) TFAM. Plot profiles show the fluorescence of MtCK (black) relative to (d) PRX3, (e) Mic60/Mitofilin and (f) TFAM (red). 4x ExM can resolve if mitochondrial proteins localize at mitochondrial cristae as demonstrated for Mic60 and TFAM. Scale bars, 2 µm (Kunz et al., 2020).

and **Fig 15d-f**). Finally, we used our novel tool in combination with expansion microscopy to determine the localization of the mitochondrial transcription factor A (TFAM), a protein discussed to associate with mitochondrial DNA (mtDNA) nucleoids in the matrix of mitochondria (Li et al., 2016) and Mic60 (Yang et al., 2015). While the matrix protein PRX3 again shows no colocalization with cristae, the signal of mitochondrial matrix protein TFAM closely associates with MtCK-GFP (**Figure 14c,f** and **Figure 15g-i**).
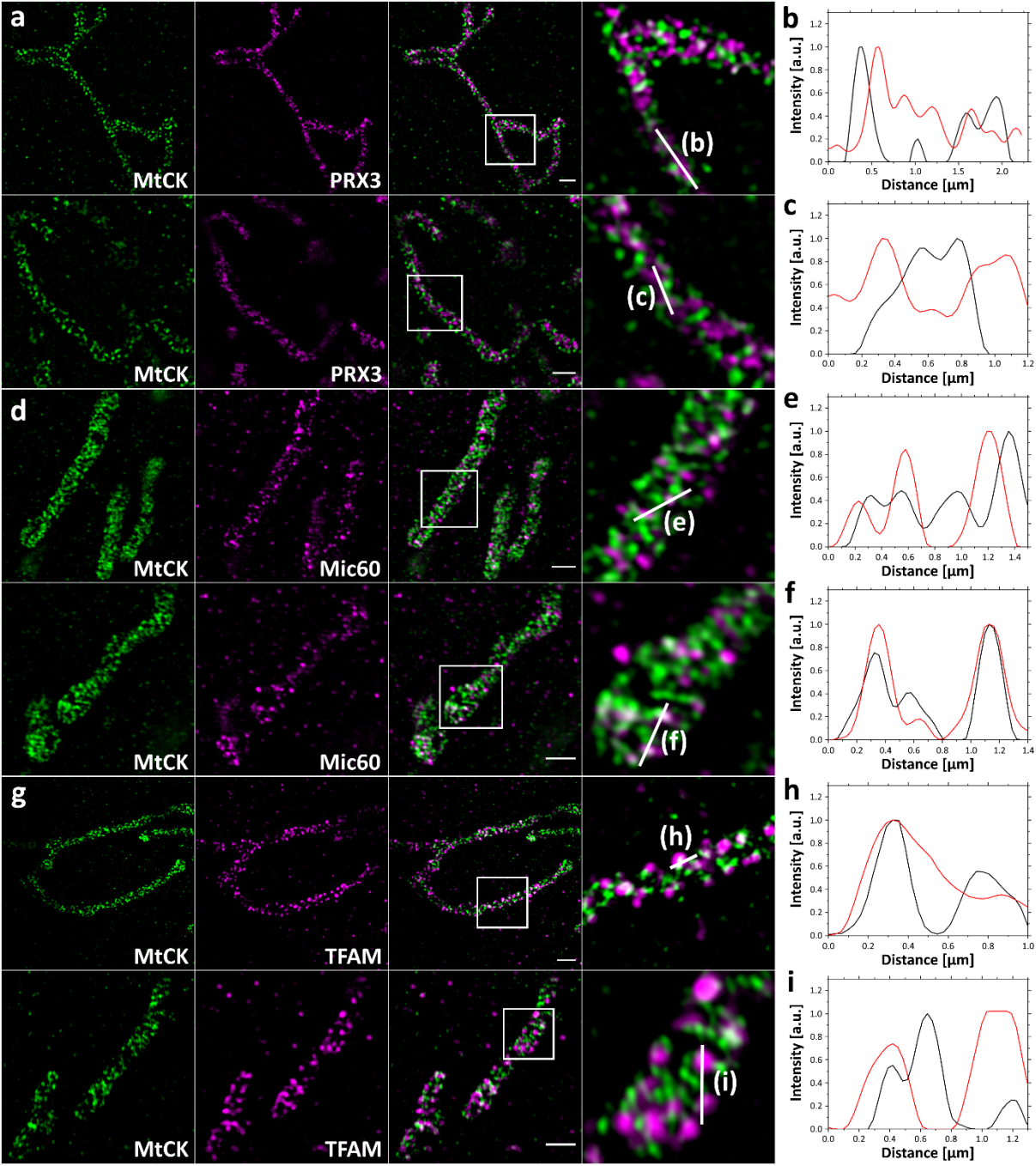
Figure 15: SIM-ExM of MtCK and mitochondrial marker proteins further improves resolution.

4x ExM-SIM images of HeLa229 cells transfected with MtCK-GFP (green) for 24 hours and immunolabeled for GFP and (a) PRX3, (d) Mic60 or (g) TFAM (magenta). Within the zoomed region the line profile (b-c, e-f, h-i) is indicated. While PRX3 alternates with MtCK, Mic60 and TFAM partially colocalize with MtCK. Scale bars, 2 µm (Kunz et al., 2020).

Furthermore, we wanted to know if our novel construct in combination with expansion microscopy offers the possibility to distinguish the mitochondrial cristae membrane and the inner boundary membrane or OMM. Hence, we co-labeled MtCK-GFP-labeled mitochondria with TIM44 and TOM20 (Kulawiak et al., 2013). Our approach enables in both cases the efficient discrimination of cristae membrane to other mitochondrial membranes (**Figure 16**).

To better compare mitochondrial proteins and their localization, we performed 3-colour confocal (**Figure 17a-e**) and SIM (**Figure 17g-m** and **Figure 18a-j**) imaging of cristae. Here, we aimed to compare Mic60 and TFAM. The signals of all three proteins were largely colocalizing and interestingly the colocalization of Mic60 and TFAM was stronger than the colocalization of Mic60 with MtCK-GFP, indicating that TFAM not only localizes at mitochondrial cristae but also juxtaposed to cristae junctions, which are marked by the presence of Mic60.
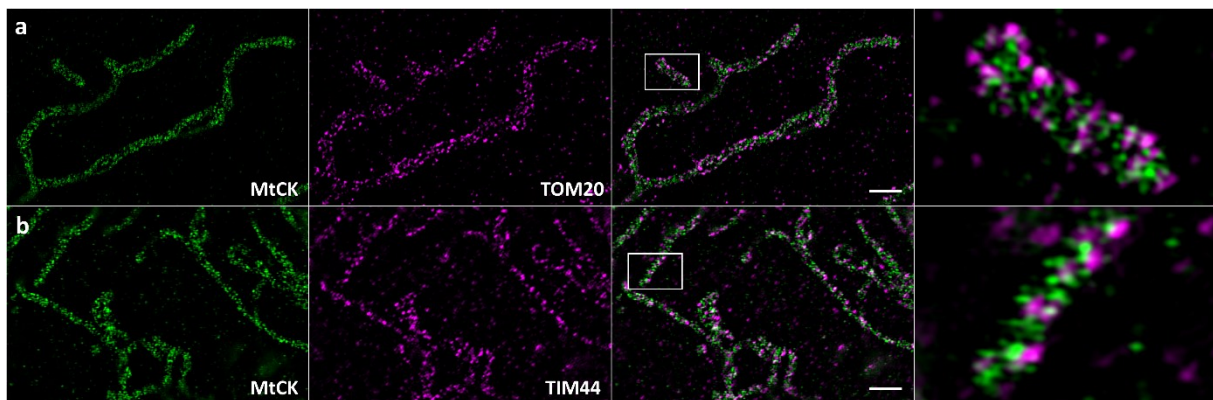

Figure 16: SIM-ExM of MtCK-GFP and TOM20/TIM44 offers the possibility to distinguish between cristae membrane and outer membrane/inner boundary membrane.

4x SIM-ExM images of HeLa229 cells transfected with MtCK-GFP for 24 hours and immunolabeled for GFP and (a) TOM20 or (b) TIM44 (magenta). Within the overlay the zoomed region is indicated. Scale bars, 2 µm (Kunz et al., 2020).
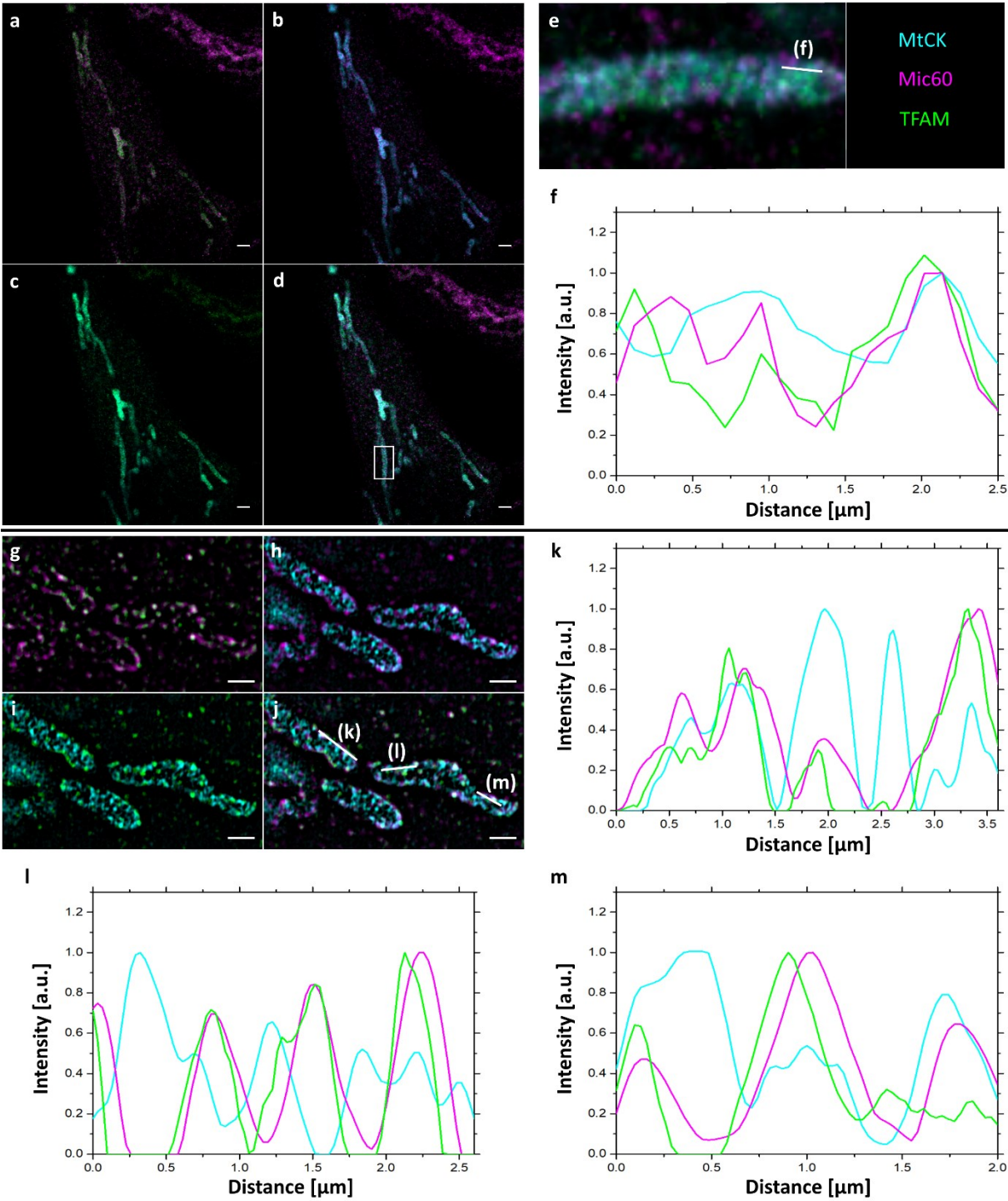
Figure 17: 3-color ExM to visualize the colocalization of TFAM and Mic60 at mitochondrial cristae.

4x ExM 3-color confocal (a-e) and SIM (g-j) images of HeLa229 cells transfected with MtCK-GFP for 24 hours and immunolabeled for GFP, Mitofilin and TFAM. (a, g) Mitofilin (magenta) and TFAM (green), (b, h) MtCK (cyan) and Mitofilin (magenta), (c, i) MtCK (cyan) and TFAM (green), (d, j) merge, (e) zoom from (d) with line indicating plot profiling shown in (f). (k-m) plot profiling of the lines shown in (j). Scale bars, 5 μm for confocal images, 2 μm for SIM images (Kunz et al., 2020).
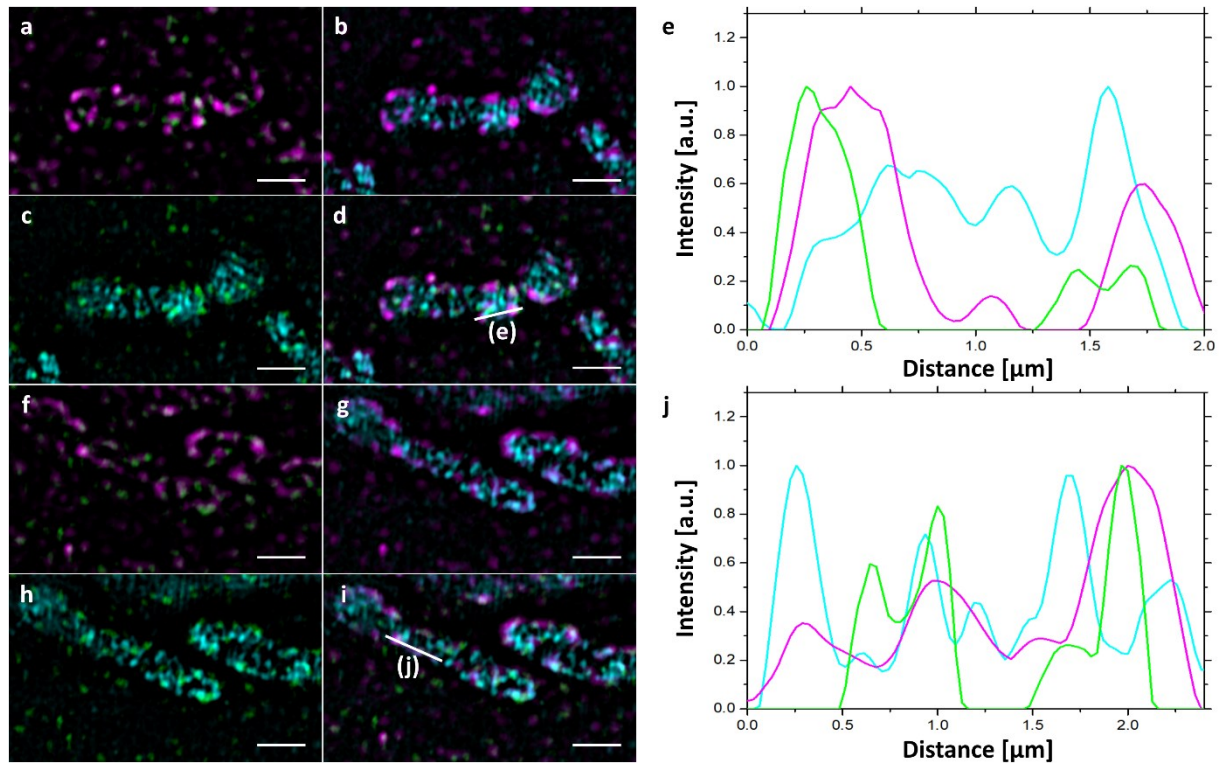
Figure 18: 3-color ExM to visualize the colocalization of TFAM and Mic60 at mitochondrial cristae.

4x SIM-ExM 3-color images (a-d; f-i) of HeLa229 cells transfected with MtCK-GFP for 24 hours and immunolabeled for GFP, Mitofilin and TFAM. (a, f) Mitofilin (magenta) and TFAM (green), (b, g) MtCK (cyan) and Mitofilin (magenta), (c, h) MtCK (cyan) and TFAM (green), (d, i) merge, with line indicating plot profiling shown in (e, j). Scale bars, 2 µm (Kunz et al., 2020).

In order to not only demonstrate the applicability of 4x expansion microscopy for localization studies but also to determine cristae morphology, we treated cells transfected with MtCK-GFP with 1 µM CCCP. CCCP is a strong uncoupling agent that can abruptly depolarize the membrane potential (Park et al., 1997). The mitochondria of cells incubated with CCCP exhibited rounding and swelling of mitochondria over time (**Figure 19a**). Even though we could still observe cristae in swollen mitochondria, the density was reduced drastically compared to non-treated mitochondria. As a second control, we transfected HeLa229 cells, where the knockdown of Sam50 is inducible by doxycycline (Dox)-mediated shRNA expression (*sam50kd-2*). As mentioned before, this complex has been demonstrated to be of importance for cristae morphology by bending the IMM for cristae formation and the interaction with the F_1F_O-ATP synthase. As previously demonstrated by electron microscopy (Ott et al., 2015), we could observe an enlargement of mitochondria and the loss of cristae structure (**Figure 19b**).
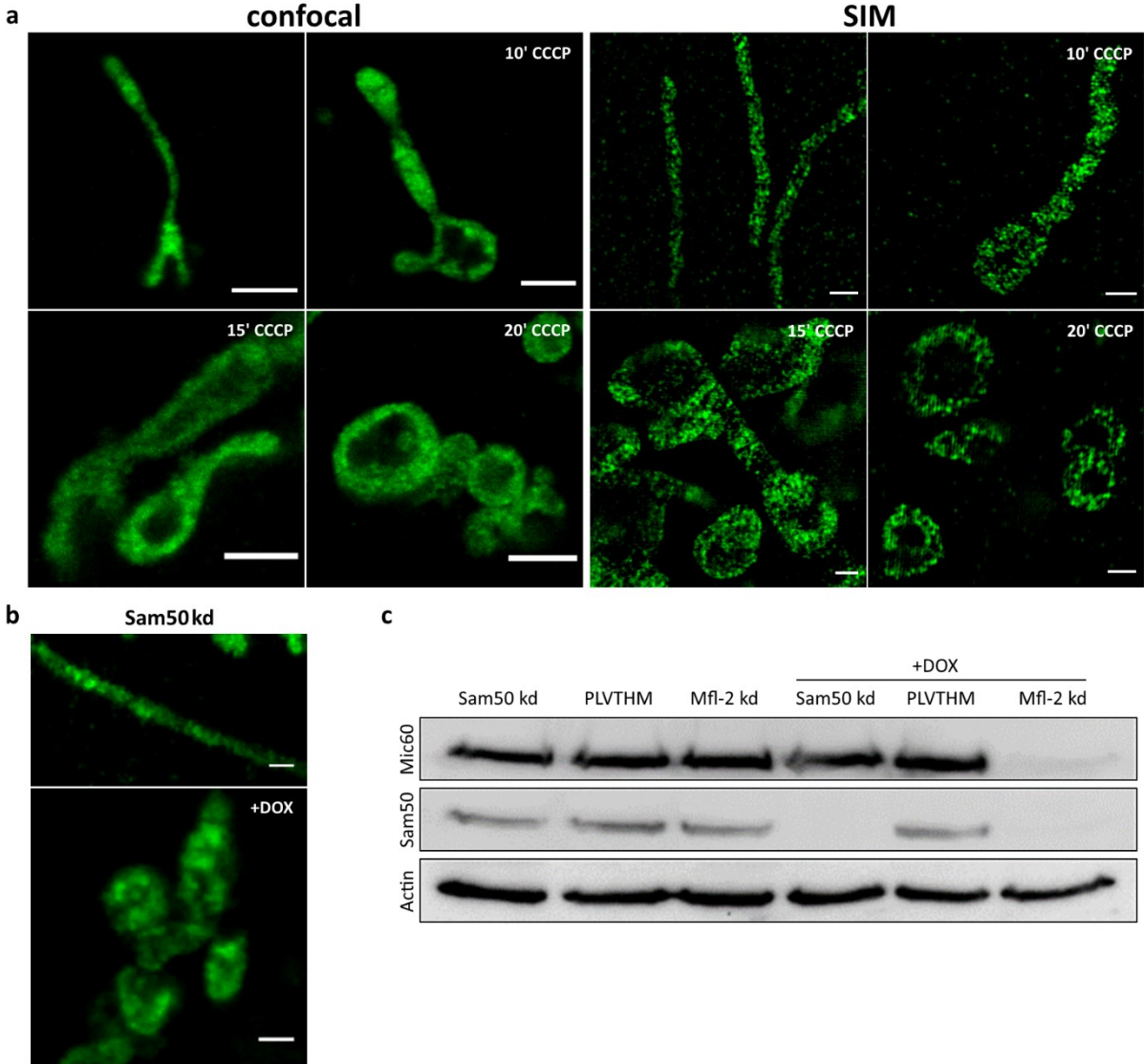
Figure 19: 4x ExM enables visualization of changes in cristae morphology.

(a) Confocal and SIM images of 4x expanded HeLa229 cells transfected with MtCK-GFP (green) and treated with 1 μM CCCP for 0, 10, 15 or 20 minutes. (b) Confocal images of 4x expanded Sam50 knockdown cells (sam50kd-2) transfected with MtCK-GFP (green) and treated with 1 μg/ml doxycycline for 72 hours to induce Sam50 knockdown. Scales, 2 μm. (c) Western blot of Sam50 knockdown cells and control PLVTHM cells treated with 1 μg/ml doxycycline for 72 hours. Protein amounts of Sam50 have been compared to Mic60 and Actin. Modified after (Kunz et al., 2020).

Expansion of intracellular pathogens

The structure of the bacterial membrane and cell wall differs enormously between different bacterial species. For expansion microscopy, a complete digestion of the sample is crucial for isotropic expansion. While member of the order Chlamydiales, *C. trachomatis* and *S. negevensis*, can be expanded with only proteinase K treatment, the expansion of a plethora of bacteria was demonstrated to require additional digestion with lysozyme (Lim et al., 2019). While expansion microscopy of *N. gonorrhoeae* indeed requires additional lysozyme, we show that the expansion of *S. aureus* requires besides lysozyme additionally lysostaphin, an endopeptidase secreted by *Staphyloccocus simulans* possessing bactericidal properties against *S. aureus* by cleaving the crosslinking pentaglycine bridges of staphylococcal peptidoglycan (Bastos et al., 2010), for isotropic expansion (**Figure 20**).
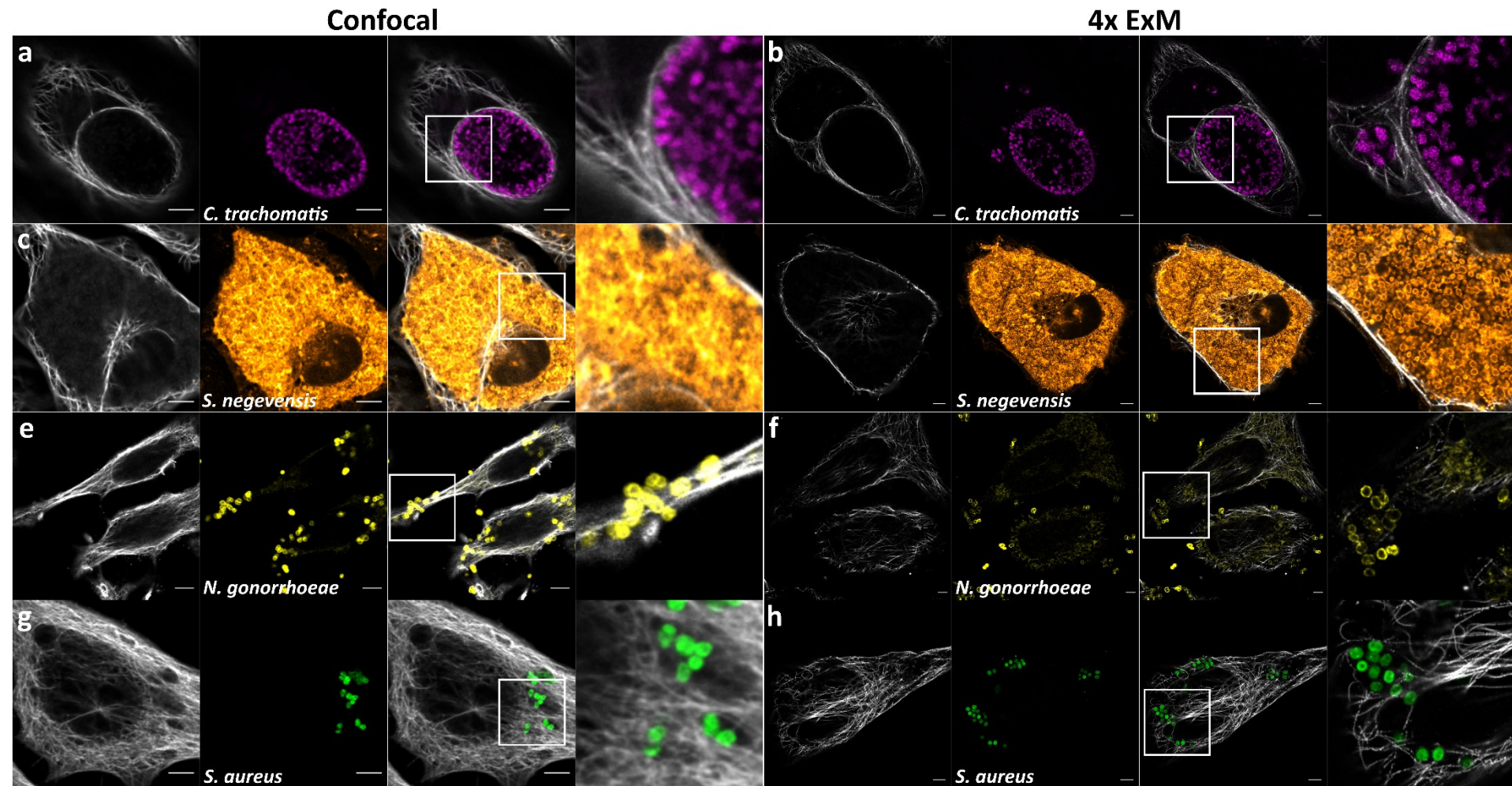
Figure 20:   Individual bacterial pathogens can be resolved on confocal setups using ExM.

Confocal fluorescence images of unexpanded (a,c,e,g) and 4x expanded (b,d,f,h) HeLa229 cells infected with (a,b) *Chlamydia trachomatis* (magenta), (c,d) *Simkania negevensis* (orange), (e,f) *Neisseria gonorrhoeae* (yellow) or (g,h) *Staphylococcus aureus* (green). Infected cells were fixed, permeabilized and labeled for tubulin (grey) and the respective pathogen. Scale bars, 10 μm. Sample preparation, infection and immunolabeling, of cells infected with *S. aureus* was performed by Marcel Rühling.

Expansion of *Chlamydia trachomatis*

C. trachomatis resides densely within a vacuole, the so-called inclusion. In addition, individual chlamydial particles are relatively small, ranging from around 300 nm for infectious elementary bodies (EBs) to between 600-1000 nm for replicative reticulate bodies (RBs). Thus, usual confocal microscopy does not offer sufficient resolution to resolve individual chlamydial particles within an inclusion. To overcome this, we applied 4x expansion microscopy to cells infected with *C. trachomatis*. The first successfully expanded chlamydial proteins were CPAF, a chlamydial protease-like activity factor (Zhong et al., 2001), in combination with HSP60, a chlamydial heat-shock protein and the protein of choice to label individual chlamydial particles (**Figure 21** and **Supplementary Movies 1-4**). CPAF is secreted via a type II secretion system
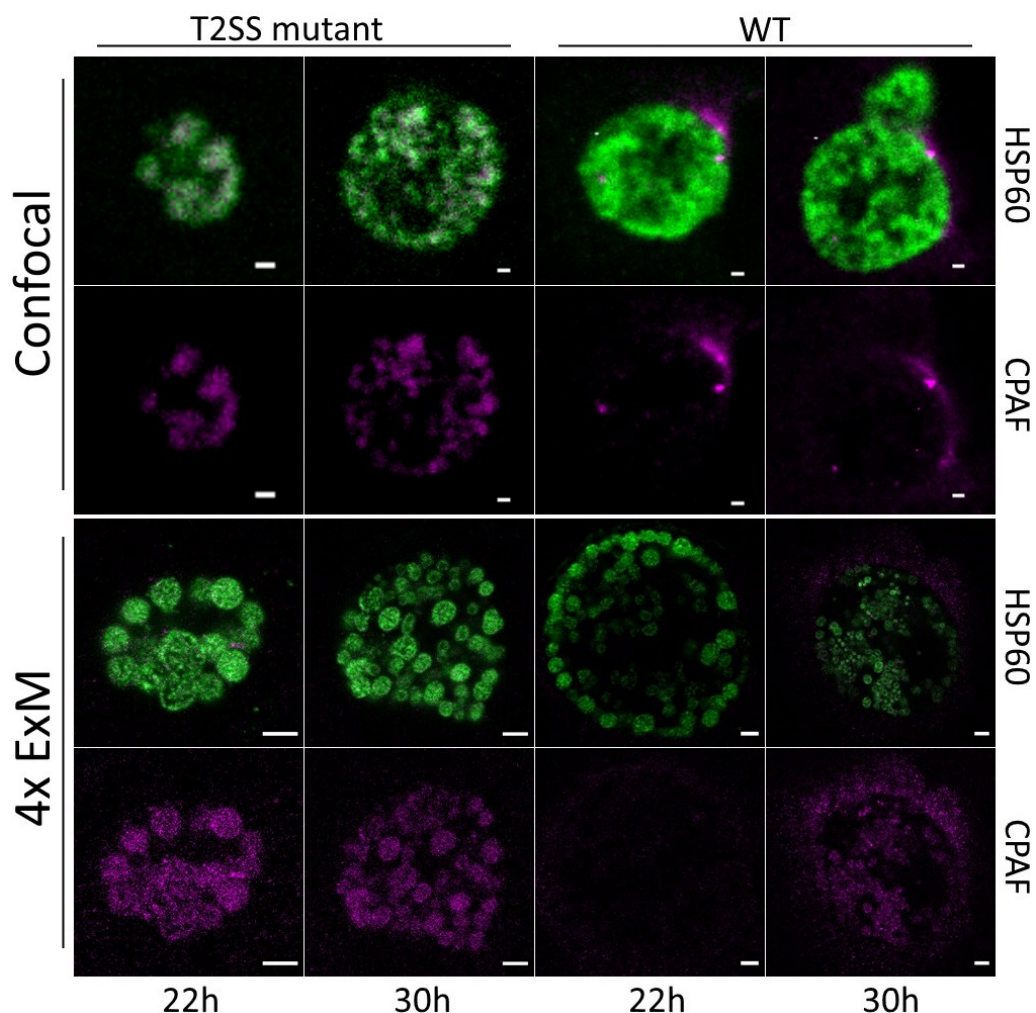

Figure 21: CPAF is secreted from the inclusion at later stages of infection by a T2SS.

4x confocal ExM images of HeLa229 cells, infected with *Chlamydia trachomatis* for 22 and 30 hours with wildtype *Chlamydia* or RSTE4 (T2SS mutant) and immunolabeled for HSP60 (green) and CPAF (magenta). Scale bars, 1 µm for unexpanded and 5 µm for expanded images (Kunz et al., 2019).

(T2SS) pathway and was initially discovered to degrade cellular proteins (Zhong et al., 2001). The localization of CPAF in the cytosol remains challenging and is still under debate (Chen et al., 2012; Conrad et al., 2013; Hacker, 2014; Johnson et al., 2015; Snavely et al., 2014; Zhong, 2014). To investigate the localization of CPAF in expanded samples, HeLa229 cells were infected with wildtype *Chlamydia* and a T2SS-mutant that is unable to secrete CPAF into the lumen of the inclusion (Snavely et al., 2014). After 4x expansion, we could show that CPAF is expressed and secreted in wildtype *Chlamydia* in higher quantities at later stages of infection. To exclude artifacts derived by the activity of CPAF during fixation, we further treated cells with clasto-lactacystin beta-lactone, that was previously described as a CPAF inhibitor by Johnson et al. (Johnson et al., 2015). We could not observe an impact on CPAF localization upon clasto-lactacystin beta-lactone treatment (**Figure 22**).
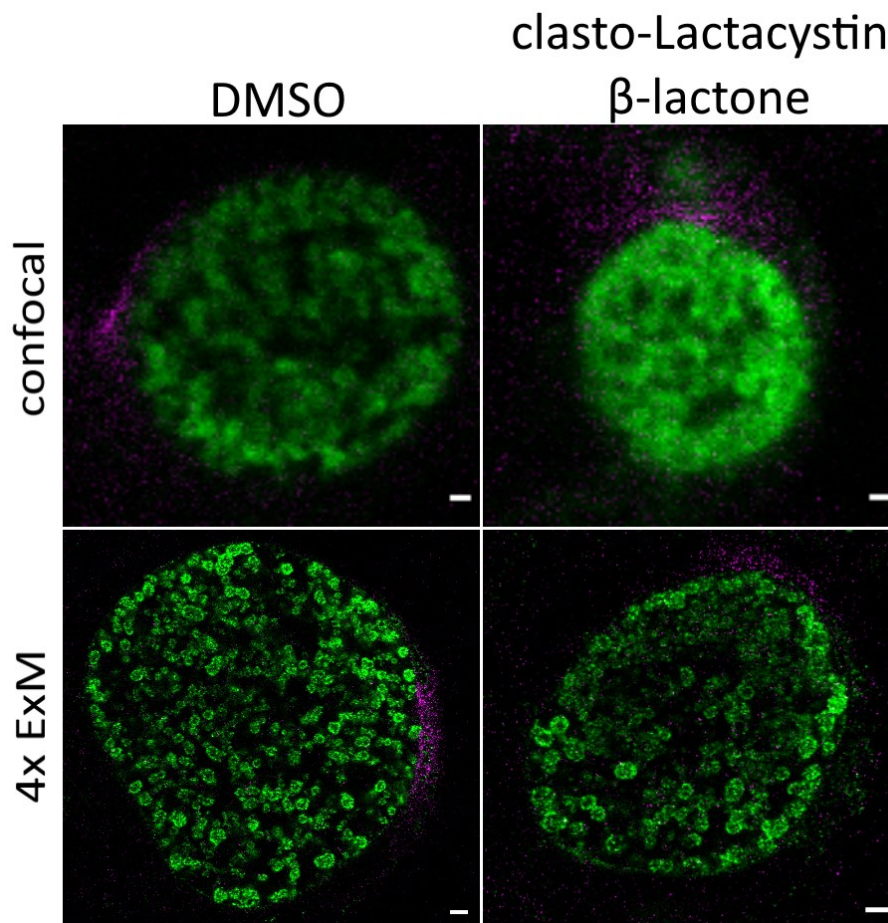
Figure 22: Inhibition of CPAF by clasto-Lactacytin ß-lactone does not affect its localization.

4x confocal ExM images of HeLa229 cells infected with wildtype *Chlamydia trachomatis* for 30 hours. Prior fixation, the cells were treated with 150 μM clasto-lactacystin beta-lactone for 1 hour. The samples were then stained for HSP60 (green) and CPAF (magenta). Scale bars, 1 μm for unexpanded and 5 μm for expanded images (Kunz et al., 2019).

The ubiquitin system is exclusively found in eukaryotic cells. It regulates several crucial processes such as autophagy, cell survival, organellar targeting and activation and inactivation of proteins (Asaoka and Ikeda, 2015; Grumati and Dikic, 2018; Kupka et al., 2016). Several viruses and bacteria developed strategies to interfere with the host ubiquitin system. *C. trachomatis* expresses a deubiquitinase located at the inclusion membrane, facing the host cell cytosol with its active site, called Cdu1 (Fischer et al., 2017). The expression of Cdu1 starts around 16 hours post infection and was shown to increase until late stages of infection (Belland et al., 2003). Expansion of infected HeLa229 cells with wildtype *C. trachomatis* and a Cdu1:: Tn bla mutant as a control reveals the localization of Cdu1 at the inclusion membrane (**Figure 23** and **Supplementary Movies 5-6**).
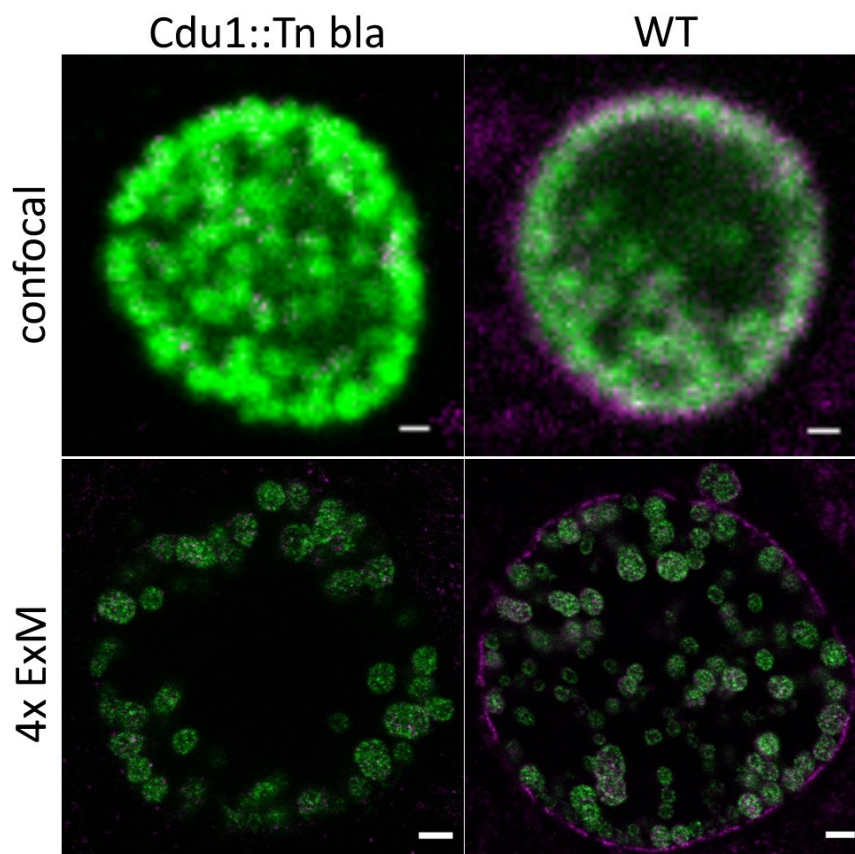

Figure 23: Cdu1 is located at the chlamydial inclusion membrane.

4x confocal ExM images of HeLa229 cells infected for 24 hours with wildtype *Chlamydia trachomatis* or Cdu1:: Tn bla mutant and immunolabeled for chlamydial HSP60 (green) and Cdu1 (magenta). Scale bars, 1 μm for unexpanded and 5 μm for expanded images (Kunz et al., 2019).

Besides visualizing individual chlamydial particles and effector proteins, we further observed that expansion microscopy revealed different sizes of chlamydial particles. Thus, we hypothesized that expansion microscopy could be suitable to distinguish the smaller infectious EBs and larger metabolically active RBs by size. To prove that a differentiation can be made according to size, we infected HeLa229 cells with the previously published *Chlamydia* strain Ct mCh(GroL2) GFP (OmcAL2), which expresses mCherry under the control of the RB-associated constitutive groESL operon promotor and GFP under the control of the EB-associated omc promotor (Cortina et al., 2019). Indeed, expansion microscopy enables a clear differentiation between EBs and RBs by size (**Figure 24-25** and **Supplementary Movie 7**).

Figure 24: Detection of distinct chlamydial forms by 4x ExM.

4x confocal ExM images of HeLa229 cells, infected for 30 hours with *Ct* mCh(GroL2) GFP(OmcAL2), expressing mCherry under the control of the RB-associated constitutive groESL operon promotor and GFP under the control of the EB-associated omc promotor. The samples were immunolabeled for GFP (green) and mCherry (magenta). Scale bars, 1 µm for unexpanded and 5 µm for expanded images (Kunz et al., 2019).

Figure 25: 3D-Imaris to visualize distinct chlamydial forms.
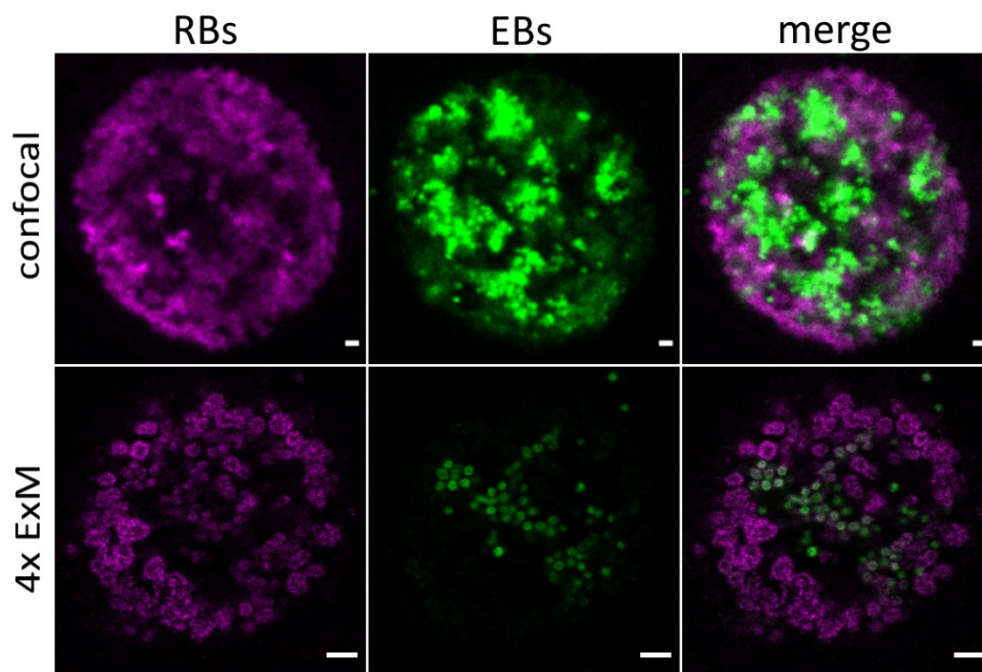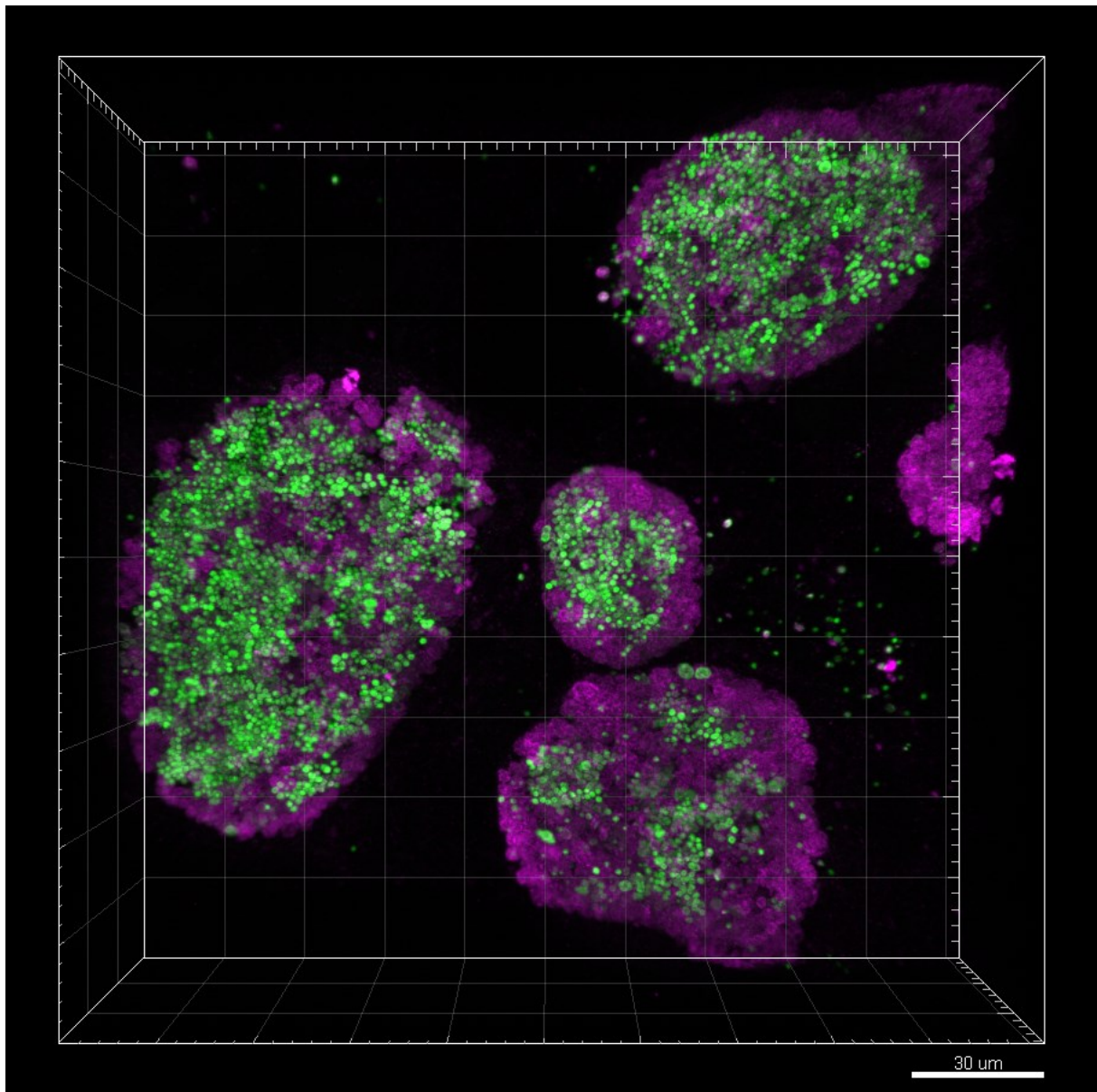
4x confocal ExM images of HeLa229 cells, infected for 30 hours with *Ct* mCh(GroL2) GFP(OmcAL2), expressing mCherry under the control of the RB-associated constitutive groESL operon promotor and GFP under the control of the EB-associated omc promotor. The samples were immunolabeled for GFP (green) and mCherry (magenta). 3D-View was created using Imaris 8.4.1.

Expansion of *Staphylococcus aureus*

As mentioned previously, Lim et al demonstrated that the expansion of various bacterial pathogens requires additional digestion with lysozyme for cell wall digestion (Lim et al., 2019). Lysozyme is a 1,4-β-N-acetylmuramidase catalyzing the glycosidic bond between N-acetyl muramic acid (MurNAc) and N-acetyl glucosamine in peptidoglycan, the major component of the cell wall of gram-positive bacteria like *S. aureus* (Ragland and Criss, 2017). The cell wall of *S. aureus*, however, has particularly high cross-link ratio between peptidoglycan chains, which consists mostly of pentaglycine motifs. This pentaglycine motifs can be cleaved by a protease called lysostaphin, a metalloendopeptidase secreted by *S. simulans* to cleave specifically the pentaglycine residues in the cell wall of *S. aureus* (Bastos et al., 2010). Here, we demonstrate that the digestion of HeLa229 cells infected with *S. aureus* by lysozyme and lysostaphin, followed by proteinase K enables the expansion of *S. aureus* (**Figure 20h** and **Figure 26**).

S. aureus was controversially described to either avoid or induce autophagy (Geng et al., 2020; Lopez de Armentia et al., 2017; Mestre and Colombo, 2012; Mestre et al., 2010; Prajsnar et al., 2020) and to reside and replicate in large numbers within lysosomes (Flannagan et al., 2016). Here we demonstrate that expansion microscopy enables the visualization and further investigation of bacteria within LAMP1 (**Figure 27a**) and LC3-II (**Figure 27b**) vesicles in HeLa229 cells 1.5 hours post infection. We also show that expansion microscopy can be used to investigate the localization of proteins at the membrane or cytosol of *Staphylococcus* by co-immunolabelling the staphylococcal protein lipoteichoic acid with cytosolic GFP (**Figure 27c**).
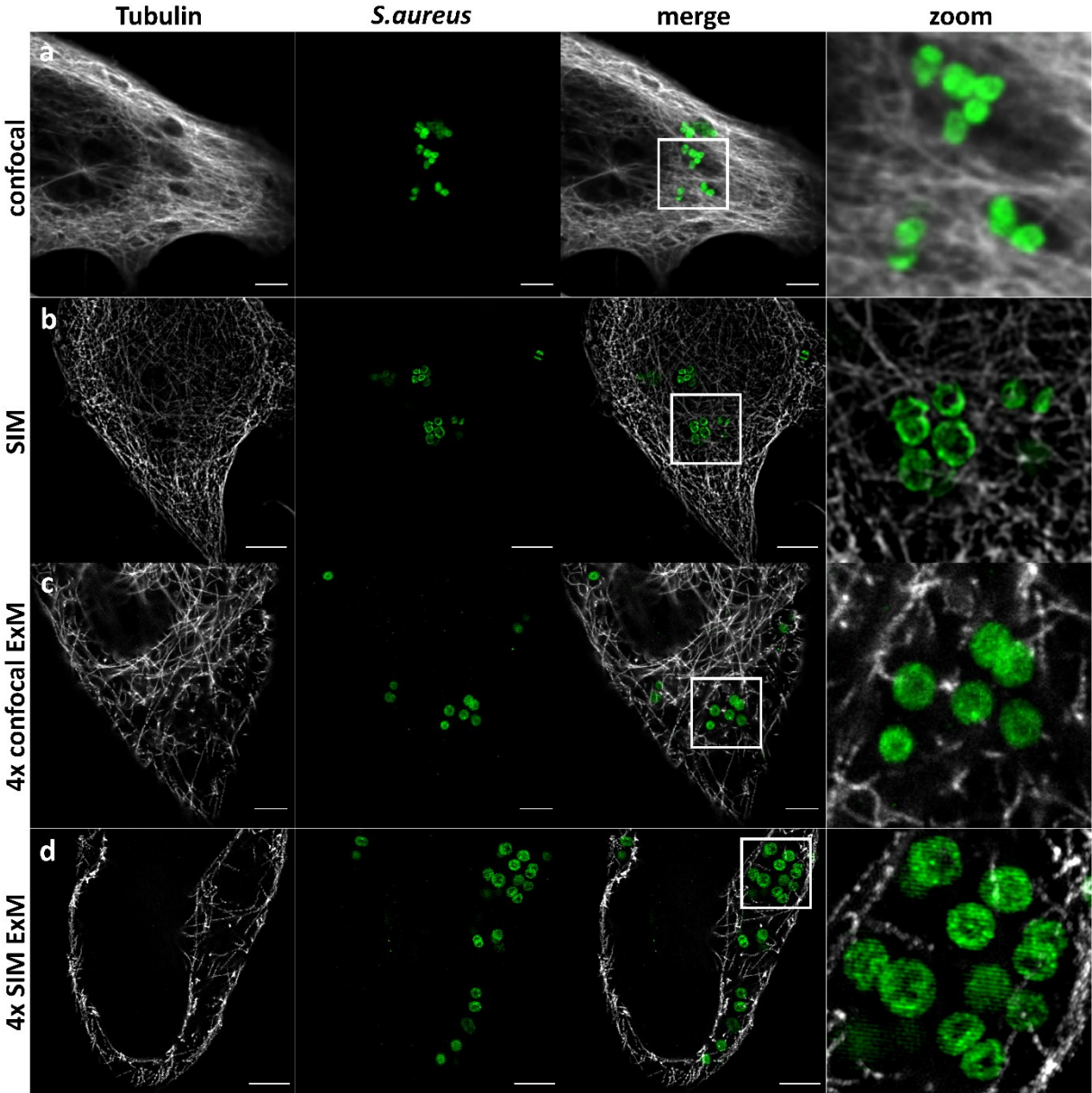
Figure 26: Combination of SIM and 4x ExM further improves the resolution of individual *Staphylococcus aureus.*

HeLa229 cells were infected with *Staphylococcus aureus* (green), fixed, permeabilized and immunolabeled for tubulin (grey) and GFP (green) and imaged before (a,b) and after 4x ExM (c,d) on a confocal (a,c) or SIM (b,d) setup. Scale bars, 5 µm unexpanded and 10 µm expanded samples. Sample preparation, infection and immunolabeling was performed by Marcel Rühling.

Figure 27: 4x ExM provides more detailed insight of *Staphylococcus aureus* within host LAMP1 and LC3-II vesicles and enables distinction of staphylococcal cytosol and membrane.

Confocal images of HeLa229 cells, infected with *Staphylococcus aureus* (green), fixed, permeabilized, immunolabeled for GFP (green) and (a) Lamp1, (b) LC3-II or (c) LTA and expanded. Scale bars, 5 µm unexpanded and 10 µm expanded samples.

Spingolipid expansion microscopy

Expansion of sphingosine in *Neisseria gonorrhoeae*

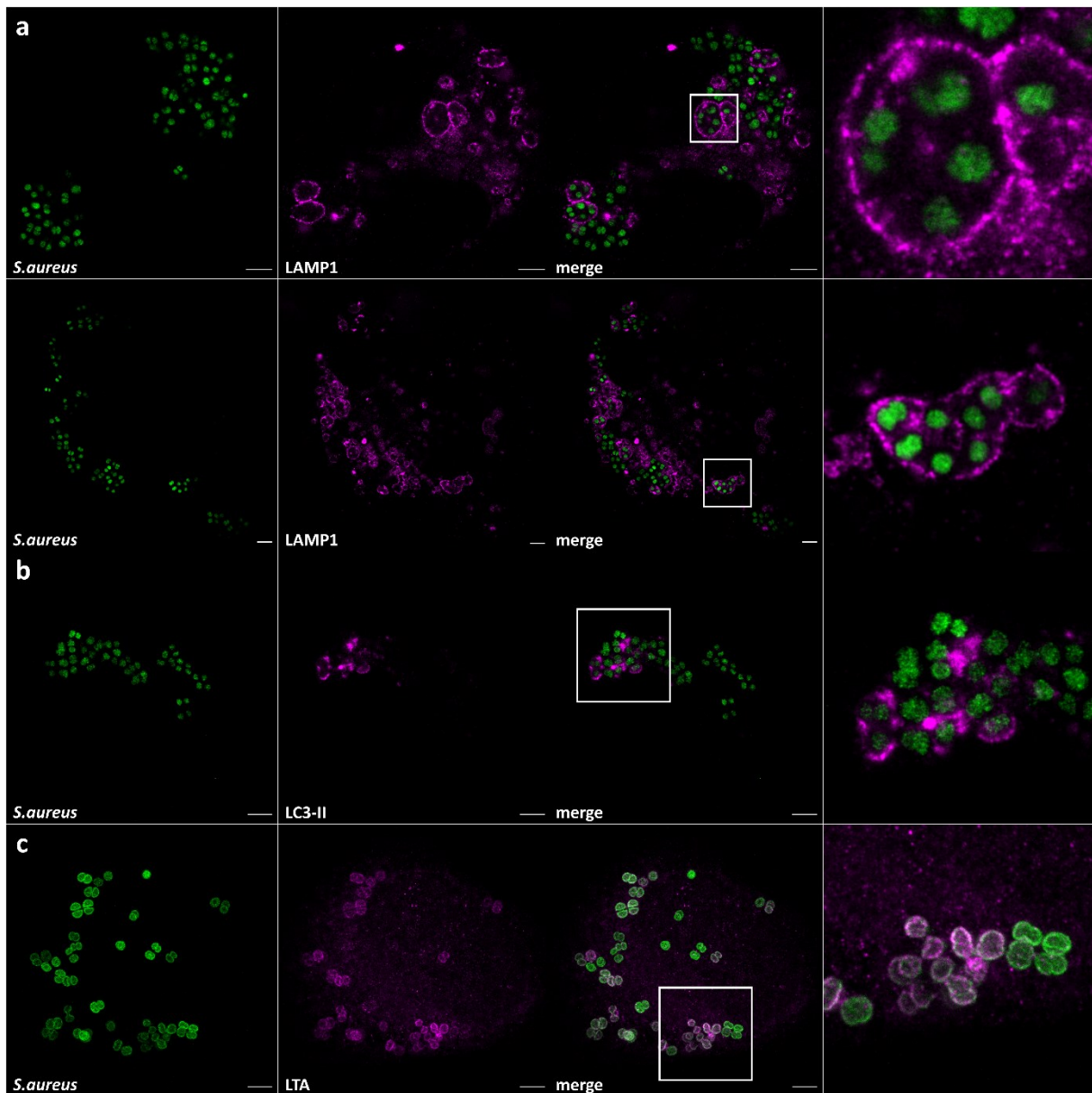To further test the applicability of expansion microscopy on lipids, we aimed to expand Chang cells, fed with ω-N$_3$-sphingosine and infected with *N. gonorrhoeae*. Previously, we could show the incorporation of our sphingosine-analogue in the membrane of *Neisseria* by structured illumination microscopy **(Figure 28)** in Chang cells that were fed with ω-N$_3$-sphingosine for 30 minutes before infection (Solger et al., 2020).
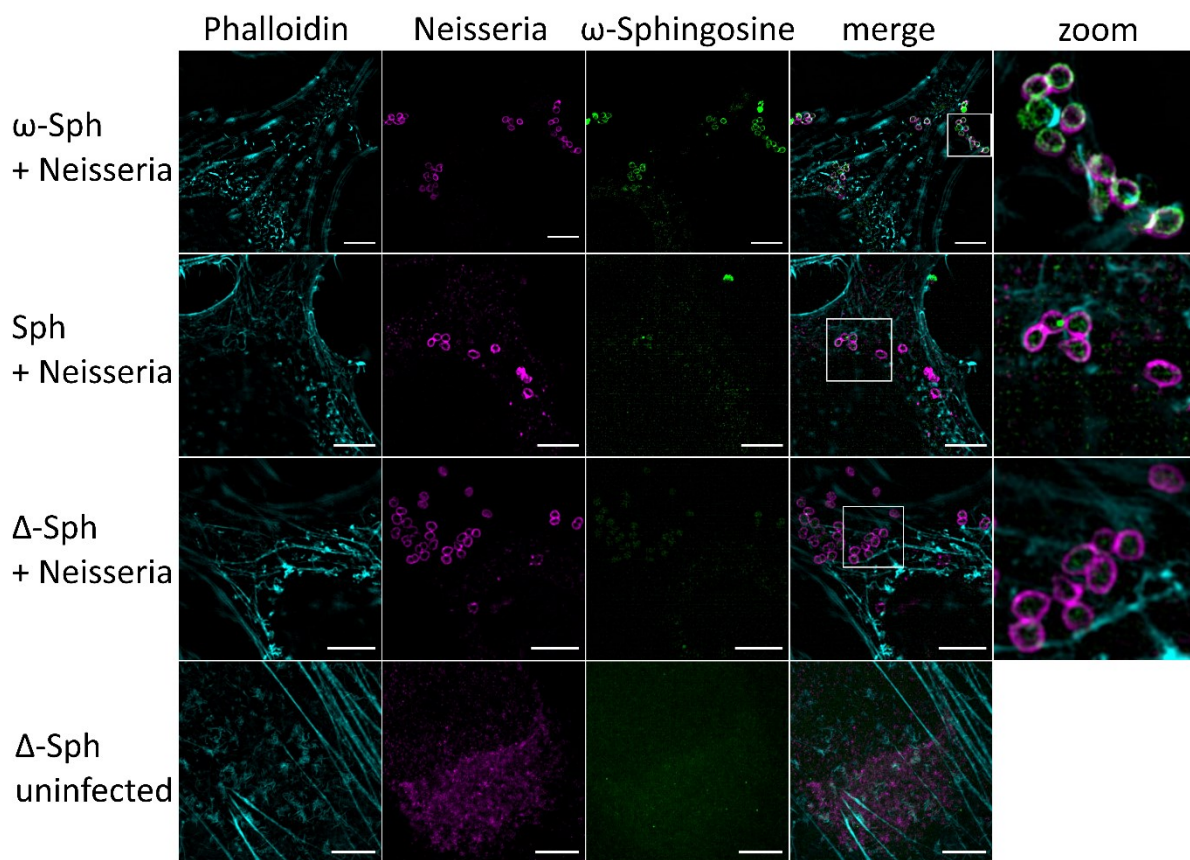
Figure 28: ω-N$_3$-Sphingosine is incorporated into the membrane of *Neisseria gonorrhoeae*.

Chang cells were fed with 10 µM ω-N$_3$-Sphingosine (ω-Sph) or sphingosine (Sph) for 30 minutes and then infected with *Neisseria gonorrhoeae* strain N927 for 4 hours. After infection, the samples were clicked with DIBO-488 (green), stained for phalloidin (cyan) and immunolabeled with anti-neisserial antibody (magenta). Scale bars, 5 µm (Solger et al., 2020). Sample preparation, infection and immunolabeling, was performed by Franziska Solger.

The addition of lysozyme, as described by Lim et al (Lim et al., 2019), at the digestion step prior to expansion enabled the successful expansion of *N. gonorrhoeae*. Moreover, we demonstrated for the first time the expansion of a lipid, ω-N$_3$-sphingosine **(Figure 29)**. Sphingosine itself carries a primary amino group, which is crucial for linkage into the hydrogel for expansion. Thus, we hypothesized that modification of lipids with a primary amino group could enable expansion of other functionalized lipids, e.g. ceramide.
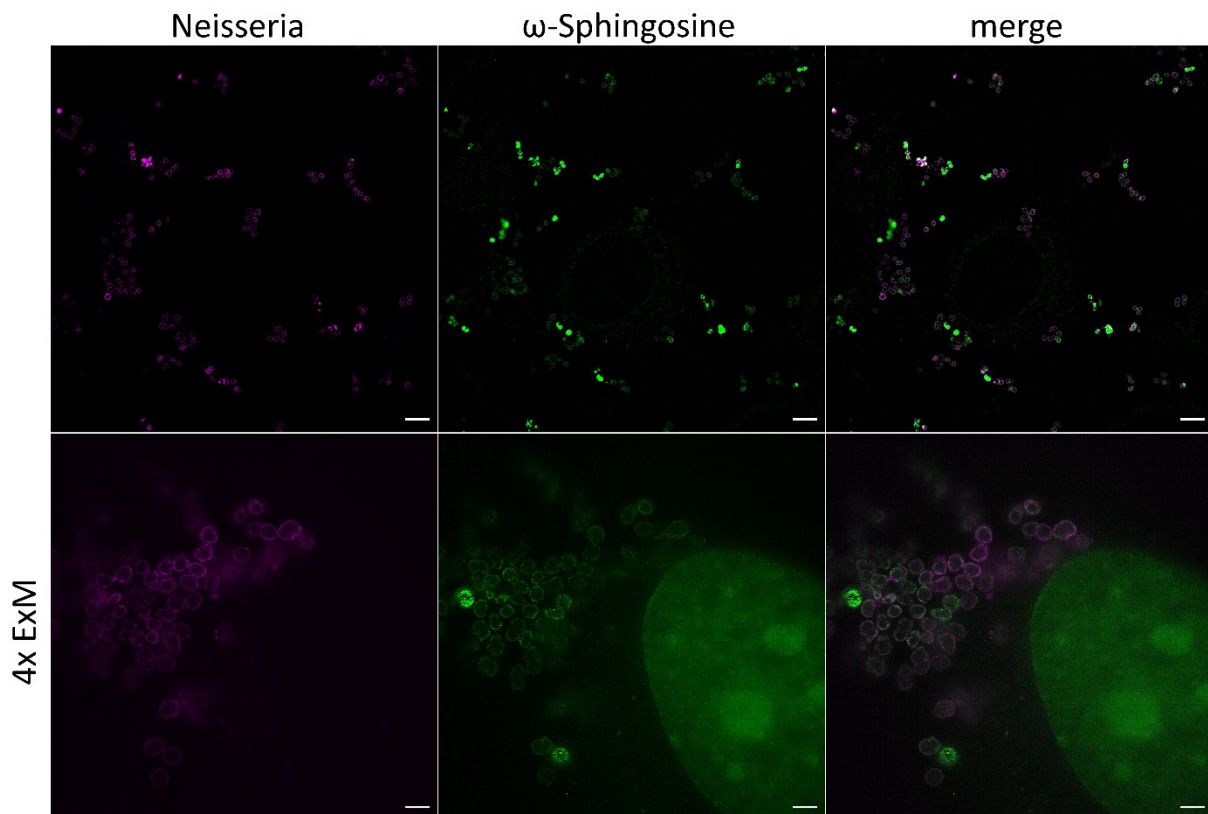
Figure 29: Lysozyme digestion enables ExM of ω-N$_3$-Sphingosine in *Neisseria gonorrhoeae*.

Unexpanded (upper row) and 4x expanded (lower row) SIM images of Chang cells, fed with 10 μM ω-N$_3$-sphingosine for 30 minutes and infected with *Neisseria gonorrhoeae* strain N927 for 4 hours. After infection, the samples were clicked with DIBO-Alexa Fluor 488 (green), and immunolabeled with anti-neisserial antibody (magenta). Scale bars, 5 μm for unexpanded and 4 μm for expanded images. Sample preparation, infection and immunolabeling, was performed by Franziska Solger (Gotz and Kunz et al., 2020a).

Expansion of ceramide

Ceramide regulates a multitude of crucial cellular pathways, such as differentiation, proliferation, growth arrest and apoptosis. Moreover, ceramide-rich membrane areas promote structural changes in the plasma membrane, segregating membrane receptors, and affect membrane curvature and vesicle formation, fusion and trafficking (Burgert et al., 2017; Hannun and Obeid, 2002). Previously, it was demonstrated that short-chain ω-N_3-C_6-ceramides are incorporated into cellular membranes and can be labeled efficiently by click-chemistry (Collenburg et al., 2016; Walter et al., 2016). On the other hand, efficient click-labeling of the longer ω-N_3-C_{16}-ceramides was impossible, likely due to a hindered accessibility of the ω-N_3-group upon membrane incorporation (Walter et al., 2017). Hence, for further investigation of ceramide distribution and membrane labeling, Julian Fink introduced a primary amino group to ω-N_3-C_6-ceramide, creating α-NH_2-ω-N_3-C_6-ceramide (**Figure 30a** and **Supporting Figures 1-13**) to enable linkage into hydrogels.

We then tested if our novel ceramide analogue is incorporated into cellular membranes similar to control ω-N_3-C_6-ceramide. In order to do so, we fed HeLa229 cells with 10 µM ceramide for 1 hour and after fixation and permeabilization click-labeled with DBCO-Alexa Fluor 488. Indeed, we observed equal distribution of ω-N_3-C_6-ceramide in the plasma membrane and the membrane of intracellular organelles (**Figure 30c**). In theory, the introduction of a primary amine should enable the fixation of the novel ceramide analogue. Thus, we treated the fixed and stained samples with various concentrations of the detergent Triton X-100. While increasing concentration of detergent drastically reduced the signal of samples fed with control ω-N_3-C_6-ceramide, it had only very little effect on the samples fed with α-NH_2-ω-N_3-C_6-ceramide (**Figure 30c**). Fluorescence recovery after photobleaching (FRAP) experiments performed by Jan Schlegel could in addition demonstrate a higher mobility in samples fed with control ω-N_3-C_6-ceramide (48.1%) compared to α-NH_2-ω-N_3-C_6-ceramide (22.2%) (**Figure 30b**).

While ceramide controls important pathways regulating the cells viability, such as apoptosis, LDH-Cytotoxicity assays revealed that the treatment of HeLa229 cells for 1 hour with 10 µM of our functionalized α-NH_2-ω-N_3-C_6-ceramide, ω-N_3-C_6-ceramide or C_6-ceramide did not exhibit cytotoxicity. After 24 hours of treatment, the cytotoxicity exhibited by the different analogues was similar - around 15% (**Figure 31**).
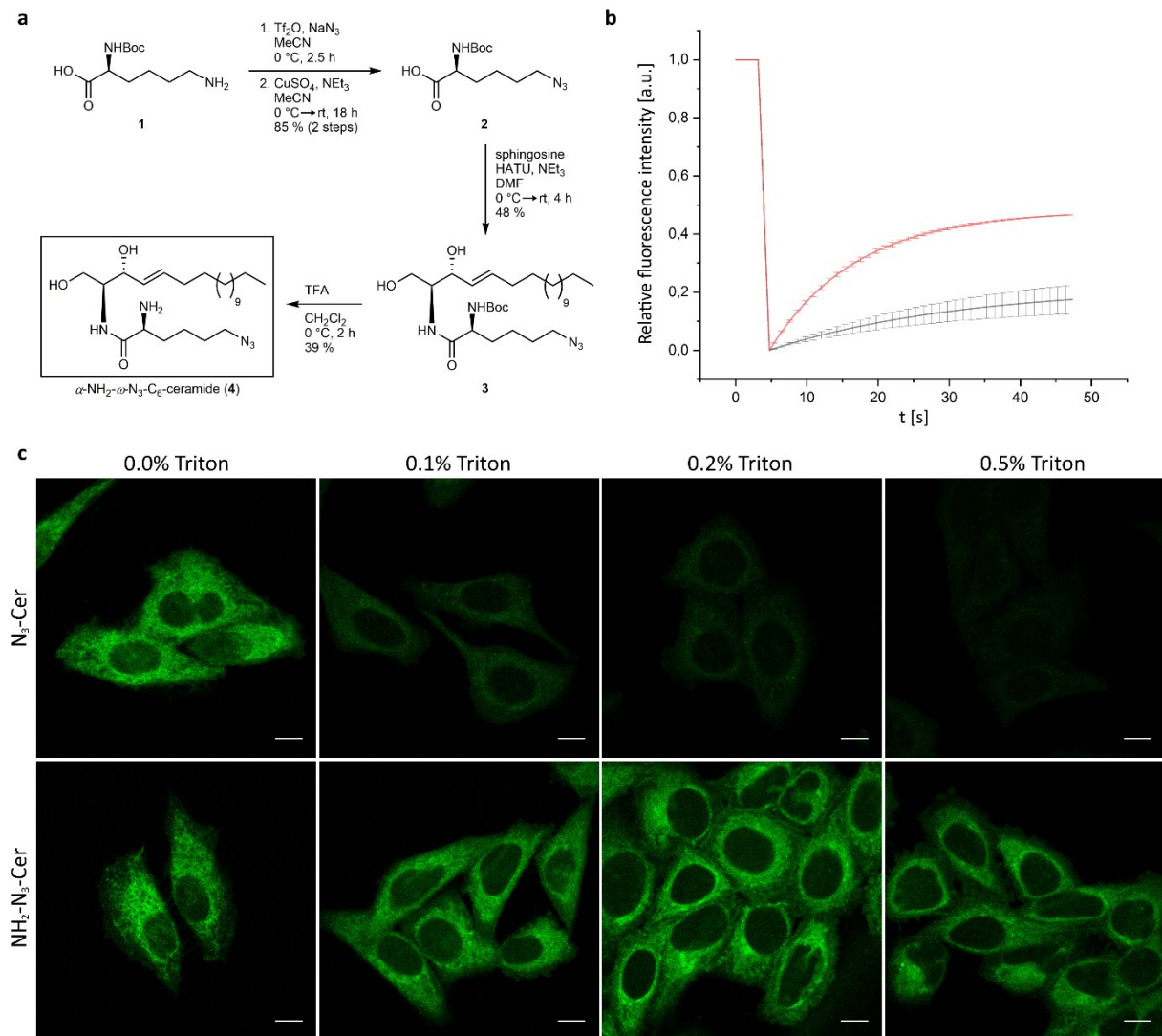
Figure 30: Introduction of -NH$_2$ at α-position of ω-N$_3$-C$_6$-Ceramide enables ceramide fixation.

(a) Schematic overview of the synthesis of α-NH$_2$-ω-N$_3$-C$_6$-Ceramide performed by Julian Fink. (b,c) To investigate the mobility and fixability of membrane-incorporated α-NH$_2$-ω-N$_3$-C$_6$-Ceramide, HeLa229 cells were fed with 10 µM α-NH$_2$-ω-N$_3$-C$_6$-ceramide or control ω-N$_3$-C$_6$-Ceramide, fixed with 4% PFA and 0.1% GA and permeabilized. The samples were then clicked with DBCO-Alexa Fluor 488. (b) FRAP experiments performed by Jan Schlegel. After three confocal fluorescence imaging frames, a circular region of interest with a diameter of 1.8 µm was bleached and fluorescence recovery followed over time. The α-NH$_2$-ω-N$_3$-C$_6$-ceramide (black) shows a lower mobility (mean mobile fraction of 22.2 %) than the ω-N$_3$-C$_6$-ceramide (red) lacking the primary amino group (mobile fraction of 48.1 %). (c) Confocal fluorescence images of fixed and labeled cells in the presence of increasing concentrations of the detergent Triton-X100. With increasing Triton-X100 concentration ω-N$_3$-C$_6$-ceramide is efficiently washed out while the α-NH$_2$-ω-N$_3$-C$_6$-ceramide signal remains preserved. Scale bars, 10 µm (Gotz and Kunz et al., 2020a).
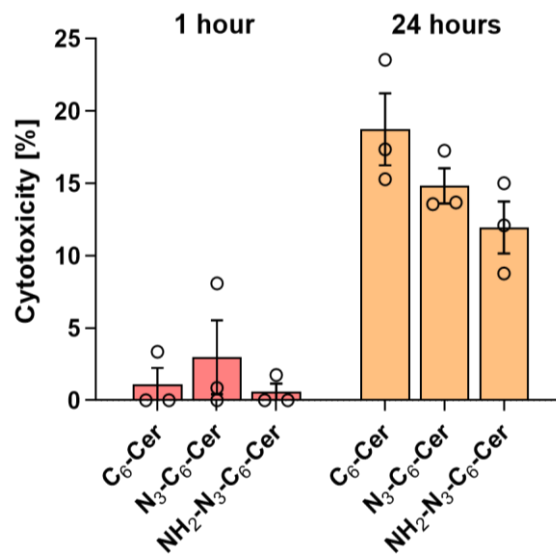
Figure 31: Functionalized C$_6$-Ceramides do not show altered cytotoxicity.

LDH-assay of HeLa229 cells fed with C$_6$-ceramide, ω-N$_3$-C$_6$-ceramide or α-NH$_2$-ω-N$_3$-C$_6$-ceramide for 1 or 24 hours. While cytotoxicity was not altered after treatment with the functionalized ceramides for one hour compared to controls, cytotoxicity was altered similarly, around 15%, after 24 hours (Gotz and Kunz et al., 2020a).

Since glutaraldehyde enabled the linkage of ω-N$_3$-sphingosine in *Neisseria* into hydrogels (**Figure 29**), we further investigated whether the introduction of a primary amine in our functionalized α-NH$_2$-ω-N$_3$-C$_6$-ceramide also allows the linkage into the hydrogel. Therefore, we expanded HeLa229 cells treated with α-NH$_2$-ω-N$_3$-C$_6$-ceramide, fixed with glutaraldehyde, permeabilized and labeled with DBCO-Alexa Fluor 488. Indeed, 4x as well as 10x expanded confocal fluorescence images show that the ceramide analogue is linked to the hydrogel and revealed staining of the plasma membrane, as well as the membrane of organelles, such as mitochondria and Golgi (**Figure 32**). Here, we demonstrate the colocalization of ceramide signal with mitochondrial Peroxiredoxin 3 (Prx3) (**Figure 32a**). Moreover, we compared the efficiency of membrane labeling of our ceramide analogue with membrane-binding fluorophore-cysteine-lysine-palmitoyl group (mCling), a molecule which is taken up during endocytosis, labels the plasma membrane and also carries a primary amine necessary for expansion (**Figure 32b**) (Revelo et al., 2014). While ceramide is taken up in the plasma membrane and different organelles, staining with mCling is efficiently incorporated solely in the plasma membrane of the cell. To verify isotropic expansion and a correct expansion factor, we performed imaging of the same cell pre- and post 4x and 10x expansion (**Figure 33**). We

determined effective expansion factors of 4.1x and 9.8x. The images further reveal that the labeling by α-NH$_2$-ω-N$_3$-C$_6$-ceramide is dense enough to support nanoscale resolution imaging of continuous membrane structures (**Figure 32** and **Figure 33**).
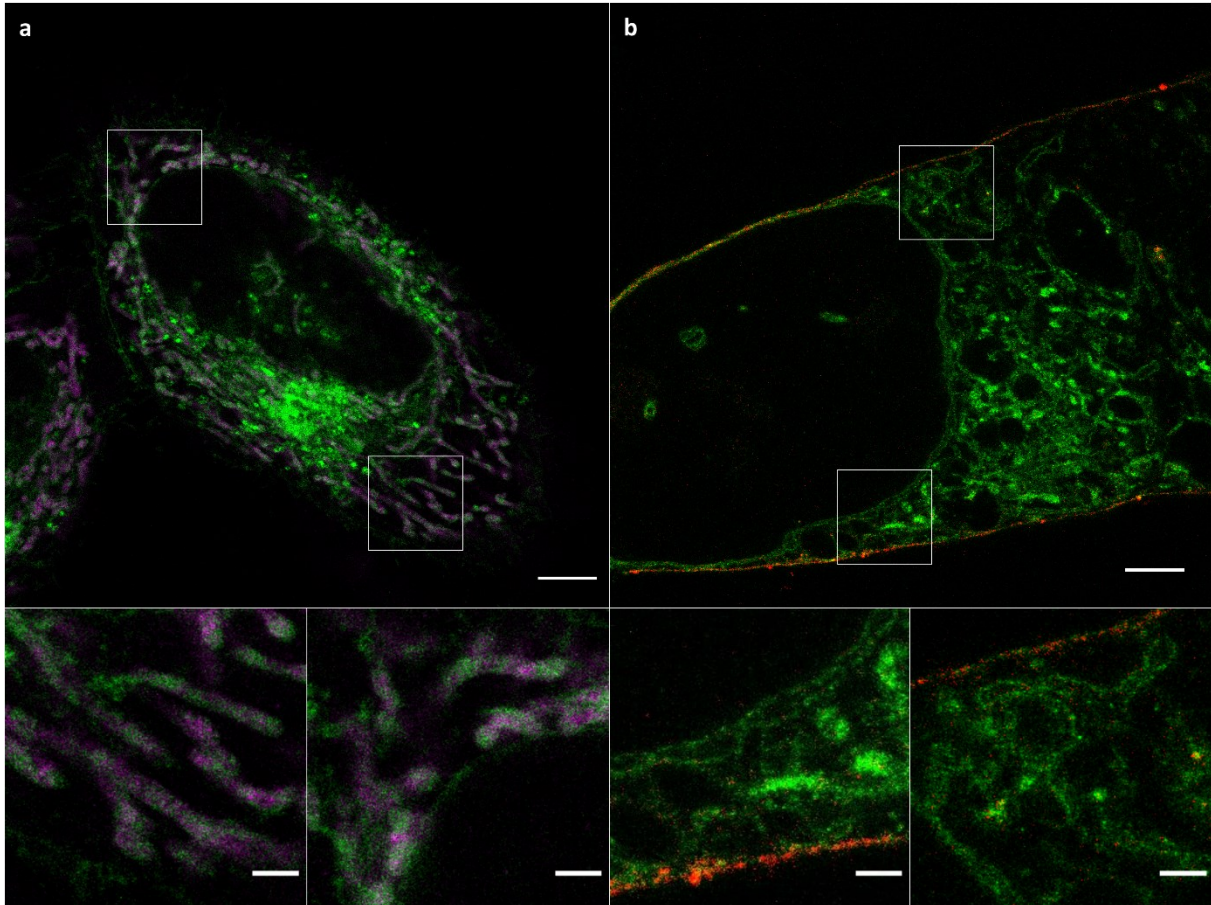
Figure 32: Sphingolipid ExM enables super-resolution imaging of cellular membranes and protein interactions.

(a) Confocal fluorescence image of 4x expanded HeLa229 cells. Cells were fed with α-NH$_2$-ω-N$_3$-C$_6$-ceramide, fixed, permeabilized, and labeled with DBCO-Alexa Fluor 488 (green). In addition, Prx3 (magenta), which is located in the mitochondrial matrix was stained by immunolabeling using ATTO 647N labeled secondary antibodies. (b) Confocal fluorescence image of a 10x expanded HeLa229 cell fed with ATTO643-mCling (red) and α-NH$_2$-ω-N$_3$-C$_6$-ceramide clicked with DBCO-Alexa Fluor 488 (green). Scale bars, 20 μm. The images at the bottom show magnified views of the regions outlined by the white boxes in the main images. Scale bars, 5 μm (Gotz and Kunz et al., 2020a).
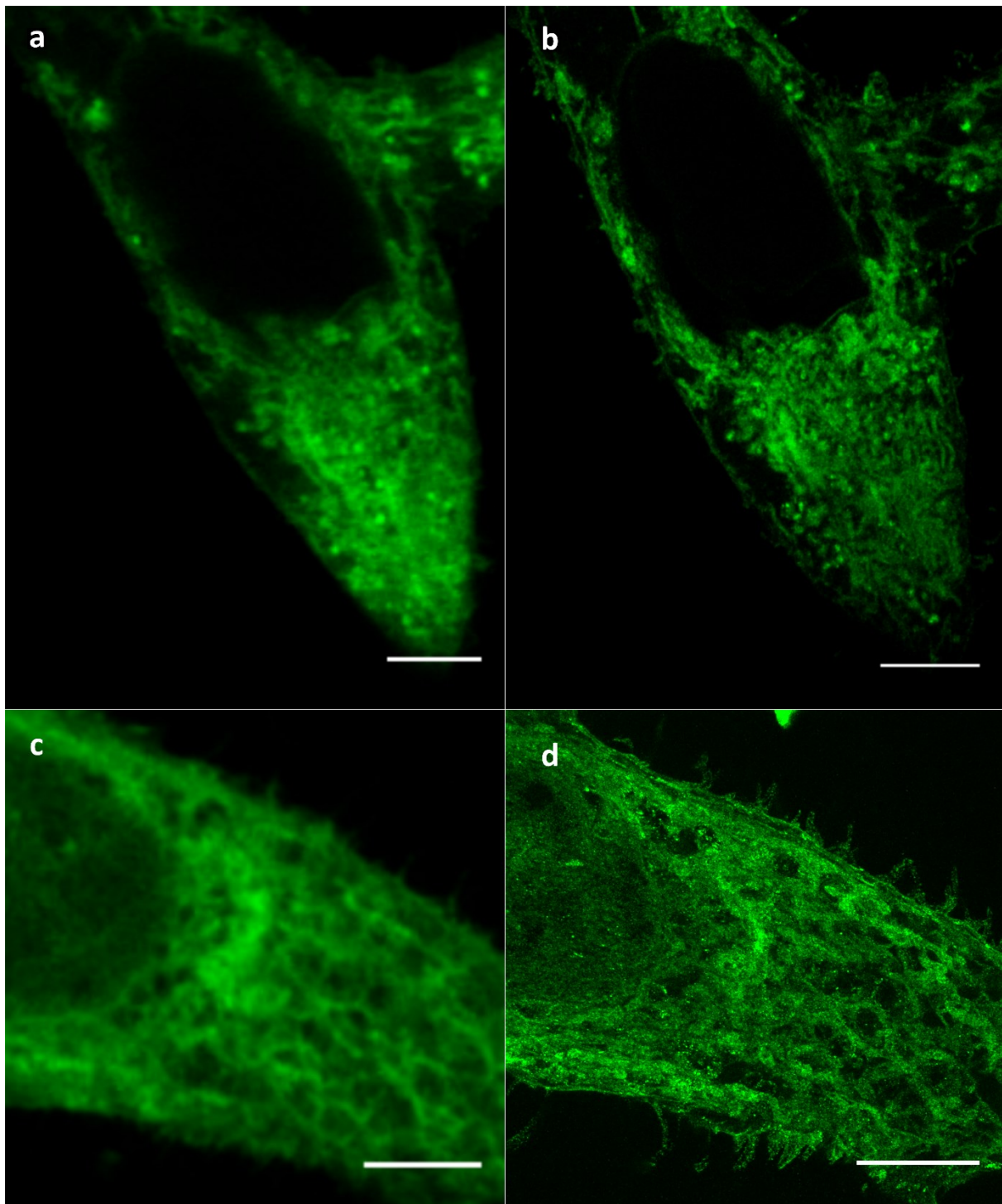
Figure 33: Pre- and postexpansion images demonstrate isotropic expansion and improvement in resolution.

Confocal fluorescence images of the same HeLa229 cells pre- (a,c) and post-4x (b) and 10x (d) expansion. Cells were fed with α-NH$_2$-ω-N$_3$-C$_6$-ceramide, fixed, permeabilized, stained with DBCO-Alexa Fluor 488 and expanded. The images demonstrate isotropic expansion. The effective expansion factors were determined to 4.1x and 9.8x, respectively, from the cell's diameters before and after expansion. Scale bars, unexpanded 5 µm (a,c), 4x expanded 20 µm (b) and 10x expanded 50 µm (d) (Gotz and Kunz et al., 2020a).

α-NH₂-ω-N₃-C₆-ceramide in *Chlamydia*

Besides regulating a plethora of crucial cellular processes, ceramide has been shown to play an essential role during the infection with various bacteria (Kunz and Kozjak-Pavlovic, 2019), among others *N. gonorrhoeae* (Faulstich et al., 2015), *S. negevensis* (Herweg et al., 2016) and *C. trachomatis* (Hackstadt et al., 1996). *Chlamydia* was revealed to not only manipulate sphingolipid metabolism but also to directly take up ceramide by hijacking the host ceramide transporter CERT, a transporter mediating Golgi-ER-trafficking, through the bacterial inclusion protein IncD (Banhart et al., 2019; Derre et al., 2011; Hanada, 2010). To study ceramide uptake and distribution by *C. trachomatis* in more detail, we fed HeLa229 cells for 5-60 minutes 32 hours post infection with 10 µM α-NH₂-ω-N₃-C₆-ceramide. Afterwards, the cells were fixed and click-labeled with DBCO-Alexa 488. The images demonstrate a rapid integration of ceramide into the membrane of *C. trachomatis* already after 5 minutes, which further increased with longer incubation times (**Figure 34**). Furthermore, 24 hours post infection we applied HPA-12, a CERT inhibitor, for 8 hours to impede integration of ceramide into the membrane of *Chlamydia*. HPA-12 inhibits ceramide uptake efficiently at higher concentrations for short
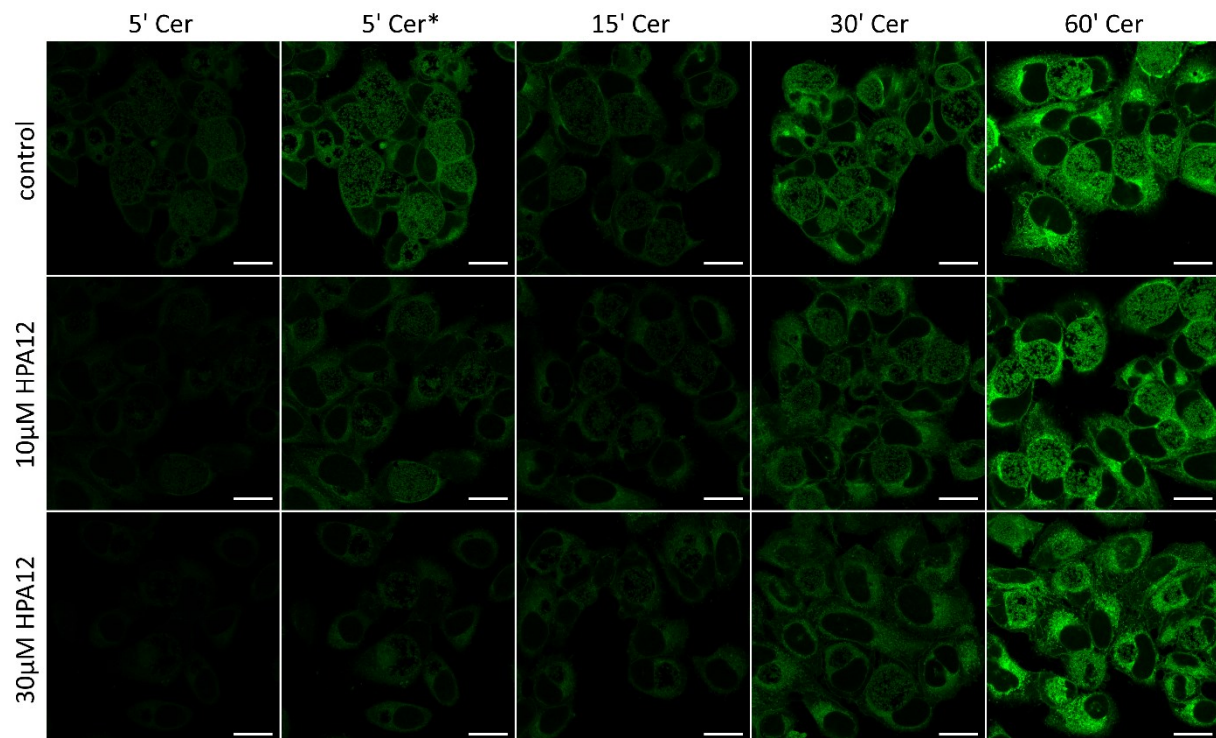
Figure 34: HPA-12 inhibits the uptake of α-NH₂-ω-N₃-C₆-ceramide.

HeLa229 cells were infected with *Chlamydia trachomatis* and treated with HPA-12 for 8 hours at 24 hours post infection, fed with 10 µM α-NH₂-ω-N₃-C₆-ceramide for 5-60 minutes, fixed, permeabilized and stained with DBCO-Alexa Fluor 488 (green). The uptake of ceramides is reduced during the first 5-15 minutes, while little to no difference is observed at longer incubation times. 5' Cer* has enhanced contrast for better comparison. Scale bars, 20 µm (Gotz and Kunz et al., 2020a).

ceramide incubations of 5 to 15 minutes, while it did not exhibit obvious effects for longer ceramide incubation (**Figure 34**). This suggests the involvement of different uptake pathways, such as vesicle trafficking and fusion from the Golgi apparatus.

The loss of lipopolysaccharide (LPS) has drastic effects on the viability of many bacteria and was also shown to inhibit the development of chlamydial infectious elementary bodies (Nguyen et al., 2011). Therefore, we tested if incorporation of α-NH$_2$-ω-N$_3$-C$_6$-ceramide changes the levels of chlamydial LPS in the outer bacterial membrane. In HeLa229 cells infected with *C. trachomatis* for 24 hours and fed with α-NH$_2$-ω-N$_3$-C$_6$-ceramide for 1 hour before fixation, we could not observe any changes in LPS levels. (**Figure 35**). Previously, it has been established that sphingolipids can exert toxic effects on bacteria in vitro (Becam et al., 2017; Fischer et al., 2012) and in vivo (Solger et al., 2020). When feeding HeLa229 cells with α-NH$_2$-ω-N$_3$-C$_6$-ceramide 1 hour before infection, continuously during infection or 1 hour before fixation we could neither observe an impact on chlamydial development (**Figure 36a**) nor on the infectivity of chlamydial progeny (**Figure 36b,c**). Interestingly, *Chlamydia* took up α-NH$_2$-ω-N$_3$-C$_6$-ceramide even when the cells were fed before infection, indicating a direct uptake of ceramides from the host. However, feeding α-NH$_2$-ω-N$_3$-C$_6$-ceramide directly before fixation resulted in the highest incorporation efficiency (**Figure 36a**).
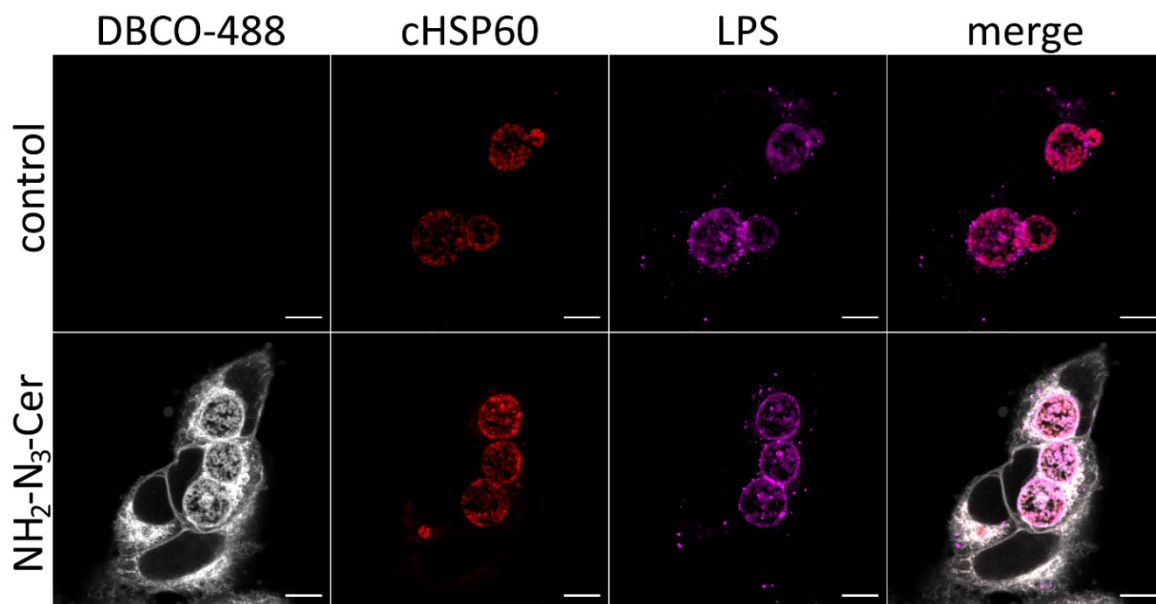
Figure 35: Incorporation of α-NH$_2$-ω-N$_3$-C$_6$-ceramide does not alter levels of chlamydial LPS.

HeLa229 cells were infected with *Chlamydia trachomatis* for 24 hours, fed with α-NH$_2$-ω-N$_3$-C$_6$-ceramide, fixed, permeabilized and stained with DBCO-Alexa Fluor 488 (gray), cHSP60 (red) and chlamydial LPS (magenta). Scale bars, 10 μm (Gotz and Kunz et al., 2020a).
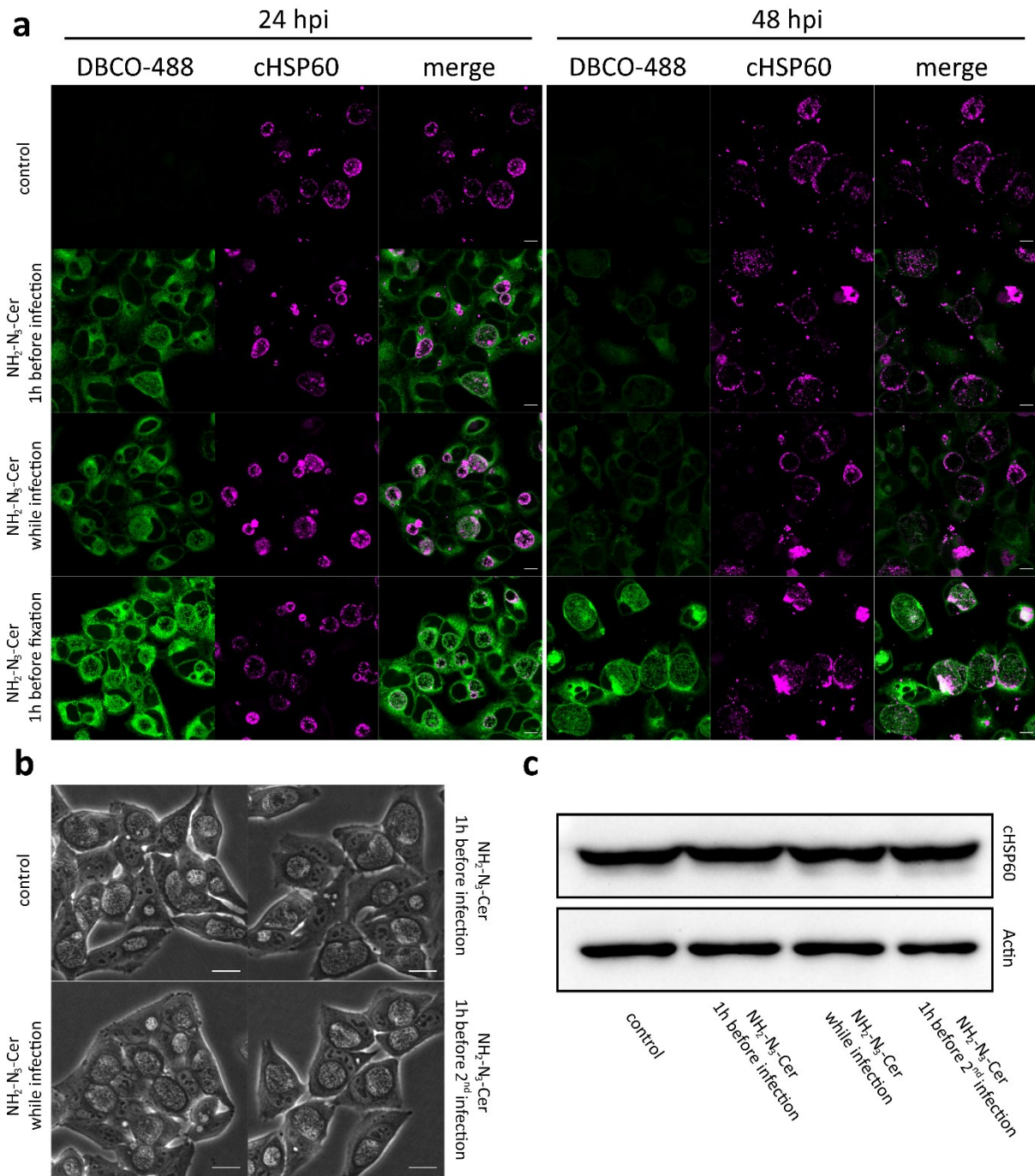
Figure 36: α-NH₂-ω-N₃-C₆-ceramide has no impact on chlamydial growth and progeny.

(a) HeLa229 cells infected with *Chlamydia trachomatis* for 24 hours and 48 hours were fed with α-NH₂-ω-N₃-C₆-ceramide before infection, continuously during infection or before fixation, permeabilized and stained with DBCO-Alexa 488 (green) and cHSP60 (magenta). The treatment did not alter the size of chlamydial inclusions. Scale bars, 10 μm. (b,c) Secondary infection of HeLa229 cells with the chlamydial progeny of HeLa229 cells infected for 48 hours, fed before primary infection, continuously during primary infection and before secondary infection. Analysis by light microscopy (b), scale bars 20 μm, and Western Blot (c) (Gotz and Kunz et al., 2020a).

Expansion of α-NH$_2$-ω-N$_3$-C$_6$-ceramide in *Chlamydia* and *Simkania*

Since we proved that α-NH$_2$-ω-N$_3$-C$_6$-ceramide can be linked to the hydrogel, is taken up by *C. trachomatis* and does not affect chlamydial growth or viability, we performed 4x (**Figure 38b,e**) and 10x (**Figure 38c,f**) expansion of HeLa229 cells infected with *S. negevensis* (**Figure 38a-c** and **Figure 40**), a member of the order of Chlamydiales, or *C. trachomatis* (**Figure 38d-h**) to investigate ceramide localization within the inclusion and individual bacterial particles. Expansion revealed that the ceramide signal accumulates strongly in the membrane of both pathogens. In comparison, the fluorescence signal of host cell membranes appeared relatively dim under identical experimental settings. Interestingly, while, as previously demonstrated (**Figure 24** and **Figure 25**), 4x expansion already enables the visualization of individual chlamydial particles and to distinguish between the two distinct developmental forms of *C. trachomatis*, 10x expansion is required to do so for *S. negevensis* due to even more densely packed inclusions (**Figure 38a-c**). In a control experiment we fed HeLa229 cells infected with *C. trachomatis* with ω-N$_3$-C$_6$-ceramide or α-NH$_2$-ω-N$_3$-C$_6$-ceramide and click-labeled with DBCO-Alexa Fluor 488. As dye control and ω-N$_3$-C$_6$-ceramide showed only weak background staining, we reveal once more that the introduction of the primary amino group in α-NH$_2$-ω-N$_3$-C$_6$-ceramide indeed enables the linkage into the hydrogel and that we do not display unspecific staining of bacterial membranes (**Figure 37**).
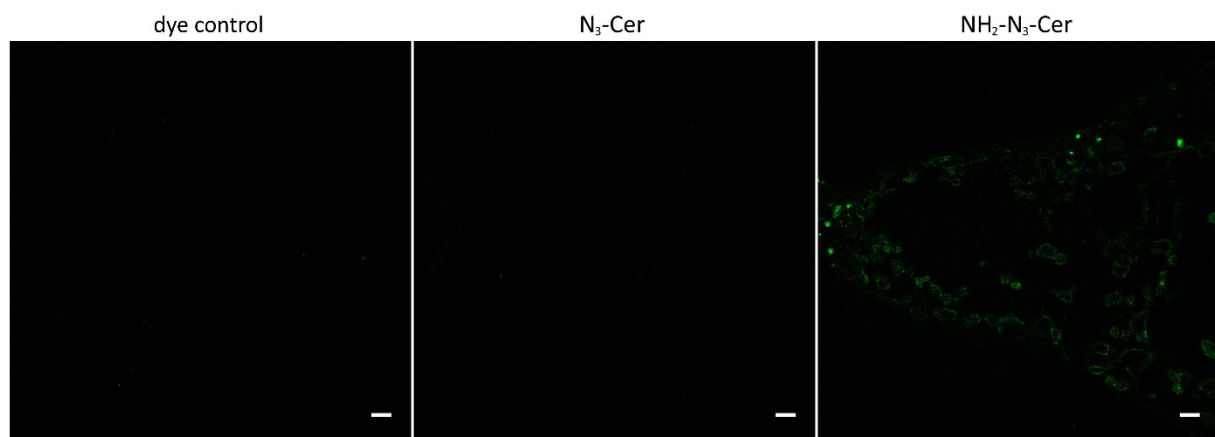
Figure 37: Introduction of primary amino groups enables expansion of functionalized lipids.

Confocal fluorescence images of 10 expanded HeLa229 cells infected with *Chlamydia trachomatis* for 24 hours, without ceramide feeding (dye control), fed with ω-N$_3$-C$_6$-ceramide or α-NH$_2$-ω-N$_3$-C$_6$-ceramide, fixed, permeabilized and stained with DBCO-Alexa Fluor 488. Scale bars, 10 μm (Gotz and Kunz et al., 2020a).
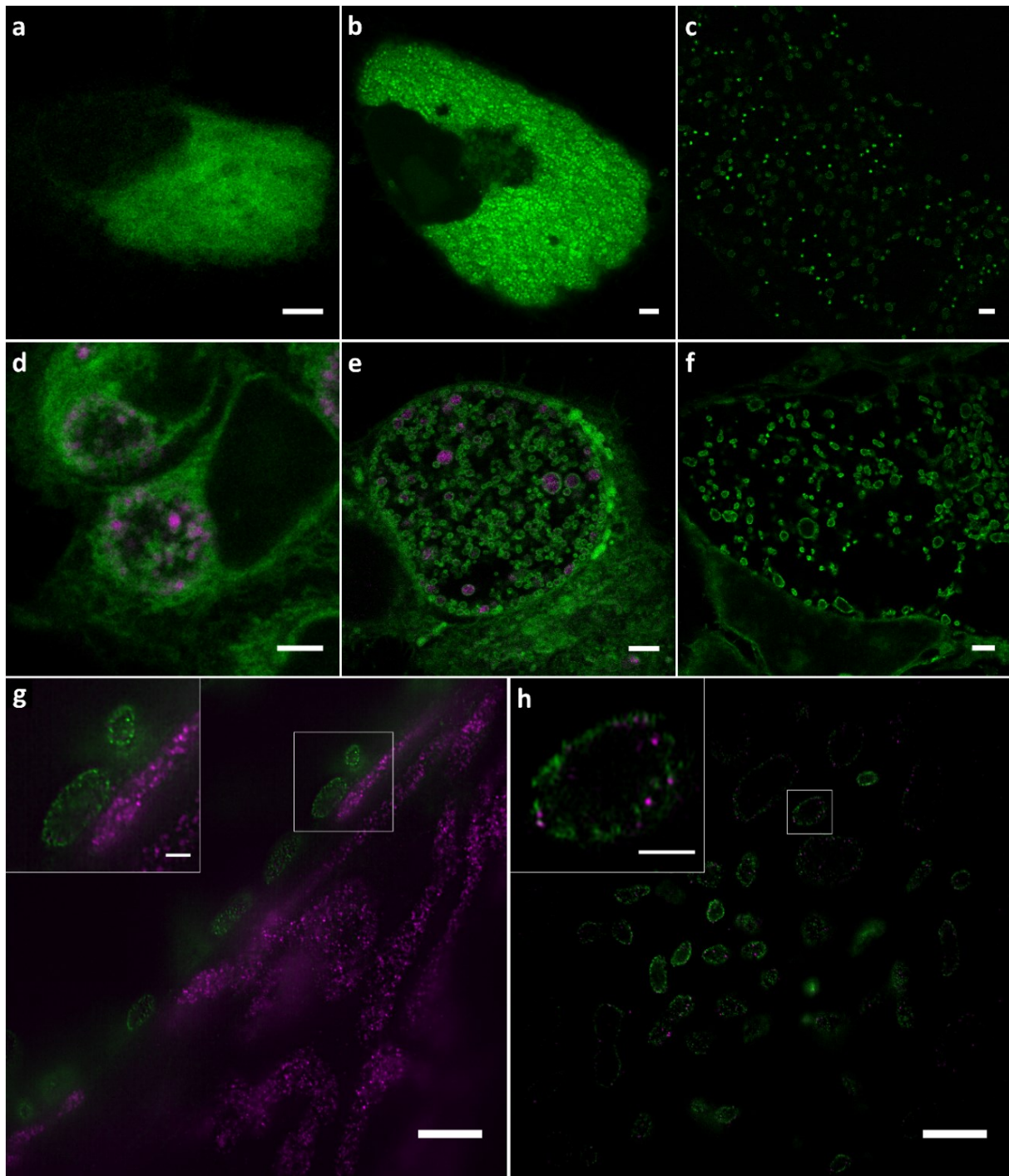
Figure 38: Sphingolipid ExM visualizes intracellular pathogens and their interactions with mitochondrial proteins.

(a-c) HeLa229 cells were infected with *Simkania negevensis* for 96 hours or (d-h) with *Chlamydia trachomatis* for 24 hours, fed with α-NH$_2$-ω-N$_3$-C$_6$-ceramide, fixed, permeabilized and stained with DBCO-Alexa Fluor 488 (green) and (d,e) cHSP60 (magenta) or (g,h) Prx3 (magenta). The images show different cells before expansion (a,d), after 4x expansion (b,e), and 10x expansion (c, f-h) recorded by confocal microscopy (a-g) or SIM (h). The images reveal close contact of *C. trachomatis* and mitochondria (g) and uncover that some Prx3 molecules are inserted into the bacterial membrane. Scale bars, 5 μm (unexpanded images a,d), 10 μm (4x and 10x expanded images b-c,e-h), and 2 μm (magnified views in images g,h) (Gotz and Kunz et al., 2020a).

To further demonstrate the applicability of sphingolipid expansion microscopy for investigating the interaction of bacteria and host organelles, we investigated *Chlamydia* and mitochondria. It has been shown that *Chlamydia* reorganize the host organelles and are highly dependent on host mitochondria (Chowdhury et al., 2017; Chowdhury and Rudel, 2017). In HeLa229 cells, infected with *C. trachomatis*, fed with α-NH$_2$-ω-N$_3$-C$_6$-ceramide and immunolabeled for Prx3 as a mitochondrial matrix marker, we observed the mitochondrial rearrangement around the chlamydial inclusion (**Figure 38g**). Furthermore, we observed Prx3 signals within individual bacteria, indicating unspecific protein uptake (**Figure 38h**). Similar control experiments in the absence of primary antibodies did not show unspecific binding of the same secondary antibody, ATTO647N (**Figure 39**).
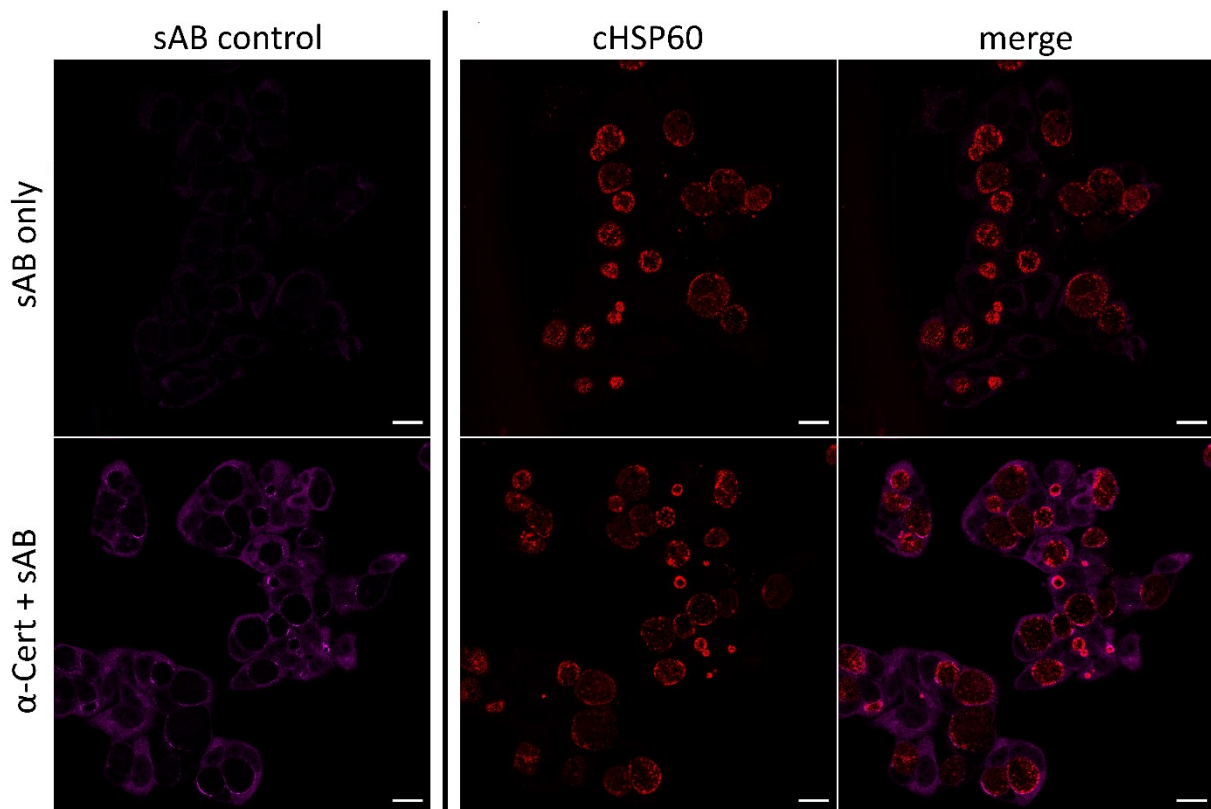
Figure 39: ATTO647N coupled antibodies do not unspecifically bind chlamydial particles.

Confocal images of unexpanded HeLa229 cells infected with *Chlamydia trachomatis* for 24 hours, fed with α-NH$_2$-ω-N$_3$-C$_6$-ceramide, fixed, permeabilized and immunolabeled for α-Cert with ATTO 647N (magenta) and chlamydial HSP60 with Cy3 (red). Upon labeling with secondary antibody but without primary antibody, no signal was detectable in chlamydial particles (sAB only/sAB control). Scale bars, 20 µm (Gotz and Kunz et al., 2020a).
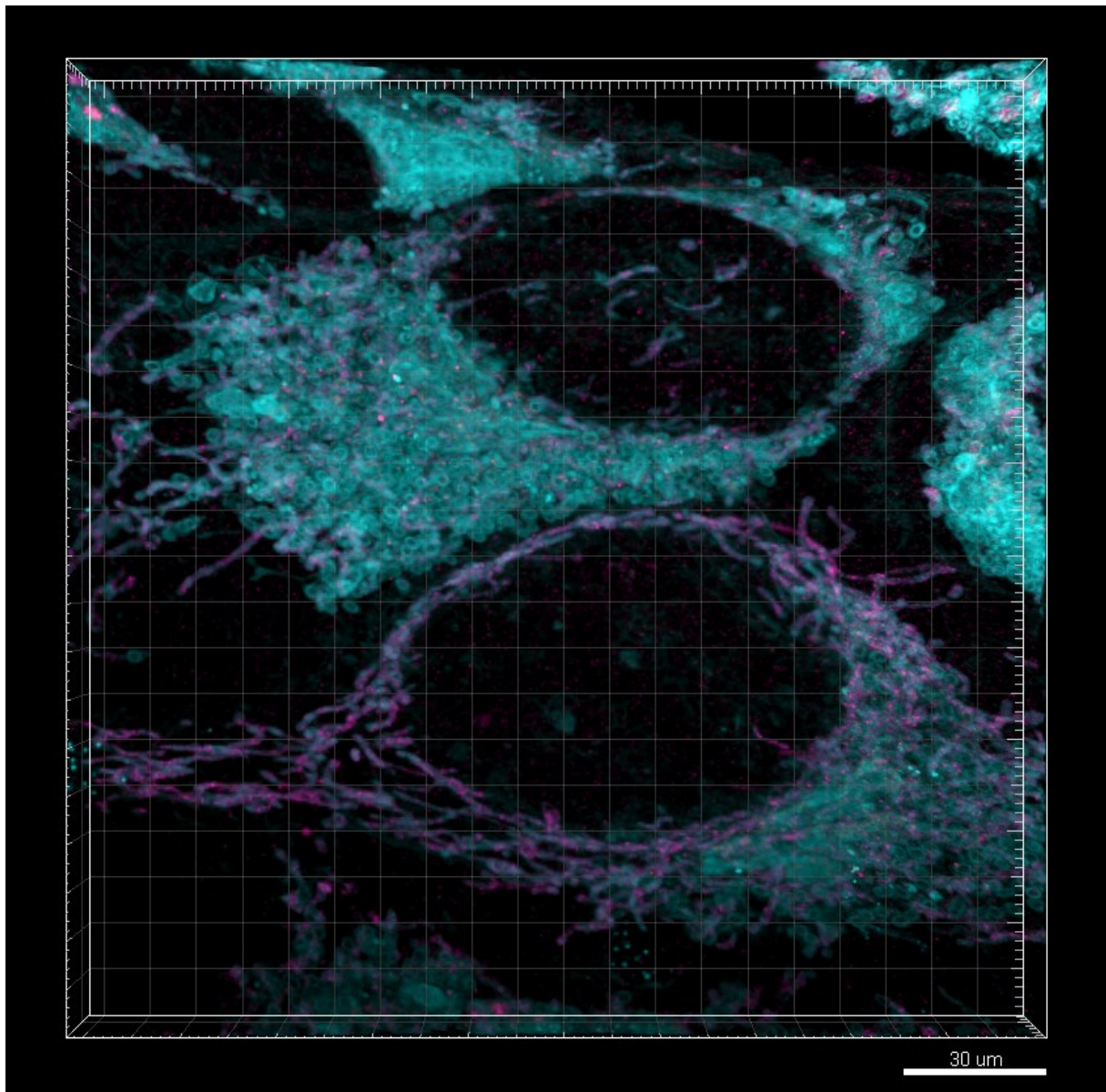
Figure 40: *Simkania negevensis* **closely interacts with host cell mitochondria.**

Confocal z-stack of HeLa229 cells infected with *Simkania negevensis* for 48 hours, fed with α-NH$_2$-ω-N$_3$-C$_6$-ceramide, fixed, permeabilized and stained with DBCO-Alexa Fluor 488 (cyan) and Prx3 (magenta). 3D-View was created using Imaris 8.4.1.

To ensure isotropic expansion, we imaged the same inclusions before and after 10x expansion and showed that the shape and number of bacteria is not altered after expansion. Additionally, post-expansion images demonstrate the strong accumulation of ceramide in bacterial membranes (**Figure 41**).
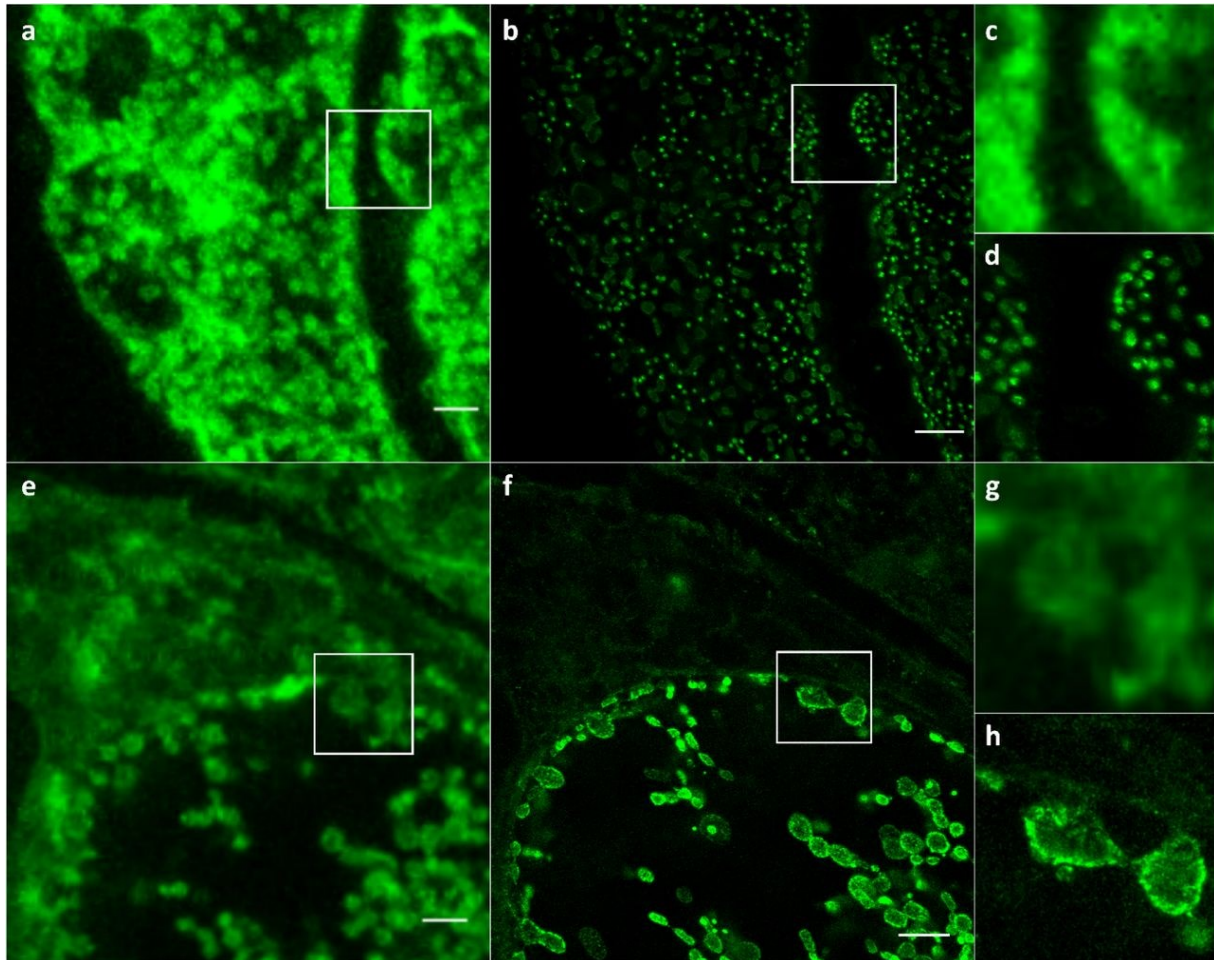
Figure 41: Pre- and postexpansion images of *Simkania negevensis* and *Chlamydia trachomatis* demonstrate isotropic expansion and distinguishability of individual bacterial particles.

Confocal fluorescence images of the same areas of HeLa229 cells infected with *Simkania negevensis* (a-d) or *Chlamydia trachomatis* (e-h), before (a,c,e,g) and after (b,d,f,h) 10x expansion. The infected cells were fed with α-NH$_2$-ω-N$_3$-C$_6$-ceramide, fixed, permeabilized, stained with DBCO-Alexa 488 and expanded. (c,d) and (g,h) show magnified views of the regions outlined by the white boxes in the main images. Scale bars, unexpanded images 2 µm and 10x expanded images 20 µm (Gotz and Kunz et al., 2020a).

10x Sphingolipid SIM-ExM to resolve chlamydial double membrane

It is well-known that ceramide is transported to the chlamydial inclusion (Hackstadt et al., 1996). However, one unanswered question remaining was whether ceramide is incorporated to the bacterial outer (BOM) or inner membrane (BIM) or to both membranes. While 10x confocal expansion partially revealed double-membrane-like structures (**Figure 42a**), the doubling of spatial resolution in combination with SIM pushed the resolution further to around 10-12 nm enabling the clear visualization of the incorporation of ceramide in both BOM and BIM (**Figure 42b** and **Figure 44k**). By measuring 23 cross sectional intensity profiles of chlamydial double-membranes we determined the distance of the two membranes to 27.6 ± 7.7 nm (s.d.) (**Figure 43** and **Figure 44)**.
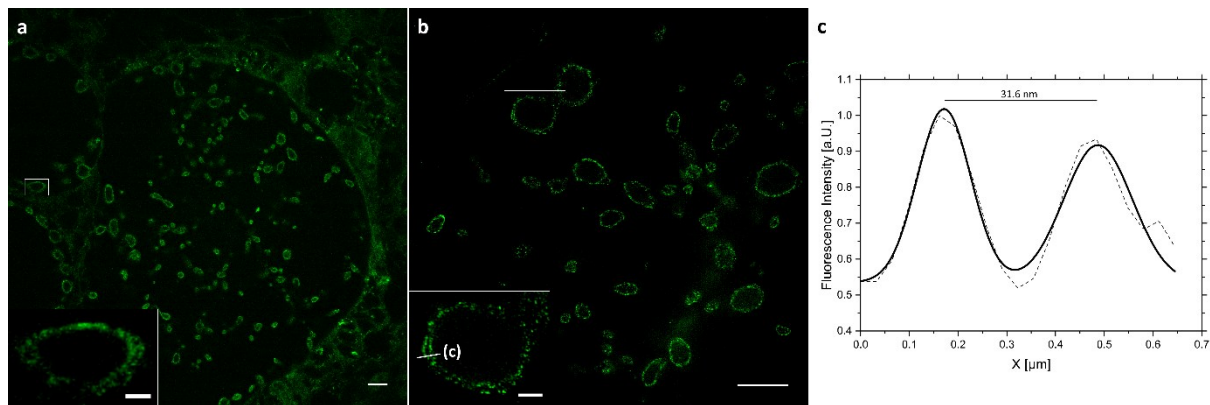
Figure 43: 10x SIM-ExM enables visualization of ceramide in the inner and outer chlamydial membrane.

HeLa229 cells infected with *Chlamydia trachomatis* for 24 hours, fed with α-NH$_2$-ω-N$_3$-C$_6$-ceramide, fixed, permeabilized and click-labeled with DBCO-Alexa Fluor 488 (green). Confocal (a) and SIM images (b) disclose that ceramides are incorporated into the BOM and BIM. (c) Example of a fitting intensity cross sectional profile of the chlamydial double membrane. Scale bars 10 µm (a,b), 2 µm (white boxes) (Gotz and Kunz et al., 2020a).
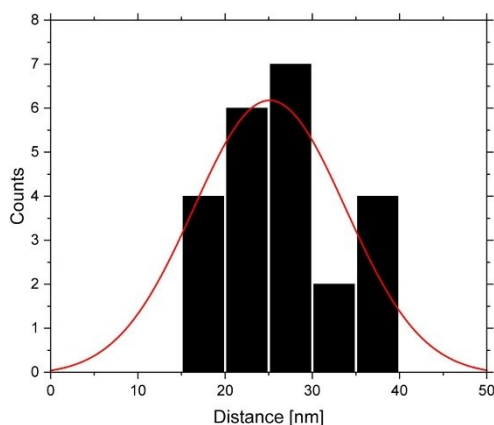
Figure 42: Histogram and fit of 23 distances determined from cross sectional intensity profiles of ceramide in chlamydial particles.

HeLa229 cells were infected with *Chlamydia trachomatis*, fed with α-NH$_2$-ω-N$_3$-C$_6$-Ceramide, fixed, permeabilized, labeled with DBCO-Alexa 488, 10x expanded and imaged with SIM to visualize double membranes of chlamydial particles. In total 23 cross sectional intensity profiles were measured from 3 biological replicates. Only those bacteria were selected whose orientation allowed us to visualize spatially separated BOM and BIM (i.e. frontal views of bacteria) and determine the distance between the two membranes to 27.6 ± 7.7 nm (s.d.) (Gotz and Kunz et al., 2020a).
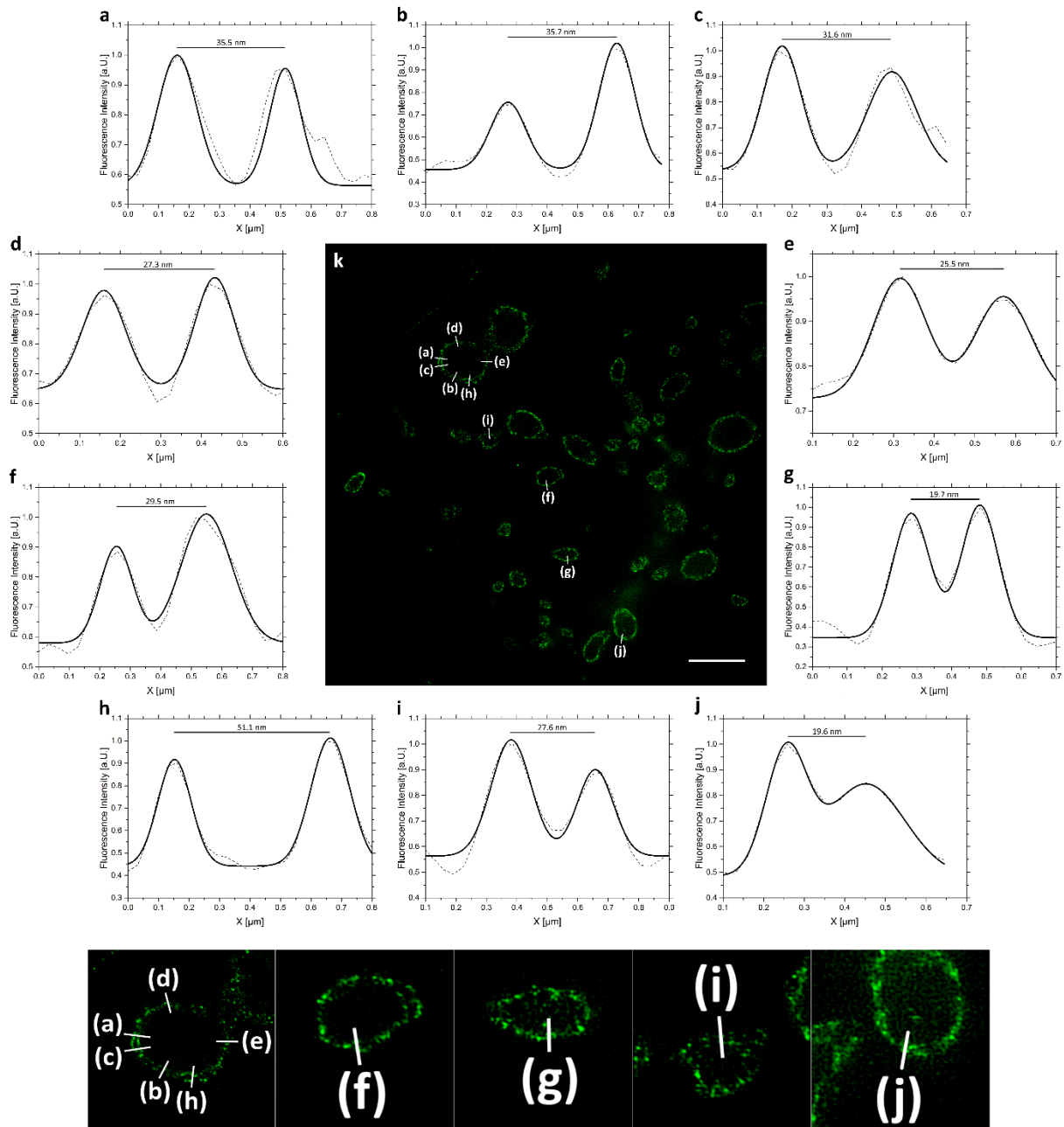
Figure 44: Examples of cross-sectional intensity profiles of ceramide in chlamydial particles.

Cross sectional intensity profiles (**a-j**) of the chlamydial double membrane in 10x expanded HeLa229 cells, infected for 24 hours with *Chlamydia trachomatis,* fed with α-NH₂-ω-N₃-C₆-Ceramide (green) and imaged with SIM to visualize double membranes of chlamydial particles. The distance between the BOM and BIM varies between 19.7 nm and 51.1 nm. (k) SIM image of one of three 10x expanded samples used for data analysis shown in Figure 43 (Gotz and Kunz et al., 2020a).

Discussion and Outlook

In comparison to other superresolution microscopy methods, expansion microscopy does not require high-cost setups or intensive training. Additionally, expansion microscopy is perfectly suited for multi-color imaging, does not suffer in reduced axial resolution and does not require long image acquisition, which are typical problems in superresolution microscopy. On the other hand, expansion microscopy requires high label density. High expansion factors of ten- or even twentyfold will dilute the signal 1000 or 8000-fold, which may ultimately lead to insufficient signal to noise ratio. Furthermore, many dyes are not suitable for expansion microscopy and suffer severely during gelation and digestion of the sample, e.g. cyanine dyes (Wassie et al., 2019). In the study of Tillberg et al., it was tested to which degree individual fluorophoric proteins are suited for expansion microscopy (Tillberg et al., 2016). The study demonstrates that, while mTomato, mRuby, and EGFP are well suited for expansion, that mCherry and ECFP are more impacted by the treatment. Within this work, we identified Alexa Fluor 488, CF568, Atto643 and Atto647N to be the most reliable dyes. When performing expansion microscopy, it is important to consider possible artifacts deriving from anisotropic expansion or insufficient digestion. In this regard, it was recently shown that the digestion of more complex specimen, such as fungi or bacterial pathogens, must be adjusted for complete digestion and hence isotropic expansion (Gotz et al., 2020b; Lim et al., 2019). It is also important to note, that expansion microscopy is only possible for fixed samples and is therefore not suitable for live cell imaging.

Expansion microscopy to visualize mitochondrial cristae

The first part of the thesis demonstrates the successful application of expansion microscopy for the visualization of mitochondrial cristae, their morphology and the localization of mitochondrial proteins relative to cristae (Kunz et al., 2020).

As a cristae marker, we overexpressed the mitochondrial creatine kinase labeled with GFP (herein referred to MtCK-GFP) (Schlattner et al., 2006). Contrary to other established cristae markers, such as COX8A (Stephan et al., 2019) or ATP5I (Kondadi et al., 2020), we believe that the overexpression of MtCK-GFP does not interfere with the naïve ATP production cycle, which has been demonstrated in several studies to be linked to the morphology of mitochondrial

cristae. In this case, especially the F_O subunit (intermembrane unit) of the F_1F_O ATP synthase was shown to determine cristae morphology by bending the inner boundary membrane (Blum et al., 2019; Davies et al., 2011; Hahn et al., 2016; Strauss et al., 2008; Wittig et al., 2007). Furthermore, the F_1F_O ATP synthase is interacting with OPA1 (Quintana-Cabrera et al., 2018) and the MICOS-complex (Eydt et al., 2017; Rabl et al., 2009; Rampelt et al., 2017), which were both confirmed in several studies to be involved in cristae formation and morphology. Interestingly, when overexpressing the $F_1\beta$-subunit linked to a fluorophore, e.g. GFP or mCherry, we could observe that higher protein amounts led to disrupted cristae or even apoptotic cells and therefore did not enable visualization of native cristae (data not shown). Hence, we assume that expressing a marker like MtCK-GFP, which is not interfering with the mitochondrial ATP production and is further not linked to the cristae membrane, is an ideal way for cristae imaging. Nevertheless, one should keep in mind that the overexpression of proteins within cristae itself, even without the direct interference, might have an impact on the mitochondrial viability and cristae morphology. Upon MtCK-GFP overexpression, we could not observe any effects on cell viability or mitochondrial length and distribution (**Figure 13**). Nevertheless, a Seahorse XF Mito Stress Test, providing key parameters of mitochondrial function as basal respiration or maximal respiration, could be performed as a further and more detailed control.

Besides the importance of choosing the right cristae marker, the visualization of individual cristae is further complicated by the fact that the distance between two individual cristae has been determined by electron microscopy to be often below 100 nm (Jakobs and Wurm, 2014). As the resolution limit of conventional confocal microscopy is limited by the diffraction limit of light defined by Abbe and the numerical aperture of the objective to around 240 nm (Abbe, 1873), the visualization of individual mitochondrial cristae requires superresolution microscopy. Unfortunately, regular structured illumination microscopy (SIM) is also limited in resolution to around 100-120 nm. Fourfold expansion increases the resolution on a confocal microscope to 60 nm and in combination with SIM to 30 nm without the need of high-cost equipment. However, first promising results of cristae imaging on light microscopes were only performed by applying high-cost SMLM (Shim et al., 2012) or STED (Schmidt et al., 2009). The cristae intensity of fixed cristae remained relatively poor due to the quality of the antibodies against the F_1F_O ATP synthase (Schmidt et al., 2009) or the quality of fixed MitoTracker Red

(Shim et al., 2012). Recent publications, on the other hand, display great improvements in live-cell imaging using STED, STORM and Airyscan microscopy in combination with fluorescent live-cell dyes, such as Mitotracker (Shim et al., 2012; Wolf et al., 2019) and MitoPB Yellow (Wang et al., 2019). These are both cationic dyes accumulating on the IMM due to the negative mitochondrial membrane potential. MitoPB Yellow labeling remains unaffected by membrane potential reduction, which on the other hand corresponds with the labeling intensity of Mitotracker. The latter can therefore be used advantageously to measure membrane potential of individual cristae in combination with a second cristae marker, e.g. 0-*N*-nonyl acridine orange (NAO), a dye preferentially binding cardiolipin, as shown by Wolf et al. (Wolf and Hackstadt, 2001). These live cell dyes as well as the overexpression of proteins of the OXPHOS complex as cristae markers (Stephan et al., 2019) were successfully used to analyze the mitochondrial ultrastructure and to observe cristae dynamics. Even though such dyes enable live cell observation of cristae dynamics in real time with high signal intensity, they also exhibit very fast damaging of mitochondrial vitality and therefore may not visualize cristae in native shape. Furthermore, such approaches are not suitable for localization studies of mitochondrial proteins by immunolabeling. Due to the lack of primary amino groups, these dyes are also not suitable for expansion microscopy.

Given this background, we expanded cells overexpressing our cristae marker MtCK-GFP (**Figure 13**). While the fourfold expansion enabled the visualization of individual cristae already on a confocal setup, the combination of fourfold expansion and SIM provided more insight into the internal mitochondrial structure, approaching super-resolution methods like dSTORM (**Supplementary Figure 14**). Within our study, we further demonstrated that Mitofilin/Mic60, the central unit of the MICOS-complex localized at the CJs and essential for cristae formation (Hessenberger et al., 2017; John et al., 2005), and TFAM, a mitochondrial transcription factor located in the matrix and crucial for the expression of mitochondrial proteins (Campbell et al., 2012), are in close proximity to cristae. When comparing TFAM to PRX3, a mitochondrial thioredoxin-dependent hydroperoxidase which is also exclusively found in the mitochondrial matrix (Donsante, 2017), we could observe clear differences in protein localization (**Figure 14** and **Figure 15**). While PRX3, as expected for a freely soluble protein in the mitochondrial matrix, shows an alternating signal to cristae, TFAM co-localizes with cristae to a large extent. Thus, the improved resolution obtained by expansion microscopy enables

distinguishability of the localization of different proteins within the same mitochondrial compartment, herein the mitochondrial matrix. 3-color imaging of expanded samples in combination with SIM revealed the colocalization of TFAM and Mitofilin/Mic60 (**Figure 17** and **Figure 18**). Interestingly, Li et al. previously observed that the depletion of Mic60/Mitofilin changes maintenance and morphology of mtDNA nucleoids (Li et al., 2016). Moreover, in 2015, it was reported of the possible interaction of Mitofilin/Mic60 and TFAM (Yang et al., 2015). In our study, we supported the theory of a possible functional connection of TFAM and/or other mtDNA-associated proteins with the MICOS complex that may enable sensing and responding of the mitochondrial nucleoid to mitochondrial morphological changes (Kunz et al., 2020). For this, our cristae marker MtCK-GFP in combination with expansion microscopy might be a great tool for further investigations of possible interactions between the MICOS complex and the mitochondrial nucleoid or between proteins and other complexes associated with mitochondrial cristae, e.g. OXPHOS-complexes or ATP-synthase (Kondadi et al., 2019). Interestingly, MICOS was also proposed to be a central core complex of a larger ER-mitochondria interaction network (ERMIONE) (van der Laan et al., 2012). Moreover, we reported about a new subunit of the mammalian MICOS/MIB complex, the armadillo repeat-containing protein 1 (ARMC1), which is located in the cytosol and at the OMM, where it interacts with the MICOS complex. We observed that Armc1 is important for mitochondrial motility, indicating a possible interaction with the cytoskeleton (Wagner et al., 2019). Expansion microscopy could be used to investigate such connections of the MICOS complex outside mitochondria as well as its effects, e.g. on cristae structure.

Besides localizing mitochondrial proteins relative to cristae, our tool enables the visualization of cristae defects upon treatment with CCCP, a strong uncoupling agent that can abruptly depolarize the membrane potential leading to the swelling of mitochondria (**Figure 19a**) (Park et al., 1997). The partial loss of cristae integrity could be observed with increasing length of incubation, which has previously been shown by electron microscopy (Ding et al., 2012). Furthermore, we transfected HeLa229 cells with an inducible knockdown of Sam50 by doxycycline (Dox)-mediated shRNA expression (*sam50kd-2*). As mentioned before, this complex has been confirmed in previous studies to be of importance for cristae morphology by bending the inner membrane for cristae formation and the interaction with the F_1F_O-ATP synthase. When inducing the Sam50 knockdown, we could observe a complete loss of cristae

membranes (**Figure 19b**). Accordingly, it was previously illustrated by transmission electron microscopy that the loss of Sam50 leads to an enlargement of mitochondria and loss of cristae structure (Ott et al., 2015). While our tool is perfectly suitable to visualize major changes or the loss of cristae structure, more delicate changes might be more difficult to observe due to the resolution limit of around 60 nm on confocal and 30 nm on SIM after fourfold expansion. Unfortunately, the labeling density of the overexpressed MtCK-GFP might be the limiting factor for higher expansion factors, as expansion factors of ten or even twenty will dilute the signal 1000 or 8000-fold. To possibly overcome this problem, MtCK could be linked to different tags rather than fluorophoric proteins as GFP, e.g. SNAP or HALO-tags, which can be used for signal amplification.

Expansion of intracellular pathogens

So far, infections by various pathogens have mainly been studied by diffraction-limited conventional microscopy. Superresolution microscopy, such as dSTORM (Heilemann et al., 2008), PALM (Betzig et al., 2006) or STED (Hell, 2007), require, as previously mentioned, high-cost setups and intense training and thus are limited to specialized laboratories. Additionally, infection laboratories are already highly specialized in infection processes to provide sufficient safety standards and are required to perform a broad range of methods of molecular biology and microbiology. Thus, expansion microscopy offers an alternative by providing superresolution on conventional microscopes that are more accessible for most infection laboratories and do not require additional training.

In a study in 2019, we showed for the first time the applicability of expansion microscopy on intracellular bacteria, more specifically *C. trachomatis* (Kunz et al., 2019). Shortly after, Lim et al. established that many bacteria, such as *Salmonella*, require additional treatment with lysozyme, a 1,4-β-N-acetylmuramidase cleaving the glycosidic bond between N-acetyl muramic acid (MurNAc) and N-acetyl glucosamine in peptidoglycan of bacteria, in order to sufficiently digest the bacterial cell wall and hence enable isotropic expansion (Lim et al., 2019). Interestingly, while all members of the genus *Chlamydia* have a nearly complete pathway for the synthesis of peptidoglycan (Hesse et al., 2003; McCoy et al., 2006; McCoy and Maurelli, 2005; McCoy et al., 2003; Patin et al., 2009; Patin et al., 2012) and exhibit susceptibility to antibiotics targeting peptidoglycan (Moulder et al., 1963; Tamura and Manire,

1968), the existence of peptidoglycan in chlamydial cell envelopes has long been debated as all attempts to purify or detect peptidoglycan were unsuccessful. The lack of peptidoglycan in chlamydial species, also shown for *S. negevensis* (Pilhofer et al., 2013), is hence referred to as chlamydial anomaly. However, in 2014 Liechti et al. demonstrated that peptidoglycan is synthesized and present in the septum of dividing reticulate bodies, which could be removed by lysozyme treatment (Liechti et al., 2014). Nevertheless, within our study we revealed that the expansion of *C. trachomatis* does not require lysozyme, possibly due to the lack or low expression of peptidoglycan (**Figure 20b**). Moreover, as expected, lysozyme treatment is not required for the expansion of *S. negevensis* (**Figure 20d**). In agreement with this, the expansion of *N. gonorrhoeae*, which exhibits thicker peptidoglycan layers (Dougherty, 1985), necessitates treatment with additional lysozyme (**Figure 20f**). The even more complex cell wall of the gram-positive *S. aureus*, possesses a particularly high cross-link ratio between peptidoglycan chains, predominantly consisting of a pentaglycine motif (**Figure 45**) (Monteiro et al., 2019). In this work we reveal that the expansion of *S. aureus* requires, besides lysozyme and proteinase K, the digestion with lysostaphin, an endopeptidase secreted by *S. simulans* to specifically cleave the pentaglycine residues in the cell wall of *S. aureus* (**Figure 20h**) (Francius et al., 2008). In comparison to *N. gonorrhoeae*, the digestion of *S. aureus* for isotropic expansion further requires higher amounts of lysozyme. Theoretically, both bacteria are highly exposed to lysozyme within their niches and hence less susceptible to its lytic activity since N-acetylmuramic residues in their peptidoglycan layers are O-acetylated by secreted enzymes, lowering the binding affinity to lysozyme (Brott and Clarke, 2019; Laux et al., 2019; Ragland and Criss, 2017; Schielke et al., 2010). However, it was previously shown that peptidoglycan of both species can still be degraded by lysozyme, even though the efficiency is reduced (Reinicke et al., 1983). The higher amounts of lysozyme needed for proper digestion of the staphylococcal cell wall can possibly be explained by the higher O-acetylation ratio of MurNAc (around 60%) compared to the neisserial cell wall (34-52%) (Ghuysen and Strominger, 1963; Swim et al., 1983). Additionally, it was demonstrated that the ratio of O-acetylation of the cell wall of *S. aureus* increases within the stationary phase (Dupont and Clarke, 1991). Higher O-acetylation might cause difficulties with the digestion of the staphylococcal cell wall, which may be overcome by higher concentration of lysozyme, longer incubation or by treatment with mutanolysin, an 1,4-β-N-acetylmuramidase from *Streptomyces globisporus* that, like lysozyme, is cleaving the glycosidic bond between N-acetyl muramic acid (MurNAc) and
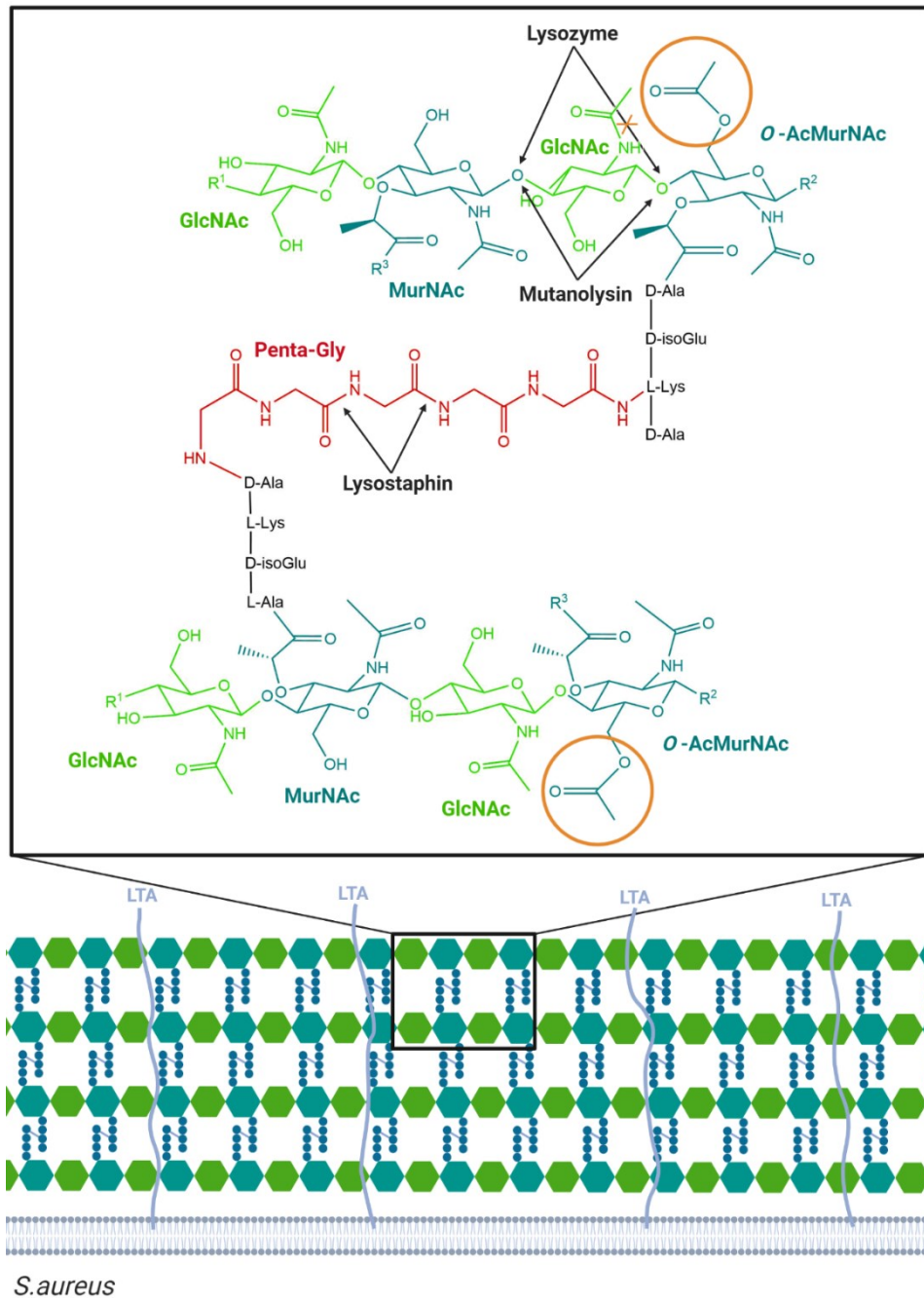
Figure 45: Schematic illustration of the cell wall of *Staphylococcus aureus* and the cutting sides for digestion enzymes

The cell wall of *Staphylococcus aureus* has thick layers of peptidoglycan, which consists of polysaccharide chains that are highly cross-linked, predominantly by pentaglycine motifs. These motifs can be degraded with lysostaphin, an endopeptidase secreted by *Staphylococcus simulans* to specifically cleave pentaglycine residues in the cell wall of *S. aureus*. Due to the niche within the human nares as a commensal, *S. aureus* is confronted with the bacteriolytic lysozyme, a 1,4-β-N-acetylmuramidase cleaving the glycosidic bond between N-acetyl muramic acid (MurNAc) and N-acetyl glucosamine in peptidoglycan of bacteria. Thus, *S. aureus* secretes enzymes to O-acylate peptidoglycan to lower the affinity of lysozyme. While it was previously shown that staphylococcal peptidoglycan can still be degraded by lysozyme, even though with reduced efficiency, treatment with mutanolysin might improve cell wall digestion. Mutanolysin is an 1,4-β-N-acetylmuramidase from *Streptomyces globisporus* that, like lysozyme, is cleaving the glycosidic bond between N-acetyl muramic acid (MurNAc) and N-acetyl glucosamine in peptidoglycan of bacteria but is not inhibited by O-acetylation.

N-acetyl glucosamine in peptidoglycan of bacteria, but is not inhibited by O-acetylation and could hence improve cell wall digestion (Yuan et al., 2012). Within our study, we demonstrate the improved resolution of samples infected with *S. aureus* from 240 nm on conventional confocal microscopy and 120 nm on structured illumination microscopy (SIM) to 60 nm on confocal and 30 nm on SIM after expansion (**Figure 26**). Furthermore, *S. aureus* was controversially described to either avoid or induce autophagy (Geng et al., 2020; Lopez de Armentia et al., 2017; Mestre and Colombo, 2012; Mestre et al., 2010; Prajsnar et al., 2020) and to reside and replicate in large numbers within lysosomes (Flannagan et al., 2016). Here, we demonstrate that expansion microscopy enables the visualization and further investigation of bacteria within Lamp1 (**Figure 27a**) and LC3-II (**Figure 27b**) vesicles of HeLa229 cells 1.5 hours post infection. In addition, we confirm that expansion microscopy can be used to investigate the localization of proteins at the membrane or cytosol of *S. aureus* by co-immunolabelling the staphylococcal protein lipoteichoic acid with cytosolic GFP (**Figure 27c**) 1.5 hours post infection. Until now, several studies used SIM-imaging to display membrane changes or disruptions. For example, in 2019, Thalsø-Madsen et al. demonstrated that sle1, a cell wall amidase, is important for the β-lactam resistance of MRSA by showing characteristic morphological abnormalities upon treating sle1 mutant strains with the antibiotic oxacillin (Thalso-Madsen et al., 2019). For many antibiotics, a limiting factor is the poor penetration of bacterial membranes. While SIM imaging is sufficient to observe major changes within the staphylococcal membrane, expansion microscopy could further enhance resolution and enable visualization of minor membrane changes. Therefore, expansion microscopy could be a valuable tool for the development of antibiotics, which is especially interesting since there is a strong emergence of antibiotic-resistant staphylococcal strains (Chambers and Deleo, 2009).

In our study from 2019, we could demonstrate the applicability of expansion microscopy with *C. trachomatis* without the need of further digestion adjustments (Kunz et al., 2019). Within this study, we aimed to investigate the localization of the serine protease CPAF, that is claimed by several reports to cleave or degrade host proteins during infection to control cellular and chlamydial interactions (Rajeeve et al., 2018; Tang et al., 2015; Yang et al., 2016). However, the exact localization of CPAF within the inclusion and cytoplasm is currently under debate (Chen et al., 2012; Conrad et al., 2013; Hacker, 2014; Johnson et al., 2015; Snavely et al., 2014;

Zhong, 2014). An interesting observation of our study was the strong association of CPAF with individual chlamydial particles and increasing expression at later stages of infection (**Figure 21**). By treating infected cells with clasto-lactacystin beta-lactone, a CPAF inhibitor (Johnson et al., 2015), we excluded potential artefacts due to remaining CPAF activity during fixation (**Figure 22**). Like many other chlamydial effector proteins, CPAF was shown to be secreted from the inclusion by a type II secretion system (T2SS) into the cytoplasm (Snavely et al., 2014). Indeed, we could observe a strong accumulation of CPAF in RSTE4-strain *C. trachomatis* (T2SS-mutant) (**Figure 21**). Besides CPAF, we demonstrated the improvement in resolution for a second chlamydial effector protein, namely Cdu1, encoded in one of two chlamydial genes of deubiquitinases, ChlaDUB1 (Cdu1) and ChlaDUB2 (Cdu2). The deubiquitinase Cdu1 is located within the chlamydial inclusion membrane, facing the host cell cytoplasm with its active site (Fischer et al., 2017). So far, Cdu1 has been implicated in the stabilization of κBa and inhibition of NFκB-induced inflammatory response of the cell (Le Negrate et al., 2008), the fragmentation of the Golgi apparatus (Pruneda et al., 2018) and the stabilization of the antiapoptotic protein Mcl-1 (Fischer et al., 2017). Expansion microscopy allows the visualization of Cdu1 in much clearer detail within the chlamydial inclusion membrane and may enable the visualization of Cdu1 accumulation at specific parts of the membrane (**Figure 23**). We believe that expansion microscopy could hence permit the observation of the interaction of e.g. Golgi apparatus and Cdu1 on conventional confocal microscopes.

Lastly, when observing *Chlamydia* after fourfold expansion, we found differences in sizes of chlamydial particles and hypothesized that we could possibly differentiate between the smaller elementary bodies (EBs) and larger and metabolically active reticulate bodies (RBs). For this, we infected HeLa229 cells with a recently introduced *Chlamydia* strain *Ct* mCh(GroL2) GFP(OmcAl2) expressing mCherry under the control of constitutive *groESL* operon (expressed within RBs) and GFP fused to the *omc* promotor (expressed within EBs) (Cortina et al., 2019). Indeed, we could observe that all smaller chlamydial particles expressed GFP, while the larger particles expressed mCherry (**Figure 24** and **Figure 25**). Therefore, our study revealed that expansion microscopy enables the detection of individual chlamydial particles and can further be used to distinguish between different chlamydial developmental stages due to their known size, which was so far only shown by electron microscopy. In 2018, using 3D electron microscopy, Lee et al. analysed chlamydial inclusions and hypothesized that the size of

chlamydial RBs controls timing of RB-to-EB conversion independently of external signals (Lee et al., 2018). For this, several sections of the samples were imaged individually in order to give a complete picture of the ratio of the different chlamydial stages. However, while achieving impressive results, the average acquisition time of one section was around 3 minutes and a cell monolayer required around 500 sections, resulting in an acquisition time of around 25 hours for only one region of interest. While electron microscopy certainly has better resolution than fourfold expansion microscopy, we can nevertheless also distinguish different chlamydial particles due to the known size on conventional confocal microscopy and reduce imaging time of a whole mature inclusion to around 20-30 minutes. Hence, our approach enables quantification studies in much higher throughput. Moreover, expansion microscopy is simpler, cheaper and requires way shorter preparation time and could be used to determine the developmental stage of inclusions and developmental changes under different conditions, e.g. nutrient depletion, inhibition of important chlamydial effector proteins or antibiotic treatment. Lastly, we believe that bacterial expansion microscopy is a great tool to investigate the interaction between different pathogens at high resolution. An interesting model would be the coinfection with *C. trachomatis* and *N. gonorrhoeae*, which ,while poorly understood, was shown to often occur in patients (Guy et al., 2015). Furthermore, as the occurrence of these coinfections are assumed to be far too high to be random, it is believed that there is an active interplay between both pathogens (Althaus et al., 2014).

Sphingolipid expansion microscopy

Sphingolipids are of broad interest in various aspects of cellular and infection biology. However, sphingolipid imaging is extremely difficult as the performance of antibodies against most lipids remains relatively inadequate, resulting in insufficient signal-to-noise ratio and making antibodies therefore not suitable for superresolution microscopy. To overcome this problem, many studies make use of azido-functionalized lipids to perform click-chemistry for labeling, resulting in much stronger signals (Solger et al., 2020; Walter et al., 2017). However, one must consider that feeding in excess does not represent natural conditions. Potentially, one could overcome or reduce side effects through excess feeding by repeatedly feeding lower concentrations of the modified analogue to progressively replace cellular lipids.

Due to the lack of primary amino groups, most lipids cannot be fixed by formaldehyde, glutaraldehyde or other chemical fixatives. Furthermore, the primary amino group is crucial in order to link the molecule of interest into the hydrogel through the reaction with glutaraldehyde (GA), MA-NHS (Chozinski et al., 2016) or AcX (Tillberg et al., 2016) or Label-X (Chen et al., 2016). The latter, Label-X, has been developed in order to link RNA to the gel, which was labeled by fluorescent *in situ* hybridization (ExFISH) after expansion. So far, expansion has been limited to only proteins and RNA. Recently, we established that ω-N$_3$-sphingosine is incorporated into the membrane of intracellular *N. gonorrhoeae*, possibly for bacterial killing by the host cell (**Figure 28**) (Solger et al., 2020). As sphingosine itself carries a primary amino group, we hypothesized that ω-N$_3$-sphingosine is the ideal candidate to test whether a single primary amino group of a lipid enables expansion of functionalized lipids. Indeed, we could confirm our hypothesis by visualizing incorporated ω-N$_3$-sphingosine in *N. gonorrhoeae* after fourfold expansion (**Figure 29**). However, in order to form ceramide, the primary amino group of sphingosine gets N-acetylated, which therefore disables linkage to the hydrogel. Furthermore, the N-acetylation can be done by fatty acids of various chain length (Grosch et al., 2012). In the study of Walter et al. in 2017, it was demonstrated that long-chain ω-N$_3$-C$_{16}$-ceramide is incorporated into cellular membranes but cannot be efficiently click-labeled with DBCO-functionalized dyes, which was explained by the hindered accessibility of the ω-N$_3$-group after membrane incorporation (Walter et al., 2017). In contrast, the unnatural short-chain ω-N$_3$-C$_6$-ceramide could be efficiently incorporated into cellular membranes and click-labeled by DBCO-functionalized dyes (Collenburg et al., 2016; Walter et al., 2016; Walter et al., 2017). Albeit short-chain ceramides are unnatural, we therefore reasoned the evenly distributed short-chain ω-N$_3$-C$_6$-ceramide to be the perfect candidate for testing our theory for fixing and expanding functionalized lipids. We therefore aimed to introduce a primary amino-group into the unnatural short-chain ω-N$_3$-C$_6$-ceramide, synthesizing the α-NH$_2$-ω-N$_3$-C$_6$-ceramide from (tert-butoxycarbonyl)-L-lysine (**Figure 30a** and **Supplementary Figure 1-13**). While short-chain ceramides have previously been described to exhibit apoptotic effects (Banerjee et al., 2012), we could demonstrate by LDH-cytotoxicity-assays that 10 µM of the unmodified C$_6$-ceramide, the control ω-N$_3$-C$_6$-ceramide and our novel α-NH$_2$-ω-N$_3$-C$_6$-ceramide did not exhibit cytotoxic effects after one hour incubation. However, long-term feeding (24 hours) resulted in an increase of cytotoxicity of around 20% for all three analogues (**Figure 31**).

In contrast to control ω-N$_3$-C$_6$-ceramide, we could show that the introduction of a primary amine in α-NH$_2$-ω-N$_3$-C$_6$-ceramide enabled lipid fixation (**Figure 30**), which we further confirmed by lower mobility post fixation in FRAP experiments (**Figure 30b**). Due to the fixability and the ability to link ω-N$_3$-sphingosine in *Neisseria* to the hydrogel (**Figure 29**), we reasoned that we could link and expand α-NH$_2$-ω-N$_3$-C$_6$-ceramide. Conformingly, we demonstrated that the introduction of a primary amine enabled isotropic expansion of α-NH$_2$-ω-N$_3$-C$_6$-ceramide by comparing the structures of the same cell pre- and post-expansion for both 4x and 10x expansion (**Figure 33**) and determined the effective expansion factors to be 4.1 and 9.8. Our images also revealed intense signals of α-NH$_2$-ω-N$_3$-C$_6$-ceramide in organelles, such as Golgi or mitochondria (**Figure 32a**). The membrane-binding fluorophore-cysteine-lysine-palmitoyl group (mCling) is a molecule that is taken up during endocytosis, labels the plasma membrane and also carries a primary amine necessary for expansion (Revelo et al., 2014). We show that it is efficiently incorporated mainly in the plasma membrane of the cell (**Figure 32b**). Our functional ceramide, on the other hand, is much more evenly distributed within cellular membranes. In summary, we show that labeling with the novel sphingolipid analogue is dense enough to support nanoscale resolution of continuous membrane structures. Interestingly, the labeling density was in fact too high for dSTORM imaging, resulting in artifacts due to overlapping point spread functions because of high emitter density (**Supplementary Figure 15**). Recently, Boyden and coworkers introduced an alternative approach for the expansion of membranes (mExM) (Karagiannis et al., 2019). Within this study, they developed a membrane intercalating probe containing a chain of lysines for hydrogel linkage, a glycine for mechanical flexibility, a lipid tail for membrane insertion and a biotin residue for fluorescent labeling of the sample by streptavidin. While this method enables another elegant way of membrane labeling for expansion microscopy, we hypothesize that the introduction of a primary amine also permits the investigation of specific lipids of interest and may be suitable also for so far inaccessible molecule classes including carbohydrates.

Sphingolipid expansion microscopy in *Chlamydia*

Chlamydia was shown to directly take up ceramide by hijacking the host ceramide transporter CERT, a transporter mediating Golgi-ER-trafficking, through the bacterial inclusion protein IncD (Banhart et al., 2019; Derre et al., 2011; Hanada, 2010). Interestingly, we could show that

C. trachomatis efficiently takes up α-NH$_2$-ω-N$_3$-C$_6$-ceramide already after 5 minutes, which further increased over time, suggesting an effective and fast ceramide uptake. When applying the CERT inhibitor HPA-12, we revealed a delayed uptake of α-NH$_2$-ω-N$_3$-C$_6$-ceramide, especially within the first 15 minutes and with higher inhibitor concentrations. For longer incubation times, however, we observed an efficient and comparable uptake of the ceramide analogue even when the cells were treated with HPA-12, suggesting the involvement of different lipid uptake pathways (**Figure 34**). A potential uptake pathway could be the trafficking of vesicles from the Golgi apparatus, possibly through the interaction with IncE, which has been reported to specifically bind to the Sorting Nexin 5 Phox domain (SNX5-PX) and to disrupt retromer trafficking between the endosomes and the Golgi apparatus (Sun et al., 2017). Moreover, we observed that *C. trachomatis* incorporated α-NH$_2$-ω-N$_3$-C$_6$-ceramide even when the cells were fed before infection, confirming the direct uptake of short-chain ceramides from the host (**Figure 36a**). Nevertheless, the mechanisms involved in ceramide distribution to the inclusion and within the inclusion to individual chlamydial particles remain to be investigated. Like other groups reported before (Elwell et al., 2011), we observed that RBs often localize in close vicinity to the inclusion membrane, likely for nutrient uptake (**Supplementary Figure 16** and **Supplementary Movie 8**). In a study of 2008, it was suggested that RBs take up nutrients to grow and eventually "fall-off" the inclusion membrane to the inclusion lumen to redifferentiate into the infectious EBs (Hoare et al., 2008).

Due to the significance of natural long-chain ceramide for *Chlamydia* and as many sphingolipids exhibit bactericidal effects (Kunz and Kozjak-Pavlovic, 2019), we reasoned that the modifications of our α-NH$_2$-ω-N$_3$-C$_6$-ceramide and the strong uptake might lead to impaired chlamydial propagation. Hence, we tested whether our functionalized and unnatural short-chain ceramide analogue exhibits toxic effects on *Chlamydia*. Both formation of inclusions and infectious progeny was unaffected in cells treated with α-NH$_2$-ω-N$_3$-C$_6$-ceramide before infection, continuously during infection or before fixation (**Figure 36**), suggesting that the incorporation of unnatural short-chain ceramides does not have a major impact on chlamydial viability. In agreement with this, Heuer and coworkers showed that artificial NBT-C$_{16}$-ceramide also does not affect chlamydial growth or progeny (Banhart et al., 2014). Furthermore, as the loss of (LPS) has dramatic effects on the viability of gram-negative bacteria and was shown to inhibit the development of chlamydial infectious elementary

bodies (Nguyen et al., 2011), we wondered if treatment with α-NH$_2$-ω-N$_3$-C$_6$-ceramide leads to replacement of chlamydial LPS at the outer membrane but could not observe any changes (**Figure 35**). Feeding α-NH$_2$-ω-N$_3$-C$_6$-ceramides directly before fixation resulted in the highest incorporation efficiency and was therefore chosen as the protocol of choice for expansion experiments.

Fourfold expansion of *C. trachomatis* fed with the unnatural α-NH$_2$-ω-N$_3$-C$_6$-ceramides enabled differentiation of smaller EBs and larger RBs (**Figure 38e**), as shown in our previous study (**Figure 24** and **Figure 25**) (Kunz et al., 2019). Due to the high labeling density we performed tenfold expansion, which further improved the resolution (**Figure 38f**). In fact, when observing individual chlamydial particles after tenfold expansion on confocal microscopy, we could observe structures that appeared to be double membranes. Interestingly, while the transport of ceramide to *Chlamydia* has been reported earlier (Hackstadt et al., 1996), one of the unanswered questions remaining was whether ceramides form parts of the BOM or BIM. Indeed, SIM images after tenfold expansion clearly demonstrated α-NH$_2$-ω-N$_3$-C$_6$-ceramide in both BOM and BIM (**Figure 42**). We measured the distance of the BOM and BIM of *Chlamydia* where the orientation allowed us to visualize spatially separated membranes (i.e. frontal views of bacteria) of three different experiments of in total 23 cross sectional intensity profiles and determined the distance between both membranes to 27.6 ± 7.7 nm (s.d.) (**Figure 43** and **Figure 44**), which is in agreement with electron microscopy data. While we show that the incorporation of α-NH$_2$-ω-N$_3$-C$_6$-ceramide enables the visualization of the chlamydial double membrane, we cannot comment on whether it is purposely incorporated in both membranes or because of unspecific integration. As mentioned before, a limiting factor for many antibiotics is the poor penetration of bacterial membranes. We therefore hypothesize, that, by enabling imaging of the inner and outer bacterial membrane, our new compound in combination with expansion microscopy may be a useful tool for development of antibiotics, especially against multidrug-resistant bacteria (Ghai and Ghai, 2018).

To demonstrate that sphingolipid expansion microscopy can further be advantageously used to visualize the interaction of pathogens with host proteins or organelles, we investigated the chlamydial interactions with mitochondria. *Chlamydia* was shown before to influence mitochondrial dynamics and to reorganize mitochondria around the inclusion most likely due

to a high dependence on mitochondrial nutrients (Chowdhury et al., 2017; Kurihara et al., 2019). However, so far these investigations were performed on confocal microscopy, SIM or electron microscopy. When immunolabeling for the mitochondrial matrix protein PRX3, we observed very tight connections between mitochondria and the inclusion, where juxtaposed RBs were practically attached to the inclusion membrane (**Figure 38g**). Moreover, we found PRX3 signals to be located within individual RBs indicating unspecific protein uptake (**Figure 38h**). In similar experiments, performed in the absence of primary antibodies, we did not observe nonspecific binding of the used secondary antibody, ATTO647N (**Figure 39**). However, it is possible that the primary antibody PRX3 is unspecifically binding chlamydial particles and therefore we do not observe actual PRX3 signal. Thus, it would be interesting to repeat such experiments immunolabeling for different soluble mitochondrial matrix proteins to see if we observe unspecific mitochondrial protein uptake. An explanation might be that, similar to the nanotube formation of *E. coli* (Pal et al., 2019), *Chlamydia* might use its type III secretion system (T3SS) to not only secrete effector proteins but also to soak up nutrients from the host cell, in this case directly from mitochondria. The detection of mitochondrial proteins seems even more convincing as Szaszák et al. already showed in 2011 NAD(P)H at and within the inclusion (Szaszak et al., 2011). Importantly and contrary to the negligible linkage error by clicking DBCO to our functional α-NH$_2$-ω-N$_3$-C$_6$-ceramide, one should keep in mind that due to the size of antibodies, immunolabeling of around 17.5 nm results in a linkage error at tenfold expansion of around 175 nm. To bypass this issue, it is possible to stain the sample after expansion, as already demonstrated in the MAP (Ku et al., 2016) and U-ExM protocol (Gambarotto et al., 2019).

Besides *Chlamydia*, we further investigated the compatibility of α-NH$_2$-ω-N$_3$-C$_6$-ceramides to investigate the infection of *S. negevensis*. Contrary to *Chlamydia*, the clear distinguishability and differentiation of different developmental forms of simkanial particles required not only fourfold but tenfold expansion due to the high density of simkanial particles within the inclusion (**Figure 38 a-c**). We observed that the fluorescence signal in host cell membranes appeared relatively weak compared to the signal in both *Chlamydia* and *Simkania* indicating the strong uptake of α-NH$_2$-ω-N$_3$-C$_6$-ceramide in bacteria (**Figure 38** and **Figure 40-41**). As the simkanial inclusion is tubular and not round shaped like the inclusion of *Chlamydia* (Mehlitz et al., 2014), the interaction with *Simkania* and mitochondria appears even tighter as

mitochondria and simkanial inclusions are basically intertwining (**Figure 40**). Interestingly, it was shown that *Simkania* interact closely within the first three days of infection, but afterwards cause rapid mitochondrial degradation. Moreover, when observing *Simkania* three days post infection, we observed straight lines of simkanial particles (mostly smaller EBs) connecting the simkanial inclusion to the plasma membrane of the host cell (**Supplementary Figure 17**). In the study of Mehlitz et al., they showed a similar phenotype with dSTORM imaging, which they explained by the growth of the SnCV from the peri-nuclear region into the cell periphery (Mehlitz et al., 2014). Since simkanial host cell release typically starts three days post infection (Kahane et al., 2002), we hypothesize that it could also show the possible transport of *Simkania* along the host cell cytoskeleton to the plasma membrane for release. However, very little is known so far about simkanial host cell release. We believe our novel compound may therefore be an ideal tool for its investigation.

Overall, this work successfully demonstrates the broad applicability of expansion microscopy in cellular and infection biology by introducing a marker for the expansion of mitochondrial cristae, expansion of several bacterial pathogens (*C. trachomatis*, *S. negevensis*, *N. gonorrhoeae* and *S. aureus*) and enabling the expansion of lipids by the introduction of a primary amino group to functional lipids, here shown for ω-N$_3$-C$_6$-ceramide. Additionally, expansion of our novel compound, α-NH$_2$-ω-N$_3$-C$_6$-ceramide, enabled for the first time the visualization of both inner and outer chlamydial membrane on a fluorescence microscope.

List of publications

Publications included in this thesis:

Detection of *Chlamydia* Developmental Forms and Secreted Effectors by Expansion Microscopy
Tobias C. Kunz* & Ralph Götz*, Markus Sauer & Thomas Rudel
*Shared first author
Front Cell Infect Microbiol **9**, 276 (2019)

Diverse Facets of Sphingolipid Involvement in Bacterial Infections
Tobias C. Kunz & Vera Kozjak-Pavlovic
Front Cell Dev. Biol. **7**, 203 (2019)

Using Expansion Microscopy to Visualize and Characterize the Morphology of Mitochondrial Cristae
Tobias C. Kunz* & Ralph Götz*, Shiqiang Gao, Markus Sauer & Vera Kozjak-Pavlovic
*Shared first author
Front Cell Dev. Biol. **8**, 617 (2020)

A Role of Sphingosine in the Intracellular Survival of *Neisseria gonorrhoeae*
Franziska Solger, **Tobias C. Kunz**, Julian Fink, Kerstin Paprotka, Pauline Pfister, Franziska Hagen, Fabian Schumacher, Burkhard Kleuser, Jürgen Seibel & Thomas Rudel
Front Cell Infect Microbiol **10**, 215 (2020)

Nanoscale imaging of cellular and bacterial membranes by sphingolipid expansion microscopy
Ralph Götz*, **Tobias C. Kunz***, Julian Fink, Franziska Solger, Jan Schlegel, Jürgen Seibel, Vera Kozjak-Pavlovic, Thomas Rudel & Markus Sauer
*Shared first author
In Print at Nat commun

The Expandables: Cracking the staphylococcal cell wall for expansion microscopy
Tobias C. Kunz* & Marcel Rühling*, Adriana Moldovan, Kerstin Paprotka, Vera Kozjak-Pavlovic, Thomas Rudel & Martin Fraunholz
*Shared first author
In preparation

Further publications:

Armadillo repeat-containing protein 1 is a dual localization protein associated with mitochondrial intermembrane space bridging complex
Fabienne Wagner, **Tobias C. Kunz**, Roy Chowdhury, Bernd Thiede, Martin Fraunholz, Debora Eger, Vera-Kozjak-Pavlovic
PLOS One 14(10) (2019)

***Staphylococcus aureus* α-toxin induces acid sphingomyelinase release from mammalian endothelial cells**
David Krones, Katrin Anne Becker, Marcel Rühling, **Tobias C. Kunz**, Carolin Sehl, Kerstin Paprotka, Erich Gulbins & Martin Fraunholz
In Revision at Front Cell Dev. Biol.

BCAA acquisition by intracellular *S. aureus*: a fundamental role of the BrnQ1 transporter in intracellular replication, survival and persistency
Adriana Moldovan, Clara Hans, Kathrin Stelzner, **Tobias C. Kunz**, Kerstin Paprotka, Thomas Rudel & Martin Fraunholz
In Preparation

Supporting Information

N^2-(*tert*-butoxycarbonyl)-N^6-diazo-L-lysine (2)

To a suspension of NaN$_3$ (380 mg, 5.85 mml, 1.44 eq.) in MeCN (5 mL) was added Tf$_2$O (820 μL, 4.87 mmol, 1.20 eq.) dropwise at 0 °C. The mixture was stirred for 2.5 h at 0 °C and the resulting solution was then transferred to a mixture of (*tert*-butoxycarbonyl)-L-lysine (**1**) (1.00 g, 4.06 mmol, 1.00 eq.), NEt$_3$ (1.13 mL, 8.12 mmol, 2.00 eq.) and CuSO$_4$ (6.48 mg, 40.6 μmol, 0.01 eq.) in MeCN (10 mL) at 0 °C. The ice bath was removed, and the reaction mixture was stirred at rt for 18 h. After the addition of H$_2$O (50 mL) and 1 M aq. HCl (20 mL), the aqueous phase was extracted with EtOAc (4 x 60 mL). The combined organic phases were dried (MgSO$_4$) and concentrated under reduced pressure. The yellow residue was purified by column chromatography on silica gel (CH$_2$Cl$_2$/MeOH 20:1) to give **2** (936 mg, 3.44 mmol, 85 %) as a colourless oil, which partly crystallized.
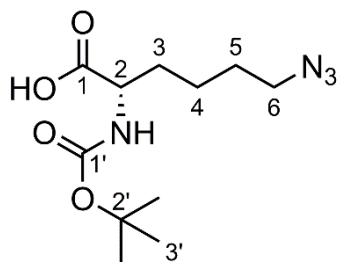
Formula: C$_{11}$H$_{20}$N$_4$O$_4$ (272.31 g/mol).

R_f (CH$_2$Cl$_2$/MeOH 30:1): 0.27.

^{1}H NMR (CDCl$_3$, 400 MHz): δ (2 rotamers) = 1.45 (s, 9H, *H*-3'), 1.46–1.57 (m, 2H, *H*-4), 1.57–1.66 (m, 2H, *H*-5), 1.66–1.80 (m, 1H, *H*-3), 1.80–1.96 (m, 1H, *H*-3), 3.29 (t, $^3J_{6,5}$ = 6.7 Hz, 2H, *H*-6), 4.07–4.40 (m, 1H, *H*-2), 5.06/6.55 (each br d, $^3J_{NH,2}$ = 8.1/5.5 Hz, together 1H, N*H*), 9.93 (br s, 1H, O*H*) ppm.

^{13}C NMR (CDCl$_3$, 100 MHz): δ (2 rotamers) = 22.7 (*C*-4), 28.4 (3C, *C*-3'), 28.5 (*C*-5), 32.0/32.2 (*C*-3), 51.2 (*C*-6), 53.3/54.5 (*C*-2), 80.6/82.1 (*C*-2'), 155.8/157.0 (*C*-1'), 176.8/177.4 (*C*-1) ppm.

HRMS (ESI$^+$): *m/z* calcd. for C$_{11}$H$_{20}$N$_4$NaO$_4$ [M+Na]$^+$: 295.1377; found: 295.1383 (|Δ*m/z*| = 2.0 ppm); *m/z* calcd. for C$_{22}$H$_{40}$N$_8$NaO$_8$ [2M+Na]$^+$: 567.2861; found: 567.2866 (|Δ*m/z*| = 0.8 ppm).

FTIR (ATR): $\tilde{v}$ = 3313, 3186, 3073, 2979, 2936, 2870, 2095, 1712, 1686, 1514, 1479, 1456, 1392, 1368, 1281, 1234, 1189, 1150, 1106, 1051, 1024, 940, 852, 779, 753, 736, 643, 608, 564 cm^{-1}.

The measured spectroscopic data are in agreement with previously reported data.

tert-Butyl ((*S*)-6-azido-1-(((2*S*,3*R*,*E*)-1,3-dihydroxyoctadec-4-en-2-yl)amino)-1-oxohexan-2-yl)carbamate (3)

To a solution of azido-acid **2** (45.5 mg, 167 µmol, 1.00 eq.) in dry DMF (3 mL) were added NEt$_3$ (69.9 µL, 501 µmol, 3.00 eq.) and HATU (69.8 mg, 184 µmol, 1.10 eq.) at 0 °C. After stirring at this temperature for 20 min, sphingosine (50.0 mg, 167 µmol, 1.00 eq.) and dry DMF (3 mL) were added. The ice bath was removed and the reaction mixture was stirred at rt for 3.5 h. After the addition of H$_2$O (10 mL) and saturated aq. NH$_4$Cl solution (30 mL), the aqueous layer was extracted with EtOAc (5 x 20 mL). The combined organic phases were washed with brine (20 mL), dried (MgSO$_4$) and concentrated under reduced pressure. The oily residue was purified by column chromatography on silica gel (CHCl$_3$/MeOH 40:1 to 30:1) to give **3** (44.1 mg, 79.6 µmol, 48 %) as a colourless, waxy solid.
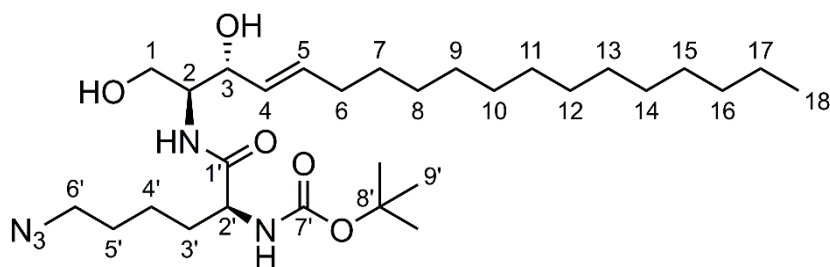
Formula: C$_{29}$H$_{55}$N$_5$O$_5$ (553.79 g/mol).

R$_f$ (CH$_2$Cl$_2$/MeOH 30:1): 0.15.

^{1}H NMR (CDCl$_3$, 400 MHz): δ = 0.88 (t, $^3J_{18,17}$ = 6.9 Hz, 3H, *H*-18), 1.25–1.31 (m, 20H, *H*-8–17), 1.35–1.38 (m, 2H, *H*-7), 1.44 (s, 9H, *H*-9'), 1.48–1.90 (m, 6H, *H*-3'–5'), 2.03–2.08 (m, 2H, *H*-6), 3.29 (t, $^3J_{6',5'}$ = 6.7 Hz, 2H, *H*-6'), 3.71 (dd, $^2J_{1,1}$ = 11.6 Hz, $^3J_{1,2}$ = 3.3 Hz, 1H, *H*-1), 3.83–3.86 (m, 1H, *H*-2), 3.96 (dd, $^2J_{1,1}$ = 11.6 Hz, $^3J_{1,2}$ = 3.3 Hz, 1H, *H*-1), 3.99–4.04 (m, 1H, *H*-2'), 4.36–4.38 (m, 1H, *H*-3), 5.07 (d, $^3J_{NH,2'}$ = 6.9 Hz, 1H, N*H*), 5.51 (ddt, $^3J_{4,4}$ = 15.4 Hz, $^3J_{4,3}$ = 6.0 Hz, $^4J_{4,6}$ = 1.3 Hz, 1H, *H*-4), 5.80 (dtd, $^3J_{5,4}$ = 15.4 Hz, $^3J_{5,6}$ = 6.8 Hz, $^4J_{5,3}$ = 1.4 Hz, 1H, *H*-5), 6.86 (d, $^3J_{NH,2}$ = 8.0 Hz, 1H, N*H*) ppm.

Supporting Information

13C NMR (CDCl$_3$, 100 MHz): δ = 14.3 (*C*-18), 22.8 (*C*-17), 23.0 (*C*-4'), 28.4 (3C, *C*-9'), 28.6 (*C*-5'), 29.3 (*C*-7), 29.4, 29.5, 29.6, 29.8, 29.8, 29.8 (8C, *C*-8–15), 32.0 (2C, C-3' & C-16), 32.5 (*C*-6), 51.3 (*C*-6'), 54.6 (*C*-2), 55.1 (*C*-2'), 61.9 (*C*-1), 74.0 (*C*-3), 80.7 (*C*-8'), 128.6 (*C*-4), 134.2 (*C*-5), 156.2 (*C*-7'), 172.5 (*C*-1') ppm.

HRMS (ESI$^+$): *m/z* calcd. for C$_{29}$H$_{55}$N$_5$NaO$_5$ [M+Na]$^+$: 576.4095; found: 576.4073 (|Δ*m/z*| = 3.8 ppm); *m/z* calcd. for C$_{58}$H$_{110}$N$_{10}$NaO$_{10}$ [2M+Na]$^+$: 1129.8299; found: 1129.8274 (|Δ*m/z*| = 2.2 ppm).

(S)-2-Amino-6-azido-N-((2S,3R,E)-1,3-dihydroxyoctadec-4-en-2-yl)hexanamide / α-NH$_2$-ω-N$_3$-C$_6$-ceramide (4)

To a solution of carbamate **3** (37.0 mg, 6.68 µL) in CH$_2$Cl$_2$ (1 mL) was added TFA (200 µL) at 0 °C. The reaction mixture was stirred at this temperature for 2 h and was then quenched by the addition of H$_2$O (5 mL) and 1 M aq. NaOH (8 mL). After the extraction with EtOAc (5 x 10 mL), the combined organic phases were washed with brine (10 mL), dried (MgSO$_4$) and the solvent was removed under reduced pressure. The residue was purified by column chromatography on silica gel (CHCl$_3$/MeOH/25 % aq. NH$_3$ 9:1:0.1) to give the crude product containing some NH$_3$ salts. To remove these impurities, the residue was dissolved in CH$_2$Cl$_2$ (15 mL) and washed with saturated aq. NaHCO$_3$ solution (10 mL). The aqueous phase was extracted with CH$_2$Cl$_2$ (6 x 5 mL), washed with brine (5 mL) and dried (MgSO$_4$). The solvent was removed under reduced pressure to give **4** (11.9 mg, 26.2 µmol, 39 %) as a colourless solid.
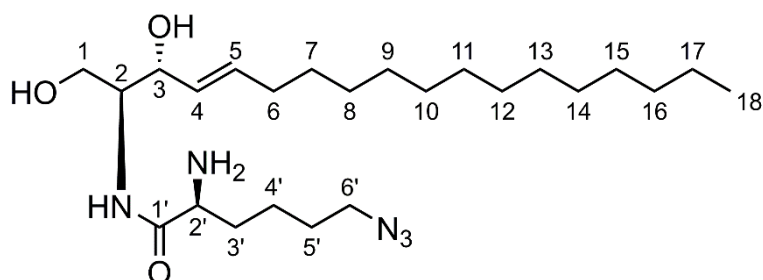
Formula: C$_{24}$H$_{47}$N$_5$O$_3$ (453.67 g/mol).

R$_f$ (CHCl$_3$/MeOH/25 % aq. NH$_3$ 9:1:0.1):0.26.

1H NMR (CDCl$_3$, 600 MHz): δ = 0.87 (t, $^3J_{18,17}$ = 7.1 Hz), 1.25–1.30 (m, 20H, *H*-8–17), 1.33–1.37 (m, 2H, *H*-7), 1.43–1.52 (m, 2H, *H*-4'), 1.53–1.59 (m, 1H, *H*-3'), 1.59–1.67 (m, 2H, *H*-5'), 1.83–

103

1.88 (m, 1H, H-3'), 2.03–2.07 (m, 2H, H-6), 2.21 (br s, 4H, 2 x OH & NH_2), 3.26–3.33 (m, 2H, H-6'), 3.39 (dd, $^3J_{2',3'}$ = 7.9 Hz, $^3J_{2',3'}$ = 4.7 Hz, 1H, H-2'), 3.71 (dd, $^2J_{1,1}$ = 11.4 Hz, $^3J_{1,2}$ = 3.5 Hz, 1H, H-1), 3.83–3.86 (m, 1H, H-2), 3.91 (dd, $^2J_{1,1}$ =11.4 Hz, $^3J_{1,2}$ =4.3 Hz, 1H, H-1), 4.30–4.32 (m, 1H, H-3), 7.82 (d, $^3J_{NH,2}$ = 7.7 Hz, 1H, NH), 5.52 (ddt, $^3J_{4,4}$ = 15.4 Hz, $^3J_{4,3}$ = 6.5 Hz, $^4J_{4,6}$ = 1.4 Hz, 1H, H-4), 5.78 (dtd, $^3J_{5,4}$ = 15.4 Hz, $^3J_{5,6}$ = 6.8 Hz, $^4J_{5,3}$ = 1.2 Hz, 1H, H-5) ppm.

^{13}C NMR (CDCl$_3$, 150 MHz): δ = 14.3 (C-18), 22.8 (C-17), 23.1 (C-4'), 28.8 (C-5'), 29.3 (C-7), 29.4, 29.5, 29.6, 29.8, 29.8, 29.8, 29.8 (8C, C-8–15), 32.1 (C-16), 32.5 (C-6), 34.8 (C-3'), 51.3 (C-6'), 55.0 (C-2), 55.3 (C-2'), 62.7 (C-1), 74.3 (C-3), 128.8 (C-4), 134.5 (C-5), 175.7 (C-1') ppm.

^{15}N NMR (CDCl$_3$, 60 MHz): δ = −352.3 (NH$_2$), −309.4 (C-N-N-N), −265.8 (NH), −132.8 (C-N-N-N) ppm.

HRMS (ESI$^+$): m/z calcd. for C$_{24}$H$_{47}$N$_5$NaO$_3$ [M+Na]$^+$: 476.35711; found: 476.35763 (|$\Delta m/z$| = 1.08 ppm).

FTIR (ATR): $\tilde{v}$ = 3414, 3315, 3271, 3183, 3087, 2677, 2096, 1651, 1614, 1552, 1467, 1455, 1438, 1365, 1348, 1304, 1249, 1165, 1126, 1082, 1044, 1012, 992, 962, 932, 822, 801, 720, 801, 720, 650, 616, 590, 557 cm^{-1}.

NMR Spectra
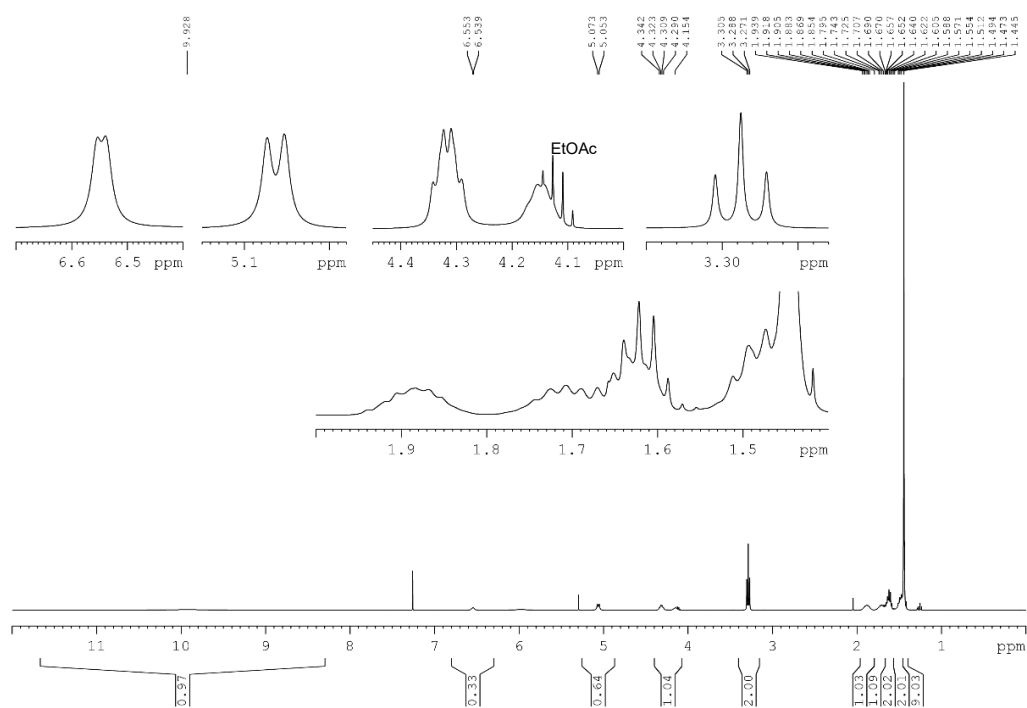
Supplementary Figure 1: ^{1}H NMR spectrum of **2** (CDCl$_3$, 400 MHz) (Gotz and Kunz et al., 2020a).
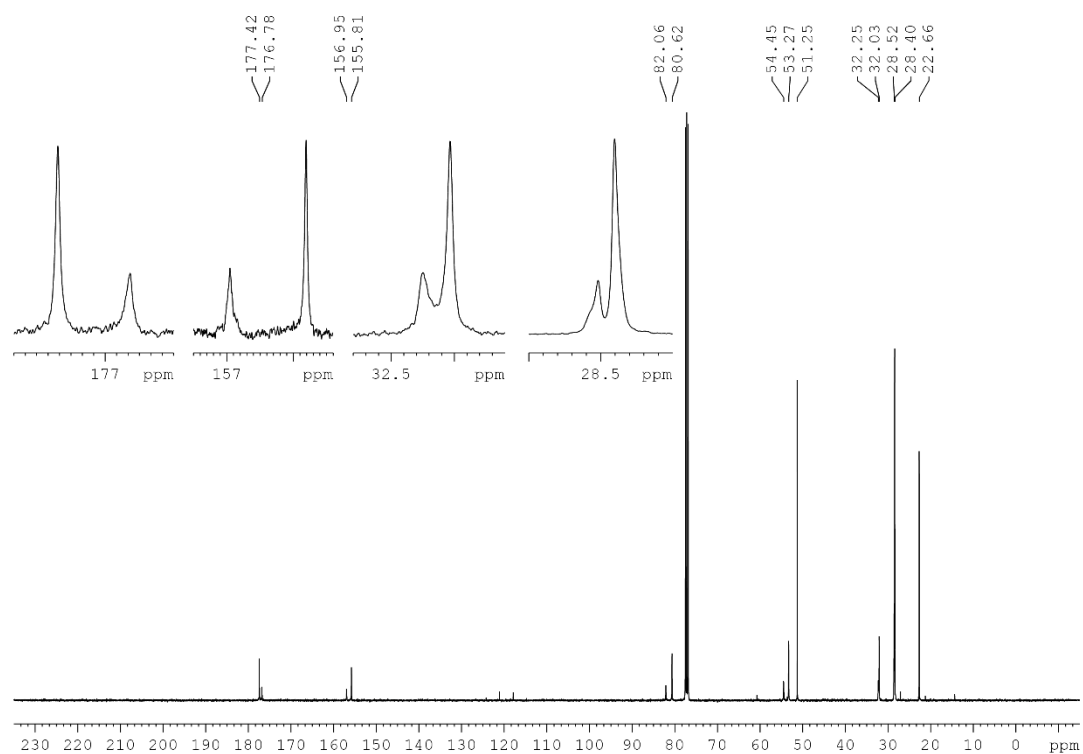
Supplementary Figure 2: ^{13}C NMR spectrum of **2** (CDCl$_3$, 100 MHz) (Gotz and Kunz et al., 2020a).
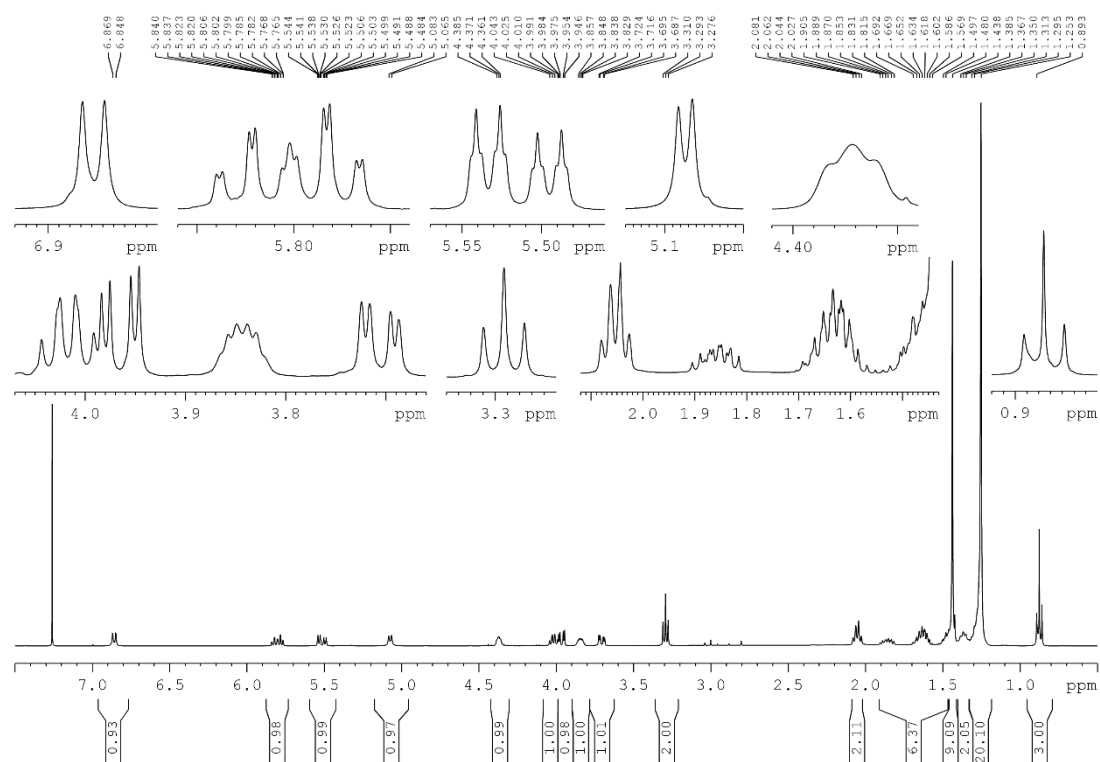
Supplementary Figure 3: ^{1}H NMR spectrum of **3** (CDCl$_3$, 400 MHz) (Gotz and Kunz et al., 2020a).
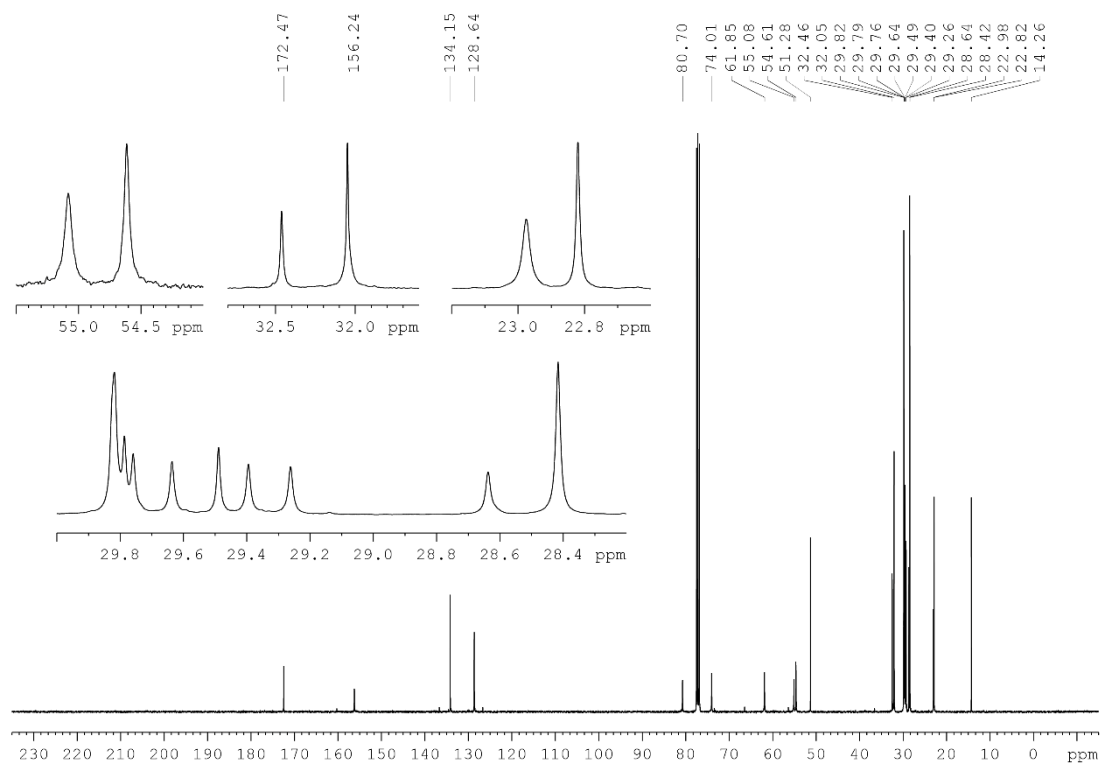
Supplementary Figure 4: ^{13}C NMR spectrum of **3** (CDCl$_3$, 100 MHz) (Gotz and Kunz et al., 2020a).
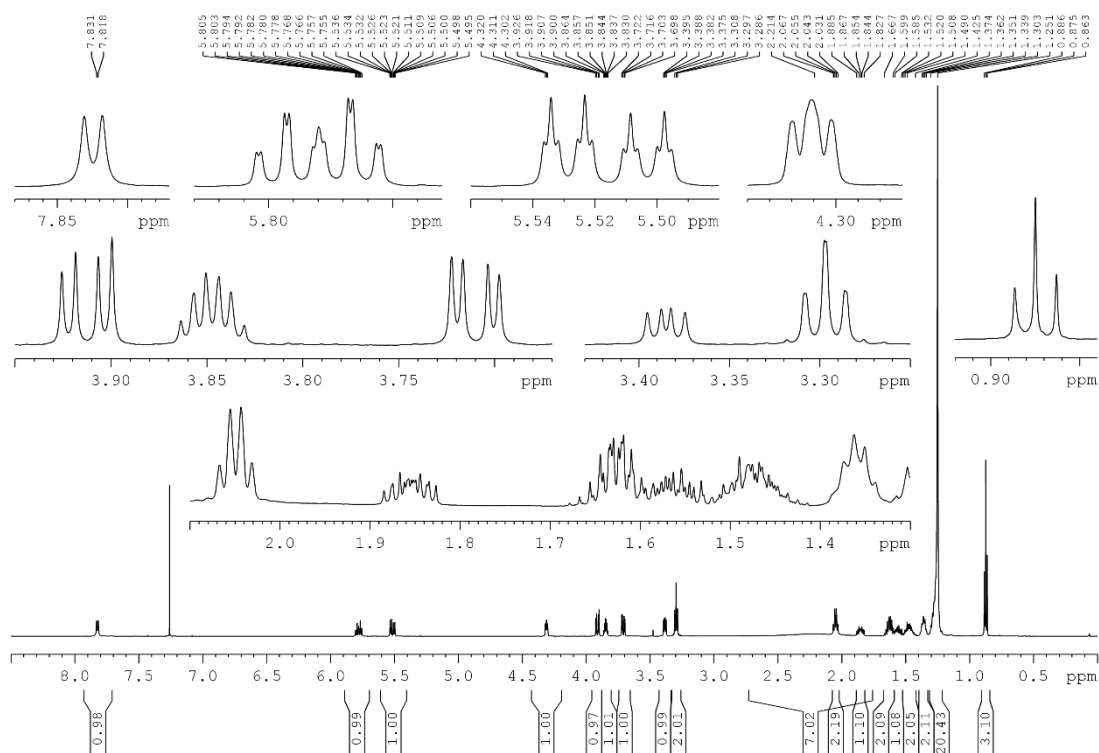
Supplementary Figure 5: ^{1}H NMR spectrum of **4** (CDCl$_3$, 600 MHz) (Gotz and Kunz et al., 2020a).
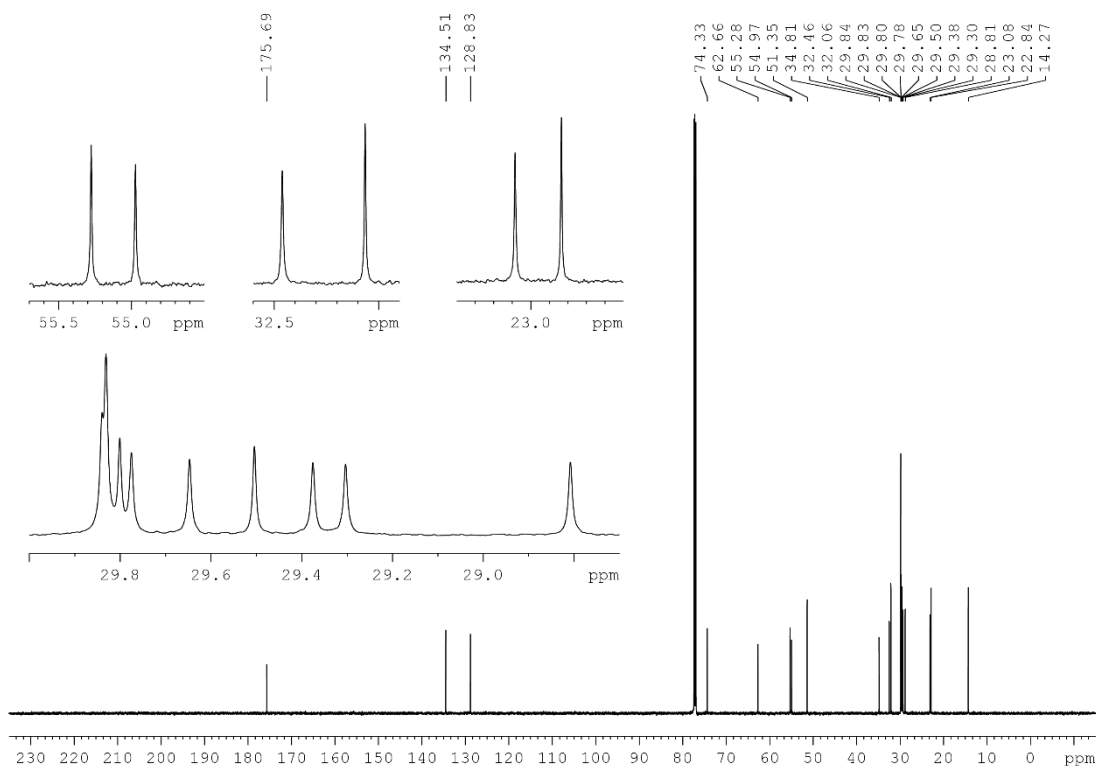
Supplementary Figure 6: ^{13}C NMR spectrum of **4** (CDCl$_3$, 150 MHz) (Gotz and Kunz et al., 2020a).
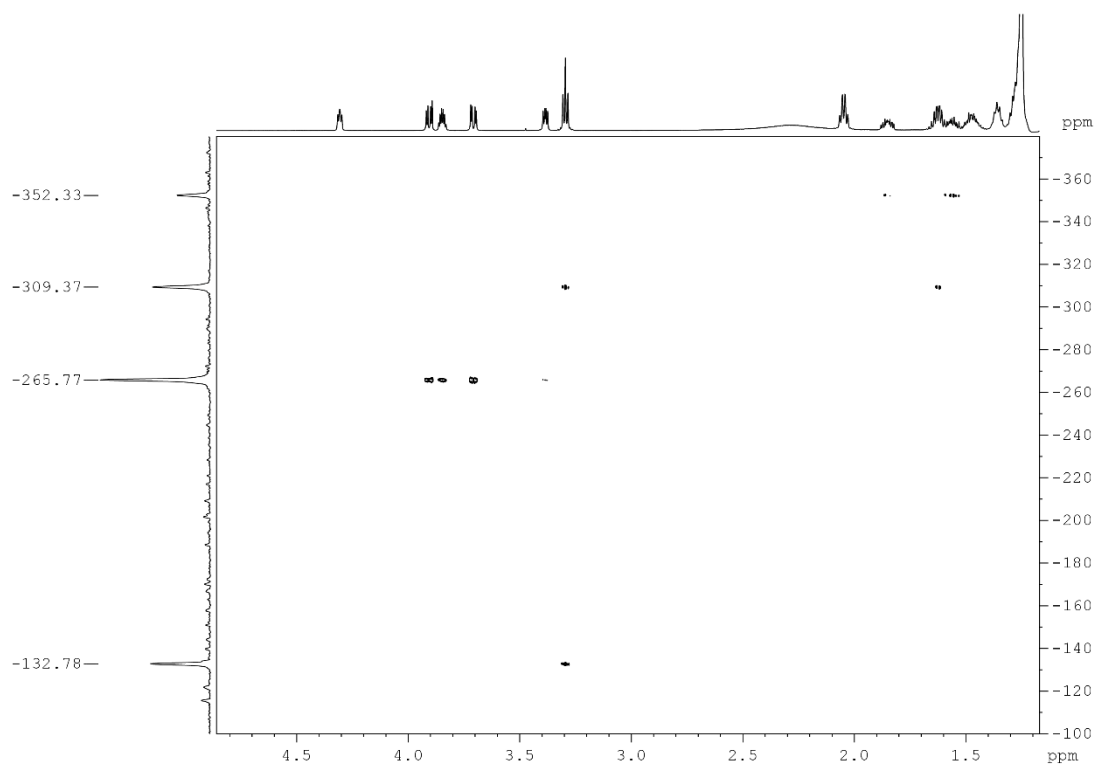
Supplementary Figure 7: (^{1}H,^{15}N)-HMBC NMR spectrum of **4** (CDCl$_3$, 600 MHz) (Gotz and Kunz et al., 2020a).
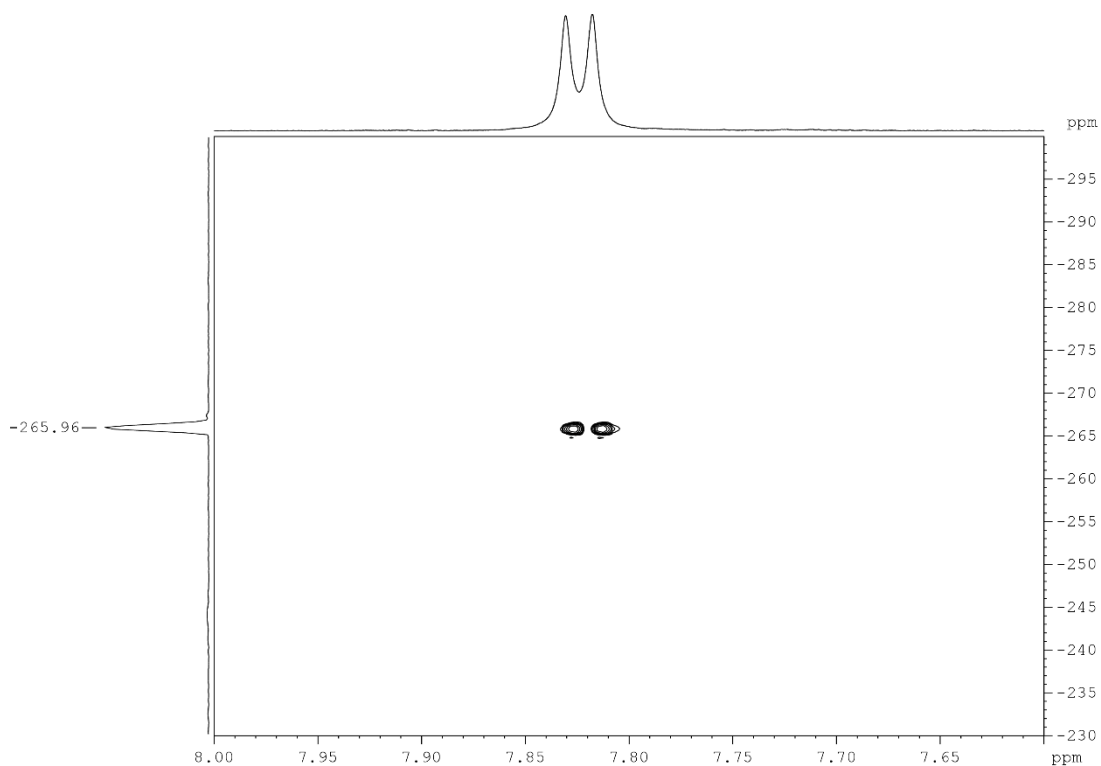
Supplementary Figure 8: (^{1}H,^{15}N)-HSQC NMR spectrum of **4** (CDCl$_3$, 600 MHz) (Gotz and Kunz et al., 2020a).

Mass Spectra

Compound Spectrum SmartFormula Report

Analysis Info   Acquisition Date   6/24/2019 3:42:37 PM

Analysis Name   D:\Data\spektren2019\24062019_SB080_SEI_44_01_4188.d

Method   Automation_esi_tune_pos_low.m   Operator   admin

Sample Name   24062019_SB080_SEI   Instrument   micrOTOF   213750.00088

Comment   in MeCN/CHCl3

Acquisition Parameter
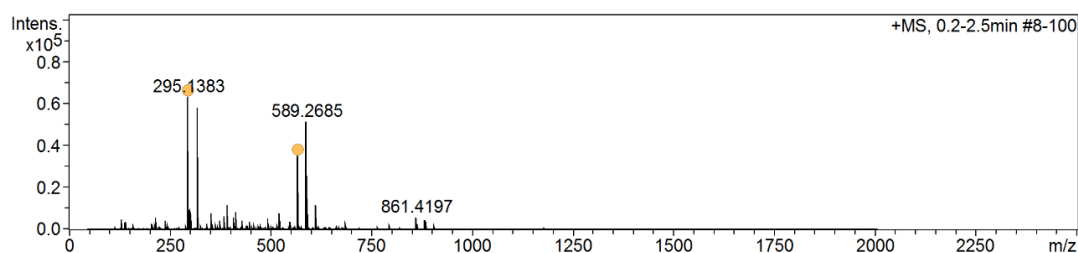
Source Type	ESI	Ion Polarity	Positive	Set Nebulizer	0.7 Bar
Focus	Not active	Set Capillary	4500 V	Set Dry Heater	200 °C
Scan Begin	50 m/z	Set End Plate Offset	-500 V	Set Dry Gas	5.0 l/min
Scan End	2000 m/z	n/a	n/a	Set Divert Valve	Source

+MS, 0.2-2.5min #8-100

Meas. m/z	#	Ion Formula	m/z	err [ppm]	mSigma	# mSigma	Score	rdb	e⁻ Conf	N-Rule
295.1383	1	C11H20N4NaO4	295.1377	-2.0	4.1	1	100.00	3.5	even	ok
567.2866	1	C22H40N8NaO8	567.2861	-0.8	8.6	1	100.00	6.5	even	ok

Supplementary Figure 9: Mass spectrum of **2** (ESI⁺) (Gotz and Kunz et al., 2020a).

Compound Spectrum SmartFormula Report

Analysis Info   Acquisition Date   6/24/2019 1:54:26 PM

Analysis Name   D:\Data\spektren2019\24062019_JF238_SEI_44_01_4177.d

Method   Automation_esi_tune_pos_mid.m   Operator   admin

Sample Name   24062019_JF238_SEI   Instrument   micrOTOF   213750.00088

Comment   in MeCN/CHCl3

Acquisition Parameter

Source Type	ESI	Ion Polarity	Positive	Set Nebulizer	0.7 Bar
Focus	Not active	Set Capillary	4500 V	Set Dry Heater	200 °C
Scan Begin	150 m/z	Set End Plate Offset	-500 V	Set Dry Gas	5.0 l/min
Scan End	3500 m/z	n/a	n/a	Set Divert Valve	Source

+MS, 0.2-2.5min #12-154

Meas. m/z	#	Ion Formula	m/z	err [ppm]	mSigma	# mSigma	Score	rdb	e⁻ Conf	N-Rule
576.4073	1	C29H55N5NaO5	576.4095	3.8	3.4	1	100.00	4.5	even	ok
592.3864	1	C29H55KN5O5	592.3835	-4.9	85.2	1	100.00	4.5	even	ok
1129.8274	1	C58H110N10NaO10	1129.8299	2.2	3.4	1	100.00	8.5	even	ok

Supplementary Figure 10: Mass spectrum of **3** (ESI⁺) (Gotz and Kunz et al., 2020a).

Mass Spectrum SmartFormula Report
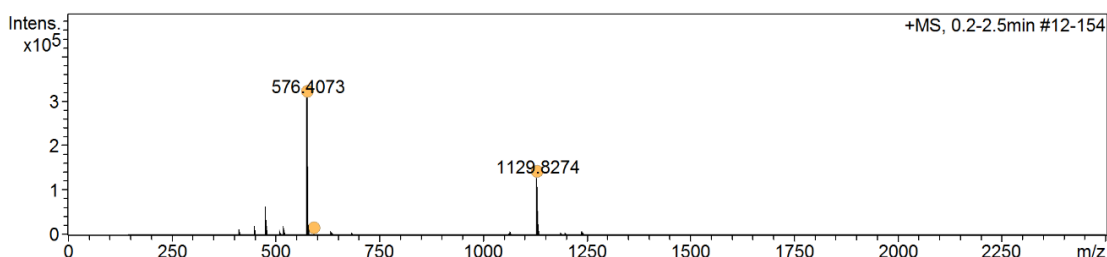
Analysis Info

Analysis Name	D:\Data\Spektren2019\2019_1505_SEI_JF241_3.d			Acquisition Date	7/5/2019 1:27:25 PM
Method	tune_pos_wide.m			Operator	Sebastian
Sample Name	2019_1505_SEI_JF241			Instrument	micrOTOF-Q III 8228888.20516
Comment	Fink Julian				
	JF241				
	5 pmol/ul in MeOH/CHCl3				

Acquisition Parameter

Source Type	ESI	Ion Polarity	Positive	Set Nebulizer	0.4 Bar
Focus	Not active	Set Funnel 1 RF	200.0 Vpp	Set Dry Heater	200 °C
Scan Begin	50 m/z	Set Funnel 2 RF	300.0 Vpp	Set Dry Gas	4.0 l/min
Scan End	4000 m/z	Set Hexapole RF	400.0 Vpp	Set Divert Valve	Waste
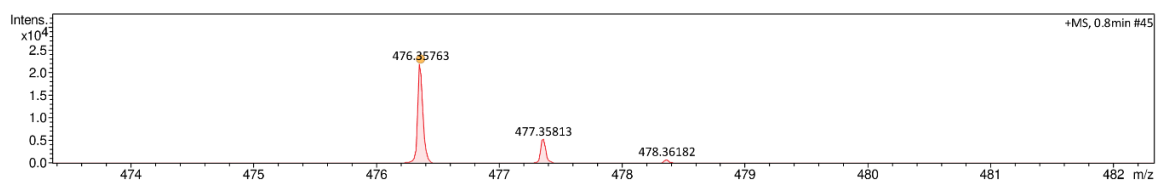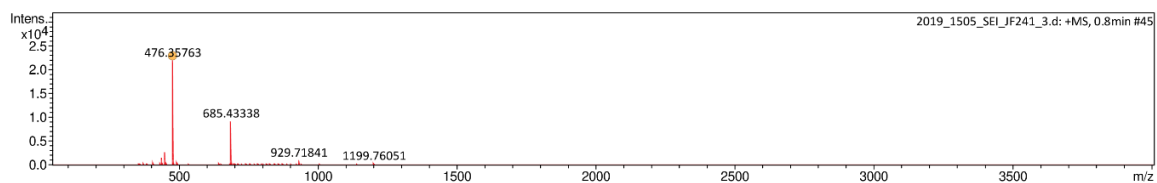
Meas. m/z	#	Ion Formula	m/z	err [ppm]	mSigma	# mSigma	Score	rdb	e⁻ Conf	N-Rule
476.35763	1	C24H47N5NaO3	476.35711	-1.08	26.7	1	100.00	3.5	even	ok

Bruker Compass DataAnalysis 4.2   printed: 7/5/2019 1:30:56 PM   by: Sebastian   Page 1 of 1

Supplementary Figure 11: Mass spectrum of **4** (ESI⁺) (Gotz and Kunz et al., 2020a).

IR Spectra
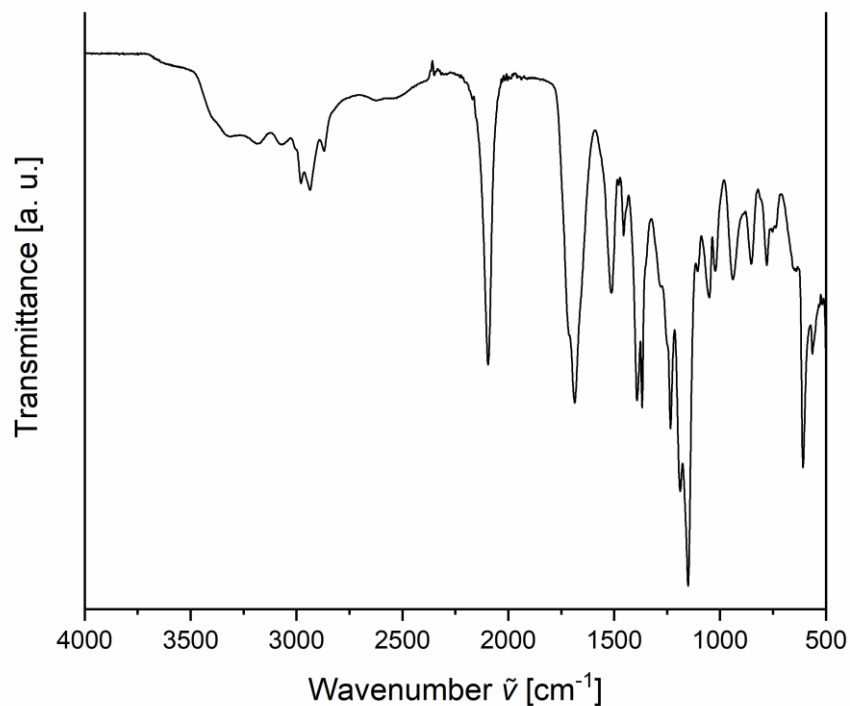
Supplementary Figure 12: FTIR spectrum of **2** (ATR) (Gotz and Kunz et al., 2020a).
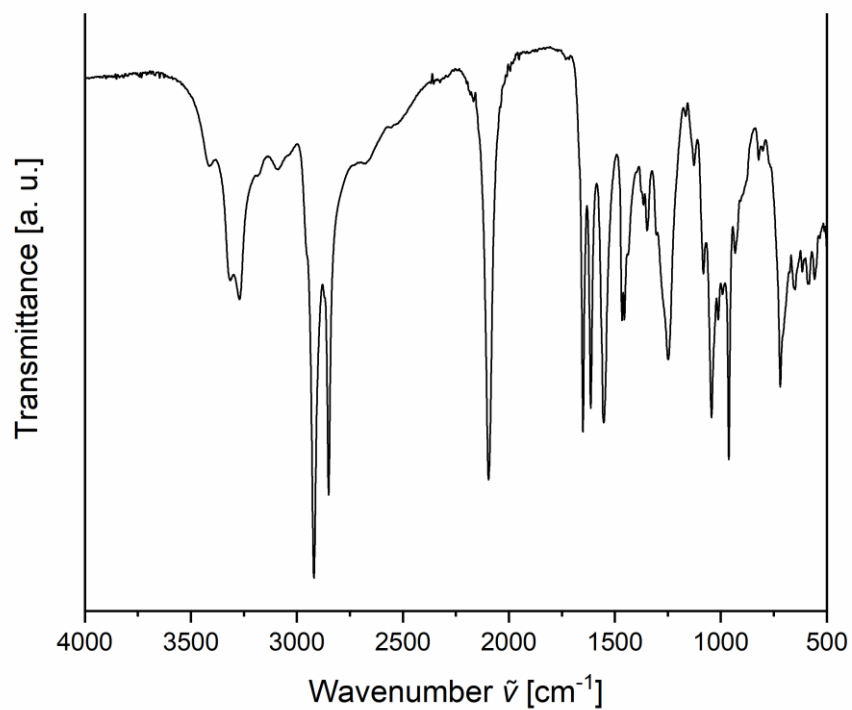
Supplementary Figure 13: FTIR spectrum of **4** (ATR) (Gotz and Kunz et al., 2020a).
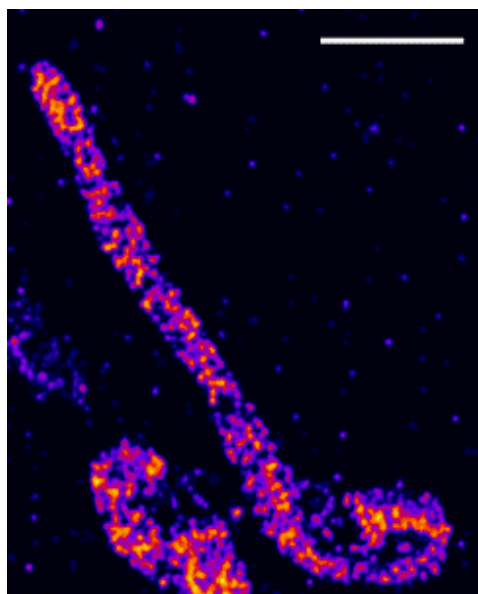
Supplementary Figure 14: dSTORM image of HeLa229 cells expressing cristae marker MtCK-GFP

dSTORM imaging of HeLa229 cells, transfected for 24 hours with MtCK-GFP and immunolabeled for GFP and Cy5 to visualize mitochondrial cristae. Scale bar, 1 µm. Image acquisition performed by Ralph Götz (Kunz et al., 2020).
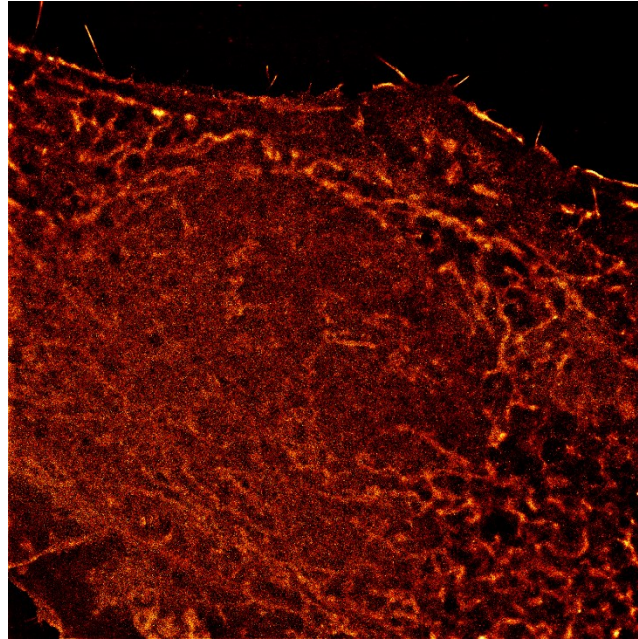
Supplementary Figure 15: dSTORM image of α-NH₂-ω-N₃-C₆-ceramide in HeLa229 cells

dSTORM images of HeLa229 cells, fed with α-NH$_2$-ω-N$_3$-C$_6$-ceramide, fixed, permeabilized and stained with DBCO-Cy5. Image acquisition performed by Ralph Götz.
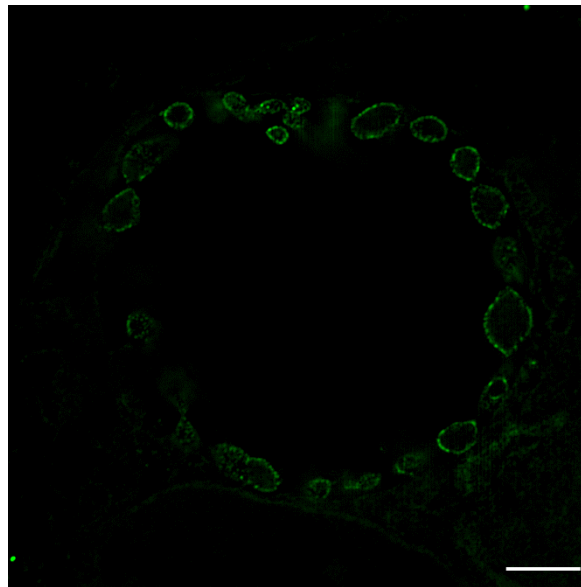
Supplementary Figure 16: Chlamydial RBs localizing close to the inclusion membrane.

10x expanded SIM images of HeLa229 cells, infected 24 hours with *Chlamydia trachomatis*, fed with α-NH$_2$-ω-N$_3$-C$_6$-ceramide, fixed, permeabilized and stained with DBCO-Alexa Fluor 488. Scale bar, 10 μm (Gotz et al., 2020a).
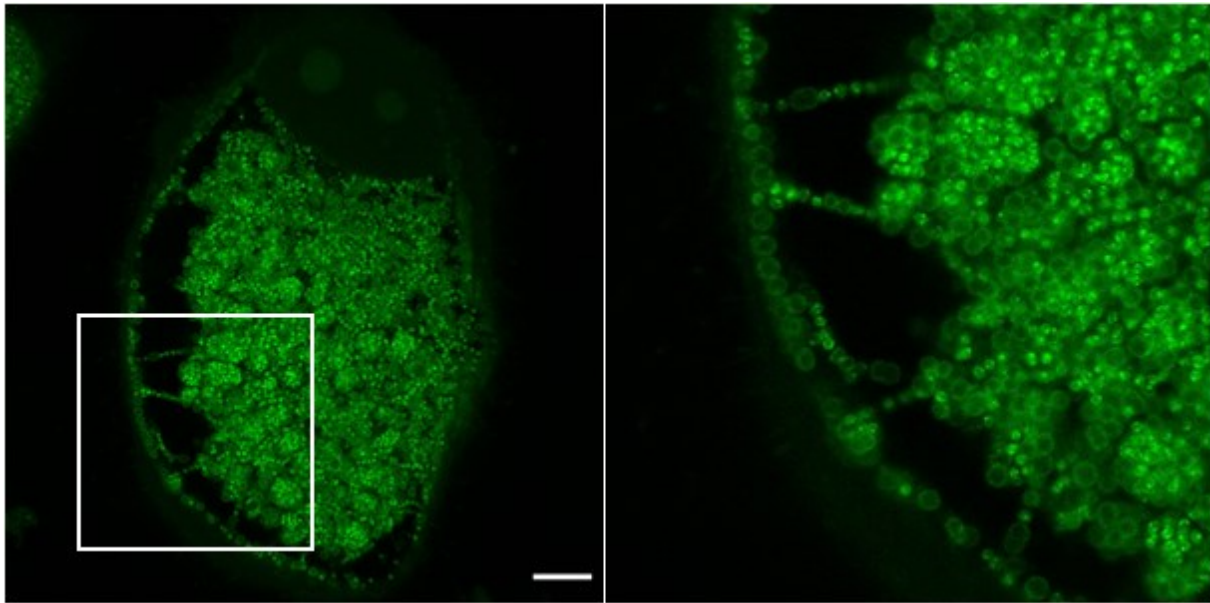
Supplementary Figure 17: Simkanial "highways" connecting the inclusion to the host plasma membrane.

4x expanded confocal images of HeLa229 cells, infected for 72 hours with *Simkania negevensis*, fed with α-NH$_2$-ω-N$_3$-C$_6$-ceramide, fixed, permeabilized and stained with DBCO-Alexa Fluor 488. Scale bar, 10 µm.

Supplementary Movie 1: Z-stacks of HeLa229 cells, infected with RSTE4 for 22 hours and immunolabeled for HSP60 (green) and CPAF (magenta) (Kunz et al., 2019). The video was created using Imaris 8.4.1.

Supplementary Movie 2: Z-stacks of HeLa229 cells, infected with RSTE4 for 30 hours and immunolabeled for HSP60 (green) and CPAF (magenta) (Kunz et al., 2019). The video was created using Imaris 8.4.1.

Supplementary Movie 3: Z-stacks of HeLa229 cells, infected with wildtype *Chlamydia trachomatis* for 22 hours and immunolabeled for HSP60 (green) and CPAF (magenta) (Kunz et al., 2019). The video was created using Imaris 8.4.1.

Supplementary Movie 4: Z-stacks of HeLa229 cells, infected with wildtype *Chlamydia trachomatis* for 30 hours and immunolabeled for HSP60 (green) and CPAF (magenta) (Kunz et al., 2019). The video was created using Imaris 8.4.1.

Supplementary Movie 5: Z-stacks of HeLa229 cells, infected with *C. tr* Cdu1:: Tn bla for 24 hours and immunolabeled for HSP60 (green) and Cdu1 (magenta) (Kunz et al., 2019). The video was created using Imaris 8.4.1.

Supplementary Movie 6: Z-stacks of HeLa229 cells, infected with wildtype *Chlamydia trachomatis* for 24 hours and immunolabeled for HSP60 (green) and Cdu1 (magenta) (Kunz et al., 2019). The video was created using Imaris 8.4.1.

Supplementary Movie 7: Z-stacks of HeLa229 cells, infected with *Ct* mCh(GroL2) GFP(OmcAL2) for 30 hours and immunolabeled for GFP (green) and mCherry (magenta) (Kunz et al., 2019). The video was created using Imaris 8.4.1.

Supplementary Movie 8: Z-stacks of HeLa229 cells, infected 24 hours with *Chlamydia trachomatis*, fed with α-NH$_2$-ω-N$_3$-C$_6$-ceramide, fixed, permeabilized and stained with DBCO-Alexa Fluor 488.

Sources

Abbe, E. 1873. Beiträge zur Theorie des Mikroskops und der mikroskopischen Wahrnehmung. *Archiv für Mikroskopische Anatomie*. 9:413–468.

Abdelrahman, Y., S.P. Ouellette, R.J. Belland, and J.V. Cox. 2016. Correction: Polarized Cell Division of Chlamydia trachomatis. *PLoS Pathog*. 12:e1005866.

Abdelrahman, Y.M., and R.J. Belland. 2005. The chlamydial developmental cycle. *FEMS Microbiol Rev*. 29:949-959.

Abe, Y., T. Shodai, T. Muto, K. Mihara, H. Torii, S. Nishikawa, T. Endo, and D. Kohda. 2000. Structural basis of presequence recognition by the mitochondrial protein import receptor Tom20. *Cell*. 100:551-560.

Abrams, A.J., R.B. Hufnagel, A. Rebelo, C. Zanna, N. Patel, M.A. Gonzalez, I.J. Campeanu, L.B. Griffin, S. Groenewald, A.V. Strickland, F. Tao, F. Speziani, L. Abreu, R. Schule, L. Caporali, C. La Morgia, A. Maresca, R. Liguori, R. Lodi, Z.M. Ahmed, K.L. Sund, X. Wang, L.A. Krueger, Y. Peng, C.E. Prada, C.A. Prows, E.K. Schorry, A. Antonellis, H.H. Zimmerman, O.A. Abdul-Rahman, Y. Yang, S.M. Downes, J. Prince, F. Fontanesi, A. Barrientos, A.H. Nemeth, V. Carelli, T. Huang, S. Zuchner, and J.E. Dallman. 2015. Mutations in SLC25A46, encoding a UGO1-like protein, cause an optic atrophy spectrum disorder. *Nat Genet*. 47:926-932.

Agaisse, H., and I. Derre. 2014. Expression of the effector protein IncD in Chlamydia trachomatis mediates recruitment of the lipid transfer protein CERT and the endoplasmic reticulum-resident protein VAPB to the inclusion membrane. *Infect Immun*. 82:2037-2047.

Airy, G.B. 1835. On the Diffraction of an Object-glass with Circular Aperture. *Transactions of the Cambridge Philosophical Society*. 5:283–291.

Allan, I., and J.H. Pearce. 1983. Differential amino acid utilization by Chlamydia psittaci (strain guinea pig inclusion conjunctivitis) and its regulatory effect on chlamydial growth. *J Gen Microbiol*. 129:1991-2000.

Althaus, C.L., K.M. Turner, C.H. Mercer, P. Auguste, T.E. Roberts, G. Bell, S.A. Herzog, J.A. Cassell, W.J. Edmunds, P.J. White, H. Ward, and N. Low. 2014. Effectiveness and cost-effectiveness of traditional and new partner notification technologies for curable sexually transmitted infections: observational study, systematic reviews and mathematical modelling. *Health Technol Assess*. 18:1-100, vii-viii.

Anand, R., V. Strecker, J. Urbach, I. Wittig, and A.S. Reichert. 2016. Mic13 Is Essential for Formation of Crista Junctions in Mammalian Cells. *PLoS One*. 11:e0160258.

Anderson, S., A.T. Bankier, B.G. Barrell, M.H. de Bruijn, A.R. Coulson, J. Drouin, I.C. Eperon, D.P. Nierlich, B.A. Roe, F. Sanger, P.H. Schreier, A.J. Smith, R. Staden, and I.G. Young. 1981. Sequence and organization of the human mitochondrial genome. *Nature*. 290:457-465.

Asaoka, T., and F. Ikeda. 2015. New Insights into the Role of Ubiquitin Networks in the Regulation of Antiapoptosis Pathways. *Int Rev Cell Mol Biol*. 318:121-158.

Banerjee, H.N., M. Blackshear, J. Williams, Z. Hawkins, C. Sawyer, V. Manglik, and S. Giri. 2012. C-6 Ceramide Induces p53 Dependent Apoptosis in Human Astrocytoma Grade4 (Glioblastoma Multiforme) Cells. *J Cancer Sci Ther*. 4:12.

Banhart, S., E.M. Saied, A. Martini, S. Koch, L. Aeberhard, K. Madela, C. Arenz, and D. Heuer. 2014. Improved plaque assay identifies a novel anti-Chlamydia ceramide derivative with altered intracellular localization. *Antimicrob Agents Chemother*. 58:5537-5546.

Banhart, S., E.K. Schafer, J.M. Gensch, and D. Heuer. 2019. Sphingolipid Metabolism and Transport in Chlamydia trachomatis and Chlamydia psittaci Infections. *Front Cell Dev Biol*. 7:223.

Barbot, M., D.C. Jans, C. Schulz, N. Denkert, B. Kroppen, M. Hoppert, S. Jakobs, and M. Meinecke. 2015. Mic10 oligomerizes to bend mitochondrial inner membranes at cristae junctions. *Cell Metab*. 21:756-763.

Baricault, L., B. Segui, L. Guegand, A. Olichon, A. Valette, F. Larminat, and G. Lenaers. 2007. OPA1 cleavage depends on decreased mitochondrial ATP level and bivalent metals. *Exp Cell Res*. 313:3800-3808.

Sources

Barrera, M., S. Koob, D. Dikov, F. Vogel, and A.S. Reichert. 2016. OPA1 functionally interacts with MIC60 but is dispensable for crista junction formation. *FEBS Lett*. 590:3309-3322.

Bastos, M.D., B.G. Coutinho, and M.L. Coelho. 2010. Lysostaphin: A Staphylococcal Bacteriolysin with Potential Clinical Applications. *Pharmaceuticals (Basel)*. 3:1139-1161.

Becam, J., T. Walter, A. Burgert, J. Schlegel, M. Sauer, J. Seibel, and A. Schubert-Unkmeir. 2017. Antibacterial activity of ceramide and ceramide analogs against pathogenic Neisseria. *Sci Rep*. 7:17627.

Becker, K.A., B. Fahsel, H. Kemper, J. Mayeres, C. Li, B. Wilker, S. Keitsch, M. Soddemann, C. Sehl, M. Kohnen, M.J. Edwards, H. Grassme, C.C. Caldwell, A. Seitz, M. Fraunholz, and E. Gulbins. 2018. Staphylococcus aureus Alpha-Toxin Disrupts Endothelial-Cell Tight Junctions via Acid Sphingomyelinase and Ceramide. *Infect Immun*. 86.

Becker, R.E., and J. Bubeck Wardenburg. 2015. Staphylococcus aureus and the skin: a longstanding and complex interaction. *Skinmed*. 13:111-119; quiz 120.

Becker, T., L.S. Wenz, V. Kruger, W. Lehmann, J.M. Muller, L. Goroncy, N. Zufall, T. Lithgow, B. Guiard, A. Chacinska, R. Wagner, C. Meisinger, and N. Pfanner. 2011. The mitochondrial import protein Mim1 promotes biogenesis of multispanning outer membrane proteins. *J Cell Biol*. 194:387-395.

Belland, R.J., S.P. Ouellette, J. Gieffers, and G.I. Byrne. 2004. Chlamydia pneumoniae and atherosclerosis. *Cell Microbiol*. 6:117-127.

Belland, R.J., G. Zhong, D.D. Crane, D. Hogan, D. Sturdevant, J. Sharma, W.L. Beatty, and H.D. Caldwell. 2003. Genomic transcriptional profiling of the developmental cycle of Chlamydia trachomatis. *Proc Natl Acad Sci U S A*. 100:8478-8483.

Bera, A., S. Herbert, A. Jakob, W. Vollmer, and F. Gotz. 2005. Why are pathogenic staphylococci so lysozyme resistant? The peptidoglycan O-acetyltransferase OatA is the major determinant for lysozyme resistance of Staphylococcus aureus. *Mol Microbiol*. 55:778-787.

Betzig, E., G.H. Patterson, R. Sougrat, O.W. Lindwasser, S. Olenych, J.S. Bonifacino, M.W. Davidson, J. Lippincott-Schwartz, and H.F. Hess. 2006. Imaging intracellular fluorescent proteins at nanometer resolution. *Science*. 313:1642-1645.

Bibel, D.J., R. Aly, S. Shah, and H.R. Shinefield. 1993. Sphingosines: antimicrobial barriers of the skin. *Acta Derm Venereol*. 73:407-411.

Bibel, D.J., R. Aly, and H.R. Shinefield. 1992. Antimicrobial activity of sphingosines. *J Invest Dermatol*. 98:269-273.

Bibel, D.J., R. Aly, and H.R. Shinefield. 1995. Topical sphingolipids in antisepsis and antifungal therapy. *Clin Exp Dermatol*. 20:395-400.

Blum, T.B., A. Hahn, T. Meier, K.M. Davies, and W. Kuhlbrandt. 2019. Dimers of mitochondrial ATP synthase induce membrane curvature and self-assemble into rows. *Proc Natl Acad Sci U S A*. 116:4250-4255.

Bohnert, M., R.M. Zerbes, K.M. Davies, A.W. Muhleip, H. Rampelt, S.E. Horvath, T. Boenke, A. Kram, I. Perschil, M. Veenhuis, W. Kuhlbrandt, I.J. van der Klei, N. Pfanner, and M. van der Laan. 2015. Central role of Mic10 in the mitochondrial contact site and cristae organizing system. *Cell Metab*. 21:747-755.

Britigan, B.E., M.S. Cohen, and P.F. Sparling. 1985. Gonococcal infection: a model of molecular pathogenesis. *N Engl J Med*. 312:1683-1694.

Brott, A.S., and A.J. Clarke. 2019. Peptidoglycan O-Acetylation as a Virulence Factor: Its Effect on Lysozyme in the Innate Immune System. *Antibiotics (Basel)*. 8.

Burgert, A., S. Letschert, S. Doose, and M. Sauer. 2015. Artifacts in single-molecule localization microscopy. *Histochem Cell Biol*. 144:123-131.

Burgert, A., J. Schlegel, J. Becam, S. Doose, E. Bieberich, A. Schubert-Unkmeir, and M. Sauer. 2017. Characterization of Plasma Membrane Ceramides by Super-Resolution Microscopy. *Angew Chem Int Ed Engl*. 56:6131-6135.

Bush, R.M., and K.D. Everett. 2001. Molecular evolution of the Chlamydiaceae. *Int J Syst Evol Microbiol*. 51:203-220.

Sources

Byrne, G.I. 2003. Chlamydia uncloaked. *Proc Natl Acad Sci U S A*. 100:8040-8042.

Campbell, C.T., J.E. Kolesar, and B.A. Kaufman. 2012. Mitochondrial transcription factor A regulates mitochondrial transcription initiation, DNA packaging, and genome copy number. *Biochim Biophys Acta*. 1819:921-929.

Capmany, A., and M.T. Damiani. 2010. Chlamydia trachomatis intercepts Golgi-derived sphingolipids through a Rab14-mediated transport required for bacterial development and replication. *PLoS One*. 5:e14084.

Capmany, A., J. Gambarte Tudela, M. Alonso Bivou, and M.T. Damiani. 2019. Akt/AS160 Signaling Pathway Inhibition Impairs Infection by Decreasing Rab14-Controlled Sphingolipids Delivery to Chlamydial Inclusions. *Front Microbiol*. 10:666.

Castro-Garza, J., F. Gonzalez-Salazar, F.D. Quinn, R.K. Karls, L.H. De La Garza-Salinas, F.J. Guzman-de la Garza, and J. Vargas-Villarreal. 2016. An acidic sphingomyelinase Type C activity from Mycobacterium tuberculosis. *Rev Argent Microbiol*. 48:21-26.

Cazalet, C., C. Rusniok, H. Bruggemann, N. Zidane, A. Magnier, L. Ma, M. Tichit, S. Jarraud, C. Bouchier, F. Vandenesch, F. Kunst, J. Etienne, P. Glaser, and C. Buchrieser. 2004. Evidence in the Legionella pneumophila genome for exploitation of host cell functions and high genome plasticity. *Nat Genet*. 36:1165-1173.

Chacinska, A., S. Pfannschmidt, N. Wiedemann, V. Kozjak, L.K. Sanjuan Szklarz, A. Schulze-Specking, K.N. Truscott, B. Guiard, C. Meisinger, and N. Pfanner. 2004. Essential role of Mia40 in import and assembly of mitochondrial intermembrane space proteins. *EMBO J*. 23:3735-3746.

Chambers, H.F., and F.R. Deleo. 2009. Waves of resistance: Staphylococcus aureus in the antibiotic era. *Nat Rev Microbiol*. 7:629-641.

Chang, J.B., F. Chen, Y.G. Yoon, E.E. Jung, H. Babcock, J.S. Kang, S. Asano, H.J. Suk, N. Pak, P.W. Tillberg, A.T. Wassie, D. Cai, and E.S. Boyden. 2017. Iterative expansion microscopy. *Nat Methods*. 14:593-599.

Chaturvedi, A.K., C.A. Gaydos, P. Agreda, J.P. Holden, N. Chatterjee, J.J. Goedert, N.E. Caporaso, and E.A. Engels. 2010. Chlamydia pneumoniae infection and risk for lung cancer. *Cancer Epidemiol Biomarkers Prev*. 19:1498-1505.

Chau, S., E.Y. Tso, W.S. Leung, and K.S. Fung. 2015. Three cases of atypical pneumonia caused by Chlamydophila psittaci. *Hong Kong Med J*. 21:272-275.

Chen, A.L., K.A. Johnson, J.K. Lee, C. Sutterlin, and M. Tan. 2012. CPAF: a Chlamydial protease in search of an authentic substrate. *PLoS Pathog*. 8:e1002842.

Chen, F., P.W. Tillberg, and E.S. Boyden. 2015. Optical imaging. Expansion microscopy. *Science*. 347:543-548.

Chen, F., A.T. Wassie, A.J. Cote, A. Sinha, S. Alon, S. Asano, E.R. Daugharthy, J.B. Chang, A. Marblestone, G.M. Church, A. Raj, and E.S. Boyden. 2016. Nanoscale imaging of RNA with expansion microscopy. *Nat Methods*. 13:679-684.

Chen, X.J., and R.A. Butow. 2005. The organization and inheritance of the mitochondrial genome. *Nat Rev Genet*. 6:815-825.

Cheng, M.Y., F.U. Hartl, J. Martin, R.A. Pollock, F. Kalousek, W. Neupert, E.M. Hallberg, R.L. Hallberg, and A.L. Horwich. 1989. Mitochondrial heat-shock protein hsp60 is essential for assembly of proteins imported into yeast mitochondria. *Nature*. 337:620-625.

Chowdhury, S.R., A. Reimer, M. Sharan, V. Kozjak-Pavlovic, A. Eulalio, B.K. Prusty, M. Fraunholz, K. Karunakaran, and T. Rudel. 2017. Chlamydia preserves the mitochondrial network necessary for replication via microRNA-dependent inhibition of fission. *J Cell Biol*. 216:1071-1089.

Chowdhury, S.R., and T. Rudel. 2017. Chlamydia and mitochondria - an unfragmented relationship. *Microb Cell*. 4:233-235.

Chozinski, T.J., A.R. Halpern, H. Okawa, H.J. Kim, G.J. Tremel, R.O. Wong, and J.C. Vaughan. 2016. Expansion microscopy with conventional antibodies and fluorescent proteins. *Nat Methods*. 13:485-488.

Clifton, D.R., K.A. Fields, S.S. Grieshaber, C.A. Dooley, E.R. Fischer, D.J. Mead, R.A. Carabeo, and T. Hackstadt. 2004. A chlamydial type III translocated protein is tyrosine-phosphorylated at the

site of entry and associated with recruitment of actin. *Proc Natl Acad Sci U S A*. 101:10166-10171.

Cogan, E. 2020. Trachoma. *World Health Organization*.

Cogliati, S., J.A. Enriquez, and L. Scorrano. 2016. Mitochondrial Cristae: Where Beauty Meets Functionality. *Trends Biochem Sci*. 41:261-273.

Cole, N.B. 2013. Site-specific protein labeling with SNAP-tags. *Curr Protoc Protein Sci*. 73:30 31 31-30 31 16.

Collenburg, L., T. Walter, A. Burgert, N. Muller, J. Seibel, L. Japtok, B. Kleuser, M. Sauer, and S. Schneider-Schaulies. 2016. A Functionalized Sphingolipid Analogue for Studying Redistribution during Activation in Living T Cells. *J Immunol*. 196:3951-3962.

Collingro, A., P. Tischler, T. Weinmaier, T. Penz, E. Heinz, R.C. Brunham, T.D. Read, P.M. Bavoil, K. Sachse, S. Kahane, M.G. Friedman, T. Rattei, G.S. Myers, and M. Horn. 2011. Unity in variety--the pan-genome of the Chlamydiae. *Mol Biol Evol*. 28:3253-3270.

Conrad, A., Z. Yang, D. Ojcius, and G. Zhong. 2013. A path forward for the chlamydial virulence factor CPAF. *Microbes Infect*. 15:1026-1032.

Constable, F.L. 1959. Psittacosis elementary bodies. *Nature*. 184(Suppl 7):473-474.

Cortina, M.E., R.J. Ende, R.C. Bishop, C. Bayne, and I. Derre. 2019. Chlamydia trachomatis and Chlamydia muridarum spectinomycin resistant vectors and a transcriptional fluorescent reporter to monitor conversion from replicative to infectious bacteria. *PLoS One*. 14:e0217753.

Croxatto, A., and G. Greub. 2010. Early intracellular trafficking of Waddlia chondrophila in human macrophages. *Microbiology (Reading)*. 156:340-355.

Croxatto, A., N. Rieille, T. Kernif, I. Bitam, S. Aeby, O. Peter, and G. Greub. 2014. Presence of Chlamydiales DNA in ticks and fleas suggests that ticks are carriers of Chlamydiae. *Ticks Tick Borne Dis*. 5:359-365.

Cukkemane, N., F.J. Bikker, K. Nazmi, H.S. Brand, J. Sotres, L. Lindh, T. Arnebrant, and E.C. Veerman. 2015. Anti-adherence and bactericidal activity of sphingolipids against Streptococcus mutans. *Eur J Oral Sci*. 123:221-227.

Cunniff, B., A.N. Wozniak, P. Sweeney, K. DeCosta, and N.H. Heintz. 2014. Peroxiredoxin 3 levels regulate a mitochondrial redox setpoint in malignant mesothelioma cells. *Redox Biol*. 3:79-87.

Cuvillier, O., G. Pirianov, B. Kleuser, P.G. Vanek, O.A. Coso, S. Gutkind, and S. Spiegel. 1996. Suppression of ceramide-mediated programmed cell death by sphingosine-1-phosphate. *Nature*. 381:800-803.

Davies, K.M., M. Strauss, B. Daum, J.H. Kief, H.D. Osiewacz, A. Rycovska, V. Zickermann, and W. Kuhlbrandt. 2011. Macromolecular organization of ATP synthase and complex I in whole mitochondria. *Proc Natl Acad Sci U S A*. 108:14121-14126.

Delettre, C., J.M. Griffoin, J. Kaplan, H. Dollfus, B. Lorenz, L. Faivre, G. Lenaers, P. Belenguer, and C.P. Hamel. 2001. Mutation spectrum and splicing variants in the OPA1 gene. *Hum Genet*. 109:584-591.

Derre, I., R. Swiss, and H. Agaisse. 2011. The lipid transfer protein CERT interacts with the Chlamydia inclusion protein IncD and participates to ER-Chlamydia inclusion membrane contact sites. *PLoS Pathog*. 7:e1002092.

Dimmer, K.S., D. Papic, B. Schumann, D. Sperl, K. Krumpe, D.M. Walther, and D. Rapaport. 2012. A crucial role for Mim2 in the biogenesis of mitochondrial outer membrane proteins. *J Cell Sci*. 125:3464-3473.

Ding, W.X., M. Li, J.M. Biazik, D.G. Morgan, F. Guo, H.M. Ni, M. Goheen, E.L. Eskelinen, and X.M. Yin. 2012. Electron microscopic analysis of a spherical mitochondrial structure. *J Biol Chem*. 287:42373-42378.

Donsante, A. 2017. Chapter 8 - Gene Therapy for Amyotrophic Lateral Sclerosis: Therapeutic Transgenes. *Molecular and Cellular Therapies for Motor Neuron Diseases, eds N. Boulis, D. O'Connor, and A. Donsante (Cambridge, MA: Academic Press)*:167–205.

Dougherty, T.J. 1985. Analysis of Neisseria gonorrhoeae peptidoglycan by reverse-phase, high-pressure liquid chromatography. *J Bacteriol*. 163:69-74.

Sources

Dupont, C., and A.J. Clarke. 1991. Dependence of lysozyme-catalysed solubilization of Proteus mirabilis peptidoglycan on the extent of O-acetylation. *Eur J Biochem*. 195:763-769.

Duvezin-Caubet, S., R. Jagasia, J. Wagener, S. Hofmann, A. Trifunovic, A. Hansson, A. Chomyn, M.F. Bauer, G. Attardi, N.G. Larsson, W. Neupert, and A.S. Reichert. 2006. Proteolytic processing of OPA1 links mitochondrial dysfunction to alterations in mitochondrial morphology. *J Biol Chem*. 281:37972-37979.

Elachouri, G., S. Vidoni, C. Zanna, A. Pattyn, H. Boukhaddaoui, K. Gaget, P. Yu-Wai-Man, G. Gasparre, E. Sarzi, C. Delettre, A. Olichon, D. Loiseau, P. Reynier, P.F. Chinnery, A. Rotig, V. Carelli, C.P. Hamel, M. Rugolo, and G. Lenaers. 2011. OPA1 links human mitochondrial genome maintenance to mtDNA replication and distribution. *Genome Res*. 21:12-20.

Elwell, C., K. Mirrashidi, and J. Engel. 2016. Chlamydia cell biology and pathogenesis. *Nat Rev Microbiol*. 14:385-400.

Elwell, C.A., S. Jiang, J.H. Kim, A. Lee, T. Wittmann, K. Hanada, P. Melancon, and J.N. Engel. 2011. Chlamydia trachomatis co-opts GBF1 and CERT to acquire host sphingomyelin for distinct roles during intracellular development. *PLoS Pathog*. 7:e1002198.

Everett, K.D., and A.A. Andersen. 1997. The ribosomal intergenic spacer and domain I of the 23S rRNA gene are phylogenetic markers for Chlamydia spp. *Int J Syst Bacteriol*. 47:461-473.

Everett, K.D., R.M. Bush, and A.A. Andersen. 1999. Emended description of the order Chlamydiales, proposal of Parachlamydiaceae fam. nov. and Simkaniaceae fam. nov., each containing one monotypic genus, revised taxonomy of the family Chlamydiaceae, including a new genus and five new species, and standards for the identification of organisms. *Int J Syst Bacteriol*. 49 Pt 2:415-440.

Eydt, K., K.M. Davies, C. Behrendt, I. Wittig, and A.S. Reichert. 2017. Cristae architecture is determined by an interplay of the MICOS complex and the F1FO ATP synthase via Mic27 and Mic10. *Microb Cell*. 4:259-272.

Fainardi, E., M. Castellazzi, S. Seraceni, E. Granieri, and C. Contini. 2008. Under the microscope: focus on Chlamydia pneumoniae infection and multiple sclerosis. *Curr Neurovasc Res*. 5:60-70.

Faulstich, M., F. Hagen, E. Avota, V. Kozjak-Pavlovic, A.C. Winkler, Y. Xian, S. Schneider-Schaulies, and T. Rudel. 2015. Neutral sphingomyelinase 2 is a key factor for PorB-dependent invasion of Neisseria gonorrhoeae. *Cell Microbiol*. 17:241-253.

Fey, P.D., J.L. Endres, V.K. Yajjala, T.J. Widhelm, R.J. Boissy, J.L. Bose, and K.W. Bayles. 2013. A genetic resource for rapid and comprehensive phenotype screening of nonessential Staphylococcus aureus genes. *mBio*. 4:e00537-00512.

Fischer, A., K.S. Harrison, Y. Ramirez, D. Auer, S.R. Chowdhury, B.K. Prusty, F. Sauer, Z. Dimond, C. Kisker, P.S. Hefty, and T. Rudel. 2017. Chlamydia trachomatis-containing vacuole serves as deubiquitination platform to stabilize Mcl-1 and to interfere with host defense. *Elife*. 6.

Fischer, C.L., D.R. Drake, D.V. Dawson, D.R. Blanchette, K.A. Brogden, and P.W. Wertz. 2012. Antibacterial activity of sphingoid bases and fatty acids against Gram-positive and Gram-negative bacteria. *Antimicrob Agents Chemother*. 56:1157-1161.

Fischer, C.L., K.S. Walters, D.R. Drake, D.R. Blanchette, D.V. Dawson, K.A. Brogden, and P.W. Wertz. 2013. Sphingoid bases are taken up by Escherichia coli and Staphylococcus aureus and induce ultrastructural damage. *Skin Pharmacol Physiol*. 26:36-44.

Flannagan, R.S., B. Heit, and D.E. Heinrichs. 2016. Intracellular replication of Staphylococcus aureus in mature phagolysosomes in macrophages precedes host cell death, and bacterial escape and dissemination. *Cell Microbiol*. 18:514-535.

Francius, G., O. Domenech, M.P. Mingeot-Leclercq, and Y.F. Dufrene. 2008. Direct observation of Staphylococcus aureus cell wall digestion by lysostaphin. *J Bacteriol*. 190:7904-7909.

Frezza, C., S. Cipolat, O. Martins de Brito, M. Micaroni, G.V. Beznoussenko, T. Rudka, D. Bartoli, R.S. Polishuck, N.N. Danial, B. De Strooper, and L. Scorrano. 2006. OPA1 controls apoptotic cristae remodeling independently from mitochondrial fusion. *Cell*. 126:177-189.

Friedman, J.R., and J. Nunnari. 2014. Mitochondrial form and function. *Nature*. 505:335-343.

Sources

Fukasawa, Y., J. Tsuji, S.C. Fu, K. Tomii, P. Horton, and K. Imai. 2015. MitoFates: improved prediction of mitochondrial targeting sequences and their cleavage sites. *Mol Cell Proteomics*. 14:1113-1126.

Gabaldon, T., and M.A. Huynen. 2003. Reconstruction of the proto-mitochondrial metabolism. *Science*. 301:609.

Galloway, C.A., and Y. Yoon. 2013. Mitochondrial morphology in metabolic diseases. *Antioxid Redox Signal*. 19:415-430.

Gambarotto, D., F.U. Zwettler, M. Le Guennec, M. Schmidt-Cernohorska, D. Fortun, S. Borgers, J. Heine, J.G. Schloetel, M. Reuss, M. Unser, E.S. Boyden, M. Sauer, V. Hamel, and P. Guichard. 2019. Imaging cellular ultrastructures using expansion microscopy (U-ExM). *Nat Methods*. 16:71-74.

Gao, M., R. Maraspini, O. Beutel, A. Zehtabian, B. Eickholt, A. Honigmann, and H. Ewers. 2018. Expansion Stimulated Emission Depletion Microscopy (ExSTED). *ACS Nano*. 12:4178-4185.

Gault, C.R., L.M. Obeid, and Y.A. Hannun. 2010. An overview of sphingolipid metabolism: from synthesis to breakdown. *Adv Exp Med Biol*. 688:1-23.

Gaylord, W.H., Jr. 1954. Intracellular forms of meningopneumonitis virus. *J Exp Med*. 100:575-580.

Geng, N., X. Wang, X. Yu, R. Wang, Y. Zhu, M. Zhang, J. Liu, and Y. Liu. 2020. Staphylococcus aureus Avoids Autophagy Clearance of Bovine Mammary Epithelial Cells by Impairing Lysosomal Function. *Front Immunol*. 11:746.

Genin, E.C., M. Plutino, S. Bannwarth, E. Villa, E. Cisneros-Barroso, M. Roy, B. Ortega-Vila, K. Fragaki, F. Lespinasse, E. Pinero-Martos, G. Auge, D. Moore, F. Burte, S. Lacas-Gervais, Y. Kageyama, K. Itoh, P. Yu-Wai-Man, H. Sesaki, J.E. Ricci, C. Vives-Bauza, and V. Paquis-Flucklinger. 2016. CHCHD10 mutations promote loss of mitochondrial cristae junctions with impaired mitochondrial genome maintenance and inhibition of apoptosis. *EMBO Mol Med*. 8:58-72.

Ghai, I., and S. Ghai. 2018. Understanding antibiotic resistance via outer membrane permeability. *Infect Drug Resist*. 11:523-530.

Ghuysen, J.M., and J.L. Strominger. 1963. Structure of the Cell Wall of Staphylococcus Aureus, Strain Copenhagen. Ii. Separation and Structure of Disaccharides. *Biochemistry*. 2:1119-1125.

Gillard, B.K., R.G. Clement, and D.M. Marcus. 1998. Variations among cell lines in the synthesis of sphingolipids in de novo and recycling pathways. *Glycobiology*. 8:885-890.

Glytsou, C., E. Calvo, S. Cogliati, A. Mehrotra, I. Anastasia, G. Rigoni, A. Raimondi, N. Shintani, M. Loureiro, J. Vazquez, L. Pellegrini, J.A. Enriquez, L. Scorrano, and M.E. Soriano. 2016. Optic Atrophy 1 Is Epistatic to the Core MICOS Component MIC60 in Mitochondrial Cristae Shape Control. *Cell Rep*. 17:3024-3034.

Gomez-Valero, L., and C. Buchrieser. 2013. Genome dynamics in Legionella: the basis of versatility and adaptation to intracellular replication. *Cold Spring Harb Perspect Med*. 3.

Gotz, R., T.C. Kunz, J. Fink, F. Solger, J. Schlegel, J. Seibel, V. Kozjak-Pavlovic, T. Rudel, and M. Sauer. 2020a. Nanoscale imaging of cellular and bacterial membranes by sphingolipid expansion microscopy. *Nat commun*:In Print.

Gotz, R., S. Panzer, N. Trinks, J. Eilts, J. Wagener, D. Turra, A. Di Pietro, M. Sauer, and U. Terpitz. 2020b. Expansion Microscopy for Cell Biology Analysis in Fungi. *Front Microbiol*. 11:574.

Grassme, H., E. Gulbins, B. Brenner, K. Ferlinz, K. Sandhoff, K. Harzer, F. Lang, and T.F. Meyer. 1997. Acidic sphingomyelinase mediates entry of N. gonorrhoeae into nonphagocytic cells. *Cell*. 91:605-615.

Grassme, H., V. Jendrossek, A. Riehle, G. von Kurthy, J. Berger, H. Schwarz, M. Weller, R. Kolesnick, and E. Gulbins. 2003. Host defense against Pseudomonas aeruginosa requires ceramide-rich membrane rafts. *Nat Med*. 9:322-330.

Grayston, J.T., L.A. Campbell, C.C. Kuo, C.H. Mordhorst, P. Saikku, D.H. Thom, and S.P. Wang. 1990. A new respiratory tract pathogen: Chlamydia pneumoniae strain TWAR. *J Infect Dis*. 161:618-625.

Greub, G. 2010. International Committee on Systematics of Prokaryotes. Subcommittee on the taxonomy of the Chlamydiae: minutes of the closed meeting, 21 June 2010, Hof bei Salzburg, Austria. *Int J Syst Evol Microbiol*. 60:2694.

Sources

Grieshaber, S.S., N.A. Grieshaber, and T. Hackstadt. 2003. Chlamydia trachomatis uses host cell dynein to traffic to the microtubule-organizing center in a p50 dynamitin-independent process. *J Cell Sci*. 116:3793-3802.

Grimm, J.B., T. Klein, B.G. Kopek, G. Shtengel, H.F. Hess, M. Sauer, and L.D. Lavis. 2016. Synthesis of a Far-Red Photoactivatable Silicon-Containing Rhodamine for Super-Resolution Microscopy. *Angew Chem Int Ed Engl*. 55:1723-1727.

Griparic, L., T. Kanazawa, and A.M. van der Bliek. 2007. Regulation of the mitochondrial dynamin-like protein Opa1 by proteolytic cleavage. *J Cell Biol*. 178:757-764.

Grosch, S., S. Schiffmann, and G. Geisslinger. 2012. Chain length-specific properties of ceramides. *Prog Lipid Res*. 51:50-62.

Grumati, P., and I. Dikic. 2018. Ubiquitin signaling and autophagy. *J Biol Chem*. 293:5404-5413.

Guarani, V., C. Jardel, D. Chretien, A. Lombes, P. Benit, C. Labasse, E. Lacene, A. Bourillon, A. Imbard, J.F. Benoist, I. Dorboz, M. Gilleron, E.S. Goetzman, P. Gaignard, A. Slama, M. Elmaleh-Berges, N.B. Romero, P. Rustin, H. Ogier de Baulny, J.A. Paulo, J.W. Harper, and M. Schiff. 2016. QIL1 mutation causes MICOS disassembly and early onset fatal mitochondrial encephalopathy with liver disease. *Elife*. 5.

Guarani, V., E.M. McNeill, J.A. Paulo, E.L. Huttlin, F. Frohlich, S.P. Gygi, D. Van Vactor, and J.W. Harper. 2015. QIL1 is a novel mitochondrial protein required for MICOS complex stability and cristae morphology. *Elife*. 4.

Guillery, O., F. Malka, T. Landes, E. Guillou, C. Blackstone, A. Lombes, P. Belenguer, D. Arnoult, and M. Rojo. 2008. Metalloprotease-mediated OPA1 processing is modulated by the mitochondrial membrane potential. *Biol Cell*. 100:315-325.

Gustafsson, M.G. 2000. Surpassing the lateral resolution limit by a factor of two using structured illumination microscopy. *J Microsc*. 198:82-87.

Guy, R., J. Ward, H. Wand, A. Rumbold, L. Garton, B. Hengel, B. Silver, D. Taylor-Thomson, J. Knox, S. McGregor, A. Dyda, C. Fairley, L. Maher, B. Donovan, J. Kaldor, and S.I. Group. 2015. Coinfection with Chlamydia trachomatis, Neisseria gonorrhoeae and Trichomonas vaginalis: a cross-sectional analysis of positivity and risk factors in remote Australian Aboriginal communities. *Sex Transm Infect*. 91:201-206.

Hackenbrock, C.R. 1966. Ultrastructural bases for metabolically linked mechanical activity in mitochondria. I. Reversible ultrastructural changes with change in metabolic steady state in isolated liver mitochondria. *J Cell Biol*. 30:269-297.

Hackenbrock, C.R. 1968. Chemical and physical fixation of isolated mitochondria in low-energy and high-energy states. *Proc Natl Acad Sci U S A*. 61:598-605.

Hacker, G. 2014. The chlamydial protease CPAF: important or not, important for what? *Microbes Infect*. 16:367-370.

Hackstadt, T., D.D. Rockey, R.A. Heinzen, and M.A. Scidmore. 1996. Chlamydia trachomatis interrupts an exocytic pathway to acquire endogenously synthesized sphingomyelin in transit from the Golgi apparatus to the plasma membrane. *EMBO J*. 15:964-977.

Hackstadt, T., M.A. Scidmore, and D.D. Rockey. 1995. Lipid metabolism in Chlamydia trachomatis-infected cells: directed trafficking of Golgi-derived sphingolipids to the chlamydial inclusion. *Proc Natl Acad Sci U S A*. 92:4877-4881.

Hahn, A., K. Parey, M. Bublitz, D.J. Mills, V. Zickermann, J. Vonck, W. Kuhlbrandt, and T. Meier. 2016. Structure of a Complete ATP Synthase Dimer Reveals the Molecular Basis of Inner Mitochondrial Membrane Morphology. *Mol Cell*. 63:445-456.

Hahn, D.L., R.W. Dodge, and R. Golubjatnikov. 1991. Association of Chlamydia pneumoniae (strain TWAR) infection with wheezing, asthmatic bronchitis, and adult-onset asthma. *JAMA*. 266:225-230.

Halberstaedter, L. 1907. Ueber Zelleinschluesse parasitaerer Natur beim Trachom. *Arb K Gesundh Amt*. 26:44-47.

Hanada, K. 2005. Sphingolipids in infectious diseases. *Jpn J Infect Dis*. 58:131-148.

Sources

Hanada, K. 2010. Intracellular trafficking of ceramide by ceramide transfer protein. *Proc Jpn Acad Ser B Phys Biol Sci*. 86:426-437.

Hannun, Y.A., and L.M. Obeid. 2002. The Ceramide-centric universe of lipid-mediated cell regulation: stress encounters of the lipid kind. *J Biol Chem*. 277:25847-25850.

Harner, M., C. Korner, D. Walther, D. Mokranjac, J. Kaesmacher, U. Welsch, J. Griffith, M. Mann, F. Reggiori, and W. Neupert. 2011. The mitochondrial contact site complex, a determinant of mitochondrial architecture. *EMBO J*. 30:4356-4370.

Harner, M.E., A.K. Unger, W.J. Geerts, M. Mari, T. Izawa, M. Stenger, S. Geimer, F. Reggiori, B. Westermann, and W. Neupert. 2016. An evidence based hypothesis on the existence of two pathways of mitochondrial crista formation. *Elife*. 5.

Harrop, G.A., G.W. Rake, and M.F. Shaffer. 1940. A Group of Laboratory Infections Ascribed to Lymphogranuloma Venereum. *Trans Am Clin Climatol Assoc*. 56:154-159.

Harvald, E.B., A.S. Olsen, and N.J. Faergeman. 2015. Autophagy in the light of sphingolipid metabolism. *Apoptosis*. 20:658-670.

Harvey, H.A., W.E. Swords, and M.A. Apicella. 2001. The mimicry of human glycolipids and glycosphingolipids by the lipooligosaccharides of pathogenic neisseria and haemophilus. *J Autoimmun*. 16:257-262.

Hauck, C.R., H. Grassme, J. Bock, V. Jendrossek, K. Ferlinz, T.F. Meyer, and E. Gulbins. 2000. Acid sphingomyelinase is involved in CEACAM receptor-mediated phagocytosis of Neisseria gonorrhoeae. *FEBS Lett*. 478:260-266.

Heilemann, M., S. van de Linde, M. Schuttpelz, R. Kasper, B. Seefeldt, A. Mukherjee, P. Tinnefeld, and M. Sauer. 2008. Subdiffraction-resolution fluorescence imaging with conventional fluorescent probes. *Angew Chem Int Ed Engl*. 47:6172-6176.

Heintzmann, R., and T. Huser. 2017. Super-Resolution Structured Illumination Microscopy. *Chem Rev*. 117:13890-13908.

Hell, K. 2008. The Erv1-Mia40 disulfide relay system in the intermembrane space of mitochondria. *Biochim Biophys Acta*. 1783:601-609.

Hell, S.W. 2007. Far-field optical nanoscopy. *Science*. 316:1153-1158.

Herweg, J.A., V. Pons, D. Becher, M. Hecker, G. Krohne, J. Barbier, H. Berger, T. Rudel, and A. Mehlitz. 2016. Proteomic analysis of the Simkania-containing vacuole: the central role of retrograde transport. *Mol Microbiol*. 99:151-171.

Hesse, L., J. Bostock, S. Dementin, D. Blanot, D. Mengin-Lecreulx, and I. Chopra. 2003. Functional and biochemical analysis of Chlamydia trachomatis MurC, an enzyme displaying UDP-N-acetylmuramate:amino acid ligase activity. *J Bacteriol*. 185:6507-6512.

Hessenberger, M., R.M. Zerbes, H. Rampelt, S. Kunz, A.H. Xavier, B. Purfurst, H. Lilie, N. Pfanner, M. van der Laan, and O. Daumke. 2017. Regulated membrane remodeling by Mic60 controls formation of mitochondrial crista junctions. *Nat Commun*. 8:15258.

Heuer, D., A. Rejman Lipinski, N. Machuy, A. Karlas, A. Wehrens, F. Siedler, V. Brinkmann, and T.F. Meyer. 2009. Chlamydia causes fragmentation of the Golgi compartment to ensure reproduction. *Nature*. 457:731-735.

Hoare, A., P. Timms, P.M. Bavoil, and D.P. Wilson. 2008. Spatial constraints within the chlamydial host cell inclusion predict interrupted development and persistence. *BMC Microbiol*. 8:5.

Hogan, S., N.T. Stevens, H. Humphreys, J.P. O'Gara, and E. O'Neill. 2015. Current and future approaches to the prevention and treatment of staphylococcal medical device-related infections. *Curr Pharm Des*. 21:100-113.

Hohr, A.I.C., C. Lindau, C. Wirth, J. Qiu, D.A. Stroud, S. Kutik, B. Guiard, C. Hunte, T. Becker, N. Pfanner, and N. Wiedemann. 2018. Membrane protein insertion through a mitochondrial beta-barrel gate. *Science*. 359.

Hoppins, S., S.R. Collins, A. Cassidy-Stone, E. Hummel, R.M. Devay, L.L. Lackner, B. Westermann, M. Schuldiner, J.S. Weissman, and J. Nunnari. 2011. A mitochondrial-focused genetic interaction map reveals a scaffold-like complex required for inner membrane organization in mitochondria. *J Cell Biol*. 195:323-340.

Sources

Hoppins, S., L. Lackner, and J. Nunnari. 2007. The machines that divide and fuse mitochondria. *Annu Rev Biochem*. 76:751-780.

Huang, F.C. 2017. The Role of Sphingolipids on Innate Immunity to Intestinal Salmonella Infection. *Int J Mol Sci*. 18.

Hulett, J.M., F. Lueder, N.C. Chan, A.J. Perry, P. Wolynec, V.A. Likic, P.R. Gooley, and T. Lithgow. 2008. The transmembrane segment of Tom20 is recognized by Mim1 for docking to the mitochondrial TOM complex. *J Mol Biol*. 376:694-704.

Huynen, M.A., M. Muhlmeister, K. Gotthardt, S. Guerrero-Castillo, and U. Brandt. 2016. Evolution and structural organization of the mitochondrial contact site (MICOS) complex and the mitochondrial intermembrane space bridging (MIB) complex. *Biochim Biophys Acta*. 1863:91-101.

Hybiske, K., and R.S. Stephens. 2007. Mechanisms of host cell exit by the intracellular bacterium Chlamydia. *Proc Natl Acad Sci U S A*. 104:11430-11435.

Ieva, R., S.G. Schrempp, L. Opalinski, F. Wollweber, P. Hoss, A.K. Heisswolf, M. Gebert, Y. Zhang, B. Guiard, S. Rospert, T. Becker, A. Chacinska, N. Pfanner, and M. van der Laan. 2014. Mgr2 functions as lateral gatekeeper for preprotein sorting in the mitochondrial inner membrane. *Mol Cell*. 56:641-652.

Ingerman, E., E.M. Perkins, M. Marino, J.A. Mears, J.M. McCaffery, J.E. Hinshaw, and J. Nunnari. 2005. Dnm1 forms spirals that are structurally tailored to fit mitochondria. *J Cell Biol*. 170:1021-1027.

Ishihara, N., Y. Fujita, T. Oka, and K. Mihara. 2006. Regulation of mitochondrial morphology through proteolytic cleavage of OPA1. *EMBO J*. 25:2966-2977.

Jablonski, A. 1935. Ueber den Mechanismus der Photolumineszenz von Farbstoffphosphoren. *Zeitschrift für Physik*. 94:38–46.

Jakobs, S., and C.A. Wurm. 2014. Super-resolution microscopy of mitochondria. *Curr Opin Chem Biol*. 20:9-15.

Jezek, J., K.F. Cooper, and R. Strich. 2018. Reactive Oxygen Species and Mitochondrial Dynamics: The Yin and Yang of Mitochondrial Dysfunction and Cancer Progression. *Antioxidants (Basel)*. 7.

John, G.B., Y. Shang, L. Li, C. Renken, C.A. Mannella, J.M. Selker, L. Rangell, M.J. Bennett, and J. Zha. 2005. The mitochondrial inner membrane protein mitofilin controls cristae morphology. *Mol Biol Cell*. 16:1543-1554.

Johnson, K.A., J.K. Lee, A.L. Chen, M. Tan, and C. Sutterlin. 2015. Induction and inhibition of CPAF activity during analysis of Chlamydia-infected cells. *Pathog Dis*. 73:1-8.

Jores, T., A. Klinger, L.E. Gross, S. Kawano, N. Flinner, E. Duchardt-Ferner, J. Wohnert, H. Kalbacher, T. Endo, E. Schleiff, and D. Rapaport. 2016. Characterization of the targeting signal in mitochondrial beta-barrel proteins. *Nat Commun*. 7:12036.

Joshi, R., B. Khandelwal, D. Joshi, and O.P. Gupta. 2013. Chlamydophila pneumoniae infection and cardiovascular disease. *N Am J Med Sci*. 5:169-181.

Josse, J., F. Velard, and S.C. Gangloff. 2015. Staphylococcus aureus vs. Osteoblast: Relationship and Consequences in Osteomyelitis. *Front Cell Infect Microbiol*. 5:85.

Kahane, S., B. Dvoskin, and M.G. Friedman. 2008. The role of monocyte/macrophages as vehicles of dissemination of Simkania negevensis: an in vitro simulation model. *FEMS Immunol Med Microbiol*. 52:219-227.

Kahane, S., B. Dvoskin, M. Mathias, and M.G. Friedman. 2001. Infection of Acanthamoeba polyphaga with Simkania negevensis and S. negevensis survival within amoebal cysts. *Appl Environ Microbiol*. 67:4789-4795.

Kahane, S., K.D. Everett, N. Kimmel, and M.G. Friedman. 1999. Simkania negevensis strain ZT: growth, antigenic and genome characteristics. *Int J Syst Bacteriol*. 49 Pt 2:815-820.

Kahane, S., D. Fruchter, B. Dvoskin, and M.G. Friedman. 2007. Versatility of Simkania negevensis infection in vitro and induction of host cell inflammatory cytokine response. *J Infect*. 55:e13-21.

Kahane, S., R. Gonen, C. Sayada, J. Elion, and M.G. Friedman. 1993. Description and partial characterization of a new Chlamydia-like microorganism. *FEMS Microbiol Lett*. 109:329-333.

Sources

Kahane, S., D. Greenberg, M.G. Friedman, H. Haikin, and R. Dagan. 1998. High prevalence of "Simkania Z," a novel Chlamydia-like bacterium, in infants with acute bronchiolitis. *J Infect Dis*. 177:1425-1429.

Kahane, S., N. Kimmel, and M.G. Friedman. 2002. The growth cycle of Simkania negevensis. *Microbiology (Reading)*. 148:735-742.

Karagiannis, E.D., J.S. Kang, T.W. Shin, A. Emenari, S. Asano, L. Lin, E.K. Costa, A.H. Marblestone, N. Kasthuri, and E.S. Boyden. 2019. Expansion Microscopy of Lipid Membranes. *bioRxiv*:829903.

Kavaliauskiene, S., A.B. Dyve Lingelem, T. Skotland, and K. Sandvig. 2017. Protection against Shiga Toxins. *Toxins (Basel)*. 9.

Klein, A., L. Israel, S.W. Lackey, F.E. Nargang, A. Imhof, W. Baumeister, W. Neupert, and D.R. Thomas. 2012. Characterization of the insertase for beta-barrel proteins of the outer mitochondrial membrane. *J Cell Biol*. 199:599-611.

Knittler, M.R., and K. Sachse. 2015. Chlamydia psittaci: update on an underestimated zoonotic agent. *Pathog Dis*. 73:1-15.

Koch-Edelmann, S., S. Banhart, E.M. Saied, L. Rose, L. Aeberhard, M. Laue, J. Doellinger, C. Arenz, and D. Heuer. 2017. The cellular ceramide transport protein CERT promotes Chlamydia psittaci infection and controls bacterial sphingolipid uptake. *Cell Microbiol*. 19.

Koch, J.R., and F.X. Schmid. 2014. Mia40 combines thiol oxidase and disulfide isomerase activity to efficiently catalyze oxidative folding in mitochondria. *J Mol Biol*. 426:4087-4098.

Koehler, C.M., S. Merchant, W. Oppliger, K. Schmid, E. Jarosch, L. Dolfini, T. Junne, G. Schatz, and K. Tokatlidis. 1998. Tim9p, an essential partner subunit of Tim10p for the import of mitochondrial carrier proteins. *EMBO J*. 17:6477-6486.

Kolter, T., and K. Sandhoff. 2005. Principles of lysosomal membrane digestion: stimulation of sphingolipid degradation by sphingolipid activator proteins and anionic lysosomal lipids. *Annu Rev Cell Dev Biol*. 21:81-103.

Kondadi, A.K., R. Anand, S. Hansch, J. Urbach, T. Zobel, D.M. Wolf, M. Segawa, M. Liesa, O.S. Shirihai, S. Weidtkamp-Peters, and A.S. Reichert. 2020. Cristae undergo continuous cycles of membrane remodelling in a MICOS-dependent manner. *EMBO Rep*. 21:e49776.

Kondadi, A.K., R. Anand, and A.S. Reichert. 2019. Functional Interplay between Cristae Biogenesis, Mitochondrial Dynamics and Mitochondrial DNA Integrity. *Int J Mol Sci*. 20.

Koob, S., M. Barrera, R. Anand, and A.S. Reichert. 2015. The non-glycosylated isoform of MIC26 is a constituent of the mammalian MICOS complex and promotes formation of crista junctions. *Biochim Biophys Acta*. 1853:1551-1563.

Korner, C., M. Barrera, J. Dukanovic, K. Eydt, M. Harner, R. Rabl, F. Vogel, D. Rapaport, W. Neupert, and A.S. Reichert. 2012. The C-terminal domain of Fcj1 is required for formation of crista junctions and interacts with the TOB/SAM complex in mitochondria. *Mol Biol Cell*. 23:2143-2155.

Kozjak-Pavlovic, V. 2017. The MICOS complex of human mitochondria. *Cell Tissue Res*. 367:83-93.

Kozjak-Pavlovic, V., K. Ross, N. Benlasfer, S. Kimmig, A. Karlas, and T. Rudel. 2007. Conserved roles of Sam50 and metaxins in VDAC biogenesis. *EMBO Rep*. 8:576-582.

Kozjak, V., N. Wiedemann, D. Milenkovic, C. Lohaus, H.E. Meyer, B. Guiard, C. Meisinger, and N. Pfanner. 2003. An essential role of Sam50 in the protein sorting and assembly machinery of the mitochondrial outer membrane. *J Biol Chem*. 278:48520-48523.

Kruger, V., T. Becker, L. Becker, M. Montilla-Martinez, L. Ellenrieder, F.N. Vogtle, H.E. Meyer, M.T. Ryan, N. Wiedemann, B. Warscheid, N. Pfanner, R. Wagner, and C. Meisinger. 2017. Identification of new channels by systematic analysis of the mitochondrial outer membrane. *J Cell Biol*. 216:3485-3495.

Ku, T., J. Swaney, J.Y. Park, A. Albanese, E. Murray, J.H. Cho, Y.G. Park, V. Mangena, J. Chen, and K. Chung. 2016. Multiplexed and scalable super-resolution imaging of three-dimensional protein localization in size-adjustable tissues. *Nat Biotechnol*. 34:973-981.

Kuhlewein, C., C. Rechner, T.F. Meyer, and T. Rudel. 2006. Low-phosphate-dependent invasion resembles a general way for Neisseria gonorrhoeae to enter host cells. *Infect Immun*. 74:4266-4273.

Sources

Kulawiak, B., J. Hopker, M. Gebert, B. Guiard, N. Wiedemann, and N. Gebert. 2013. The mitochondrial protein import machinery has multiple connections to the respiratory chain. *Biochim Biophys Acta*. 1827:612-626.

Kunz, T.C. 2017. Modulation of mitochondrial function by light-inducible protein bPAC and *Chlamydia* infection. *Master thesis*.

Kunz, T.C., R. Gotz, S. Gao, M. Sauer, and V. Kozjak-Pavlovic. 2020. Using Expansion Microscopy to Visualize and Characterize the Morphology of Mitochondrial Cristae. *Front Cell Dev Biol*. 8:617.

Kunz, T.C., R. Gotz, M. Sauer, and T. Rudel. 2019. Detection of Chlamydia Developmental Forms and Secreted Effectors by Expansion Microscopy. *Front Cell Infect Microbiol*. 9:276.

Kunz, T.C., and V. Kozjak-Pavlovic. 2019. Diverse Facets of Sphingolipid Involvement in Bacterial Infections. *Front Cell Dev Biol*. 7:203.

Kupka, S., M. Reichert, P. Draber, and H. Walczak. 2016. Formation and removal of poly-ubiquitin chains in the regulation of tumor necrosis factor-induced gene activation and cell death. *FEBS J*. 283:2626-2639.

Kurihara, Y., R. Itoh, A. Shimizu, N.F. Walenna, B. Chou, K. Ishii, T. Soejima, A. Fujikane, and K. Hiromatsu. 2019. Chlamydia trachomatis targets mitochondrial dynamics to promote intracellular survival and proliferation. *Cell Microbiol*. 21:e12962.

Kuszak, A.J., D. Jacobs, P.A. Gurnev, T. Shiota, J.M. Louis, T. Lithgow, S.M. Bezrukov, T.K. Rostovtseva, and S.K. Buchanan. 2015. Evidence of Distinct Channel Conformations and Substrate Binding Affinities for the Mitochondrial Outer Membrane Protein Translocase Pore Tom40. *J Biol Chem*. 290:26204-26217.

Kutik, S., D. Stojanovski, L. Becker, T. Becker, M. Meinecke, V. Kruger, C. Prinz, C. Meisinger, B. Guiard, R. Wagner, N. Pfanner, and N. Wiedemann. 2008. Dissecting membrane insertion of mitochondrial beta-barrel proteins. *Cell*. 132:1011-1024.

Laux, C., A. Peschel, and B. Krismer. 2019. Staphylococcus aureus Colonization of the Human Nose and Interaction with Other Microbiome Members. *Microbiol Spectr*. 7.

Le Negrate, G., A. Krieg, B. Faustin, M. Loeffler, A. Godzik, S. Krajewski, and J.C. Reed. 2008. ChlaDub1 of Chlamydia trachomatis suppresses NF-kappaB activation and inhibits IkappaBalpha ubiquitination and degradation. *Cell Microbiol*. 10:1879-1892.

Lee, J.K., G.A. Enciso, D. Boassa, C.N. Chander, T.H. Lou, S.S. Pairawan, M.C. Guo, F.Y.M. Wan, M.H. Ellisman, C. Sutterlin, and M. Tan. 2018. Replication-dependent size reduction precedes differentiation in Chlamydia trachomatis. *Nat Commun*. 9:45.

Lee, M.H., J. Byun, M. Jung, J.J. Yang, K.H. Park, S.Y. Moon, H.J. Lee, and M.S. Lee. 2015. Disseminated gonococcal infection presenting as bacteremia and liver abscesses in a healthy adult. *Infect Chemother*. 47:60-63.

Li, H., Y. Ruan, K. Zhang, F. Jian, C. Hu, L. Miao, L. Gong, L. Sun, X. Zhang, S. Chen, H. Chen, D. Liu, and Z. Song. 2016. Mic60/Mitofilin determines MICOS assembly essential for mitochondrial dynamics and mtDNA nucleoid organization. *Cell Death Differ*. 23:380-392.

Lieberman, D., S. Kahane, D. Lieberman, and M.G. Friedman. 1997. Pneumonia with serological evidence of acute infection with the Chlamydia-like microorganism "Z". *Am J Respir Crit Care Med*. 156:578-582.

Liechti, G.W., E. Kuru, E. Hall, A. Kalinda, Y.V. Brun, M. VanNieuwenhze, and A.T. Maurelli. 2014. A new metabolic cell-wall labelling method reveals peptidoglycan in Chlamydia trachomatis. *Nature*. 506:507-510.

Lim, Y., A.L. Shiver, M. Khariton, K.M. Lane, K.M. Ng, S.R. Bray, J. Qin, K.C. Huang, and B. Wang. 2019. Mechanically resolved imaging of bacteria using expansion microscopy. *PLoS Biol*. 17:e3000268.

Lohret, T.A., R.E. Jensen, and K.W. Kinnally. 1997. Tim23, a protein import component of the mitochondrial inner membrane, is required for normal activity of the multiple conductance channel, MCC. *J Cell Biol*. 137:377-386.

Sources

Lopez de Armentia, M.M., M.C. Gauron, and M.I. Colombo. 2017. Staphylococcus aureus Alpha-Toxin Induces the Formation of Dynamic Tubules Labeled with LC3 within Host Cells in a Rab7 and Rab1b-Dependent Manner. *Front Cell Infect Microbiol*. 7:431.

Los, G.V., L.P. Encell, M.G. McDougall, D.D. Hartzell, N. Karassina, C. Zimprich, M.G. Wood, R. Learish, R.F. Ohana, M. Urh, D. Simpson, J. Mendez, K. Zimmerman, P. Otto, G. Vidugiris, J. Zhu, A. Darzins, D.H. Klaubert, R.F. Bulleit, and K.V. Wood. 2008. HaloTag: a novel protein labeling technology for cell imaging and protein analysis. *ACS Chem Biol*. 3:373-382.

Loson, O.C., Z. Song, H. Chen, and D.C. Chan. 2013. Fis1, Mff, MiD49, and MiD51 mediate Drp1 recruitment in mitochondrial fission. *Mol Biol Cell*. 24:659-667.

Mannella, C.A., M. Marko, and K. Buttle. 1997. Reconsidering mitochondrial structure: new views of an old organelle. *Trends Biochem Sci*. 22:37-38.

Mannella, C.A., D.R. Pfeiffer, P.C. Bradshaw, Moraru, II, B. Slepchenko, L.M. Loew, C.E. Hsieh, K. Buttle, and M. Marko. 2001. Topology of the mitochondrial inner membrane: dynamics and bioenergetic implications. *IUBMB Life*. 52:93-100.

McCoy, A.J., N.E. Adams, A.O. Hudson, C. Gilvarg, T. Leustek, and A.T. Maurelli. 2006. L,L-diaminopimelate aminotransferase, a trans-kingdom enzyme shared by Chlamydia and plants for synthesis of diaminopimelate/lysine. *Proc Natl Acad Sci U S A*. 103:17909-17914.

McCoy, A.J., and A.T. Maurelli. 2005. Characterization of Chlamydia MurC-Ddl, a fusion protein exhibiting D-alanyl-D-alanine ligase activity involved in peptidoglycan synthesis and D-cycloserine sensitivity. *Mol Microbiol*. 57:41-52.

McCoy, A.J., R.C. Sandlin, and A.T. Maurelli. 2003. In vitro and in vivo functional activity of Chlamydia MurA, a UDP-N-acetylglucosamine enolpyruvyl transferase involved in peptidoglycan synthesis and fosfomycin resistance. *J Bacteriol*. 185:1218-1228.

Mears, J.A., L.L. Lackner, S. Fang, E. Ingerman, J. Nunnari, and J.E. Hinshaw. 2011. Conformational changes in Dnm1 support a contractile mechanism for mitochondrial fission. *Nat Struct Mol Biol*. 18:20-26.

Mehlitz, A., K. Karunakaran, J.A. Herweg, G. Krohne, S. van de Linde, E. Rieck, M. Sauer, and T. Rudel. 2014. The chlamydial organism Simkania negevensis forms ER vacuole contact sites and inhibits ER-stress. *Cell Microbiol*. 16:1224-1243.

Meijer, C.J., J.J. Calame, E.J. de Windt, E.K. Risse, O.P. Bleker, P. Kenemans, W.G. Quint, and M.J. Meddens. 1989. Prevalence of Chlamydia trachomatis infection in a population of asymptomatic women in a screening program for cervical cancer. *Eur J Clin Microbiol Infect Dis*. 8:127-130.

Meisinger, C., A. Sickmann, and N. Pfanner. 2008. The mitochondrial proteome: from inventory to function. *Cell*. 134:22-24.

Melin, J., C. Schulz, L. Wrobel, O. Bernhard, A. Chacinska, O. Jahn, B. Schmidt, and P. Rehling. 2014. Presequence recognition by the tom40 channel contributes to precursor translocation into the mitochondrial matrix. *Mol Cell Biol*. 34:3473-3485.

Menaldino, D.S., A. Bushnev, A. Sun, D.C. Liotta, H. Symolon, K. Desai, D.L. Dillehay, Q. Peng, E. Wang, J. Allegood, S. Trotman-Pruett, M.C. Sullards, and A.H. Merrill, Jr. 2003. Sphingoid bases and de novo ceramide synthesis: enzymes involved, pharmacology and mechanisms of action. *Pharmacol Res*. 47:373-381.

Mencarelli, C., and P. Martinez-Martinez. 2013. Ceramide function in the brain: when a slight tilt is enough. *Cell Mol Life Sci*. 70:181-203.

Mestre, M.B., and M.I. Colombo. 2012. Staphylococcus aureus promotes autophagy by decreasing intracellular cAMP levels. *Autophagy*. 8:1865-1867.

Mestre, M.B., C.M. Fader, C. Sola, and M.I. Colombo. 2010. Alpha-hemolysin is required for the activation of the autophagic pathway in Staphylococcus aureus-infected cells. *Autophagy*. 6:110-125.

Michie, M.S., R. Gotz, C. Franke, M. Bowler, N. Kumari, V. Magidson, M. Levitus, J. Loncarek, M. Sauer, and M.J. Schnermann. 2017. Cyanine Conformational Restraint in the Far-Red Range. *J Am Chem Soc*. 139:12406-12409.

Sources

Milenkovic, D., and N.G. Larsson. 2015. Mic10 Oligomerization Pinches off Mitochondrial Cristae. *Cell Metab*. 21:660-661.

Mital, J., and T. Hackstadt. 2011. Role for the SRC family kinase Fyn in sphingolipid acquisition by chlamydiae. *Infect Immun*. 79:4559-4568.

Monteiro, J.M., G. Covas, D. Rausch, S.R. Filipe, T. Schneider, H.G. Sahl, and M.G. Pinho. 2019. The pentaglycine bridges of Staphylococcus aureus peptidoglycan are essential for cell integrity. *Sci Rep*. 9:5010.

Moore, E.R., D.J. Mead, C.A. Dooley, J. Sager, and T. Hackstadt. 2011. The trans-Golgi SNARE syntaxin 6 is recruited to the chlamydial inclusion membrane. *Microbiology (Reading)*. 157:830-838.

Moulder, J.W. 1966. The relation of the psittacosis group (Chlamydiae) to bacteria and viruses. *Annu Rev Microbiol*. 20:107-130.

Moulder, J.W., D.L. Novosel, and J.E. Officer. 1963. Inhibition of the Growth of Agents of the Psittacosis Group by D-Cycloserine and Its Specific Reversal by D-Alanine. *J Bacteriol*. 85:707-711.

Ness, R.B., M.T. Goodman, C. Shen, and R.C. Brunham. 2003. Serologic evidence of past infection with Chlamydia trachomatis, in relation to ovarian cancer. *J Infect Dis*. 187:1147-1152.

Newton, J., S. Lima, M. Maceyka, and S. Spiegel. 2015. Revisiting the sphingolipid rheostat: Evolving concepts in cancer therapy. *Exp Cell Res*. 333:195-200.

Nguyen, B.D., D. Cunningham, X. Liang, X. Chen, E.J. Toone, C.R. Raetz, P. Zhou, and R.H. Valdivia. 2011. Lipooligosaccharide is required for the generation of infectious elementary bodies in Chlamydia trachomatis. *Proc Natl Acad Sci U S A*. 108:10284-10289.

Nicastro, D., A.S. Frangakis, D. Typke, and W. Baumeister. 2000. Cryo-electron tomography of neurospora mitochondria. *J Struct Biol*. 129:48-56.

Okamoto, H., A. Miyagawa, T. Shiota, Y. Tamura, and T. Endo. 2014. Intramolecular disulfide bond of Tim22 protein maintains integrity of the TIM22 complex in the mitochondrial inner membrane. *J Biol Chem*. 289:4827-4838.

Okino, N., and M. Ito. 2007. Ceramidase enhances phospholipase C-induced hemolysis by Pseudomonas aeruginosa. *J Biol Chem*. 282:6021-6030.

Okino, N., M. Tani, S. Imayama, and M. Ito. 1998. Purification and characterization of a novel ceramidase from Pseudomonas aeruginosa. *J Biol Chem*. 273:14368-14373.

Olichon, A., L. Baricault, N. Gas, E. Guillou, A. Valette, P. Belenguer, and G. Lenaers. 2003. Loss of OPA1 perturbates the mitochondrial inner membrane structure and integrity, leading to cytochrome c release and apoptosis. *J Biol Chem*. 278:7743-7746.

Omsland, A., J. Sager, V. Nair, D.E. Sturdevant, and T. Hackstadt. 2012. Developmental stage-specific metabolic and transcriptional activity of Chlamydia trachomatis in an axenic medium. *Proc Natl Acad Sci U S A*. 109:19781-19785.

Ostermann, J., A.L. Horwich, W. Neupert, and F.U. Hartl. 1989. Protein folding in mitochondria requires complex formation with hsp60 and ATP hydrolysis. *Nature*. 341:125-130.

Ott, C., E. Dorsch, M. Fraunholz, S. Straub, and V. Kozjak-Pavlovic. 2015. Detailed analysis of the human mitochondrial contact site complex indicate a hierarchy of subunits. *PLoS One*. 10:e0120213.

Ott, C., K. Ross, S. Straub, B. Thiede, M. Gotz, C. Goosmann, M. Krischke, M.J. Mueller, G. Krohne, T. Rudel, and V. Kozjak-Pavlovic. 2012. Sam50 functions in mitochondrial intermembrane space bridging and biogenesis of respiratory complexes. *Mol Cell Biol*. 32:1173-1188.

Page, L.A. 1968. Proposal for the recognition of two species in the genus Chlamydia. *International Journal of Systematic and Evolutionary Microbiology*:51-66.

Pal, R.R., A.K. Baidya, G. Mamou, S. Bhattacharya, Y. Socol, S. Kobi, N. Katsowich, S. Ben-Yehuda, and I. Rosenshine. 2019. Pathogenic E. coli Extracts Nutrients from Infected Host Cells Utilizing Injectisome Components. *Cell*. 177:683-696 e618.

Papic, D., K. Krumpe, J. Dukanovic, K.S. Dimmer, and D. Rapaport. 2011. Multispan mitochondrial outer membrane protein Ugo1 follows a unique Mim1-dependent import pathway. *J Cell Biol*. 194:397-405.

Sources

Park, J.W., S.Y. Lee, J.Y. Yang, H.W. Rho, B.H. Park, S.N. Lim, J.S. Kim, and H.R. Kim. 1997. Effect of carbonyl cyanide m-chlorophenylhydrazone (CCCP) on the dimerization of lipoprotein lipase. *Biochim Biophys Acta*. 1344:132-138.

Paschen, S.A., T. Waizenegger, T. Stan, M. Preuss, M. Cyrklaff, K. Hell, D. Rapaport, and W. Neupert. 2003. Evolutionary conservation of biogenesis of beta-barrel membrane proteins. *Nature*. 426:862-866.

Patin, D., J. Bostock, D. Blanot, D. Mengin-Lecreulx, and I. Chopra. 2009. Functional and biochemical analysis of the Chlamydia trachomatis ligase MurE. *J Bacteriol*. 191:7430-7435.

Patin, D., J. Bostock, I. Chopra, D. Mengin-Lecreulx, and D. Blanot. 2012. Biochemical characterisation of the chlamydial MurF ligase, and possible sequence of the chlamydial peptidoglycan pentapeptide stem. *Arch Microbiol*. 194:505-512.

Paumard, P., J. Vaillier, B. Coulary, J. Schaeffer, V. Soubannier, D.M. Mueller, D. Brethes, J.P. di Rago, and J. Velours. 2002. The ATP synthase is involved in generating mitochondrial cristae morphology. *EMBO J*. 21:221-230.

Perkins, G.A., M.H. Ellisman, and D.A. Fox. 2003. Three-dimensional analysis of mouse rod and cone mitochondrial cristae architecture: bioenergetic and functional implications. *Mol Vis*. 9:60-73.

Perry, D.K. 2002. Serine palmitoyltransferase: role in apoptotic de novo ceramide synthesis and other stress responses. *Biochim Biophys Acta*. 1585:146-152.

Peters, S., J. Schlegel, J. Becam, E. Avota, M. Sauer, and A. Schubert-Unkmeir. 2019. Neisseria meningitidis Type IV Pili Trigger Ca(2+)-Dependent Lysosomal Trafficking of the Acid Sphingomyelinase To Enhance Surface Ceramide Levels. *Infect Immun*. 87.

Pewzner-Jung, Y., S. Tavakoli Tabazavareh, H. Grassme, K.A. Becker, L. Japtok, J. Steinmann, T. Joseph, S. Lang, B. Tuemmler, E.H. Schuchman, A.B. Lentsch, B. Kleuser, M.J. Edwards, A.H. Futerman, and E. Gulbins. 2014. Sphingoid long chain bases prevent lung infection by Pseudomonas aeruginosa. *EMBO Mol Med*. 6:1205-1214.

Pfanner, N., B. Warscheid, and N. Wiedemann. 2019. Mitochondrial proteins: from biogenesis to functional networks. *Nat Rev Mol Cell Biol*. 20:267-284.

Pilhofer, M., K. Aistleitner, J. Biboy, J. Gray, E. Kuru, E. Hall, Y.V. Brun, M.S. VanNieuwenhze, W. Vollmer, M. Horn, and G.J. Jensen. 2013. Discovery of chlamydial peptidoglycan reveals bacteria with murein sacculi but without FtsZ. *Nat Commun*. 4:2856.

Pinero-Martos, E., B. Ortega-Vila, J. Pol-Fuster, E. Cisneros-Barroso, L. Ruiz-Guerra, A. Medina-Dols, D. Heine-Suner, J. Llado, G. Olmos, and C. Vives-Bauza. 2016. Disrupted in schizophrenia 1 (DISC1) is a constituent of the mammalian mitochondrial contact site and cristae organizing system (MICOS) complex, and is essential for oxidative phosphorylation. *Hum Mol Genet*. 25:4157-4169.

Popov-Celeketic, J., T. Waizenegger, and D. Rapaport. 2008. Mim1 functions in an oligomeric form to facilitate the integration of Tom20 into the mitochondrial outer membrane. *J Mol Biol*. 376:671-680.

Prajsnar, T.K., J.J. Serba, B.M. Dekker, J.F. Gibson, S. Masud, A. Fleming, S.A. Johnston, S.A. Renshaw, and A.H. Meijer. 2020. The autophagic response to Staphylococcus aureus provides an intracellular niche in neutrophils. *Autophagy*:1-15.

Pruneda, J.N., R.J. Bastidas, E. Bertsoulaki, K.N. Swatek, B. Santhanam, M.J. Clague, R.H. Valdivia, S. Urbe, and D. Komander. 2018. A Chlamydia effector combining deubiquitination and acetylation activities induces Golgi fragmentation. *Nat Microbiol*. 3:1377-1384.

Quintana-Cabrera, R., C. Quirin, C. Glytsou, M. Corrado, A. Urbani, A. Pellattiero, E. Calvo, J. Vazquez, J.A. Enriquez, C. Gerle, M.E. Soriano, P. Bernardi, and L. Scorrano. 2018. The cristae modulator Optic atrophy 1 requires mitochondrial ATP synthase oligomers to safeguard mitochondrial function. *Nat Commun*. 9:3399.

Rabl, R., V. Soubannier, R. Scholz, F. Vogel, N. Mendl, A. Vasiljev-Neumeyer, C. Korner, R. Jagasia, T. Keil, W. Baumeister, M. Cyrklaff, W. Neupert, and A.S. Reichert. 2009. Formation of cristae and crista junctions in mitochondria depends on antagonism between Fcj1 and Su e/g. *J Cell Biol*. 185:1047-1063.

Sources

Ragland, S.A., and A.K. Criss. 2017. From bacterial killing to immune modulation: Recent insights into the functions of lysozyme. *PLoS Pathog*. 13:e1006512.

Rajeeve, K., S. Das, B.K. Prusty, and T. Rudel. 2018. Chlamydia trachomatis paralyses neutrophils to evade the host innate immune response. *Nat Microbiol*. 3:824-835.

Rampelt, H., M. Bohnert, R.M. Zerbes, S.E. Horvath, B. Warscheid, N. Pfanner, and M. van der Laan. 2017. Mic10, a Core Subunit of the Mitochondrial Contact Site and Cristae Organizing System, Interacts with the Dimeric F1Fo-ATP Synthase. *J Mol Biol*. 429:1162-1170.

Raulston, J.E. 1997. Response of Chlamydia trachomatis serovar E to iron restriction in vitro and evidence for iron-regulated chlamydial proteins. *Infect Immun*. 65:4539-4547.

Rayleigh, L. 1903. On the Theory of Optical Images, with special reference to the Microscope. *Journal of the Royal Microscopical Society*. 23:474-482.

Reinders, J., R.P. Zahedi, N. Pfanner, C. Meisinger, and A. Sickmann. 2006. Toward the complete yeast mitochondrial proteome: multidimensional separation techniques for mitochondrial proteomics. *J Proteome Res*. 5:1543-1554.

Reinicke, B., P. Blumel, and P. Giesbrecht. 1983. Reduced degradability by lysozyme of staphylococcal cell walls after chloramphenicol treatment. *Arch Microbiol*. 135:120-124.

Revelo, N.H., D. Kamin, S. Truckenbrodt, A.B. Wong, K. Reuter-Jessen, E. Reisinger, T. Moser, and S.O. Rizzoli. 2014. A new probe for super-resolution imaging of membranes elucidates trafficking pathways. *J Cell Biol*. 205:591-606.

Riboni, L., P. Viani, R. Bassi, A. Prinetti, and G. Tettamanti. 1997. The role of sphingolipids in the process of signal transduction. *Prog Lipid Res*. 36:153-195.

Rolando, M., P. Escoll, T. Nora, J. Botti, V. Boitez, C. Bedia, C. Daniels, G. Abraham, P.J. Stogios, T. Skarina, C. Christophe, D. Dervins-Ravault, C. Cazalet, H. Hilbi, T.W. Rupasinghe, D. Tull, M.J. McConville, S.Y. Ong, E.L. Hartland, P. Codogno, T. Levade, T. Naderer, A. Savchenko, and C. Buchrieser. 2016. Legionella pneumophila S1P-lyase targets host sphingolipid metabolism and restrains autophagy. *Proc Natl Acad Sci U S A*. 113:1901-1906.

Rudel, T., O. Kepp, and V. Kozjak-Pavlovic. 2010. Interactions between bacterial pathogens and mitochondrial cell death pathways. *Nat Rev Microbiol*. 8:693-705.

Sachse, K., P.M. Bavoil, B. Kaltenboeck, R.S. Stephens, C.C. Kuo, R. Rossello-Mora, and M. Horn. 2015. Emendation of the family Chlamydiaceae: proposal of a single genus, Chlamydia, to include all currently recognized species. *Syst Appl Microbiol*. 38:99-103.

Salvador, V.B., B. Chapagain, A. Joshi, and D.J. Brennessel. 2017. Clinical Risk Factors for Infective Endocarditis in Staphylococcus aureus Bacteremia. *Tex Heart Inst J*. 44:10-15.

Sauer, L., K.M. Andersen, C. Dysli, M.S. Zinkernagel, P.S. Bernstein, and M. Hammer. 2018. Review of clinical approaches in fluorescence lifetime imaging ophthalmoscopy. *J Biomed Opt*. 23:1-20.

Schachter, J., G. Causse, and M.L. Tarizzo. 1976. Chlamydiae as agents of sexually transmitted diseases. *Bull World Health Organ*. 54:245-254.

Schermelleh, L., A. Ferrand, T. Huser, C. Eggeling, M. Sauer, O. Biehlmaier, and G.P.C. Drummen. 2019. Super-resolution microscopy demystified. *Nat Cell Biol*. 21:72-84.

Schielke, S., M. Frosch, and O. Kurzai. 2010. Virulence determinants involved in differential host niche adaptation of Neisseria meningitidis and Neisseria gonorrhoeae. *Med Microbiol Immunol*. 199:185-196.

Schindelin, J., I. Arganda-Carreras, E. Frise, V. Kaynig, M. Longair, T. Pietzsch, S. Preibisch, C. Rueden, S. Saalfeld, B. Schmid, J.Y. Tinevez, D.J. White, V. Hartenstein, K. Eliceiri, P. Tomancak, and A. Cardona. 2012. Fiji: an open-source platform for biological-image analysis. *Nat Methods*. 9:676-682.

Schlattner, U., M. Tokarska-Schlattner, and T. Wallimann. 2006. Mitochondrial creatine kinase in human health and disease. *Biochim Biophys Acta*. 1762:164-180.

Schmidt, R., C.A. Wurm, A. Punge, A. Egner, S. Jakobs, and S.W. Hell. 2009. Mitochondrial cristae revealed with focused light. *Nano Lett*. 9:2508-2510.

Sources

Scidmore, M.A., E.R. Fischer, and T. Hackstadt. 2003. Restricted fusion of Chlamydia trachomatis vesicles with endocytic compartments during the initial stages of infection. *Infect Immun*. 71:973-984.

Scorrano, L., M. Ashiya, K. Buttle, S. Weiler, S.A. Oakes, C.A. Mannella, and S.J. Korsmeyer. 2002. A distinct pathway remodels mitochondrial cristae and mobilizes cytochrome c during apoptosis. *Dev Cell*. 2:55-67.

Shim, S.H., C. Xia, G. Zhong, H.P. Babcock, J.C. Vaughan, B. Huang, X. Wang, C. Xu, G.Q. Bi, and X. Zhuang. 2012. Super-resolution fluorescence imaging of organelles in live cells with photoswitchable membrane probes. *Proc Natl Acad Sci U S A*. 109:13978-13983.

Shimomura. 1979. Structure of the chromophore of Aequorea green fluorescent protein. *FEBS Lett*. 104:220-222.

Sicheritz-Ponten, T., C.G. Kurland, and S.G. Andersson. 1998. A phylogenetic analysis of the cytochrome b and cytochrome c oxidase I genes supports an origin of mitochondria from within the Rickettsiaceae. *Biochim Biophys Acta*. 1365:545-551.

Simonis, A., S. Hebling, E. Gulbins, S. Schneider-Schaulies, and A. Schubert-Unkmeir. 2014. Differential activation of acid sphingomyelinase and ceramide release determines invasiveness of Neisseria meningitidis into brain endothelial cells. *PLoS Pathog*. 10:e1004160.

Simons, K., and E. Ikonen. 1997. Functional rafts in cell membranes. *Nature*. 387:569-572.

Siqueira, M.D.S., R.M. Ribeiro, and L.H. Travassos. 2018. Autophagy and Its Interaction With Intracellular Bacterial Pathogens. *Front Immunol*. 9:935.

Sirrenberg, C., M. Endres, H. Folsch, R.A. Stuart, W. Neupert, and M. Brunner. 1998. Carrier protein import into mitochondria mediated by the intermembrane proteins Tim10/Mrs11 and Tim12/Mrs5. *Nature*. 391:912-915.

Sixt, B.S., B. Hiess, L. Konig, and M. Horn. 2012. Lack of effective anti-apoptotic activities restricts growth of Parachlamydiaceae in insect cells. *PLoS One*. 7:e29565.

Snavely, E.A., M. Kokes, J.D. Dunn, H.A. Saka, B.D. Nguyen, R.J. Bastidas, D.G. McCafferty, and R.H. Valdivia. 2014. Reassessing the role of the secreted protease CPAF in Chlamydia trachomatis infection through genetic approaches. *Pathog Dis*. 71:336-351.

Solger, F., T.C. Kunz, J. Fink, K. Paprotka, P. Pfister, F. Hagen, F. Schumacher, B. Kleuser, J. Seibel, and T. Rudel. 2020. A Role of Sphingosine in the Intracellular Survival of Neisseria gonorrhoeae. *Front Cell Infect Microbiol*. 10:215.

Song, Z., H. Chen, M. Fiket, C. Alexander, and D.C. Chan. 2007. OPA1 processing controls mitochondrial fusion and is regulated by mRNA splicing, membrane potential, and Yme1L. *J Cell Biol*. 178:749-755.

Speer, A., J. Sun, O. Danilchanka, V. Meikle, J.L. Rowland, K. Walter, B.R. Buck, M. Pavlenok, C. Holscher, S. Ehrt, and M. Niederweis. 2015. Surface hydrolysis of sphingomyelin by the outer membrane protein Rv0888 supports replication of Mycobacterium tuberculosis in macrophages. *Mol Microbiol*. 97:881-897.

Stanhope, R., E. Flora, C. Bayne, and I. Derre. 2017. IncV, a FFAT motif-containing Chlamydia protein, tethers the endoplasmic reticulum to the pathogen-containing vacuole. *Proc Natl Acad Sci U S A*. 114:12039-12044.

Stephan, T., A. Roesch, D. Riedel, and S. Jakobs. 2019. Live-cell STED nanoscopy of mitochondrial cristae. *Sci Rep*. 9:12419.

Stiburek, L., J. Cesnekova, O. Kostkova, D. Fornuskova, K. Vinsova, L. Wenchich, J. Houstek, and J. Zeman. 2012. YME1L controls the accumulation of respiratory chain subunits and is required for apoptotic resistance, cristae morphogenesis, and cell proliferation. *Mol Biol Cell*. 23:1010-1023.

Stiller, S.B., J. Hopker, S. Oeljeklaus, C. Schutze, S.G. Schrempp, J. Vent-Schmidt, S.E. Horvath, A.E. Frazier, N. Gebert, M. van der Laan, M. Bohnert, B. Warscheid, N. Pfanner, and N. Wiedemann. 2016. Mitochondrial OXA Translocase Plays a Major Role in Biogenesis of Inner-Membrane Proteins. *Cell Metab*. 23:901-908.

Sources

Stokes, G. 1852. On the Change of Refrangibility of Light. *Philosophical Transactions of the Royal Society of London*. 142:463-562.

Strauss, M., G. Hofhaus, R.R. Schroder, and W. Kuhlbrandt. 2008. Dimer ribbons of ATP synthase shape the inner mitochondrial membrane. *EMBO J*. 27:1154-1160.

Sun, Q., X. Yong, X. Sun, F. Yang, Z. Dai, Y. Gong, L. Zhou, X. Zhang, D. Niu, L. Dai, J.J. Liu, and D. Jia. 2017. Structural and functional insights into sorting nexin 5/6 interaction with bacterial effector IncE. *Signal Transduct Target Ther*. 2:17030.

Suresh, M.K., R. Biswas, and L. Biswas. 2019. An update on recent developments in the prevention and treatment of Staphylococcus aureus biofilms. *Int J Med Microbiol*. 309:1-12.

Swim, S.C., M.A. Gfell, C.E. Wilde, 3rd, and R.S. Rosenthal. 1983. Strain distribution in extents of lysozyme resistance and O-acetylation of gonococcal peptidoglycan determined by high-performance liquid chromatography. *Infect Immun*. 42:446-452.

Szabadkai, G., A.M. Simoni, M. Chami, M.R. Wieckowski, R.J. Youle, and R. Rizzuto. 2004. Drp-1-dependent division of the mitochondrial network blocks intraorganellar Ca2+ waves and protects against Ca2+-mediated apoptosis. *Mol Cell*. 16:59-68.

Szaszak, M., P. Steven, K. Shima, R. Orzekowsky-Schroder, G. Huttmann, I.R. Konig, W. Solbach, and J. Rupp. 2011. Fluorescence lifetime imaging unravels C. trachomatis metabolism and its crosstalk with the host cell. *PLoS Pathog*. 7:e1002108.

Tamura, A., and G.P. Manire. 1968. Effect of penicillin on the multiplication of meningopneumonitis organisms (Chlamydia psittaci). *J Bacteriol*. 96:875-880.

Tang, L., J. Chen, Z. Zhou, P. Yu, Z. Yang, and G. Zhong. 2015. Chlamydia-secreted protease CPAF degrades host antimicrobial peptides. *Microbes Infect*. 17:402-408.

Tarasenko, D., M. Barbot, D.C. Jans, B. Kroppen, B. Sadowski, G. Heim, W. Mobius, S. Jakobs, and M. Meinecke. 2017. The MICOS component Mic60 displays a conserved membrane-bending activity that is necessary for normal cristae morphology. *J Cell Biol*. 216:889-899.

Tettamanti, G., R. Bassi, P. Viani, and L. Riboni. 2003. Salvage pathways in glycosphingolipid metabolism. *Biochimie*. 85:423-437.

Thalso-Madsen, I., F.R. Torrubia, L. Xu, A. Petersen, C. Jensen, and D. Frees. 2019. The Sle1 Cell Wall Amidase Is Essential for beta-Lactam Resistance in Community-Acquired Methicillin-Resistant Staphylococcus aureus USA300. *Antimicrob Agents Chemother*. 64.

Thomson, N.R., C. Yeats, K. Bell, M.T. Holden, S.D. Bentley, M. Livingstone, A.M. Cerdeno-Tarraga, B. Harris, J. Doggett, D. Ormond, K. Mungall, K. Clarke, T. Feltwell, Z. Hance, M. Sanders, M.A. Quail, C. Price, B.G. Barrell, J. Parkhill, and D. Longbottom. 2005. The Chlamydophila abortus genome sequence reveals an array of variable proteins that contribute to interspecies variation. *Genome Res*. 15:629-640.

Tillberg, P.W., F. Chen, K.D. Piatkevich, Y. Zhao, C.C. Yu, B.P. English, L. Gao, A. Martorell, H.J. Suk, F. Yoshida, E.M. DeGennaro, D.H. Roossien, G. Gong, U. Seneviratne, S.R. Tannenbaum, R. Desimone, D. Cai, and E.S. Boyden. 2016. Protein-retention expansion microscopy of cells and tissues labeled using standard fluorescent proteins and antibodies. *Nat Biotechnol*. 34:987-992.

Truckenbrodt, S., M. Maidorn, D. Crzan, H. Wildhagen, S. Kabatas, and S.O. Rizzoli. 2018. X10 expansion microscopy enables 25-nm resolution on conventional microscopes. *EMBO Rep*. 19.

Truckenbrodt, S., C. Sommer, S.O. Rizzoli, and J.G. Danzl. 2019. A practical guide to optimization in X10 expansion microscopy. *Nat Protoc*. 14:832-863.

Unemo, M., and W.M. Shafer. 2014. Antimicrobial resistance in Neisseria gonorrhoeae in the 21st century: past, evolution, and future. *Clin Microbiol Rev*. 27:587-613.

van der Laan, M., M. Bohnert, N. Wiedemann, and N. Pfanner. 2012. Role of MINOS in mitochondrial membrane architecture and biogenesis. *Trends Cell Biol*. 22:185-192.

Van Leeuwenhoek, A. 1677. Observations, communicated to the publisher by Mr. Antony van Leewenhoeck, in a dutch letter of the 9th Octob. 1676. here English'd: concerning little animals by him observed in rain-well-sea- and snow water; as also in water wherein pepper had lain infused.

Sources

van Ooij, C., L. Kalman, I. van, M. Nishijima, K. Hanada, K. Mostov, and J.N. Engel. 2000. Host cell-derived sphingolipids are required for the intracellular growth of Chlamydia trachomatis. *Cell Microbiol*. 2:627-637.

van Wilpe, S., M.T. Ryan, K. Hill, A.C. Maarse, C. Meisinger, J. Brix, P.J. Dekker, M. Moczko, R. Wagner, M. Meijer, B. Guiard, A. Honlinger, and N. Pfanner. 1999. Tom22 is a multifunctional organizer of the mitochondrial preprotein translocase. *Nature*. 401:485-489.

Vial, S., H. Lu, S. Allen, P. Savory, D. Thornton, J. Sheehan, and K. Tokatlidis. 2002. Assembly of Tim9 and Tim10 into a functional chaperone. *J Biol Chem*. 277:36100-36108.

Viswanathan, G., M. Jafurulla, G.A. Kumar, T.R. Raghunand, and A. Chattopadhyay. 2018. Macrophage sphingolipids are essential for the entry of mycobacteria. *Chem Phys Lipids*. 213:25-31.

Vogel, F., C. Bornhovd, W. Neupert, and A.S. Reichert. 2006. Dynamic subcompartmentalization of the mitochondrial inner membrane. *J Cell Biol*. 175:237-247.

Vogtle, F.N., S. Wortelkamp, R.P. Zahedi, D. Becker, C. Leidhold, K. Gevaert, J. Kellermann, W. Voos, A. Sickmann, N. Pfanner, and C. Meisinger. 2009. Global analysis of the mitochondrial N-proteome identifies a processing peptidase critical for protein stability. *Cell*. 139:428-439.

von der Malsburg, K., J.M. Muller, M. Bohnert, S. Oeljeklaus, P. Kwiatkowska, T. Becker, A. Loniewska-Lwowska, S. Wiese, S. Rao, D. Milenkovic, D.P. Hutu, R.M. Zerbes, A. Schulze-Specking, H.E. Meyer, J.C. Martinou, S. Rospert, P. Rehling, C. Meisinger, M. Veenhuis, B. Warscheid, I.J. van der Klei, N. Pfanner, A. Chacinska, and M. van der Laan. 2011. Dual role of mitofilin in mitochondrial membrane organization and protein biogenesis. *Dev Cell*. 21:694-707.

Vouga, M., D. Baud, and G. Greub. 2017. Simkania negevensis, an insight into the biology and clinical importance of a novel member of the Chlamydiales order. *Crit Rev Microbiol*. 43:62-80.

Wagner, F., T.C. Kunz, S.R. Chowdhury, B. Thiede, M. Fraunholz, D. Eger, and V. Kozjak-Pavlovic. 2019. Armadillo repeat-containing protein 1 is a dual localization protein associated with mitochondrial intermembrane space bridging complex. *PLoS One*. 14:e0218303.

Walter, T., L. Collenburg, L. Japtok, B. Kleuser, S. Schneider-Schaulies, N. Muller, J. Becam, A. Schubert-Unkmeir, J.N. Kong, E. Bieberich, and J. Seibel. 2016. Incorporation and visualization of azido-functionalized N-oleoyl serinol in Jurkat cells, mouse brain astrocytes, 3T3 fibroblasts and human brain microvascular endothelial cells. *Chem Commun (Camb)*. 52:8612-8614.

Walter, T., J. Schlegel, A. Burgert, A. Kurz, J. Seibel, and M. Sauer. 2017. Incorporation studies of clickable ceramides in Jurkat cell plasma membranes. *Chem Commun (Camb)*. 53:6836-6839.

Wang, C., M. Taki, Y. Sato, Y. Tamura, H. Yaginuma, Y. Okada, and S. Yamaguchi. 2019. A photostable fluorescent marker for the superresolution live imaging of the dynamic structure of the mitochondrial cristae. *Proc Natl Acad Sci U S A*. 116:15817-15822.

Wang, S.P., and J.T. Grayston. 1970. Immunologic relationship between genital TRIC, lymphogranuloma venereum, and related organisms in a new microtiter indirect immunofluorescence test. *Am J Ophthalmol*. 70:367-374.

Wassie, A.T., Y. Zhao, and E.S. Boyden. 2019. Expansion microscopy: principles and uses in biological research. *Nat Methods*. 16:33-41.

Weber, M.M., N.F. Noriea, L.D. Bauler, J.L. Lam, J. Sager, J. Wesolowski, F. Paumet, and T. Hackstadt. 2016. A Functional Core of IncA Is Required for Chlamydia trachomatis Inclusion Fusion. *J Bacteriol*. 198:1347-1355.

Weber, T.A., S. Koob, H. Heide, I. Wittig, B. Head, A. van der Bliek, U. Brandt, M. Mittelbronn, and A.S. Reichert. 2013. APOOL is a cardiolipin-binding constituent of the Mitofilin/MINOS protein complex determining cristae morphology in mammalian mitochondria. *PLoS One*. 8:e63683.

Weinhaupl, K., C. Lindau, A. Hessel, Y. Wang, C. Schutze, T. Jores, L. Melchionda, B. Schonfisch, H. Kalbacher, B. Bersch, D. Rapaport, M. Brennich, K. Lindorff-Larsen, N. Wiedemann, and P. Schanda. 2018. Structural Basis of Membrane Protein Chaperoning through the Mitochondrial Intermembrane Space. *Cell*. 175:1365-1379 e1325.

Westermann, B. 2010. Mitochondrial fusion and fission in cell life and death. *Nat Rev Mol Cell Biol*. 11:872-884.

Sources

Wheelhouse, N., and D. Longbottom. 2012. Endemic and emerging chlamydial infections of animals and their zoonotic implications. *Transbound Emerg Dis*. 59:283-291.

Wiedemann, N., V. Kozjak, A. Chacinska, B. Schonfisch, S. Rospert, M.T. Ryan, N. Pfanner, and C. Meisinger. 2003. Machinery for protein sorting and assembly in the mitochondrial outer membrane. *Nature*. 424:565-571.

Wiedemann, N., N. Pfanner, and M.T. Ryan. 2001. The three modules of ADP/ATP carrier cooperate in receptor recruitment and translocation into mitochondria. *EMBO J*. 20:951-960.

Wilson, D.P., P. Timms, D.L. McElwain, and P.M. Bavoil. 2006. Type III secretion, contact-dependent model for the intracellular development of chlamydia. *Bull Math Biol*. 68:161-178.

Wilson, M. 2017. Introduction to Widefield Microscopy. *Leica Microsystems*.

Wittig, I., M. Karas, and H. Schagger. 2007. High resolution clear native electrophoresis for in-gel functional assays and fluorescence studies of membrane protein complexes. *Mol Cell Proteomics*. 6:1215-1225.

Woese, C.R., and G.E. Fox. 1977. Phylogenetic structure of the prokaryotic domain: the primary kingdoms. *Proc Natl Acad Sci U S A*. 74:5088-5090.

Wolf, D.M., M. Segawa, A.K. Kondadi, R. Anand, S.T. Bailey, A.S. Reichert, A.M. van der Bliek, D.B. Shackelford, M. Liesa, and O.S. Shirihai. 2019. Individual cristae within the same mitochondrion display different membrane potentials and are functionally independent. *EMBO J*. 38:e101056.

Wolf, K., and T. Hackstadt. 2001. Sphingomyelin trafficking in Chlamydia pneumoniae-infected cells. *Cell Microbiol*. 3:145-152.

Wollweber, F., K. von der Malsburg, and M. van der Laan. 2017. Mitochondrial contact site and cristae organizing system: A central player in membrane shaping and crosstalk. *Biochim Biophys Acta Mol Cell Res*. 1864:1481-1489.

Wyrick, P.B. 2010. Chlamydia trachomatis persistence in vitro: an overview. *J Infect Dis*. 201 Suppl 2:S88-95.

Xie, J., M.F. Marusich, P. Souda, J. Whitelegge, and R.A. Capaldi. 2007. The mitochondrial inner membrane protein mitofilin exists as a complex with SAM50, metaxins 1 and 2, coiled-coil-helix coiled-coil-helix domain-containing protein 3 and 6 and DnaJC11. *FEBS Lett*. 581:3545-3549.

Yang, R.F., L.H. Sun, R. Zhang, Y. Zhang, Y.X. Luo, W. Zheng, Z.Q. Zhang, H.Z. Chen, and D.P. Liu. 2015. Suppression of Mic60 compromises mitochondrial transcription and oxidative phosphorylation. *Sci Rep*. 5:7990.

Yang, Z., L. Tang, Z. Zhou, and G. Zhong. 2016. Neutralizing antichlamydial activity of complement by chlamydia-secreted protease CPAF. *Microbes Infect*. 18:669-674.

Yoon, Y., C.A. Galloway, B.S. Jhun, and T. Yu. 2011. Mitochondrial dynamics in diabetes. *Antioxid Redox Signal*. 14:439-457.

Young, J.C., N.J. Hoogenraad, and F.U. Hartl. 2003. Molecular chaperones Hsp90 and Hsp70 deliver preproteins to the mitochondrial import receptor Tom70. *Cell*. 112:41-50.

Young, M.M., M. Kester, and H.G. Wang. 2013. Sphingolipids: regulators of crosstalk between apoptosis and autophagy. *J Lipid Res*. 54:5-19.

Yuan, S., D.B. Cohen, J. Ravel, Z. Abdo, and L.J. Forney. 2012. Evaluation of methods for the extraction and purification of DNA from the human microbiome. *PLoS One*. 7:e33865.

Zeharia, A., J.R. Friedman, A. Tobar, A. Saada, O. Konen, Y. Fellig, A. Shaag, J. Nunnari, and O. Elpeleg. 2016. Mitochondrial hepato-encephalopathy due to deficiency of QIL1/MIC13 (C19orf70), a MICOS complex subunit. *Eur J Hum Genet*. 24:1778-1782.

Zhang, Y., X. Li, A. Carpinteiro, and E. Gulbins. 2008. Acid sphingomyelinase amplifies redox signaling in Pseudomonas aeruginosa-induced macrophage apoptosis. *J Immunol*. 181:4247-4254.

Zhong, G. 2014. Question the questions on CPAF. *Pathog Dis*. 72:3-4.

Zhong, G., P. Fan, H. Ji, F. Dong, and Y. Huang. 2001. Identification of a chlamydial protease-like activity factor responsible for the degradation of host transcription factors. *J Exp Med*. 193:935-942.

Zhu, H., Z. Shen, H. Luo, W. Zhang, and X. Zhu. 2016. Chlamydia Trachomatis Infection-Associated Risk of Cervical Cancer: A Meta-Analysis. *Medicine (Baltimore)*. 95:e3077.

Sources

Zick, M., R. Rabl, and A.S. Reichert. 2009. Cristae formation-linking ultrastructure and function of mitochondria. *Biochim Biophys Acta*. 1793:5-19.

Acknowledgments

First, I would like to thank my thesis committee for the supervision, the fruitful talks and discussions and the great collaboration during my PhD-Thesis. I want to thank Dr. Vera Kozjak-Pavlovic for being my primary supervisor, her great supervision, constructive feedback, project planning and her steady support. Thank you for sharing the enthusiasm for every little result obtained during our projects and constantly pushing my motivation. Thank you as well for teaching me to work and think independently and to always question my own results. Furthermore, I would like to thank Prof. Dr. Thomas Rudel for giving me the opportunity to perform my thesis at the Chair of Microbiology, being part of my thesis committee, fruitful talks and helping to establish very successful projects. Thank you, Thomas, for supporting me since my master, for my PhD and beyond. Moreover, I would like to thank David, Marcel, Adriana, Franzi, Nadine, Roy, Elke and the whole chair of microbiology for common projects and the great and fun time at the department. I would also like to thank Prof. Dr. Georg Nagel for acting as my second supervisor, the great collaboration and open mind for all my projects as well as the steady support to achieve the planned goals. In this sense, I would also like to thank Shiqiang Gao of the Nagel group for the steady support, his thinking outside the box and for constantly bringing ideas into common projects. A special thanks goes also to Prof. Dr. Markus Sauer for the many exciting projects performed in collaboration, all the advice and feedback and for being part of my thesis committee. I want to especially thank Ralph Götz for introducing me to expansion microscopy, the fun time together in front of the microscope and sharing frustration and enthusiasm. Furthermore, I want to express my gratitude to Prof. Dr. Jürgen Seibel and Julian Fink for the synthesis of our functional α-NH$_2$-ω-N$_3$-C$_6$-ceramide analogue and the great collaboration of our project.

Mein allergrößter Dank geht an meine Familie, insbesondere meine Eltern, die mich in jeder Situation unterstützen. Danke auch an meinen älteren Bruder Felix, seine Frau Jessi und meine ältere Schwester Tini für den festen Zusammenhalt. Danke auch meiner Nichte Hannah und meinem Neffen Leo für die Ablenkung und Freude, wenn es mal etwas stressiger wurde. Des Weiteren möchte ich mich bei meiner Oma für die vielen lieben Worte und ihre Unterstützung bedanken. Zu aller Letzt gilt mein ganz besonderer Dank meiner Lebensgefährtin, Jade, für die unglaubliche Geduld, das Interesse an meiner Arbeit und die konstante Unterstützung.

Affidavit

I hereby confirm that my thesis entitled "Expansion Microscopy (ExM) as a tool to study organelles and intracellular pathogens" is the result of my own work. I did not receive any help or support from commercial consultants. All sources and / or materials applied are listed and specified in the thesis.

Furthermore, I confirm that this thesis has not yet been submitted as part of another examination process neither in identical nor in similar form.

Place, Date   Signature

Eidesstattliche Erklärung

Hiermit erkläre ich an Eides statt, die Dissertation „Expansionsmikroskopie (ExM) als Tool zur Untersuchung von Organellen und intrazellulären Pathogenen" eigenständig, d.h. insbesondere selbständig und ohne Hilfe eines kommerziellen Promotionsberaters, angefertigt und keine anderen als die von mir angegebenen Quellen und Hilfsmittel verwendet zu haben.

Ich erkläre außerdem, dass die Dissertation weder in gleicher noch in ähnlicher Form bereits in einem anderen Prüfungsverfahren vorgelegen hat.

Ort, Datum   Unterschrift